Single Cell Tracking of Therapeutic Cells Using Laser Ablation - Inductively Coupled Plasma - Mass Spectrometry

Amy Joan Managh

A Doctoral Thesis

Submitted in partial fulfilment of the requirements for the award of
Doctor of Philosophy of Loughborough University

November 2014

Abstract

Cellular therapy is emerging as a clinically viable strategy in the field of solid organ transplantation, where it is expected to reduce the dependency on conventional immunosuppression. This has produced a demand for highly sensitive methods to monitor the persistence and tissue distribution of administered cells *in vivo*. However, tracking cells presents significant challenges. In many cases transplanted cells are autologous with the immune system of the transplant recipient, and hence are invisible to typical methods of detection. To enable their differentiation, the cells must be labelled with a suitable, non-toxic and long lifetime label, prior to their administration to patients. In addition, administered cells represent only a small fraction of the recipient's endogenous cells, which necessitates the use of an extremely sensitive detection method. Laser ablation – inductively coupled plasma – mass spectrometry (LA-ICP-MS) is an exquisitely sensitive analytical technique, capable of imaging trace elements in complex samples, at high spatial resolution.

This thesis reports the use of commercially available labelling agents to tag therapeutic cells, permitting their subsequent detection on an individual cell basis using LA-ICP-MS. Label uptake rates in the order of 10^8 atoms per cell were achieved for T cells labelled with the Gd-based MRI contrast agent Omniscan, and Mregs and Tol-DC labelled with 50 nm gold nanoparticles. Close to 100% labelling and detection efficiency was observed for all three cell types. Importantly, the cells retained sufficient label to remain detectable for up to 14 days following administration to immunodeficient mice. However, the lengthy analysis times associated with current LA-ICP-MS systems preclude its use for routine clinical monitoring. Therefore, the final section of the thesis discusses a prototype fast-washout LA-ICP-MS interface, which provided a 5-6 fold increase in detection efficiency and peak widths of less than 10 ms.

Keywords: single cell analysis; cell tracking; laser ablation; ICP-MS; MRI contrast agents; gold nanoparticles; computational fluid dynamics; T cells; Mregs; Tol-DC.

Acknowledgements

I am immensely grateful to my supervisors, Barry Sharp and Helen Reid, for giving me the opportunity to work on this project, for their time, patience, enthusiasm and encouragement, and for their continued belief in me. I feel incredibly privileged to have worked with you during my PhD and am even more grateful for the opportunity to continue working with you beyond it.

Thank you to the ONE Study consortium (European Commission 7th Framework Program, project reference 260687) for funding the PhD. The project could not have succeeded without support from our ONE Study collaborative partners, who have generously given their time and resources to assist with cell tracking experiments. I sincerely thank Andrew Bushell, his student Sheldon Edwards, and his colleagues at the University of Oxford for preparing nTreg samples, James Hutchinson and colleagues at the Universität Regensburg for preparing Mreg samples, and Aurélie Moreau, Laurence Delbos and their colleagues at the Université de Nantes for preparing Tol-DC samples. I also thank Rob Hutchinson, Ciaran O’Connor and their colleagues at Electro Scientific Industries for inviting us to participate in the ONE Study and for their interest in our prototype high-speed LA-ICP-MS interface.

Thank you to my colleagues in the Centre for Analytical Science at Loughborough University. I have worked with a diverse range of characters who have each contributed to my PhD experience in their own unique way. A special thank you to David Douglas for his work on the LA-ICP-MS interface, for the valuable discussions we shared on this topic, and for setting an extremely high standard for me to aspire to. I would also like to thank Pareen Patel, Claire Camp and Aref Zayed for their support when I joined the group, and Sarah Taylor, Tharwat Abduljabbar and Grant Craig for their much valued friendship and for sharing the burden of instrument maintenance. It has been a pleasure to work with all of you. Thanks also to Paul Kelly, an honorary member of the group, for the daily entertainment.

I am grateful to all of the support staff at Loughborough University, particularly Trevor Brown, Mark Weller, Stuart Pinkney, Andy Kowalski, Charles Burrough, Bob Ludlam and Ramesh Pancholi, for their various contributions. I also thank Chris Reardon and Jose Leitao from ESI for their advice on UP-213 maintenance, David Hinds from Thermo Scientific for his advice on Element XR troubleshooting and repair, and Lothar

Rottmann and Torsten Lindemann from Thermo Scientific for their assistance with connecting our data acquisition board to the Element XR.

I have been fortunate to have been taught by a number of fantastic teachers and lecturers, who have encouraged and developed my interest in Science. I particularly wish to thank my secondary school Chemistry teachers, Mrs Fairweather and Mrs Blagden, for inspiring my interest in Chemistry and for supporting me in my ambition to study the subject at University.

On a personal note, I would like to express my gratitude to my mother and father for the sacrifices they made to give me the best possible opportunities in life and for helping me to make my dreams become a reality. Finally, I dedicate this thesis to my Nan, who was not fortunate enough to receive a good education herself, but has always passionately advocated the importance of education and provided me with the best possible start to my educational life. Thank you Nan!

Table of Contents

3 GOLD LABELLING OF REGULATORY MACROPHAGES AND DENDRITIC CELLS 68

4 DEVELOPMENT OF A HIGH-SPEED LA-ICP-MS INTERFACE FOR BIO-IMAGING 89

List of Tables

List of Figures

Glossary of Terms

µDG	Micro droplet generator
CFD	Computational fluid dynamics
CFSE	Carboxyfluorescein diacetate succinimidyl ester
CTAB	Cetyltrimethylaluminium bromide
CyTOF	Flow cytometry time-of-flight mass spectrometry
DCI	Direct concentric injector
DPBS	Dulbecco's phosphate buffered saline
ESA	Electrostatic analyser
ESI Inc.	ElectroScientific Industries Incorporated
ESI	Electrospray ionisation
FACS	Fluorescence activated cell sorting
FCS	Fetal calf serum
FW0.01M	Full width at 1% peak maximum
FW0.1M	Full width at 10% peak maximum
FWHM	Full width half maximum
GC-MS	Gas chromatography – mass spectrometry
Gd-DOTA	Gadolinium 1,4,7,10-tetraazacyclododecane-1,4,7,10-tetracarboxylic acid
Gd-DTPA-BMA	Gadolinium diethylenetriaminepentaacetic acid bismethylamide
GM-CSF	Granulocyte-macrophage colony-stimulating factor
GVHD	Graft versus host disease
HLA-DR	Human leukocyte antigen D-related
HSC	Haematopoietic stem cell
ICP	Inductively coupled plasma
ICP-MS	Inductively coupled plasma – mass spectrometry
ICP-OES	Inductively coupled plasma – optical emission spectroscopy
IL-2	Interleukin 2
LA-ICP-MS	Laser ablation – inductively coupled plasma – mass spectrometry
LFR	Laminar flow reactor
MACS	Magnetic activated cell sorting
MALDI	Matrix-assisted laser desorption ionisation
Mreg	Regulatory macrophage

MRI	Magnetic resonance imaging
NAD(P)H	Nicotinamide adenine dinucleotide phosphate
Nd:YAG	Neodymium-doped yttrium aluminium garnet
NIST	National Institute of Standards and Technology
NSF	Nephrogenic systemic fibrosis
NSG	NOD.Cg-Prkdc^{scid} Il2rg^{tm1Wjl}/SzJ (strain of immunodeficient mice)
nTreg	Naturally occurring regulatory T cells
PBS	Phosphate buffered saline
PBMC	Peripheral blood mononuclear cells
PET	Positron emission tomography
RF	Radio frequency
RSD	Relative standard deviation
SEM	Secondary electron multiplier
SF	Sector-field
SPECT	Single photon emission computed tomography
TDC	Tear-drop cell / Zircon cell
TOF	Time-of-flight
Tol-DC	Tolerogenic dendritic cell
TBS	Tris buffered saline
VOLM	Volume-optional low-memory
VPD	Violet proliferation dye
WP2	‘ONE Study’ work package 2

1 Introduction

1.1 Introduction to the ONE Study

Cellular therapy is emerging as a clinically viable strategy in the fields of haematopoietic stem cell (HSC) transplantation, autoimmune disease and solid organ transplantation. An international consortium, known as the ONE Study, is currently seeking regulatory approval for the use of several types of regulatory immune cells in living-donor kidney transplantation. The ONE Study aims to provide a unified approach to the evaluation of cell based therapies, such as nTreg,[1-3] Tr1 cells,[4, 5] dendritic cells,[6] and macrophages.[7, 8] It is expected that these tolerance promoting cells will reduce the dependence on existing pharmacological immunosuppression, providing a longer term solution to the rejection of transplanted organs, as well as lowering healthcare costs, toxicity concerns, and the problem of impaired general immunity associated with current immunosuppressant drugs.

The ONE Study is broken down into eight different Work Packages, which cover the research, development, licensing, use, monitoring, and statistical analysis of the various cellular therapies. Determining the survival and tissue distribution of administered cells is central to understanding their mechanism of action *in vivo,* which is likely to be a prerequisite for their progression beyond Phase I/II trials. Therefore, the objective of Work Package 2 (WP2) is to develop a new methodology to track administered cells after their administration to patients. This task is being undertaken by Loughborough University and will form the basis of this thesis.

Tracking therapeutic cells presents a number of significant technical challenges. In the majority of cases, cellular therapies are derived from either the transplant donor or from the transplant recipient. Thus, the administered cells are indistinguishable from the patient's own immune cells when using conventional detection methods, such as flow cytometry. To enable their differentiation, the cells must be labelled with a clinically acceptable label prior to their administration to patients. At minimum, this label should be non-toxic and remain detectable in the recipient's blood for several weeks post-administration.[9] At current planned doses, the administered cells will represent only a small fraction of the recipient's endogenous regulatory immune cells, perhaps less than 1 in 10^5 cells. Therefore a highly sensitive detection method is required for their detection, capable of the detection of single cells at very high cell detection efficiency. Laser ablation inductively coupled plasma mass spectrometry (LA-ICP-MS) is an ideal candidate for this application due to its potential to provide a combination of high sensitivity and high spatial resolution. The technique has been widely used for the detection of trace elements in complex biological samples, and is applicable to both extracted cells and tissue sections. A pictorial representation of the workflow required for the analysis is shown in Figure 1.1.

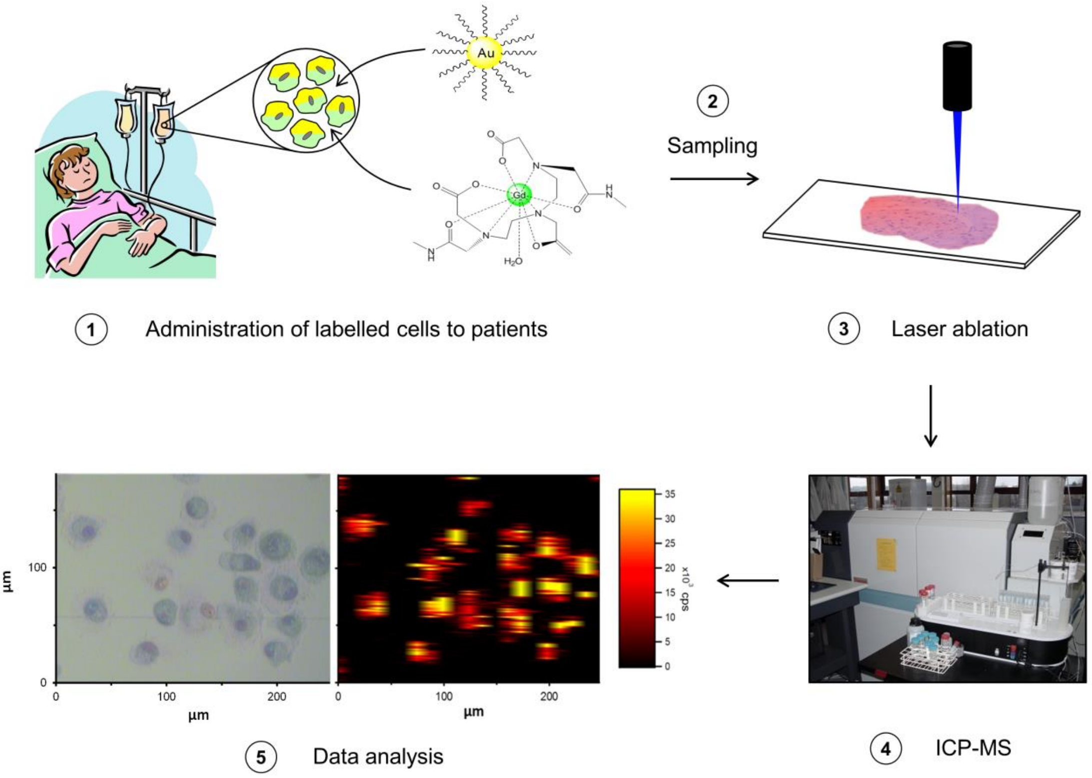

Figure 1.1 A representation of the work flow required for tracking cells by LA-ICP-MS.

1.2 Introduction to Cell Labelling

A wide variety of cellular labelling agents are currently in use for various medical applications. For example, gadolinium contrast agents for magnetic resonance imaging (MRI), iodine and indium radiolabels for single photon emission computed tomography (SPECT), fluorescent dyes for fluorescence imaging, and various nanoparticles for imaging, bio-sensing and drug delivery. Although initially developed for their respective applications, many of these agents contain elements detectable by ICP-MS. However, in addition to compatibility with ICP-MS, there are three other key areas to consider when choosing a cell labelling agent. Firstly, the amount of label taken up by the cells must be sufficient to enable their differentiation from non-labelled cells. Secondly, the label must be retained by the cells at an adequate concentration to remain detectable at several weeks post-labelling. Thirdly, the label must not induce toxic effects to either the cells themselves or the body as a whole. These key issues will be discussed in the following sections.

1.2.1 Label uptake

Although there are examples of cell labelling *in vivo*, labelling cells *in vitro* prior to cell transplantation is the more common approach to cell tracking. Following initial culture to expand the cell population, the label is added to the cell culture medium at the desired concentration. The cells are then allowed to culture in the presence of the label for a further period, promoting uptake. This incubation period varies considerably depending on the cell type, labelling agent and desired level of uptake, but is typically between 1 and 48 hours. The cells must then be washed extensively to remove any unbound label, before administration to the subject of interest.

As shown in Figure 1.2, some labels attach extra-cellularly to the cell membrane, whereas others are internalised and reside within the cytosol or intracellular vesicles. Extra-cellular labels are usually targeted towards specific features on the cell surface. This is often achieved through the use of antibody conjugated labels, which bind to their respective antigens on the cell surface (Figure 1.2 A). An additional method involves the use of linkers that form covalent bonds to proteins on the cell surface. For example, an approach reported by Digilio *et al.* used a 2-pyridyl-dithio group as a linker between the MRI contrast agent, Gd-DO3A, and exofacial protein thiols on human myeloid leukaemia cells.[10] In general, internalisation of labels is preferable to extra-cellular attachment, as these labels tend to have a higher uptake and a longer lifetime attached to the cell.[11] Additionally, internalised labels that are compartmentalised inside endosomes may exhibit reduced toxicity in comparison to their extracellular counterparts.

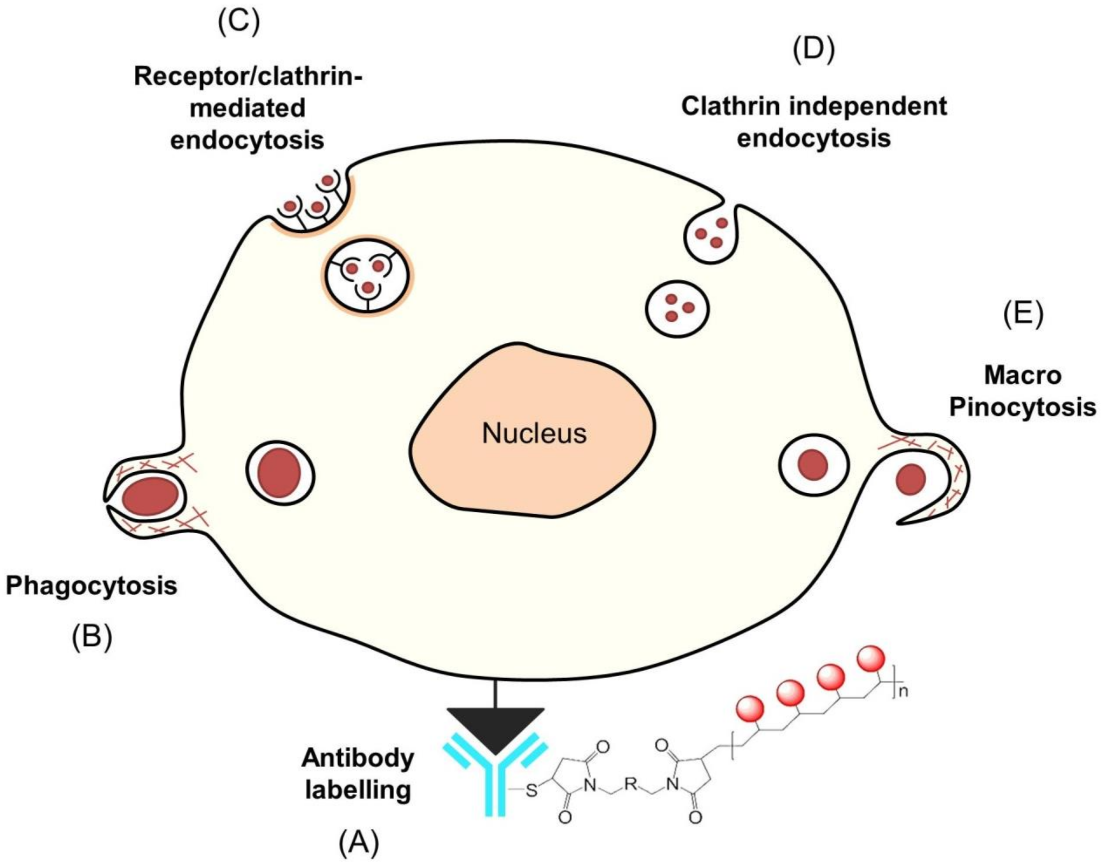

Figure 1.2 A summary of the various mechanisms by which labels can attach to cells.

Internalisation of labels usually occurs by an endocytic mechanism. There are two main categories of endocytosis. The first of these, phagocytosis (Figure 1.2 B), covers the internalisation of large solid particles. Phagocytosis is carried out extensively by specific immune cells, such as macrophages and dendritic cells, whose function is to clear dead cells and remove pathogens. The solid particles bind initially to the cell membrane, which triggers the extension of temporary projections, known as pseudopods, to engulf the particle and enclose it in a vesicle.[12] Once enclosed, the vesicle separates from the membrane and passes into the intracellular fluid, where it may fuse with other cellular components. In contrast, the second category, pinocytosis, concerns the internalisation of fluids and small particles in solution. Pinocytosis is a broad term that covers many types of fluid uptake, the most common of which are receptor/clathrin-mediated endocytosis (Figure 1.2 C), clathrin independent endocytosis (Figure 1.2 D) and micropinocytosis (Figure 1.2 E).[13] These mechanisms differ slightly in terms of their pathway and scale. However, as with phagocytosis, all involve initial contact with the plasma membrane, either through non-specific means or by specific interactions with receptors on the cell surface, followed by engulfment of the material into vesicles. In contrast to phagocytosis, pinocytosis is performed to some extent by all eukaryotic cell lines.

Optimisation of labelling agents to promote their uptake has been widely discussed. Characteristics such as the size and shape of the labelling agent, its concentration, the labelling method and the incubation time have a considerable impact on label uptake. Surface chemistry also plays a vital role. Uptake can be increased, decreased, or made specific to a type of cell by the inclusion of surface modifiers on the labelling agent,[14] or by their incorporation into liposomes.[15] Cationic liposomal carriers are frequently used to increase label uptake, as their positive charge promotes adhesion to the cell surface, triggering endocytic uptake into the cell.[15]

1.2.2 Label retention

Section 1.2.1 covered the uptake of labels by cells. Once within the cell, a mechanism exists to expel unwanted material. When substances are not bound specifically to cell features, they may be removed over a period of time by a process known as exocytosis. Exocytosis is the reverse process to endocytosis. Vesicles form around material inside the cell and fuse with the plasma membrane, where they release the material into the extra-cellular environment. As a result of this process, the cell loading of most labels is expected to decay over time.

In addition to label leakage, the cell loading will also decrease during cell reproduction. It is important to know whether the labels are retained in one cell, split equally between daughter cells, or if they wholly or partially leak out to the surrounding tissue. Complete leakage of the label during cell division limits cell monitoring to only the original cells. However, if the label is passed on to daughter cells, longer term monitoring can be achieved. This was demonstrated by Guenoun *et al.*, who performed tracking of Gd-DTPA labelled mesenchymal stem cells over several cell cycles.[16] Interestingly, whilst the amount of Gd per cell clearly reduced after each division, the net amount of Gd in the cell population remained constant, indicating excellent retention of the label by the cell population. When labels are known to split equally between daughter cells, valuable information on the *in vivo* growth of the cell population can be obtained. An example of this is the fluorescent label carboxyfluoresin diacetate succinimidyl ester (CFSE), which reacts with free amine groups on intracellular proteins.[17] Since proteins are split equally between daughter cells during cell division, the quantity of the label, and hence the intensity of the fluorescence signal, is also halved. This reduction in fluorescence can be easily quantified using flow cytometry,[17] and consequently CFSE is widely used by immunologists as a marker of cell proliferation.

It is also important to consider the fate of the label after cell death. Cell death primarily occurs via one of two pathways: apoptosis or necrosis.[18] Apoptosis is an example of programmed cell death, where the cell disassembles into small vesicles known as apoptotic bodies.[18] Whereas, during necrosis, or accidental cell death, the cell falls apart and is digested by its own enzymes, spilling its contents out to the surroundings.[18] In both instances the debris and apoptotic bodies are phagocytosed by neighbouring cells and macrophages.[18] This is potentially problematic for cell tracking, as any label present in the cell will be passed on to other cells or macrophages, providing an erroneous signal. This scenario was demonstrated by Winter *et al*., who were unable to distinguish living iron oxide labelled cells from those phagocytosed by macrophages when using MRI.[19] The use of a dual labelling strategy is a suggested solution to the problem. It is unlikely that two independent labels, with differing routes of excretion would be absorbed by the same non-implanted cell, so identification of a therapeutic cell can be confirmed by observation of both signals within the single cell.

1.2.3 Indirect labelling

As discussed above, most labelling strategies involve direct accumulation of the label by the cell, prior to administration of the cells to the subject. However, in some instances, such as when using limited lifetime labels, it may be beneficial to introduce the label at a later time point, once the cells are *in vivo*. An example of this is the reporter gene/reporter probe approach.[20] A reporter gene, rather than a label, is transfected into the cells prior to transplantation. The label, known as a reporter probe, is designed to bind to the reporter gene, and can be injected at analytically relevant intervals to label the cells. The reporter gene/reporter probe approach has two main advantages over direct labelling. Firstly, as the label is not administered until shortly before detection, the problem of label leakage and decay is reduced. Secondly, since the presence of the reporter probe is not reduced by cell division, the monitoring of daughter cells is also feasible. However, the stable transfection of reporter genes into cell lines remains challenging, and extensive testing is subsequently required to determine the impact of the inserted genes on cell function and mortality.

1.2.4 Toxicity

Toxicity is a key concern when introducing exogenous substances into cells, particularly when these cells are intended for administration to patients. The labels under consideration for this study were developed for medical applications, and accordingly their systemic toxicity has generally been assessed.[21, 22] However, whilst a label may be licensed for a specific medical application, this license doesn't necessarily cover their use for cell labelling and tracking. Indeed, substances developed for intra-venous administration may have quite different effects when introduced directly into cells. Even where cytotoxicity has been assessed,[23, 24] the results may not prove applicable to all cell types. Cell types can differ considerably in terms of their receptors and function, and this has been shown to produce differing levels of uptake and toxicity.[25] Therefore, the toxicity of any proposed label and its effect on cell survival, proliferation and function will need to be separately evaluated for the ONE Study prior to the commencement of human clinical trials.

Cytotoxicity is measured using a variety of toxicological assays. These typically use changes in colour or fluorescence intensity to monitor various indicators of cell viability. Cell membrane integrity is assessed via the addition of dyes, such as propidium iodide or trypan blue, which easily diffuse through damaged cell membranes, but cannot penetrate intact cells. The metabolic function of cells is tested by employing indicators, such as calcein AM and alamar blue, which produce fluorescent metabolites after reaction with intra-cellular esterases or reductases.[26] Measurement of cellular autofluorescence is also an indicator of cell health, since the fluorescence of some cellular compounds is altered by the presence of toxic substances. For instance, the fluorescence intensity of NAD(P)H is greatly reduced after reaction with reactive oxygen species during oxidative stress.[27] As mentioned in section 1.2.2, cell reproduction may also be studied over a limited number of cell cycles by monitoring the reduction in the fluorescence emission from internalised fluorescent labels.

1.3 Introduction to Cell Analysis and Tracking

The following section gives a brief introduction to the diverse range of techniques currently used for cell tracking and analysis. The choice of technique is based on a balance of factors such as sensitivity, resolution, cost, safety, and the speed of data acquisition. The choice is also heavily dependent on the cell type, test subject, and proposed application, with applications aimed towards human clinical use tending to favour non-invasive techniques over those requiring *ex-vivo* biopsies. At present there is no single technique that is perfect for cell tracking. Consequently the vast majority of research articles describe multi-modal imaging, using various combinations of the techniques outlined below.

1.3.1 MRI

Cells tracked by magnetic resonance imaging (MRI) are usually labelled with a contrast agent prior to implantation. The presence of the contrast agent changes the relaxation rate of surrounding water protons, producing hypo- or hyper-intense regions in the image, and thus enabling differentiation of the cells from the surrounding material. Multiple articles report the use of MRI to visualise cells or cell clusters. Examples include the *in vitro* visualisation of cells embedded in gelatine,[28, 29] and the *in vivo* tracking of transplanted cells in rats or mice.[16, 30-32] This tracking has even been performed at several weeks post-labelling.[16, 30]

In some cases, MRI has sufficient sensitivity to detect signals from individual cells, and as a result many authors in this field classify their publications as single cell work.[29, 32] However, it should be noted that even with custom built modifications, the spatial resolution achieved for this analysis is typically around 100 x 100 x 200 μm^3,[29, 32] which is considerably larger than the average dimensions of a cell. Co-registration with other techniques, such as fluorescence microscopy, is often required to differentiate the presence of a single cell from that of a cell cluster, or from other interfering artefacts, such as air pockets, haemorrhage, or non-cellular contrast agent. This co-registration is often performed *ex-vivo* and may require co-labelling with other agents, such as fluorescent probes.

1.3.2 PET and SPECT

Single photon emission computed tomography (SPECT),[7, 33] and positron emission tomography (PET)[34] have both been used to monitor the migration of cells for limited periods *in vivo*. These techniques have higher sensitivity, but lower spatial resolution than MRI, and are typically used for bulk, rather than single cell tracking. Both PET and SPECT rely on the detection of gamma rays emitted from radiolabels, and consequently exposure to radiation is an unavoidable product of these methods. The labels are also prone to radioactive decay and biological clearance, rendering tracking beyond a few days or weeks extremely difficult. Reporter gene/reporter probe labelling has the potential to permit longer-term tracking, as was noted by Sharif-Paghaleh *et al.* who used a transfected reporter gene to mediate uptake of a technetium radiolabel *in vivo*.[35]

1.3.3 Fluorescence imaging

Fluorescence based analysis relies on the detection of light emitted from a fluorophore, after its excitation by a light source. Whilst many cells are self-fluorescent, a variety of organic dyes and quantum dots may serve as fluorescent labels to aid the differentiation of cell types. In a technique known as flow cytometry, cells are treated with a range of fluorescently labelled antibodies, which bind to specific antigens within the cells.[36] The cell suspension is then passed into the flow cytometer, where the cells are identified on the basis of their fluorescence emission. Using this approach, cells may be identified in heterogeneous samples by the simultaneous detection of multiple biomarkers within individual cells. The ease of use and high-throughput nature of flow cytometry has led to its widespread use for the analysis of cell populations *in vitro*.

Whilst flow cytometry is the obvious choice for sorting cell suspensions, there are instances where information on the spatial distribution of cells within biological tissues is desirable. For this reason, fluorescence imaging is also frequently performed on solid samples. There are examples of *in vivo* imaging using fluorescent techniques,[37] however, the limited penetration depth of around 1 – 3 cm,[38] has generally restricted its application to the analysis of small animals or *ex-vivo* sections. With regards to cell tracking, the technique is predominately applied for the validation of other techniques,[28, 29] rather than as an independent imaging technique. To facilitate this, bimodal and even trimodal labels, containing combined fluorescent and paramagnetic modalities, have been developed.[39-41]

1.3.4 Mass spectrometry

1.3.4.1 Molecular mass spectrometry

In 1998 Macallan *et al.* demonstrated the use of molecular mass spectrometry to monitor T cells *in vivo*, following labelling with deuterated glucose ([6,6-$^2H_2$]-Glc).[42] The combination of mass spectrometry and stable isotope labelling has since been adopted by several groups to study T cell turnover in both human and animal models.[43-47] During DNA synthesis the deoxyribose moiety of deoxyadenosine is synthesised from cellular pentose, which is derived from glucose.[44] Therefore, intravenous (IV) administration of [6,6-$^2H_2$]-Glc leads to its incorporation into cellular DNA at a rate proportional to the ratio of labelled glucose molecules in the blood.[44] Upon cell division, the DNA in each daughter cell contains one newly synthesised strand and one strand of the original DNA, thus the amount of [6,6-$^2H_2$]-Glc per cell is halved, providing a marker of cell proliferation.[44]

Stable isotope labelling in combination with mass spectrometry offers many advantages, particularly its lack of toxicity and applicability to clinical setting. However, the method requires multiple sample preparation steps, including separation of extracted cells into cell subsets, extraction of the DNA from the cell line of interest, hydrolysis of the DNA to deoxynucleosides, and then purification of deoxyadenosine. When the analysis is performed by gas chromatography - mass spectrometry (GC-MS), a derivatisation step must also be performed prior to analysis. The number of cells required for the analysis can vary between 2×10^4 and 5×10^5 cells,[46, 47] depending on the label administration conditions, sample preparation mechanism, and the choice of the mass spectrometer. This may pose a problem when the analysis of limited or infrequent cell populations is required, such as when monitoring cellular therapy.

1.3.4.2 Atomic mass spectrometry

Inductively coupled plasma - mass spectrometry (ICP-MS) is a highly sensitive analytical technique, which is a popular choice for trace analysis due to its ability to detect and quantify most elements down to ppt levels. With regards to cell tracking, ICP-MS is regularly used to determine the average cellular uptake of new labelling agents [48-51] and their distribution after passage through animals.[52] This is commonly performed by bulk population analysis, after acid digestion of the cells.[48, 51]

In addition its use for population analysis, ICP-MS has been attracting increasing attention for the analysis of single cells. Indeed, this topic was the subject of a recent review in an issue of *Analytical and Bioanalytical Chemistry* focussed on single cell analysis.[53] To perform single cell measurements, the cells must be introduced into the ICP in a manner which ensures that the signals from individual cells are well resolved. This is typically requires heavy dilution and optimisation of flow rates. The introduction of single cells by pneumatic nebulisation was first reported by Li *et al.*, who used a micro-concentric nebuliser to introduce cells into the ICP-MS.[54] The authors observed occasional uranium signal spikes, which were thought to correspond to individual intact bacteria cells. Ho and Chan also used pneumatic nebulisation when analysing the major elements in single algae cells.[55] Magnesium, present at roughly 10^8 atoms per cell, and copper and manganese, both present at around 5×10^6 atoms per cell, were clearly detected. Detection down to 1×10^6 atoms per cell was subsequently reported by Tsang *et al*., when analysing bismuth in *Helicobacter pylori* cells, following *in vitro* treatment with an anti-ulcer drug.[56]

The drive to improve transport efficiency and reach lower detection limits has led to a recent increase in the use of piezoelectric micro droplet generators (μDG) as sample introduction systems. The use of μDG was initially demonstrated by a variety of groups for the detection of single nanoparticles.[57, 58] Subsequently, Shigeta *et al*. applied the technology to analyse single yeast cells, enabling the detection of femtogram levels of Na, Mg, Fe, Cu, Zn and Se, with signal durations of less than 500 μs.[59]

1.3.4.3 Mass cytometry

Tanner and co-workers have developed a new ICP-based technique for detecting cells. The technique, known as mass cytometry, was inspired by flow cytometry. As discussed in section 1.3.3, in traditional flow cytometry the cells are treated with a range of fluorescently labelled antibodies and subsequently identified by their simultaneous detection in individual cells.[36] However, with fluorescent labels, spectral overlap limits the number of simultaneous measurements to around ten.[36] For this reason, Tanner and co-workers developed a new range of antibody labelling reagents, known as MAXPAR^{TM} reagents,[60] which contain lanthanide rather than fluorescent tags. Lanthanides are particularly suitable for this purpose as they have a low natural abundance, resulting in a low background signal, and have similar chemical properties to each other, enabling their incorporation into the same tagged structure. They are also detectable by ICP-MS.

In 2009, a time-of-flight (TOF) based ICP-MS system was developed specifically for the simultaneous detection of multiple lanthanide labels in cells.[61] Cells labelled with MAXPAR^{TM} bound antibodies were introduced into the ICP-TOF-MS through a syringe pump, connected to a nebuliser and a custom built, heated spray chamber. This enabled the simultaneous detection of over 30 metal labelled antibodies in single cells, at a high-throughput sampling rate of around 1000 cells per second.[36] The mass cytometer is now a commercially available instrument, which is marketed by Fluidigm as CyTOF^{TM}.[62] The CyTOF system has been applied to detect a variety of antibody labelled cell samples, including human leukaemia cell lines and bone marrow samples.[36, 63] In addition to the detection of labelled antibodies, DNA intercalators have also been applied to simultaneously assess cell viability.[36, 63, 64]

1.3.4.4 Laser ablation – ICP-MS

Laser ablation (LA) is a sampling technique that uses a high power, short-pulsed laser to remove material from a sample surface. The technique allows highly specific sampling of solid samples, at a resolution down to 1 micron. Laser ablation is frequently used in combination with ICP-MS detection to map the distribution of elements in complex biological samples. Examples include the imaging of copper, zinc and platinum in liver and kidney sections,[65-67] the mapping of copper, zinc, iron and manganese in sections of brain tissue,[68-72] and the detection of various elemental tagged antibodies directly from tissue sections or immunohistochemical membranes.[73-76] LA-ICP-MS has also been applied to image the distribution of iodine, silver and gold in single fibroblast cells, following labelling with KI_3 and gold and silver nanoparticles respectively.[77, 78]

The highly specific targeting achievable with LA combined with the exquisite sensitivity of ICP-MS makes LA-ICP-MS an excellent choice for cell tracking and analysis. The capability for visualisation and specific selection of targets is particularly beneficial, since it guarantees the detection of whole cells rather than cell clusters or partially degraded cells. Furthermore, with the use of cell stains, such as trypan blue, sampling can be limited to those cells which are viable. However, LA-ICP-MS does have limitations. When compared the above techniques, the main drawback of LA-ICP-MS is the lengthy acquisition time, which can be in the order of several hours for the ablation of 1000 cells or the mapping of a 10 x 10 mm tissue biopsy. Efforts to improve the speed of acquisition are on-going and will be discussed in chapter 4. A description of the technological basis of laser ablation and ICP-MS can be found in the following sections.

1.4 Introduction to Laser Ablation

In 1985, Gray introduced laser ablation as a method to directly introduce solid materials into the ICP-MS.[79] Although traditionally used for geological analysis, LA has now been applied to a wide range of sample types, including biological tissue.[66-68, 80-82] The technique uses a high power, short-pulsed laser to remove material from the sample surface. Ablation may occur by either a thermal or a non-thermal mechanism depending on the type of laser used. In the thermal mechanism, electrons in the sample absorb the laser energy, which is distributed through the sample as heat, causing melting and vaporisation. Conversely, in the non-thermal process the laser energy is sufficient to directly break the atomic lattice, without inducing heat dissipation through the sample. The ablated material, which consists of atoms, ions, electrons and particulate,[83] forms an aerosol above the sample surface, leaving behind a crater of around 0.02 to 5 μm depth.[84] This aerosol is carried by a carrier gas down the inner tube of the ICP torch and into the plasma. In some instances the aerosol may interact with the laser beam, resulting in reduced energy deliverance to the samples. This effect is known as plasma shielding. The LA technique has been reviewed extensively by a number of authors, including Russo,[85, 86] Koch[87] and Günther.[88]

1.4.1 Challenges in the field of laser ablation

Since the introduction of laser ablation, the technique has been plagued by two main problems; namely elemental fractionation and the limited availability of certified reference materials. Elemental fractionation can be described as non-representative sampling, specifically when the relative elemental composition of the analysed material is not equivalent to that of the sample itself. There are various theories about the mechanism of fractionation, which largely relate to the size and uniformity of the ablated particles.[89] It has been shown that different sized particles may possess vastly different elemental compositions.[90] This is particularly the case when the physicochemical properties of their constituent elements differ significantly.[90] Large particles tend to become enriched in low volatility elements, whilst the smaller particles and the gas phase becomes enriched in the more volatile elements.[90] Transport efficiency is largely size dependent, so large variations in particle size contribute to fractionation. Very small particles and particles in the gas phase may impact or condense on the walls of the ablation chamber and the connective tubing,[91, 92] whereas large particles may succumb to gravitational settling. Fractionation continues inside the ICP itself, where large particles (>150 nm)[93] are inefficiently ionised, resulting in preferential ionisation, and hence analysis, of the more volatile elements.

Since the LA process is responsible for the initial particle distribution, careful consideration is required when choosing laser parameters, such as the wavelength and pulse duration. These will be discussed briefly in section 1.4.2.1. Optimisation of the ICP parameters is also important, particularly the RF forward power and the gas flows, as these control the temperature within the ICP, and therefore the proportion of particles that are completely vaporised, atomised and ionised. National Institute of Standards and Technology (NIST) glass is often used for tuning the ICP parameters.

For quantitative analysis, matrix-matching is essential because the amount of material ablated by each laser pulse is dependent on the composition and density of the sample. Many groups have attempted to create in-house calibration standards, for example by grinding and pressing powders.[94] For biological analysis, calibration standards are often prepared by spiking animal tissue, blood or serum with elemental standards.[70, 95] However, the production of such standards can be expensive and it is difficult to guarantee homogeneity.[96]

1.4.2 Instrumentation

A typical LA system consists of a laser, a series of optics, a viewing system, an ablation cell, and a transport connection to the ICP-MS. A schematic of a typical laser ablation system is shown in Figure 1.3.

1.4.2.1 The laser source

The laser source consists of an active medium, which undergoes excitation by an external stimulus to produce stimulated emission of radiation.[97] A diverse range of laser sources are available. A number of these, such as the ruby, excimer and neodymium-doped yttrium aluminium garnet (Nd:YAG), have been successfully used for laser ablation. By far the most common of these is the Nd:YAG, which consists of a rod containing a single yttrium aluminium garnet (YAG) crystal doped with neodymium ions.[97] The fundamental wavelength of this laser, 1064 nm, is poorly absorbed by many matrices.[84] Therefore, harmonic generation is often employed, allowing the Nd:YAG laser to be operated at shorter wavelengths, such as 266 nm and 213 nm.[84]

In fact, Nd:YAG based lasers operating at 193nm have also been introduced,[98] however the excimer laser is perhaps the more successful of the 193 nm types.

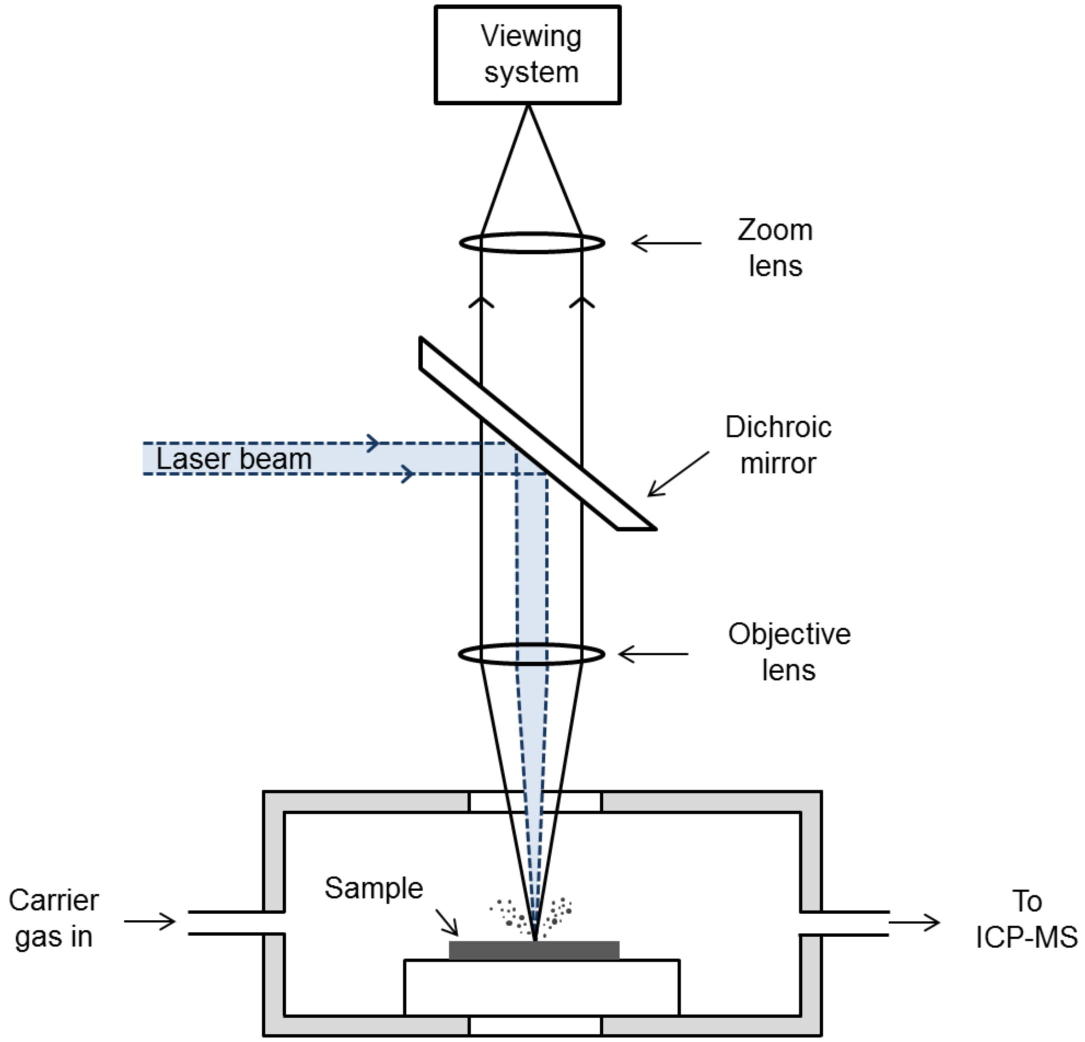

Figure 1.3 Schematic of a laser ablation system.

In general, shorter wavelengths provide smaller particles and more uniform particle distributions, thereby reducing elemental fractionation. Guillong *et al*. performed a comparison of the ablation characteristics of 266 nm, 213 nm and 193 nm Nd:YAG lasers on a series of NIST glass standards.[98] They found that 193 nm laser had a lower penetration depth, producing particles with diameters smaller than 150 nm, and hence achieving the lowest level of elemental fractionation.[98] However, the choice of wavelength is also dependent on the absorbance characteristics of the sample matrix, as this affects the ablation yield. Becker suggests that soft biological tissue is easy to ablate, and hence, the fourth harmonic, 266 nm, is sufficient for complete ablation of a tissue sample.[99]

Early LA work utilised nanosecond pulsed lasers.[100] However, at nanosecond pulse durations the interaction time between the laser and sample is sufficient for energy to dissipate into the sample matrix as heat.[100] This heat causes melting and vaporisation of the sample, producing an aerosol in with an enriched composition of the volatile elements. Consequently, there is now a trend towards shorter pulse durations, such as picosecond and femtosecond pulses, which reduce thermal heating of the sample and thereby reduce elemental fractionation.[100] Additionally, the duration of a femtosecond pulse is shorter than the time taken for ablated material to leave the sample surface,[100] so plasma shielding is not observed with this pulse width and the entire laser energy pulse is delivered to the sample surface.

1.4.2.2 Beam delivery

A range of mirrors and prisms direct the beam through the inner housing of the LA system, and an objective lens, positioned prior to the ablation cell, focusses the beam aperture onto the sample surface. The size and shape of the ablation crater can usually be adjusted by the user, for example by passing the beam through a beam expander and an aperture wheel. Ablation craters are generally either conical or cylindrical in shape and range between 4 micron and a few mm in diameter. Some modern systems even enable the use of spot sizes down to 1 micron and below.

1.4.2.3 The ablation cell

Ablation takes place inside a laser ablation cell. Various designs of LA cell exist. Typically they consist of a gas tight chamber, incorporating ports for gas entry and exit, and a fused silica window, to allow laser beam access.[84] The cell is connected to the ICP via tubing, which can be over a metre in length and is typically 3-4 mm internal diameter. The cell is mounted on a computer controlled adjustable platform for sample positioning, allowing highly precise selection of targets. Imaging is achieved by moving the stage in a defined pattern (usually a set of parallel lines), whilst firing the laser in continuous mode. If a mass spectrometer analyses the ablated material in a time resolved fashion, the acquired spectra can be converted into two-dimensional colour maps, displaying signal intensity as a function of the image dimensions. The speed of image acquisition is limited by the wash out time of the cell, which is largely controlled by its size and shape, along with the dimensions of the connective tubing. Cell design is therefore a key area for laser ablation development and it is one that will be discussed in detail in Chapter 4.

1.4.2.4 The carrier gas

A carrier gas flows continuously through the cell to provide an inert atmosphere for ablation and to sweep the ablated material into the ICP. Argon carrier gases were customary for early LA experiments, but due to its improved transport properties, many users have now switched to helium. Around ten years ago, Horn and Günther performed a comparison of the effect of different carrier gases on the size distribution and transport efficiency of glass particles.[101] They found that ablation in a helium atmosphere produces smaller particle size distributions than in argon, which leads to a gain in sensitivity. The size of the laser induced plasma is smaller in He, which along with its higher thermal conductivity, leads to rapid removal of thermal energy from the ablation site, reducing the condensation and agglomeration of particles in the vapour.[101]

1.5 Introduction to Mass Spectrometry

Mass spectrometry is frequently used to separate, detect and identify elements and molecular fragments on the basis of their relative molecular masses.[102] A variety of mass spectrometers are currently in use, which can differ considerably in design. However, all involve five key steps; sample introduction, the generation of gaseous ions, separation of the ions on the basis of their mass-to-charge ratio, detection of the ions, and finally, communication of the results to a computer.

The ionisation step has considerable impact on the format of the data generated by the mass spectrometer. Soft ionisation techniques, such as electrospray ionisation (ESI) and matrix-assisted laser desorption ionisation (MALDI), are well established in bio-molecular analysis, and provide information on the molecular structure of the sample.[103] The application of hard-ionisation techniques, such as inductively coupled plasma (ICP), results in loss of all structural information, however offers many advantages, including high sensitivity and multi-element capability. Since the technique is structure independent, the quantification of specific elements in complex samples can be more rapidly and reliably achieved.[103] Due to the composition of many cellular labelling reagents, and the high sensitivity required to detect them, the use of an ICP ionisation source is the most obvious choice for this project.

A selection of mass analysers are used in ICP-based instruments, including time-of-flight (TOF), quadrupole, magnetic sector and electric field analysers. High resolution instruments often employ two of these mass analysers in tandem. An example of this is Thermo Scientific's Element XR, which was the main mass spectrometer used in this project. A schematic of the Element XR is shown in Figure 1.4 and will be described in more detail in the following sections. For an introduction to alternative instruments the reader is pointed to reference 102.

1.5.1 Sector Field Mass Spectrometry

1.5.1.1 Solution-based sample introduction

The introduction of solid samples into the ICP was covered in section 1.4. However, the majority of current ICP-MS work is actually performed on liquid samples.

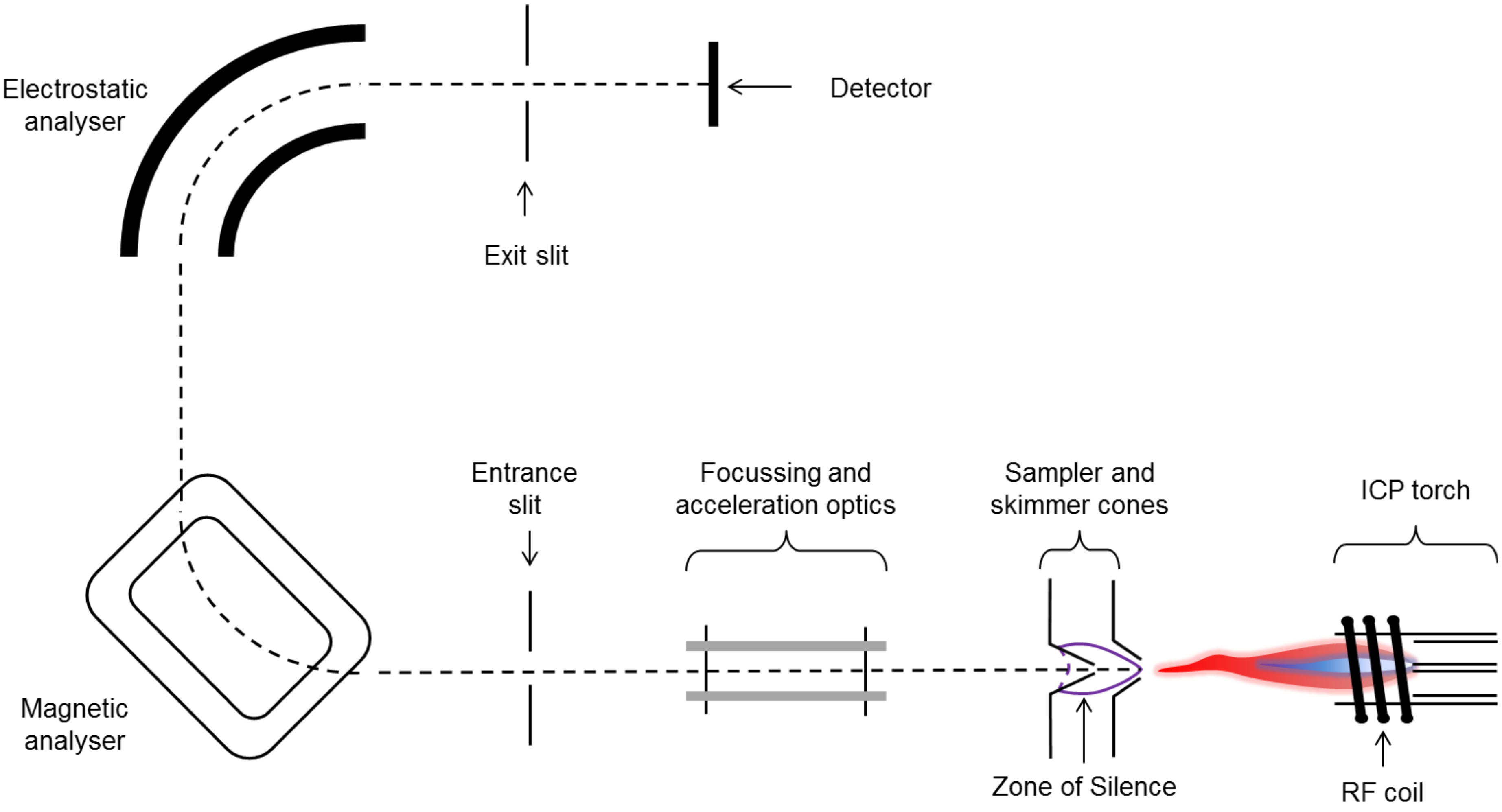

Figure 1.4 Schematic of a reverse Nier-Johnson double focussing sector-field ICP-MS.

Introduction of liquid samples is most commonly accomplished through pneumatic nebulisation. Various types of nebuliser exist for this purpose, schematics of two of which are shown in Figure 1.5. The function of the nebuliser is to convert a flowing liquid, received from a syringe pump or probe, into a stream of droplets. Nebulisers typically operate at flow rates of around 1 l min^{-1}, though micro and nano-flow nebulisers operating down to as low as 50 nl min^{-1} have been reported.[104] The resulting aerosols tend to contain a wide particle size distribution of around 0.1 – 25 µm.[105] Since only small droplets (<10 µm in diameter)[106, 107] are efficiently ionised by the plasma, spray chambers are often employed after nebulisation to remove the larger droplets and allow only those of the correct size to enter the plasma.

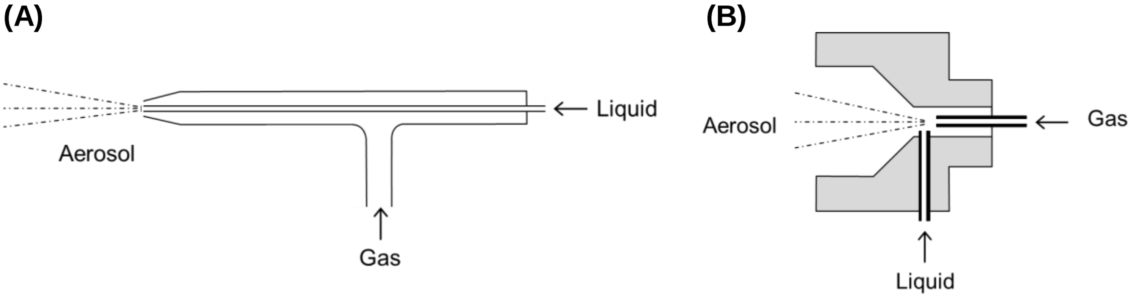

Figure 1.5 Schematic diagrams of two commercially available nebulisers. A) a concentric nebuliser, B) a cross-flow nebuliser.

A notable alternative to the nebuliser – spray chamber approach is the use of piezoelectric micro droplet generators (µDG), which can reproducibly produce droplets of less than 40 µm in diameter.[58] The droplets undergo desolvation before introduction into the plasma, usually with the aid of custom built desolvation apparatus. This approach has been shown to achieve transport efficiencies of close to 100%,[58] compared to around 2-30% for nebuliser – spray chamber sample introduction. However, despite the improved transport efficiency, µDG are prone to clogging, particularly when used with solutions containing high suspended solids, such as cells.[108] They are consequently not yet in use for routine work.

1.5.1.2 The inductively coupled plasma

The ICP torch consists of three concentric quartz tubes through which an inert gas, usually argon, flows. The main supply of argon is directed through the outer tube. This is generally termed the plasma or coolant gas, and flows at a rate of approximately 12 – 15 l min^{-1}. This flow is responsible for both shaping the plasma and shielding the outer torch from high temperatures, preventing melting. An auxiliary gas flows through the second tube at a lower flow rate of 0.5 to 2 l min^{-1}. This directs the plasma away from the ends of the injector and auxiliary tubes.[109] The final gas flow, often referred to as the sample gas, flows through the inner or injector tube at a rate of 0.5 – 2 l min^{-1}. It is through this inner tube that sample is introduced.

The top section of the outermost tube is surrounded by a copper coil, which provides a high frequency field of around 27-50 MHz.[109] Free electrons are introduced into the plasma gas by a spark and are accelerated by the high frequency field to reach the ionisation potential of the gas.[109] This results in an avalanche breakdown of the gas, leading to the formation of an inductively coupled plasma.[109] The resulting plasma has an annular shape and contains zones of differing temperatures. The sample passes through the central channel of the plasma, which has a temperature of around 6000 to 8000 K, where it is desolvated, atomised and ionised. Most elements are fully ionised to singly charged atomic ions. A schematic diagram showing the typical torch geometry is shown in Figure 1.6.

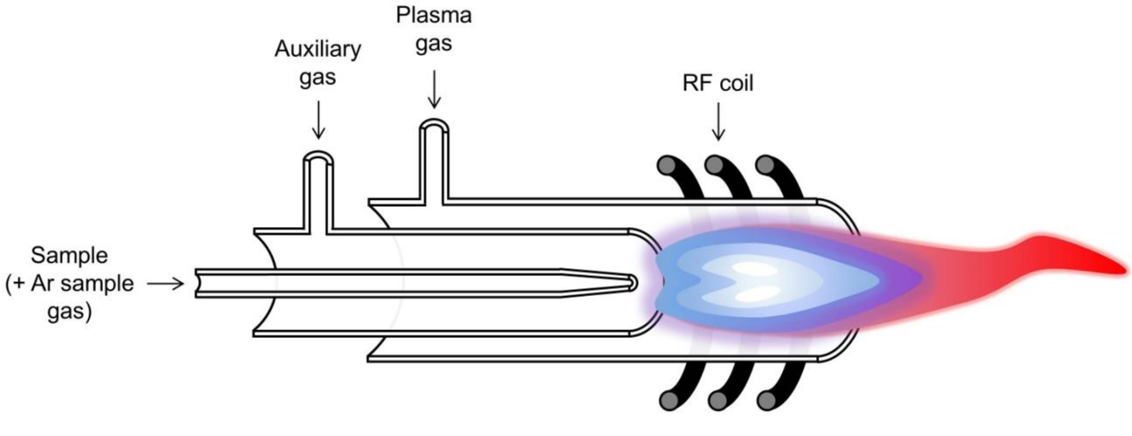

Figure 1.6 Cut-through schematic of an inductively coupled plasma torch. Figure not to scale.

1.5.1.3 The interface region

Since the plasma operates at atmospheric pressure (760 Torr) and the mass spectrometer operates at high vacuum (10^{-6} Torr), an interface region is required to reduce the pressure and allow efficient extraction of ions from the plasma to the mass spectrometer.[110] This interface consists of two water cooled metal cones, typically made from nickel or platinum. The first of these cones, the sampler cone, is positioned at the end of the plasma and has an orifice of around 0.8 – 1.2 mm. The second cone, called the skimmer cone, sits behind the sampler cone and has a smaller orifice of around 0.4 - 0.8 mm. A mechanical roughing pump reduces the pressure between the two cones to around 2 Torr, forming a region of intermediate pressure between the atmospheric pressure of the plasma and the vacuum of the mass spectrometer.[110] The gas reaches the speed of sound at the entrance to the sampler cone and becomes supersonic in the region between the two cones, which results in the formation of a shock wave, containing a region known as the zone of silence.[109] The orifice of the skimmer cone is located within the zone of silence and samples ions from this region.

1.5.1.4 The ion optics

After passing through the interface region, a series of electrostatic lenses focus and accelerate the ions through the entrance slit towards the mass analyser.[111]

1.5.1.5 Entrance and exit slits

Resolution is controlled by two slits, known as the entrance and exit slits. The first of these, the entrance slit, is positioned between the ion optics and the mass analyser, whilst the second, the exit slit, is positioned between the mass analyser and the detector. Resolution (10% valley definition) is defined as $m/\Delta m$, where m is the mass at which the peak occurs and Δm is the mass difference between two resolved peaks, when the valley between the peaks is 10% of the peak height.[112] The Element XR has three resolution settings; low resolution (R~300), medium resolution (R~4000) and high resolution (R~10000),[112] which are controlled by adjusting the width of the slits. Decreasing the slit width produces an increase in resolution, but this improvement comes at the expense of sensitivity, which can drop to as low as 1-2% of the counts seen for low resolution when high resolution is selected.[113] Peak shape also changes significantly depending on the resolution mode chosen. Flat topped peaks, produced in low resolution, are generally considered to yield higher measurement precision, compared to triangular shaped peaks, which are produced in medium and high resolutions. This is because signal intensity is less variable with sampling position over a flat topped peak, as depicted in Figure 1.7.

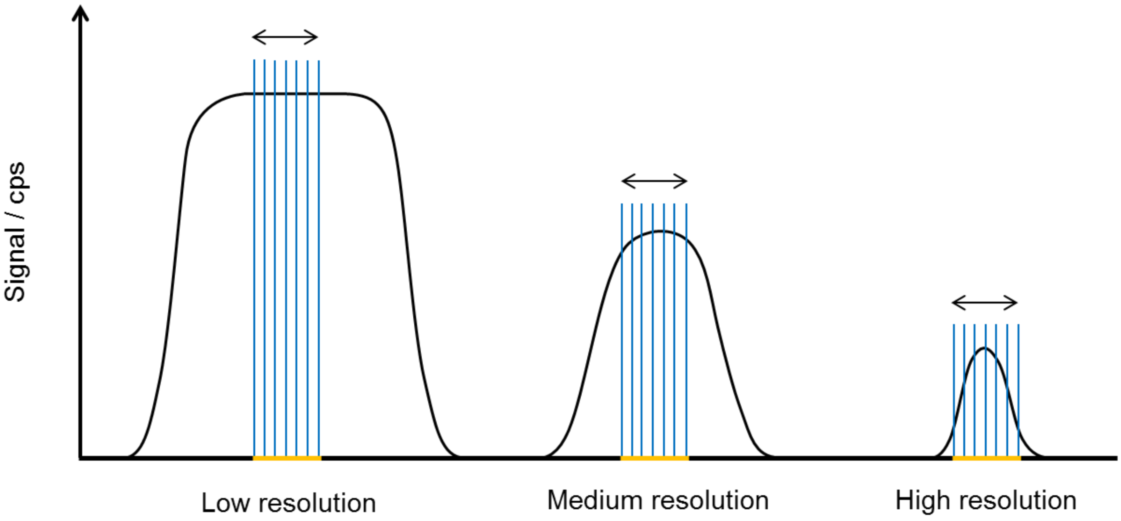

Figure 1.7 Diagram showing the typical peak shape seen for low, medium and high resolution peaks. The instrument scans across the integration window (shown in yellow) measuring a pre-defined number of samples per peak (the areas between the blue lines). Signal intensity is more variable between sampling positions for curved peaks compared to flat topped peaks, resulting in higher RSD's.

1.5.1.6 The mass analyser

High resolution instruments often employ two mass analysers, which can be found in various geometries depending on the model of instrument purchased. The Element XR uses a magnetic and an electrostatic (ESA) analyser, arranged in a configuration known as reverse Nier-Johnson geometry.

In the magnetic sector, ions are dispersed by their energy and momentum, where momentum equals the mass of the ion multiplied by its velocity.[102] A magnetic field operating perpendicular to the flight path deflects the ions, causing them to follow a curved trajectory.[102] At a given magnetic field strength, the radius of the trajectory is dependent on the momentum and charge of the ion.[102] Hence, for single charged ions of a uniform velocity, the strength of the magnetic field can be adjusted to allow ions of the desired mass to pass through the magnetic sector. Similarly, when the magnetic field is held constant, varying the acceleration voltage, and hence the velocity of the ions, also provides mass separation.

The ions exiting the magnetic sector have differing energies, depending on their point of formation in the plasma.[114] For single focussing instruments, this energy dispersion leads to peak broadening and loss of resolution. As a result, an electrostatic analyser, which is dispersive with respect to ion energy only, is employed after the magnetic sector. The ESA consists of two curved plates, which have opposing DC voltages applied to them.[115] The negatively charged inner plate attracts the ions, whilst the positively charged outer plate repels them, hence focussing and deflecting the ions. The energy focussing of the magnet and ESA are of equal magnitude, but opposite in direction. Combination of the magnetic and electric sectors provides both angular and energy focussing, whilst separating the ions according to their mass-to-charge ratio. Their combined usage is referred to as double focussing.

As discussed above, the trajectory of ions through the magnetic sector can be controlled by adjusting the acceleration voltage and/or the magnetic field strength. This feature permits a choice of three different scan types: magnetic scan (B Scan), electric scan (E Scan) or SynchroScan. E Scan is the default mode used by the Element XR. In this mode, the magnetic field moves initially to the start mass and is then held constant whilst the acceleration voltage and corresponding ESA voltage is adjusted.[112] This enables rapid scanning; however, the maximum scan range is limited from -6% to 30% of that of the magnet mass.[112] As a result, B Scan is preferred for the analysis of large, continuous mass ranges, as is required for mass calibration. During a B Scan, the accelerating and ESA voltages are kept constant, whilst the magnetic field strength is varied.[112] B Scan mode is considerably slower than E scan, since it requires a settling time to allow the magnet to recover from the hysteresis of each cycle.[112] The third mode, SynchroScan, is a combination of the B and E Scan modes. The magnet scans continuously in order of increasing mass, whilst the electric field scans each peak in in the opposite direction, freezing the measurement on the top of each mass peak.[112] Thus, with SynchroScan a larger amount of time is spent measuring the peak tops compared to magnetic scan alone.

1.5.1.7 The detector

After passing through the exit slit, the ions encounter a deflection plate. This deflects pre-defined high mass peaks away from the detector, preserving its lifetime, whilst allowing the remaining ions to hit the conversion dynode. As the ions hit the conversion dynode, secondary electrons are released from its surface, which are attracted into the secondary electron multiplier (SEM). The SEM has 19 dynodes. Impaction with the first dynode produces secondary electrons, which hit the second electrode, producing even more electrons, and so on. This cascade effect delivers an overall amplification of around 10^6 by the time the electrons reach the output electrode. The electrical pulses generated by each cascade are then counted and communicated to the computer in units of counts per second (cps).

The SEM is arranged in two sections and can be operated in different modes depending on the signal intensity. In counting mode, both sections of the detector are switched on. This mode is useful for trace analysis where the signal is expected to be below 5×10^6 cps. When signals of higher intensities than this are expected, analogue mode is used. In analogue mode, the second section of the SEM is switched off. This is to protect the dynodes from exposure to large signals, and thereby extend the lifetime of the SEM. Analogue mode operates in the region of 10^4 to 10^{10} cps.

The dynamic range of the instrument can be further increased to 10^{12} by the inclusion of a Faraday cup. In contrast to the SEM, the ions entering the Faraday cup are not deflected by the deflection plate. Instead they are directed straight into the hollow cylindrical shaped cup, where they are collected. The Faraday signals (positive charges) are collected inside a capacitor, which is then discharged, with the discharges detected by the ion detection unit. The Faraday cup is only used when triple mode is selected by the user. In this mode the detector automatically switches between the SEM (analogue and counting) and the Faraday cup, depending on the signal intensity. This switch happens in under a millisecond.

1.6 Statement of Work

This thesis is split into two main work streams. The first focusses on identifying appropriate labels to mark the therapeutic cells, and on using these to perform short term LA-ICP-MS tracking in animal models (Chapters 2 and 3). Loughborough University lacks facilities for producing, labelling and culturing mammalian cells. Thus, following literature searching to identify suitable labels and labelling protocols, the biological preparation of the samples was kindly performed by our collaborative partners at the University of Oxford (T cell samples), Universität Regensburg (Mreg samples) and Université de Nantes (Tol-DC) samples). The second stream of work (Chapter 4) involves development of a new laser ablation – ICP-MS interface, which will improve both the sensitivity and speed of detection, and thereby demonstrate the potential for LA-ICP-MS to rapidly and reliably track cells over extended periods.

2 Gadolinium Labelling of T cells

2.1 Introduction

T cells are a form of lymphocyte responsible for the regulation of the immune system. There are several types of T cell, each of which performs a discrete regulatory function. Regulatory functions include inducing apoptosis of infected cells, retaining memory of previous infections, and secreting cytokines that activate or deactivate other immune cells.[116] A team at the University of Oxford are studying a subset of T cells known as naturally occurring regulatory T cells (nTreg). These T cells, known previously as suppressor T cells, promote immunological tolerance by inhibiting the activation and expansion of donor-reactive cells.[117] nTreg are non-phagocytic; thus any labelling approach must focus on substances that are likely to be taken up by pinocytosis or receptor mediated endocytosis.

Contrast agents typically consist of a paramagnetic metal ion, such as Fe^{2+}/Fe^{3+} or Gd^{3+}, coordinated to a strong chelating ligand.[118] They are widely used in conjunction with magnetic resonance imaging (MRI) because the metal ion shortens the relaxation times of surrounding bulk water protons, enhancing the quality of the image. The presence of the paramagnetic core also permits the detection of contrast agents by ICP-MS. Indeed, previous studies have demonstrated the use of LA-ICP-MS to detect gadolinium-based contrast agents in tumour and tissue samples.[119-121] Two of these studies included a direct comparison between LA-ICP-MS and MRI, and highlighted the enhanced sensitivity and spatial resolution achievable when using LA-ICP-MS.[120, 121] In general, gadolinium contrast agents are a more suitable choice for ICP-MS than iron-based agents, on account of the low natural abundance of Gd in the human body and the absence of molecular ion interferences. Additionally, their relatively low molecular weight and a short half-life, compared to some iron-based contrast agents, renders them less likely to undergo phagocytosis by neighbouring cells.[122]

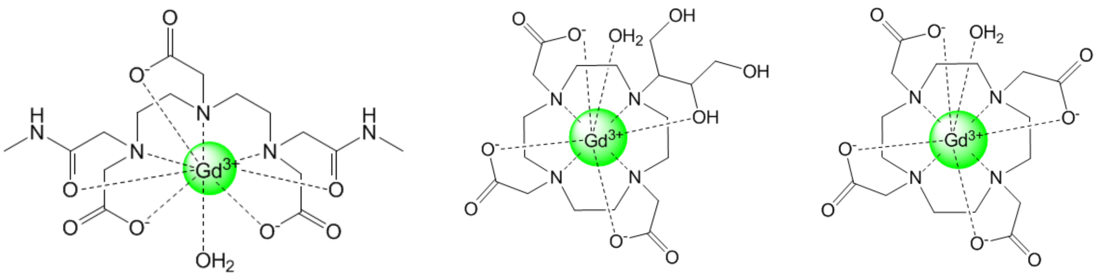

Gd-DTPA-BMA
Omniscan®

Gd-BT-DO3A
Gadovist®

Gd-DOTA^{1-}
Dotarem®

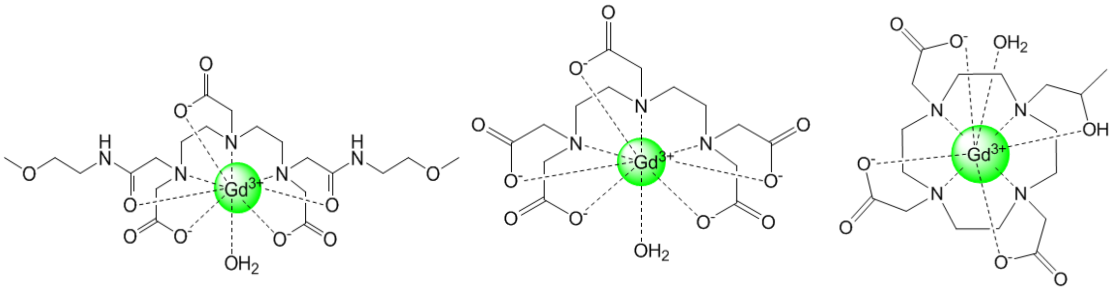

Gd-DTPA-BMEA
Optimark®

Gd-DTPA^{2-}
Magnevist®

Gd-HP-DO3A
ProHance®

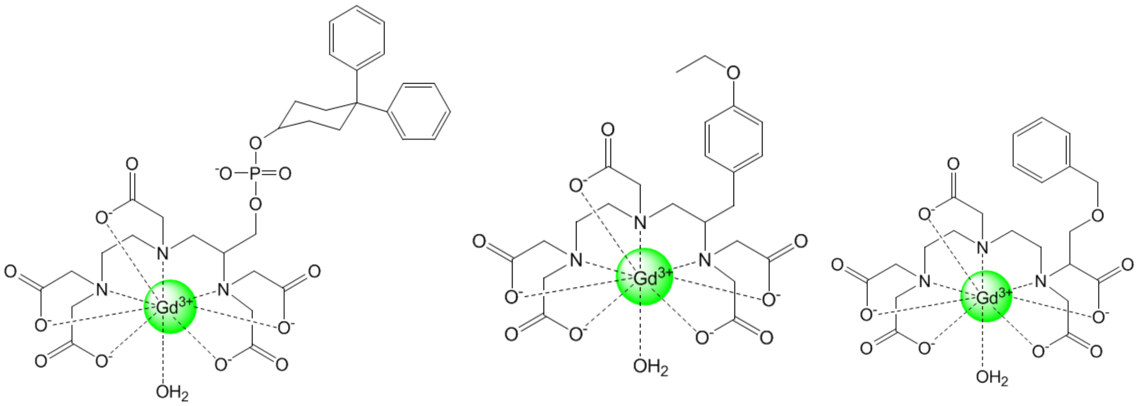

Gd-MS325^{3-}
Vasovist®

Gd-EOB-DTPA^{2-}
Primovist®

Gd-BOPTA^{2-}
MultiHance®

Figure 2.1 The structures of nine commercially available gadolinium-based MRI contrast agents.

Figure 2.1 shows the structures of nine commercially available MRI contrast agents. These are all octa-coordinated gadolinium chelates, with the addition of a water molecule resulting in a final coordination of nine. The differing structure of the chelating ligands affects both the strength of their binding to Gd and the distribution of the complex in the body.[123] Although the majority of these complexes were originally designed as blood pool or non-specific MRI agents, there are now a variety of publications that report the use of gadolinium chelates for cell labelling. Some prominent examples of this are summarised in Table 2.1.

Table 2.1 Published examples of cell labelling using gadolinium chelates.

Ref.	Cell type	Gd chelate	Uptake method / enhancement	Gd uptake / atoms cell^{-1}
124	3T3-NIH	Gd-DTPA	Pinocytosis	~4 x 10^{10}
		Gd-HPDO3A	Pinocytosis	~4 x 10^{10}
		Gd-DTPA-BMA	Pinocytosis	~7 x 10^{10}
	J774A.1	Gd-DTPA	Pinocytosis	~8 x 10^{10}
		Gd-HPDO3A	Pinocytosis	~5 x 10^{10}
		Gd-DTPA-BMA	Pinocytosis	~1 x 10^{11}
125	Rat HTC	Gd-HPDO3A	Pinocytosis	~4 x 10^{10}
			Electroporation	~1.5 x 10^{10}
126	TBV2	Gd-DTPA	Transfection (calcium phosphate, Lipofectin)	Not reported
30	Human MSC	Gd-DTPA	Transfection (effectene)	Not reported
127	HeLa	Gd-DOTA	Liposome	3.4 x 10^{9}
16	Rat MSC	Gd-DTPA	Cationic liposome	2.7 x 10^{11}
39	IGROV-I	Gd-DOTA	Cationic liposome	1.2 x 10^{7}
41	J774A.1	Gd-DTPA	Lipid coat	Not reported
128	K562	Gd-DO3A	Covalent binding to exofacial protein thiols	1.2 x 10^{10}
129	T cells	Gd-DTPA	IL-2	Not reported
40	Rat MSC	Gd-DOTA	Cyclodextrin scaffold	4.5 x 10^{8}
130	Pig MSC	$GdCl_3$	Single walled carbon nanotubes	~1 x 10^{9}

Di Gregorio *et al*. achieved uptake rates in the order 10^{10} atoms of Gd per cell when labelling macrophages and fibroblast cells with three different Gd complexes.[124] In this instance the cells were passively labelled, through doping of the commercial chelates into the cell culture medium. However, publications involving other cell lines have reported modifications to this approach in an attempt to increase uptake. Terreno *et al*. used electroporation, which induces reversible pores in the cell membrane to enable uptake of the material.[125] Other approaches involved modification to the structure of Gd complexes, which facilitated initial binding to the cell surface to trigger endocytosis. Examples include the use of commercially available transfection agents, such as calcium phosphate [126] and effectene,[30] or the inclusion of cationic lipids,[16, 39, 127] a 2-pyridyl-dithio group[10, 128] or interleukin-2 (IL-2).[129] The use of IL-2 is a good choice for assisting T cell labelling, since it binds to surface receptors on T cells, is essential for the growth and expansion of T effector cells, and is already utilised by the team at the University of Oxford as part of their T cell expansion protocol. In principle IL-2-Gd-DTPA could be used to label cells as part of the standard T cell expansion procedure. However, all reagents used in clinical trials must be produced in cGMP approved facilities. Due to the difficulty in obtaining a cGMP version of modified complexes, only commercially available MRI contrast agents will be considered in this chapter.

2.1.1 Aims for this thesis chapter

This chapter reports the use of two clinically approved MRI contrast agents, Omniscan® (Gadolinium diethylenetriaminepentaacetic acid bismethylamide, Gd-DTPA-BMA) and Dotarem® (Gadolinium 1,4,7,10-tetraazacyclododecane-1,4,7,10-tetracarboxylic acid, Gd-DOTA), to label human $CD4^+$ T cells. Following labelling, the cells were tracked for short periods in animal models using LA-ICP-MS. The specific objectives of the work were as follows:

1) To optimise the labelling method to achieve maximum uptake by the cell population, whilst minimising toxicity concerns.
2) To determine cellular retention of the label after periods of *in vitro* culture.
3) To develop an appropriate LA-ICP-MS sampling strategy capable of identifying labelled cells in mixed populations.
4) To administer labelled cells to animal models and subsequently distinguish the labelled cells using LA-ICP-MS.

2.2 Experimental

2.2.1 Instrumentation and operating parameters

Analyses were performed on a sector-field ICP-MS instrument (Element 2XR, Thermo Scientific, Bremen, Germany). For solution analyses, the instrument was fitted with a cyclonic spray chamber (Glass Expansion, Victoria, Australia), a conical glass concentric nebuliser (Glass Expansion, Victoria, Australia), and a 0.25 mm I.D. probe (Elemental Scientific, Omaha, USA). For laser ablation, a UP-213 laser ablation system (Electro Scientific Industries, Cambridgeshire, UK) was coupled to the sector-field ICP-MS instrument above. The laser system was fitted with a low-volume, tear-drop shaped cell, which has been described elsewhere.[131] Helium was used as an ablation gas, at a typical flow rate of 0.6 l/min, with argon introduced through a Y-piece, at a flow rate of 0.8 l/min, downstream of the ablation cell. The system was tuned daily for maximum ^{238}U signal intensity, whilst keeping the Th/U ratio to approximately 1 and the ThO/Th ratio to below 1%, during the ablation of NIST 611 glass.

2.2.2 Cell labelling

Cell culture and labelling procedures were performed by Sheldon Edwards and Andrew Bushell at the University of Oxford. Human peripheral blood mononuclear cells (PBMC) were isolated from an anonymised leukocyte cone, obtained from a local blood bank. Leukocytes were enriched by Ficoll density gradient centrifugation, and CD4$^+$ cells isolated (~98% purity) by MACS positive selection (Miltenyi Biotec). To isolate defined populations to greater than 98% purity, cells were labelled with anti-CD4 (Beckman-Coulter clone SFCI2T4D11), anti-CD25 (BD Biosciences clone M-A251) and anti-CD127 (BD Biosciences clone hIL-7R-M21) antibodies and flow-sorted on a BD FACSAria (BD Biosciences). After isolation, cells were plated at a density of 1 x 10^6 cells per well in 2 ml of RPMI 1640 medium, which was supplemented with 10% human albumin, penicillin, streptomycin and glutamine, plus 1 x 10^5 U/ml of human recombinant IL-2 (Proleukin, Novartis). Each well also received a volume of either Gd-DTPA-BMA (Omniscan®, GE Healthcare, UK) or Gd-DOTA (Dotarem®, Guerbet Laboratories, France). The cells were incubated overnight (~16 hours) at 37°C in 95% air/5% CO_2. Following the incubation period, the cells were washed extensively in phosphate buffered saline / 2% fetal calf serum (PBS/ 2% FCS) to remove any unbound label.

Cell viability was determined using a trypan blue exclusion test. An aliquot of the cell suspension was mixed with an equal volume of 0.4% trypan blue solution. A 10 µl aliquot of the mixed solution was then introduced into a haemocytometer. Viable cells were observed as bright and round in shape, whereas dead cells appeared blue in colour due to incorporation of the dye. Cell viability was expressed as a percentage (the number of viable cells divided by the total number of cells x 100).

2.2.3 Optimisation of the labelling process

Optimisation experiments for Omniscan and Dotarem were performed in parallel using cells from the same donor. Cell culture and sample preparation was performed in accordance with the procedure described previously in section 2.2.2. For dose optimisation, doses of 5, 10, 20, 50, 100 and 200 µl of either Omniscan or Dotarem were added to each well prior to incubation overnight. This corresponds to 0.19, 0.38, 0.75, 1.86, 3.63 and 6.72 mg Gd/ ml, and 0.20, 0.39, 0.78, 1.92, 3.74 and 7.15 mg of Gd/ml, for the Omniscan and Dotarem wells respectively. A total of three replicates were performed for each dose. In addition, three control wells containing cells without contrast agent were prepared. Following dose optimisation, the incubation time was varied using the optimum dose. Incubation times of 0, 1, 2, 4, 8 and 16 hours were assessed in triplicate. Assessment of Gd uptake by the cell population was determined by solution-based ICP-MS. The optimum dose and incubation time were then carried forward to subsequent experiments.

2.2.4 Sample preparation for solution-based ICP-MS

For solution ICP-MS, cells were spun down into pellets and digested according to the method proposed by Yamada *et al.*[132] and modified by Kerr.[133] Briefly, this involved addition of 67% HNO_3 (100 µl per $1x10^6$ cells) and heating at 70°C for 1 hour, followed by addition of 30% H_2O_2 (100 µl per $1x10^6$ cells) and heating at 70°C for a further 4 hours. The digested samples were evaporated to dryness under a stream of nitrogen, and reconstituted in 2% HNO_3. For quantification, a range of calibration standards were produced by dilution of a 10 ppm elemental standard solution (SPEX Certiprep, Middlesex, UK).

2.2.5 Sample preparation for LA-ICP-MS

Slides for LA-ICP-MS were prepared by the group at the University of Oxford, immediately after labelling. Four different slide preparation methods were tested. Each method aimed to deliver approximately 50,000 cells per slide at an adequate spacing to enable single cell targeting. The first method involved simply dropping an aliquot of cells onto the slides and allowing the droplet to air dry. For the second and third methods, the cells were fixed onto slides with acetone or paraformaldehyde respectively, followed by dehydration with a series of graded alcohols. The final method used a Cytospin to position the cells. This involved inserting a slide into a slot in the Cytospin, with a cardboard filter in place over the slide. The filter had a hole of approximately 5 mm diameter through it, into which a 50 µl aliquot of the cell suspension was introduced. The device was then allowed to spin for a few minutes, which removed the media and dispersed the cells. Subsequently, the cells were allowed to air dry. Each procedure was performed for both labelled $CD4^+$ cells and a non-labelled $CD4^+$ control.

To simulate clinical samples, where labelled cells are present amongst a background of non-labelled cells, slides containing mixed populations of labelled and non-labelled cells were prepared. For these, the relevant dilutions were made in solution before fixing the cells onto slides using the Cytospin method described above. Ratios of 1:1, 1:10 and 1:100 (labelled: non-labelled) were prepared as known samples, and a replicate of each was provided as a blind sample. Blind samples were randomised and identified with a non-descriptive character. The expected ratios of these were not communicated to the analyst until after the analysis was completed.

2.2.6 Laser ablation of single cells

Cells were examined on an individual basis by ablation of single 25 µm diameter shots at locations corresponding to cells. This spot size was chosen to ensure sampling of the complete cell, whilst minimising the chance of overlap onto neighbouring cells. A high laser energy (60%, 8.97 J cm^{-2} fluence) was chosen to ensure complete ablation of each cell; and this was verified through visual observation of the resulting laser craters. Only single cells were targeted; cells present in clusters or closer than 25 µm apart were disregarded. The presence or absence of label was determined from the ^{157}Gd signal.

2.2.7 *In vivo* mouse study

Animal experimentation procedures were conducted by Andrew Bushell at the University of Oxford. All experiments were performed in accordance with the UK Animals (Scientific Procedures) Act 1986. Human peripheral blood mononuclear cells (PBMC) were isolated from a leukocyte cone. The CD4$^+$ component was isolated using the procedure described above, and these cells were labelled using the optimised labelling procedure. Following labelling, the Gd-CD4$^+$ cells were washed extensively and recombined with the non-CD4$^+$ PBMC component. Re-mixing with the unlabelled PMBC component was found to be necessary to ensure viability of the cells in the host. The recombined cells were then injected intraperitoneally into BALB/C Rag-/- common-γ chain mice, at a level of 5 million cells per mouse. At 3, 6, and 10 days post infusion, the spleen and blood were harvested and a peritoneal lavage was performed. The extracted cells were plated onto slides for LA-ICP-MS analysis. Flow cytometry (BD FACSCanto, BD Biosciences) was used to determine the extent of human cell reconstitution.

2.2.8 *In vitro* label retention

To estimate the degree of signal loss caused by label leakage, an *in vitro* label retention study was performed in parallel to the *in vivo* study above. For this, an aliquot of the labelled cells were washed using PBS/ 2% FCS, then cultured for a further period in gadolinium free media. Samples were taken daily and plated onto slides for LA-ICP-MS analysis.

2.2.9 Analysis of skin grafts

An *in vivo* experiment was undertaken by the University of Oxford, as part of a separate project to determine the effect of gadolinium labelling on the regulatory ability of their nTreg. Briefly, CBA Rag KO – (H-2^k) mice were split into two groups. At day 0, all mice were given $1x10^5$ Teff cells and $1x10^5$ of either Gd labelled (group A) or unlabelled (group B) nTreg. At day +1, the mice received a B6 (H2-^{b}) skin graft. The mice were then monitored for signs of rejection over a 100 day period, which is the cut-off point defined by Oxford as long-term survival.[134]

At the conclusion of the above study, the mice were sacrificed and their grafts were removed. The extracted skin grafts were offered to Loughborough University for quantification of their Gd content. Approximately half of each graft was digested in concentrated HNO_3 and H_2O_2. The Gd content of the digested samples was quantified using solution ICP-MS, as described previously. The remaining half graft was frozen for future analysis.

2.3 Results and Discussion

2.3.1 Optimisation of the labelling conditions

Table 2.2 and Figure 2.2 show the impact of increasing the dose of contrast agent on the uptake of Gd by CD4$^+$ T cells. Uptake increased in a dose-dependent manner. A quadratic fit with a low second order term fitted the data set; however, no plateau was observed within the range of doses examined. Despite the increased uptake at the higher doses, a dose of 50 µl (corresponding to 1.86 and 1.96 mg Gd/mL of Omniscan and Dotarem, respectively) was chosen as the optimum. Volumes higher than 50 µl occupy a significant proportion of a 2 ml well, which leads to nutrient dilution and could potentially produce osmotic effects; thus the decision to limit labelling volumes was taken on a precautionary basis. However, cell viability was 96% or above for all doses tested and no obvious signs of toxicity were observed in any of the experiments performed.

Gadolinium uptake increased strongly with increasing incubation time for both complexes, as shown in Table 2.3 and Figure 2.3. The maximum uptake was observed at 16 hours, which was classified as the optimum incubation time for use in subsequent experiments. Incubation times of longer than 16 hours were not tested on the grounds that they were impractical and may have a detrimental effect on cell viability. A 0 hour time point was included in the study as a measure of the efficiency of the cell washing process. For this, the Gd complexes were added to the well, and then the cells washed immediately, allowing insufficient time for label internalisation. Any Gd found in these samples was deemed to be from incomplete removal of the non-internalised complex, and thus represents the method blank for the assay. The Gd content of the 0 hour samples ranged between 5 and 20 times larger than that in the non-labelled controls, but this represents only 0.7 and 3% of the final uptake at the optimised conditions for Omniscan and Dotarem respectively. The cell washing procedure was therefore considered to be sufficient for quantification of the label uptake. As seen for the dose experiments, Omniscan provided higher Gd loading than Dotarem, with an average of 1.43×10^8 atoms per cell compared to 9.36×10^7 atoms per cell at the optimum conditions. By virtue of this higher Gd loading, Omniscan rather than Dotarem was used for all subsequent labelling experiments.

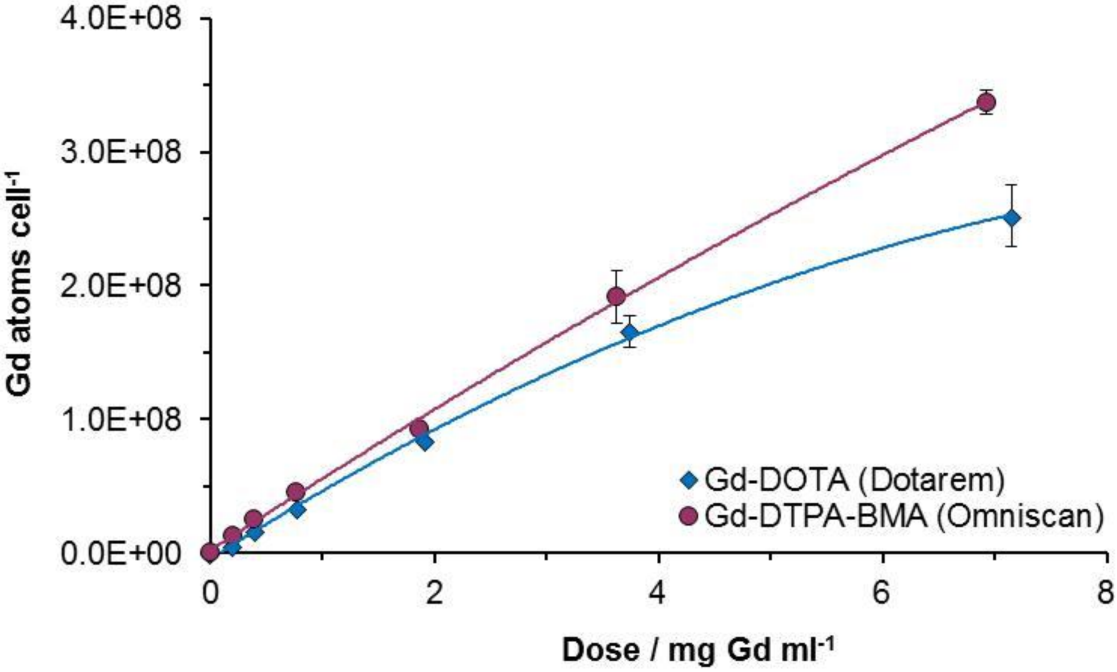

Figure 2.2 The relationship between the dose of Omniscan and Dotarem and the uptake of Gd atoms by CD4$^+$ T cells. Error bars show the standard error of the mean (n=3).

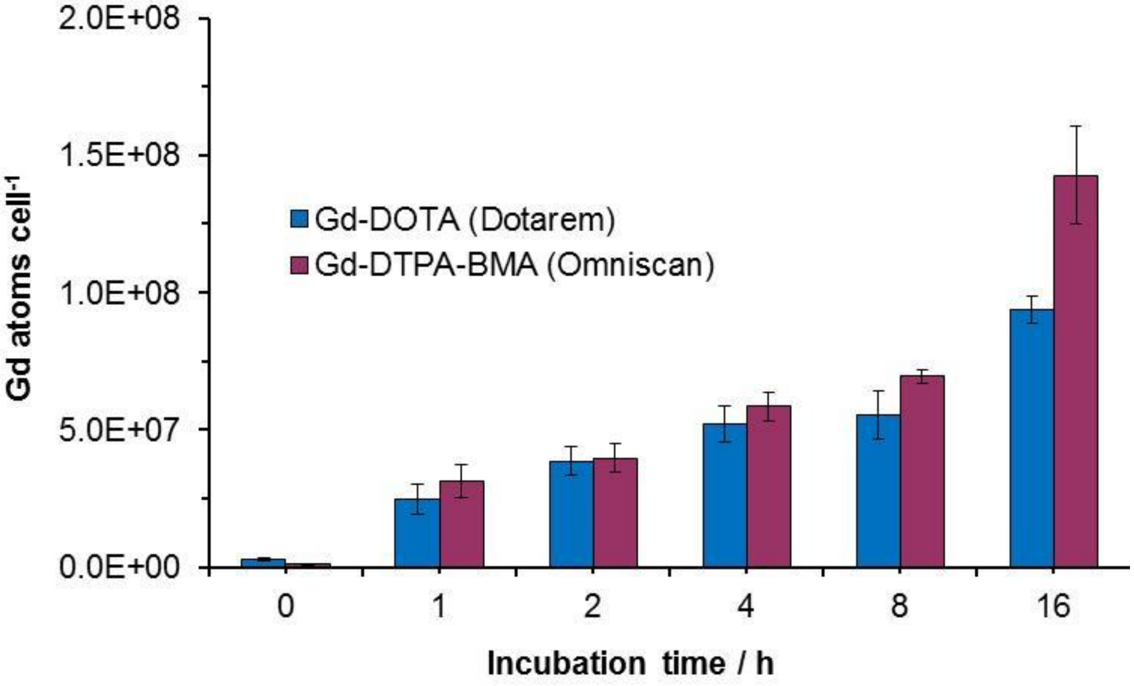

Figure 2.3 The relationship between the incubation time with Omniscan or Dotarem and the uptake of Gd atoms by CD4$^+$ T cells. Error bars show the standard error of the mean (n=3).

Table 2.2 The uptake of Gd by human CD4$^+$ T cells at varying doses of Gd contrast agent, when using an incubation time of 16 hours.

Dose / µl	Gd-DOTA (Dotarem) Atoms per cell ± % RSD (n=3)			Gd-DTPA-BMA (Omniscan) Atoms per cell ± % RSD (n=3)		
0	8.17E+04	±	31	1.49E+05	±	136
5	5.04E+06	±	52	1.28E+07	±	14
10	1.59E+07	±	3	2.51E+07	±	15
20	3.35E+07	±	7	4.56E+07	±	16
50	8.37E+07	±	3	9.35E+07	±	1
100	1.66E+08	±	13	1.92E+08	±	18
200	2.52E+08	±	16	3.37E+08	±	5

Table 2.3 The uptake of Gd by human CD4$^+$ T cells when varying the incubation time, whilst keeping the dose of contrast agent at 50 µl per well.

Incubation time / h	Gd-DOTA (Dotarem) Atoms per cell ± % RSD (n=3)			Gd-DTPA-BMA (Omniscan) Atoms per cell ± % RSD (n=3)		
0	2.83E+06	±	28	9.47E+05	±	50
1	2.47E+07	±	40	3.12E+07	±	34
2	3.85E+07	±	24	3.97E+07	±	22
4	5.20E+07	±	22	5.86E+07	±	15
8	5.55E+07	±	28	6.95E+07	±	6
16	9.36E+07	±	9	1.43E+08	±	21

2.3.2 Gadolinium uptake method

It is likely that uptake of the Gd-complexes occurred predominantly by pinocytosis, as has been reported for other cell lines.[124, 125] Gadolinium internalised via this route is known to localise to endosomes within the perinuclear region of the cell,[125] where subsequent detachment of Gd^{3+} from its chelate may occur.[124] Dechelation is expected to be more prevalent for Omniscan than Dotarem. As shown in Figure 2.1, the DTPA-BMA chelate is non-ionic and has an open chain structure, hence providing less stable binding to Gd^{3+} than the macrocylic, ionic DOTA chelate.[135] Dechelation is accelerated in the presence of phosphate or competing cations,[136] both of which are constituents of the cell culture media. Thus it is likely that by the 16 hour time point, a proportion of the Gd in the culture media was present as free rather than complexed Gd. Free Gd^{3+} ions may be subject to a different route of uptake than the complexed form. Cheng *et al*. conducted a comprehensive study into the uptake of lanthanide 3+ ions by erythrocytes.[137] Gd^{3+} was found to bind initially to membrane phospholipids, followed by a transfer to membrane proteins. This process induced conformational changes in the membrane, which resulted in the formation of pores, facilitating the entry of Gd^{3+}. It is possible that this mechanism may have provided an additional route for Gd uptake. Since Omniscan is known to be more unstable than Dotarem, this additional route may account for the differences in Gd uptake between the two chelates, particularly at the 16 hour time point.

2.3.3 Biological variation

Over the course of the project, 14 individual labelling experiments were performed under the optimum conditions, each with cells isolated from different individuals. Taking into account replicates, this involved a total of 48 different wells. The collated data from these experiments is presented in Figure 2.4, which depicts the average Gd uptake from each of the 14 experiments. The average uptake across the 14 experiments was 1.09×10^8 Gd atoms per cell. However, significant variation between individuals was visible, as demonstrated by the large inter-individual RSD of 81%. This variation has implications for cell tracking, and highlights the importance of obtaining a sample of the labelled cells, prior to infusion, for every patient. Intra-sample variances are also present and may partially relate to the cell counting process, which is based upon counting a small aliquot of the cells within the haemocytometer window, and is therefore a well-known source of random error.

The data for the optimisation experiments was obtained using cells isolated from human PBMC by MACS positive selection of $CD4^+$ cells. The resultant populations were typically greater than 95% $CD4^+$ cells, but contained 2-5% monocytes due to low level expression of CD4 by some monocytes. It is difficult to remove these contaminating cells using MACS, since the technique separates populations by positive or negative selection, but does not account for high or low expressions of a molecule. Monocytes are known to have very active phagocytic and pinocytic pathways; thus preferential uptake by these cells may have artificially inflated the average Gd uptake. To assess this, human $CD4^+$ T cells were purified to levels exceeding 99% purity, but most importantly containing less than 0.2% monocytes. ICP-MS analysis of these highly purified cells showed a gadolinium uptake of 4.53 x10^7 atoms per cell, which is roughly half of the average value presented above.

It is clear that the presence of monocytes impacts upon the average uptake by the cell population. This has a major impact on reproducibility, since different donors present different proportions of monocytes. Typically the leukocyte cones contained around 60% T cells and 20% monocytes prior to purification. However, in one extreme case the leukocyte donor presented about 50% monocytes and less than 20% T cells.[134] Purification of these cells was then an issue, since reducing the contamination to below 1% required complication of the CD4$^+$ extraction process, as described above. These extra steps resulted in cell losses and a produced a dramatic reduction in the final cell count. High cell counts are necessary for multi-factor experiments and experiments involving replicates; so consequently flow sorting was not used for subsequent experiments.

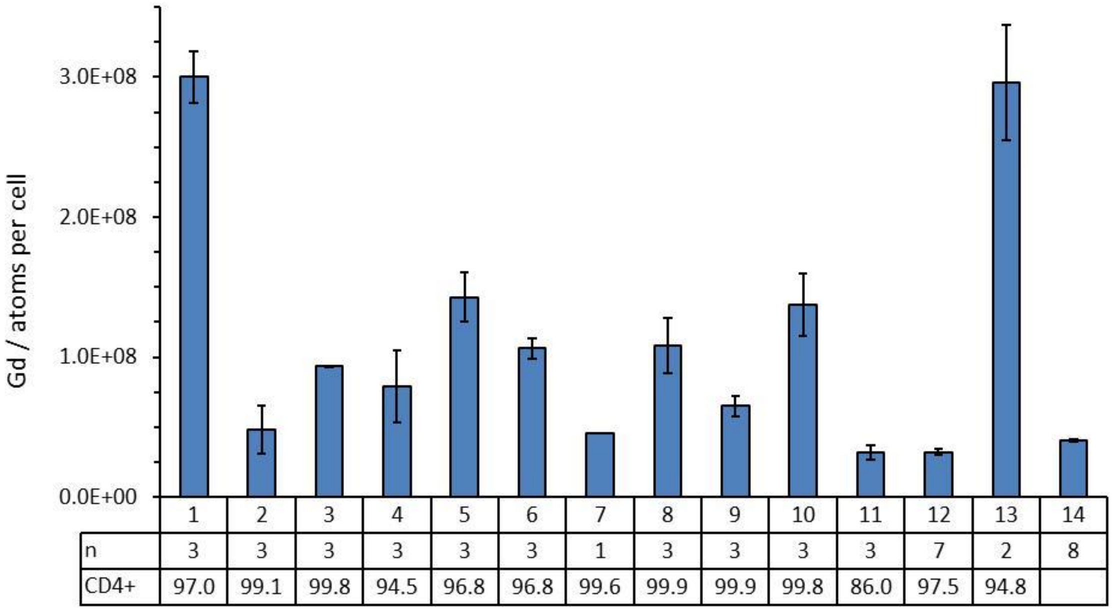

	1	2	3	4	5	6	7	8	9	10	11	12	13	14
n	3	3	3	3	3	3	1	3	3	3	3	7	2	8
CD4+	97.0	99.1	99.8	94.5	96.8	96.8	99.6	99.9	99.9	99.8	86.0	97.5	94.8	

Figure 2.4 The Gd uptake by CD4$^+$ T cells when labelling with Omniscan at the optimum conditions. Each column represents the average data from an individual labelling experiment, each with cells taken from a different donor. The number of replicates per experiment and the percentage CD4$^+$ purity, where available, is given in the table below the graph. Error bars show the standard error of the mean.

2.3.4 Sample preparation for laser ablation

The nature of sampling by laser ablation requires cells to be fixed onto a solid surface, typically a slide, before ablation can take place. This is in contrast to many biological imaging applications, where cells can simply be left in solution with a coverslip in place over the slide. In the case of T cells, sample preparation is further complicated by their non-adherent nature, which prevents the direct growth of cells on slides, and hampers the removal of the culture media surrounding the cells. This generates problems in terms of visualisation of the cells, preservation of their structure, and maintenance of their Gd burden.

Four different slide preparation methods were employed in an attempt to find the most appropriate method. Microscopic images obtained using these different methods are shown in Figure 2.5. Initially samples were prepared through dropping an aliquot of the cell suspension onto the slide and allowing the droplet to air dry. However, the samples were difficult to visualise under the laser microscope, because substances present in the cell culture media crystallised out upon drying, obscuring the cells from view. This problem was not observed for slides fixed with either acetone or paraformaldehyde, since the washing and dehydration steps in these methods removed the cell culture media from the slide. However, chemical fixation methods alter the structure of the cells and may lead to loss of antigen expression, which may be required for subsequent antibody post-labelling. It is possible that these steps also caused the cells to perforate and release their label, as lower Gd signals were observed when analysing the chemically fixed samples. Acetone fixation removes lipids and dehydrates the cells; thus any gadolinium bound to these lipids may be lost during this process.

Preparation of samples using the Cytospin proved to be by far the most effective method. Cells remained within a 5 mm area of the slide, aiding their location, whilst the rotation of the slide in the Cytospin ensured the cells were spread out adequately over this area, enabling single cell targeting. The presence of the cardboard filter also helped to absorb the cell culture media, which was spun off during the rotation of the slide; thereby preventing the problem of crystallisation. Accordingly, this method was utilised for all of the remaining experiments presented in this chapter.

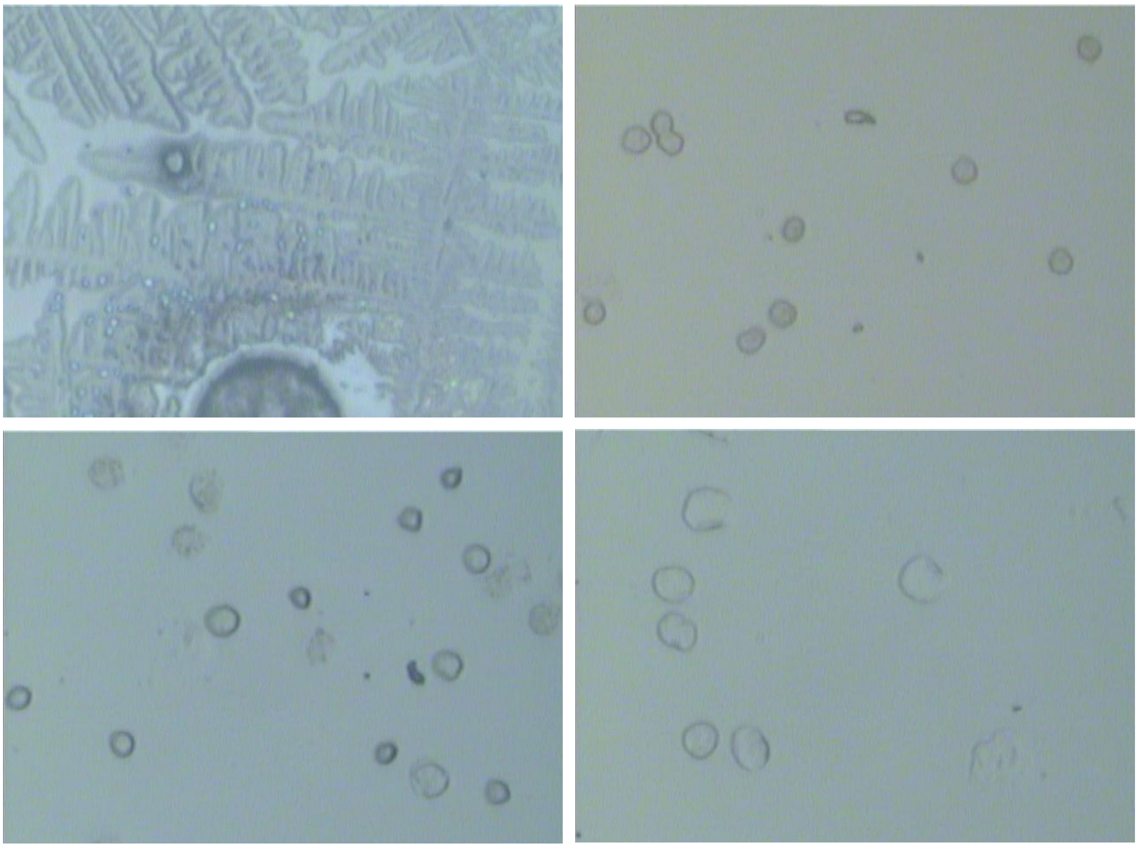

Figure 2.5 Microscopic images of cells, obtained after using four different slide preparation methods. Top left: T cells after air-drying only. Top right: T cells prepared using a Cytospin, followed by air-drying. Bottom left: Paraformaldehyde fixed T cells. Bottom right: Acetone fixed T cells. All pictures were obtained using the built-in microscope on the UP-213 laser ablation system.

2.3.5 Laser ablation of single cells

To conclusively confirm uptake by CD4$^+$ cells, and to quantify the percentage labelling efficiency, the labelled cells were analysed on an individual basis using laser ablation – ICP-MS. The spot size and high fluence used in these experiments ensured complete ablation of the cells, so the integrated peak area is representative of the total amount of Gd per individual cell. Figure 2.6 shows the ^{157}Gd signal intensities for the ablation of 25 individual labelled cells (A) and 25 individual non-labelled cells (B). Distinct signals were observed for the ablation of the labelled cells, compared to only background noise for their non-labelled counterparts. Of the 1000 cells ablated, 998 gave clear signals, confirming uptake of Gd by CD4$^+$ cells at close to 100% labelling efficiency.

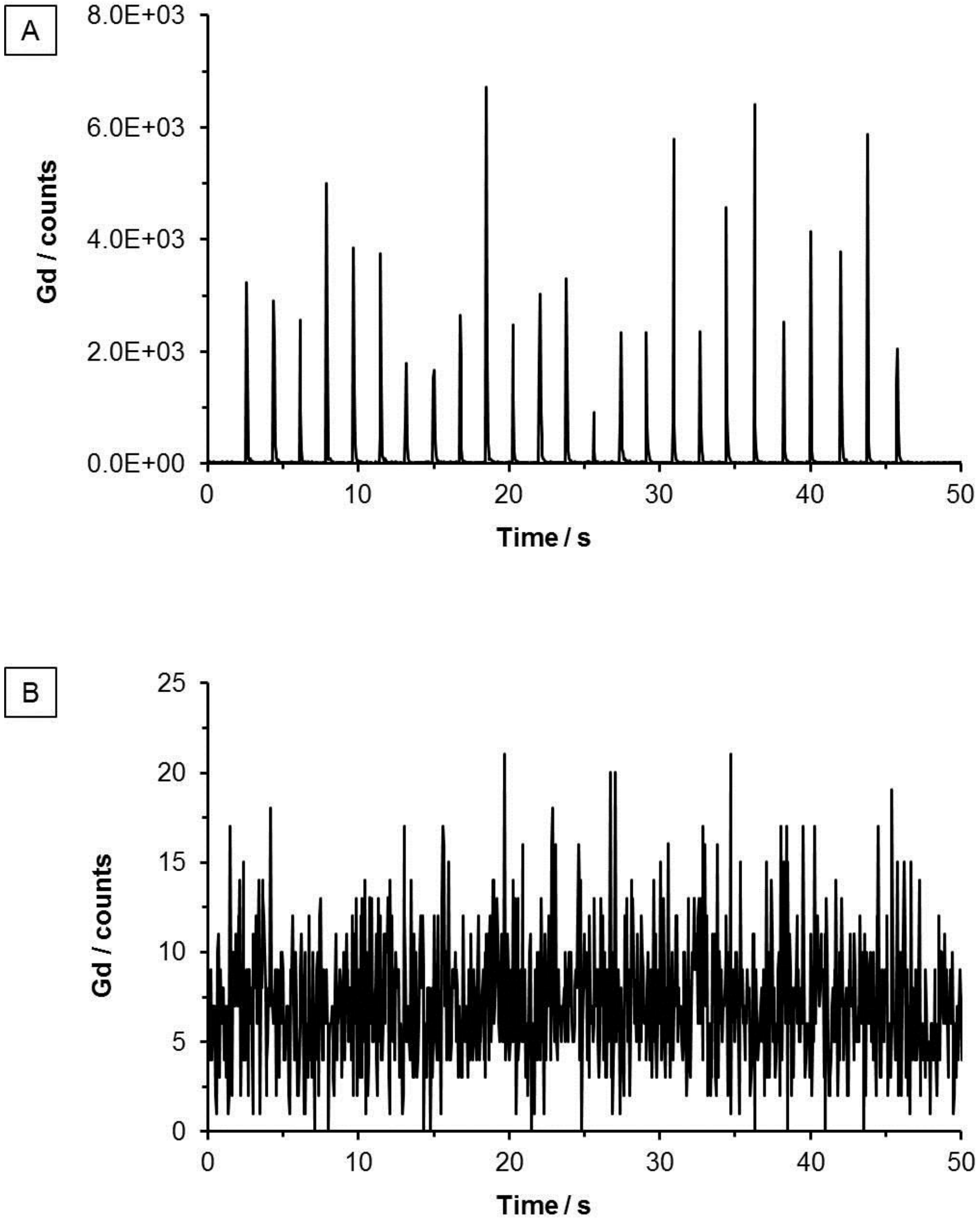

Figure 2.6 Signal intensities obtained when ablating 25 µm shots on A) 25 single Gd-DTPA-BMA labelled CD4$^+$ cells and B) 25 single non-labelled CD4$^+$ cells.

Figure 2.7 is a histogram showing the variation in label uptake observed when ablating 1000 individual labelled cells. For this, the ^{157}Gd signal intensities were grouped into blocks, with the number of occurrences for each block plotted on the y-axis. In the range of 0 - 15,000 counts, the distribution of signals was approximately Gaussian, with a RSD of 39%. The large variance in uptake is likely to prevent the differentiation of second or third generation cells from the original population. A potential explanation for the variance is the laser fluence, which is known to be variable with the old laser system used for this study. It is clear that temporary reductions in laser fluence may result in an unablated residue remaining for some cells. This effect was not observed visually when inspecting the craters in this study. However, it is possible that the variations in fluence altered the ablation mechanism between cells, which may have introduced diversity in particle transport or ionisation efficiency between each ablation event. Heterogeneity of the cell population may also arise from differences in the individual micro-environment, stochasticity in gene expression and protein synthesis,[138] or differences in cell cycle phase between cells.[139] A small percentage (1.6%) of signals occurred above the Gaussian region. These higher signals are likely to correspond to the ablation of phagocytic monocytes. Accordingly, the number of high signals observed matches closely with the 2.8% CD14$^+$ monocyte impurity measured by FACS for this sample.

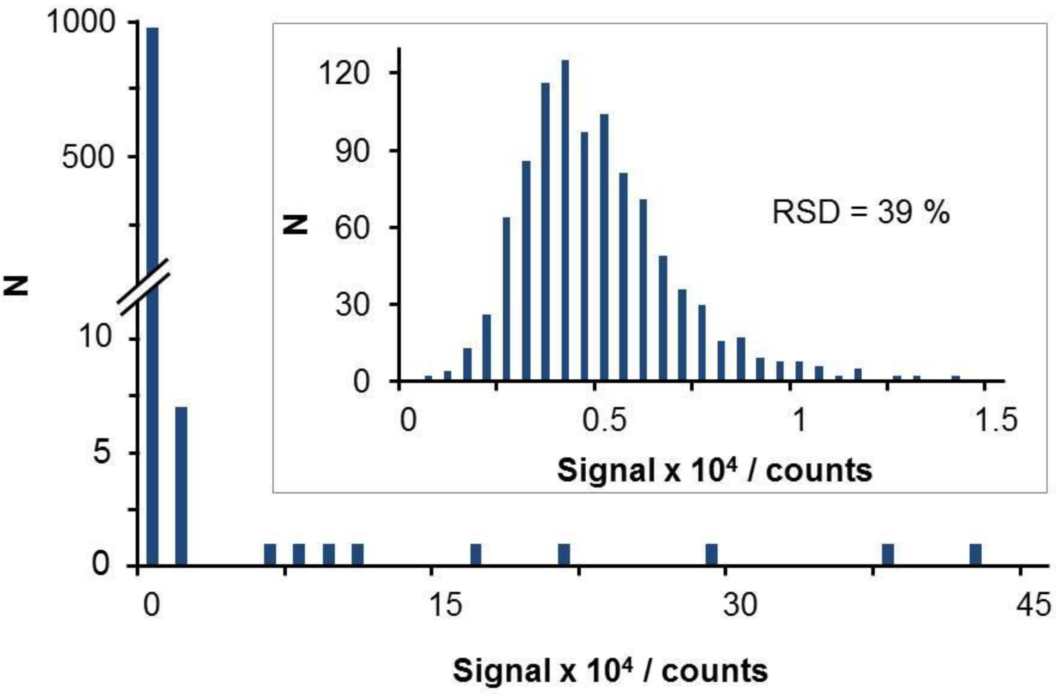

Figure 2.7 Histogram showing the distribution of ^{157}Gd signal intensities for the ablation of 1000 Gd labelled cells. The inset shows an expanded view of the distribution within the first peak (0 – 15,000 counts).

Application of the technique to cell tracking requires discrimination of labelled cells from a background of non-labelled cells. To simulate this scenario, labelled cells were mixed with non-labelled cells in various ratios, prior to analysis by LA-ICP-MS. As shown previously in Figure 2.6, the signal-to-background ratio is large; hence differentiation between labelled and non-labelled cells is straightforward and can be performed visually. The percentage of labelled cells determined by LA-ICP-MS matched approximately with the ratios prepared, see Table 2.4. Differences can be accounted for by a combination of incomplete mixing and pipetting errors. As shown, the ratios observed from the blind experiments corresponded remarkably closely to the expected ratios, adding further confirmation to the reliability of the technique.

Table 2.4 The percentage of labelled cells found when ablating slides containing various ratios of labelled to non-labelled cells. 1000 cells were ablated per sample.

	Labelled : Non-labelled ratio	% labelled cells identified	% labelled cells expected
Known	1:0	99.8	100
	1:1	39.6	50
	1:10	5.5	9.1
	1:100	0.6	1
	0:1	0.1	0
Blind	1:1	39.1	50
	1:10	5.2	9.1
	1:100	0.7	1

A single gadolinium signal was observed in the non-labelled samples, setting a false-positive rate of 0.1%. It is possible that this signal was caused by carryover of material from a previous sample, which may have adhered to the walls of the cell or tubing and become dislodged during the run. Similarly, a false negative rate of 0.2% was observed. False negatives may be due to lack of label uptake by some cells, or alternatively laser misalignment may have prevented complete ablation of the cells in question. In clinical samples, it is expected that administered T cells may represent between 5 and 25 cells per 1000, after isolation of the leukocytes from peripheral blood. Therefore, false positive and negative rates of the order reported here are not expected to obstruct detection of the presence of labelled cells.

2.3.6 *In vitro* label retention

In addition to label uptake, the key second characteristic for cell tracking is label retention. To assess this, Gd labelled CD4$^+$ T cells were cultured *in vitro* in gadolinium-free growth medium, with samples taken daily for LA-ICP-MS analysis. As shown in Table 2.5, the average signal intensities reduced with increasing follow-on time, reaching roughly 50% of the day 1 value after 10 days in culture. A similar decreasing trend was recently reported for other Gd labelled cell lines.[124] It is likely that this reduction represents a combination of cell division and exocytosis of the label. However, despite this, the label remained detectable at all of the time points examined, with 98.8% of cells retaining Gd after 10 days in culture. In view of the low background signals observed for the non-labelled cells, it seems likely that Gd labelled cells should be detectable for periods well beyond the 10 days studied here.

Table 2.5 The number of labelled cells observed after incubation *in vitro* for various intervals after labelling. 250 cells were ablated per sample.

Day	% labelled cells observed	Average signal
1	100	4118
2	100	3296
3	100	2901
4	99.6	2959
5	100	2744
6	100	2473
7	99.6	2220
10	98.8	2014

2.3.7 *In vivo* mouse study

Although *in vitro* label retention was encouraging, the more important question with respect to cellular therapy is whether cells retain gadolinium *in vivo*. A well characterised humanised mouse model, where immunodeficient mice lacking T cells, B cells, and functional NK cells are reconstituted with human immune cells, was utilised to demonstrate *in vivo* tracking. Cells were injected intraperitoneally, with samples taken at 3, 6 and 10 days post-administration. Previous studies have shown that nTreg are enriched within the peripheral blood [140, 141] and spleen[142] of tolerant transplant recipients, so demonstration tracking experiments aimed to identify cells extracted from these sites. In addition, a peritoneal lavage was performed to recover any labelled cells remaining in the peritoneum (the site of administration).

Slides for the *in vivo* experiments were visually different to those analysed in previous experiments. While cells analysed after *in vitro* culture were relatively uniform in size, those examined from the *in vivo* experiments contained significant numbers of blasting cells, which were around twice the diameter of the cells ablated previously. It is hypothesised that this effect was due to a reaction of the human regulatory cells to the immunodeficient mouse environment, which may have induced the cells to rapidly proliferate. Accordingly, these cells produced lower ^{157}Gd signal intensities than their *in vitro* counterparts, indicating increased division of the label in the mouse model. To accommodate the larger cell diameters, the ablation spot size was increased from 25 µm to 30 µm. However, increasing the spot size made the selection of single cells more challenging; particularly considering that the larger nature of the cells produced less free space between cells on the slide. Given these targeting difficulties, it is conceivable that overlap of the ablated region with the edges of neighbouring cells may have occurred in some cases. To allow for this possibility, a threshold value was set at 5% of the average signal intensity of the corresponding *in vitro* sample. Signals below this threshold were not included in the percent labelled count.

Table 2.6 The number of labelled cells identified in mouse peritoneal lavage samples following infusion of Gd labelled CD4$^+$ cells. 250 cells were ablated per sample.

Mouse	Day	% Gd positive cells (by LA-ICP-MS)	Human cell reconstitution (by flow cytometry)
1	3	13.2	negative
2	3	66.4	positive
3	3	14.0	negative
4	6	2.0	negative
5	6	35.6	positive
6	6	48.4	positive
7	10	20.4	positive
8	10	49.2	positive

In agreement with previous experience of this model, which showed that reconstitution of spleen and blood lags behind that of the peritoneal lavage,[134] human cells were not found in the spleen or blood up to day 10 using either LA-ICP-MS or FACS. However, human cells were readily detected in the peritoneal lavage at all time points examined. Table 2.6 shows the percentage of labelled cells found in the lavage samples by LA-ICP-MS, with the human cell reconstitution results provided as a reference. Reconstitution in this model is defined as greater than 1% human CD45$^+$ cells in the leucocyte gate, as determined by flow cytometry.[143] In each case, the detection of high numbers of Gd labelled cells by LA-ICP-MS correlated with the presence of human CD4$^+$ T cells in the lavage. Thus, both the *in vitro* and the *in vivo* data indicate that human CD4$^+$ T cells retain a detectable gadolinium level for at least 10 days, when labelled with Omniscan. Example FACS plots, showing the difference between reconstituted and non-reconstituted mice are provided in Appendix 1, whilst example LA-ICP-MS data for one of the mice is presented in Figure **2.8** below.

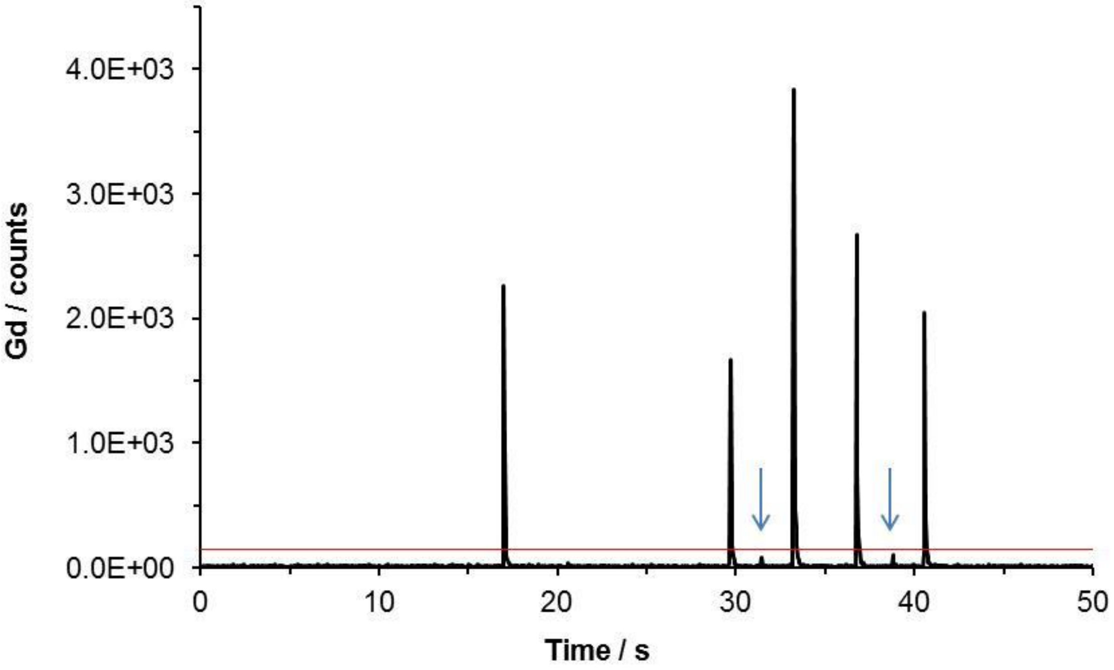

Figure 2.8 Example data from the *in vivo* experiments (Day 3), showing the presence of 5 labelled cells. Small peaks below the threshold value (red line), are indicated with arrows and were not included in the % labelled count.

2.3.8 Analysis of skin grafts

The clinical application of any cell labelling technique is subject to an assessment of its toxicity and impact on cell function. Cell viability was high for all of the experiments performed, as indicated above, and division history analysis following mitogenic stimulation of the cells revealed no effect of the label on proliferation. A further *in vivo* experiment performed by the University of Oxford indicated that Gd labelling does not affect the ability of nTreg to regulate rejection. In this experiment, two groups of mice received $1x10^5$ Teff cells and $1x10^5$ of either Gd labelled or non-labelled nTreg. The mice were given a skin graft and monitored over the course of 100 days for signs of rejection. No difference was noted between the labelled and unlabelled group in terms of their ability to tolerate the transplanted graft.[134]

Previous studies demonstrated that following enrichment of T cells in the peripheral blood and lymphoid tissue, the cells eventually migrate towards the transplanted tissue itself.[144] In some cases, accumulation within the graft can be sufficient to promote tolerance by a second recipient, following removal and re-transplantation of the graft.[145] With this in mind, the skin grafts from the above experiment were analysed for traces of Gd. Solution analysis of the digested grafts showed significant accumulation of Gd in one of the tissue grafts compared to the unlabelled control, see Table 2.7. However, the other 3 grafts showed no significant accumulation. There are two possible reasons for this. Firstly, in a tolerogenic environment, non-Treg may be recruited into the regulatory pool by a phenomenon known as 'infectious' tolerance.[146] The labelled cells may therefore represent only a small proportion of the total regulatory cells at 100 days post-transplantation. Secondly, the mice used in this experiment were profoundly lymphopenic. It is known that transfer of T cells into immunodeficient hosts induces homeostatic proliferation, where the cells replicate rapidly to populate the host.[147] Thus, it is possible that this rapid division diluted out the Gd label within the infused $CD4^+$ cells. Such an effect could have also contributed to the lower signals seen in the *in vivo* versus *in vitro* 10 day tracking studies, as reported in sections 2.3.6 and 2.3.7.

Table 2.7 Gd concentration in transplanted skin graft samples at 100 days post-administration, as determined using solution based ICP-MS.

Mouse no.	+/- Gd	pg Gd / mg tissue
1	+ Gd	10.96
2	+ Gd	0.12
3	+ Gd	0.18
4	+ Gd	1.29
5	No Gd	0.72
6	No Gd	0.93
7	No Gd	0.65
8	No Gd	0.27

2.3.9 Nephrogenic systemic fibrosis

Whilst gadolinium chelates are routinely administered during MRI imaging, their use in some patients is restricted due to reports of nephrogenic systemic fibrosis (NSF). Although rare, this condition is potentially fatal and is characterised by "extensive thickening and hardening of the skin".[148] Studies on patients with renal impairment have found a link between the intra-venous administration of gadolinium chelates and the onset of NSF.[149, 150] Consequently, the administration of gadolinium contrast agents is contra-indicated for MRI imaging in patients with impaired renal function. Any proposed use of gadolinium labelling should be treated with caution, particularly since regulatory approval is being sought for cellular therapy in renal transplant patients. However, it is important to note that at the anticipated doses for the ONE Study (3 $\times 10^6$ cells/kg patient body weight), the Gd exposure from the proposed labelling method is dramatically lower than that received from a typical MRI scan. Taking in account the average cell uptake of ~27 fg, and the proposed administration levels of 3 million cells per kg, the Gd exposure from cell labelling is ~81 ng/kg. This is over 100,000 times lower than the 15.2 mg/kg dose employed for MRI imaging (Omniscan is typically administered at a level of 0.2 ml per kg patient weight; the formulation contains 287 mg/ml Gd-DTPA-BMA, which equates to 76.1 mg/ml Gd). The risk is further minimised due to the route of administration, since with cell labelling the gadolinium chelates are compartmentalised inside the cells rather than being introduced into the systemic circulation.

2.4 Conclusion

This chapter represents the first application of LA-ICP-MS to perform individual tracking of therapeutically relevant cells. The technique was demonstrated in an immunodeficient mouse model, where the Gd chelate enabled identification of $CD4^+$ T cells for up to 10 days post-administration. A dose of 50 µl Omniscan was used for cell labelling, which enabled passive loading of around 10^8 Gd atoms per cell, with close to 100% labelling efficiency. This dose was based upon sufficiency for short-term tracking. However, since the Gd content will decrease with each cell division, it may be beneficial to increase the dose when longer term tracking is required. Detailed analysis of the effect of cell division on label conservation was not undertaken in the course of the work presented here. However, future studies to quantify this effect are feasible. This could include co-labelling with CFSE dye, as a marker of cell proliferation, stimulation with mitogenic beads to induce cell division, followed by FACS sorting of the cells according to division history, prior to ICP-MS analysis. A similar demonstration experiment to estimate label transfer would also be beneficial, which could involve incubation of the labelled cells with other cell lines prior to FACS sorting.

The experiments reported here indicate a favourable toxicity profile for the Gd chelates, with no obvious effects on cell viability or proliferation noted. A further immunological investigation, carried out by partners at the University of Oxford, confirmed that labelling with Gd chelates does not alter the ability of nTreg to promote tolerance of transplanted skin grafts. ICP-MS analysis of the digested grafts established that the label was still detectable in one of the four grafts analysed at 100 days post-transplantation. There is scope for future investigation of the localisation of Gd within this graft, for instance through high resolution LA-ICP-MS mapping of Gd within thin cryostat sections of the graft.

The LA-ICP-MS detection method described here provides several advantages over other techniques for detecting Gd chelates within cells. Firstly, elemental detection does not rely on stable binding of Gd^{3+} to the chelate; thus, the label can be detected at periods when its enhancement on MRI relaxation would be lost. Secondly, the use of laser ablation allows single cell targeting, removing interferences from other artifacts, such as air pockets or hemorrhage, which may hamper MRI detection. Thirdly, the exquisite detection capability of sector field ICP-MS allows detection at levels of 10^7 atoms per cell and below, which compares favourably to the value of 10^8 atoms per cell recently reported for molecular mass spectrometry.[124] Thus, it can be concluded that gadolinium labelling followed by LA-ICP-MS detection offers a safe and feasible method for assessing the persistence of nTreg therapies.

3 Gold Labelling of Regulatory Macrophages and Dendritic Cells

3.1 Introduction

The previous chapter focussed on labelling and tracking naturally occurring regulatory T cells (nTreg). Instead, this chapter presents the tracking of two monocyte-derived antigen presenting cell types, the regulatory macrophage (Mreg) and the tolerogenic dendritic cell (Tol-DC), which are the subject of immunological studies at the Universität Regensburg and Université de Nantes, respectively. These cells induce tolerance of transplanted organs through a variety of mechanisms, which have been reviewed extensively elsewhere.[151, 152] Both Mregs and Tol-DCs are phagocytic; thus a wider range of cell labelling options are available for these cells compared to the nTreg reported in Chapter 2.

Nanomaterials are attracting increasing attention for their potential therapeutic uses, most notably for targeted drug delivery [153] and photodynamic therapy [154] in cancer treatment. Their ability to infiltrate cells and tumours is considered a key advantage in cancer treatment, and hence there is a wealth of literature concerning their uptake by HeLa and other cancerous cell lines.[14, 24, 155, 156] The nanomaterials themselves exist in a range of shapes and sizes, including spherical nanoparticles,[157] nanotubes,[130] nanorods,[158] nanoshells[159] and nanocages.[160] They also vary in their composition, comprising a range of metallic, semi-conductor, and even carbon cores, often with the addition of a surface coating to impart stability and prevent aggregation.[24, 157] However, not all of these materials are suitable for detection by ICP-MS, since low mass elements in particular can prove challenging.[161] Iron and zinc oxide nanoparticles represent a large proportion of the available nanomaterials, but due to the high natural abundance of these elements,[162] they are a poor choice for cell tracking.

Chithrani *et al*. studied the effect of nanoparticle size and shape on the uptake of citrate stabilised gold nanoparticles by HeLa cells.[155] Spherical nanoparticles, with diameters of 14, 30, 50, 74 and 100 nm, and rod shaped nanoparticles, with dimensions of 40 x 14 nm and 74 x 14 nm, were studied. The uptake rate of spherical nanoparticles was reported to be significantly higher than for rod shaped nanoparticles, with the 14 and 74 nm spherical particles achieving a 375 and 500% higher uptake rate than the 14 x 74 nm rods.[155] Of the spherical particles, 50 nm particles achieved the highest uptake rate, with around 6 x 10^3 nanoparticles internalised per cell.[155]

Liposomal carriers can be used to increase the uptake of gold nanoparticles of non-optimal size. In a study using HeLa cells, phospholipids conjugated with 1.4 nm gold nanoparticles were exchanged into pre-formed liposomes.[156] When formed at a ratio of 2000 nanoparticles per liposome, 8.5 x 10^5 Au nanoparticles were internalised per HeLa cell, which was a thousand-fold enhancement on the uptake achieved without the use of a carrier.[156] Connor *et al*. took a slightly different approach, using surface coatings rather than liposomes to enhance cellular uptake of 4, 12 and 18 nm spherical gold nanoparticles.[24] The 4 and 12 nm particles were coated with cysteine and glucose coatings respectively, whilst the 18 nm particles had either a citrate, biotin or cetyltrimethylaluminium bromide (CTAB) surface coat. The exact levels of nanoparticle internalised in this study were not reported, however it was clear from TEM images of the cells and spectroscopic measurements of the culture media that high levels of these nanoparticles were internalised by K562 cells.

3.1.1 Aims of this thesis chapter

The previous chapter focussed primarily on the analysis of isolated cells. However, the ONE Study protocol also includes a routine biopsy of the transplanted organ, which is expected to take place at 12 weeks post-transplantation. Therefore, this chapter aims to demonstrate the potential of LA-ICP-MS to provide high-resolution imaging of Mregs and Tol-DC in biopsy samples. The specific objectives of the work were as follows:

1) To optimise a gold nanoparticle labelling method for Mregs and Tol-DC, in order to achieve maximum label uptake by the cell population, whilst minimising toxicity concerns.
2) To administer the labelled cells in animal models and to subsequently determine their general location through ICP-MS analysis of digested organ samples.
3) To demonstrate that LA-ICP-MS can be used to identify labelled cells at high specificity within thin tissue sections.

4) To evaluate the feasibility of using antibody based post-labelling to correlate gold signals with the presence of defined cell subsets.

It is recognised that there are differences in generation, culture, nature and function of the two cell types used in this chapter. There is further contrast in the administration method between groups, since Regensburg intend to administer their Mregs one week pre-transplant, whereas Nantes favour post-transplant administration of Tol-DC.[151] It is therefore accepted that there will be differences in the cell tracking methodology used for the two cell types. The primary objective of this chapter is to demonstrate that both Mregs and Tol-DC can be tracked using LA-ICP-MS; however it is not the intention to provide a comparison of their mechanism of action *in vivo* or their relative clinical suitability.

3.2 Experimental

Mreg culture and labelling procedures were performed by James Hutchinson and co-workers at the Universität Regensburg, Germany. Culture and labelling of Tol-DC was performed by Aurélie Moreau and colleagues at the Université de Nantes, France. All animal experimentation, dissection and staining procedures were performed at these sites, in accordance with the applicable ethical guidelines.

3.2.1 Culture and labelling of Mregs

Human Mregs were generated from purified CD14$^+$ peripheral blood monocytes, according to a previously published protocol.[163] The harvested Mregs were washed twice in Dulbecco's phosphate buffered saline (DPBS) and resuspended at a density of 10^6 cells/ml in pre-warmed X-Vivo 10 medium (Lonza, Cologne, Germany). A PBS stabilised 50 nm gold nanoparticle suspension (Sigma-Aldrich, Munich, Germany), known to contain ~3.5 x 10^{10} Au nanoparticles/ml, was used to dope the above medium. The cells were then incubated at 37°C in a closed 15ml tube, with end over rotation. A range of doses and incubation times were initially tested (see Table 3.2), however, the final conditions used 1 ml of the nanoparticle suspension per tube and an incubation time of 1 hour. Following labelling, the cells were washed three times in DPBS, to remove any unbound label, before further processing.

For experiments involving solution ICP-MS analysis, the cells were spun down into pellets and the supernatant removed, before shipping to Loughborough at room temperature. For laser ablation experiments, the cells were resuspended in Mreg generation medium, before replating into chamber slides (BD Falcon, Heidelberg, Germany) at a density of 10^6 viable Mregs/ml. The cells were allowed to adhere to the glass slide over a 24 hour period. The adherent cells were then washed with ice cold DPBS, air dried and stained with Diff-Quik Giemsa staining reagents (Medion Diagnostics, Munich, Germany).

3.2.2 Culture and labelling of Tol-DC

Tol-DC were generated from bone marrow precursors according to previously published protocols.[164] The cells were plated at a density of 0.5 million cells/ml in 5 ml of AIM V medium (Gibco BRL, Paisley, UK), supplemented with 100 U/ml recombinant murine GM-CSF (Novartis, Basel, Switzerland). At day 6, both adherent and non-adherent cells were harvested, counted, and re-incubated at a density of 0.5 million cells per well in 1 ml AIM V medium. A 50 nm gold nanoparticle suspension (Sigma-Aldrich, Lyon, France) was added to each well (see Table 3.3) and the cells allowed to incubate at 37°C for 1 hour. Following labelling, the cells were washed extensively (5 x PBS). Samples for solution ICP-MS were transferred into tubes and spun down into pellets, whilst samples for laser ablation were plated onto slides using a Cytospin.

3.2.3 *In vivo* tracking of Mregs in NSG mice

Mouse experiments were conducted in accordance with permission Nr. 54-2532.1-10/12 granted by the Regierung von Oberbayern. NSG (NOD.Cg-Prkdc^{scid} Il2rg^{tm1Wjl}/SzJ) mice were bred in-house. Animals were kept in individually ventilated cages and fed on a conventional diet. Immediately prior to injection, the concentration of gold-labelled Mregs was adjusted to 5 x 10^6 viable cells/ml in Ca^{2+} and Mg^{2+} free Dulbecco's PBS, supplemented with 60 IU/ml of heparin. Cell suspensions were injected through a 27-gauge needle into the tail vein of recipient NSG mice, over 30–180 s. Organs were harvested at either 24 hours or 7 days post-infusion by post-mortem dissection. Each organ was weighed prior to separation into sections. Three sections from each organ were individually weighed and placed into tubes for ICP-MS analysis, with the remainder retained for LA-ICP-MS analysis. Tissues for analysis by LA-ICP-MS were fixed in paraformaldehyde and embedded in paraffin wax, before sectioning to a thickness of 6 µm. Sections were mounted on SuperFrost slides (Thermo Fisher Scientific, Schwerte, Germany) and stored in a dry environment at 37°C for several days. Sections were dewaxed with Roti-Histol (Carl Roth, Karlsruhe, Germany), then progressively rehydrated with increasingly dilute ethanol before analysis.

3.2.4 *In vivo* tracking of Tol-DC in NSG mice

Animal experimentation was conducted in accordance with the institutional and national ethical guidelines at the Université de Nantes. At day 0, NSG mice were irradiated and injected intravenously (i.v.) with 5 x 10^6 labelled Tol-DC and intraperitoneally (i.p.) with 5 x 10^6 non-labelled PBMC. The mice were sacrificed at days 3, 6 and 10, post-administration and the organs harvested. Three mice were used for each time point, with a further three mice given non-labelled cells as a negative control. Each organ was weighed and separated into sections, with 3 individually weighed sections (~20-200 mg each) per organ provided for solution ICP-MS, and the remaining organ frozen for subsequent experiments. These frozen organs sections were stored at -80^{o}C for approximately one month, then sectioned to a thickness of approximately 5µm using a cryostat. Sections were mounted on SuperFrost slides (Thermo Fisher Scientific, Schwerte, Germany) and sent to Loughborough on dry ice.

3.2.5 MAXPAR antibody labelling

Following conventional immunohistochemical techniques, tissues were blocked with 5% normal mouse serum in Tris buffered saline (TBS) for 1 h. Tissues were stained overnight at 4°C using primary metal-tagged MAXPAR antibodies (Fluidigm Sciences, Sunnyvale, CA) diluted in TBS + 5% normal mouse serum, according to the manufacturer's recommendations. Specifically, tissues were stained with ^{154}Sm-tagged anti-CD45 (clone HI30), ^{159}Tb-tagged anti-CD11c (clone Bu15) or ^{174}Yb-tagged anti–HLA-DR (clone L243). Sections were counterstained with H&E before progressive dehydration in alcohol and air drying.

3.2.6 Solution-based ICP-MS

Digestion of the cell and organ samples was performed prior to ICP-MS analysis, according to a procedure proposed by Yamada *et al*.[132] and modified by Kerr.[133] This involved addition of 67% HNO_3 (100 µl per 1x10^{6} cells, or 0.5 ml per organ), heating at 70^{o}C for 1 hour, followed by addition of 30% H_2O_2 (100 µl per 1x10^{6} cells, or 0.5 ml per organ) and heating at 70^{o}C for a further 4 hours. The samples were evaporated to dryness under a stream of nitrogen, and then reconstituted in 5% aqua regia. For quantification, a range of standards were produced by dilution of a 10 ppm elemental standard solution (SPEX Certiprep, Middlesex, UK).

Analyses were performed on a sector-field ICP-MS instrument (Element 2XR, Thermo Scientific, Bremen, Germany). The instrument was fitted with a cyclonic spray chamber (Glass Expansion, Victoria, Australia), a conical glass concentric nebuliser

(Glass Expansion, Victoria, Australia), and a 0.25 mm I.D. probe (Elemental Scientific, Omaha, USA). Gold is known to have an affinity for the surfaces of the sample introduction system,[133] so to minimise memory effects, solutions of 5% aqua regia and 10mM cysteine were aspirated between samples.

3.2.7 LA-ICP-MS

A UP-213 laser ablation system (Electro Scientific Industries, Cambridgeshire, UK) was coupled to the sector-field ICP-MS instrument above, in external trigger mode. The laser was fitted with a low-volume, tear-drop shaped cell, which has been described in detail elsewhere.[131] Helium was used as an ablation gas, at a typical flow rate of 0.6 l/min, with argon introduced through a Y-piece, at a flow rate of 0.8 l/min, downstream of the ablation cell. The system was tuned daily for maximum ^{238}U signal intensity, whilst keeping the Th/U ratio to approximately 1 and the ThO/Th ratio to below 1%, during the ablation of NIST 611 glass.

Cells were examined on an individual basis by ablating single 55 μm diameter shots at locations corresponding to single Au labelled cells, single non-labelled cells, and areas of the media containing no cells. The spot size was chosen to ensure complete sampling of each cell, whilst minimising the chance of overlap onto neighbouring cells. However, Mreg morphology dictated that in a few cases a small portion of the cell extended beyond this region and was not ablated. A high laser energy, producing ~ 9 J cm^{-2} fluence, was chosen to ensure complete ablation of cellular material within the sampled region. Only single cells were targeted; cells present in clusters or closer than 55 μm apart were disregarded. The integrated ^{197}Au counts per peak were taken to be representative of the total Au content per cell.

Imaging of cells and tissue sections was accomplished by performing adjacent line scans across a section of the slide, whilst measuring ^{197}Au and ^{154}Sm, ^{159}Tb or ^{174}Yb in time resolved mode. The ICP measurement parameters for this analysis are shown in Table 3.1. A ~2 J/cm^2 laser fluence, 5 Hz repetition frequency, 8 μm spot size and 8 μm/s scan speed were used, with zero spacing between ablated lines. Images were constructed from the data using Iolite version 2.15 (Melbourne Isotope Group, Victoria, Australia), which is a freeware data deconvolution package that runs on the IGOR Pro 6.22A platform (WaveMetrics, Oregon, USA). The software converts each raw data point into a colour coded pixel; thus the colour profile of the resulting image depicts the distribution of the respective elements across the sampled region.

Table 3.1 The ICP-MS measurement parameters for the co-detection of Au nanoparticles and MAXPAR antibody labels.

Parameter	First isotope	Second isotope
Isotope	Sm154, Tb159 or Yb174	Au197
Mass window	20 %	20 %
Integration window	20 %	20 %
Settling time	0.001 s	0.001 s
Sample time	0.001 s	0.001 s
Samples per peak	50	50
Segment duration	0.01 s	0.01 s
Scan type	EScan	EScan
Detection mode	Triple	Triple
Integration type	Average	Average

3.3 Results and Discussion

3.3.1 Optimisation of the labelling conditions

Both cell types are known to have very rapid phagocytic ability; thus only a narrow range of incubation times were tested for Mregs and only one time point was tested for Tol-DC. The label concentration is perhaps the more defining parameter for uptake, as can be seen in Table 3.2 and Table 3.3, which show the average number of Au atoms internalised by Mregs and Tol-DC at each condition. Problems generating and expanding the cells *in vitro* produced insufficient cell numbers for an adequate number of replicates per dose, hence, where replicates were performed, the observed %RSD were large. Despite this, the general trend was clearly identifiable. Label uptake was heavily concentration dependent and did not reach saturation within the range of concentrations examined.

Table 3.2 The effect of the Au labelling dose and the incubation time on the uptake of Au nanoparticles by Mregs. Data is presented as the average number of Au atoms internalised per cell for each labelling condition.

		Incubation time		
		10 s	**1 h**	**2 h**
Dosage / µl	**0**	Not detected	Not detected	Not detected
	1	Not detected	1.79E+06	1.75E+06
	5	Not detected	1.06E+07	9.52E+06
	10	1.54E+06	3.09E+07	3.76E+07
	50	1.05E+07	1.71E+08	3.64E+08
	100	1.51E+07	3.39E+08	4.36E+08

Table 3.3 The effect of the Au labelling dose on the uptake of Au nanoparticles by Tol-DC, when using an incubation time of 1 hour. %RSD's are given as n=2, unless specified by an asterisk, where n=3.

		Au atoms per cell	**±**	**% RSD (n=2)**
Dosage / µl	**0**	5.81E+05	±	81
	10	5.06E+07	±	32 *
	100	3.94E+08	±	44 *
	200	6.42E+08	±	66
	500	6.81E+08	±	50

To ascertain whether gold labelling affects the viability, phenotype or function of the cells, flow cytometry studies was performed at the Universität Regensburg and Université de Nantes. This involved analysis of common surface markers that are expressed by each cell type, as well as an assessment of their ability to suppress proliferation of allogeneic T cells *in vitro*. No difference was observed between labelled and non-labelled Mregs in terms of their surface marker expression or suppressor activity, when using 100 µl of the nanoparticle suspension (~3.5 x 10^9 Au nanoparticles). Toxicity tests with Tol-DC examined a higher range of concentrations, up to 500 µl (~1.75 x 10^{10} Au nanoparticles). No difference in the suppressive ability of Tol-DC was noted. However, Tol-DC incubated with nanoparticles exhibited a slight increase in CD83 and CD86 expression, which increased with increasing nanoparticle concentration. For this reason, the labelling dose was limited to 100 µl nanoparticle suspension per 1 ml of media for all subsequent experiments.

3.3.2 Laser ablation of single cells

To assess the variance in nanoparticle uptake, the cells were analysed on an individual basis using LA-ICP-MS. High labelling and detection efficiencies of 100% and 97.8% were obtained for Mregs and Tol-DC respectively. LA-ICP-MS of the labelled cells yielded an average signal of 1.9 x 10^5 counts/cell (77% RSD, n=100) for Mregs and 2.1 x 10^5 counts/cell (148% RSD, n=978) for Tol-DC. As mentioned in Chapter 2, variation in label uptake across the population is expected due to intrinsic biological heterogeneity, as well as sampling constraints regarding the laser fluence and morphology of the cells. With nanoparticle labelling, a further source of variation may arise from the formation of nanoparticle aggregates in the regions surrounding cells, which may be non-uniform in size and shape and may interact with cell receptors in different ways.[165] The extent of variance in uptake is accordance with published LA-ICP-MS data on Au nanoparticle uptake,[166] which was acquired using a different laser system than the one used here. Despite the variation in uptake, each signal was clearly distinguishable from the low background of approximately 0 to 20 counts, (Figure 3.1). No signals above background were observed for the ablation of non-labelled cells (Figure 3.1). This demonstrated that the labelled cells can be rapidly and reliably distinguished from their non-labelled counterparts, which was subsequently confirmed during the analysis of mixed populations of labelled/non-labelled Mregs (see Table 3.4).

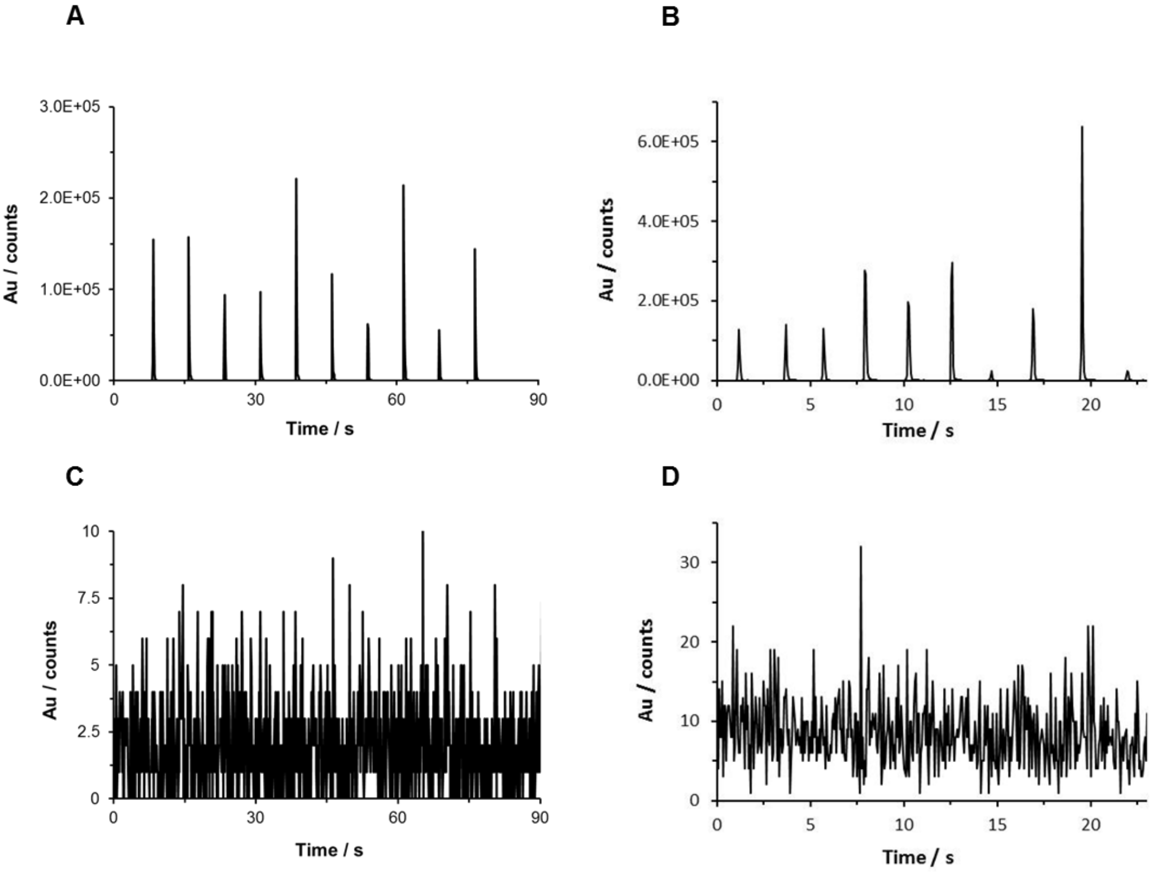

Figure 3.1 Example LA-ICP-MS signals for the ablation of 10 individual Mregs (A) and 10 individual Tol-DC (B) following incubation with 3.5 x10^9 gold nanoparticles for 1 hour. Background noise was observed during the ablation of unlabelled Mregs (C) and Tol-DC (D).

Table 3.4 LA-ICP-MS analysis of mixed populations of labelled/non-labelled Mregs.

Ratio of Labelled/ Non-labelled Cells	Culture time after labelling / h	No. of cells ablated	No. of labelled cells detected
1:0	1	100	100
0:1	1	100	0
1:1	1	100	45
1:0	36	100	100
0:1	36	100	0
1:1	36	100	43

3.3.3 Co-labelling with metal-conjugated antibodies

Release of gold nanoparticles from decaying cells and their subsequent reuptake by phagocytes could lead to false positive detection. One solution to this problem is to establish that cells bearing the tracer label express the anticipated marker phenotype, through immunohistochemical “post-labelling” with metal-conjugated antibodies. This form of phenotypical analysis may also prove useful in determining the functional status of infused Tol-DC. It is thought that immature dendritic cells are responsible for inducing tolerance, whilst mature cells play a role in establishing immunity.[6] Maturation can be monitored by measurement of changes in characteristic surface markers. For example, HLA-DR molecules are upregulated following maturation of Tol-DC.[167]

A feasibility study was conducted to assess whether Au nanoparticles and metal-conjugated antibodies can be co-detected in cells using LA-ICP-MS. Following Au labelling, cells were counter-labelled by incubation with either ^{154}Sm tagged anti-CD45, ^{159}Tb tagged anti-CD11c or ^{174}Yb tagged anti-HLA-DR. Co-detection of transient signals from different elements is challenging when using sector-field ICP-MS, due to the sequential scanning mode. Scanning using the magnetic sector requires a long settling time between measurements of each mass, but faster electrostatic scanning is possible between elements of similar mass. The metal-tagged antibodies selected for this study were therefore chosen to be close enough in mass to ^{197}Au to avoid a magnet jump.

LA-ICP-MS line scans were performed across a cluster of the labelled cells to simulate tissue imaging. Figure 3.2 and Figure 3.3 show a selection of the resulting LA-ICP-MS images. Although relatively low, the count rate was sufficient to enable detection of the cells and importantly the spot size and scan speed were sufficient to discriminate between the signals from individual cells. Co-existing signals were obtained for the antibody and nanoparticle labels, demonstrating that the method could, in principle, be applied to detect dual labelling of cells in tissues. In this study, where the cells were Au labelled for 1 hour with no follow-on culture, both labels appeared to be homogeneously distributed across the cells. However, a recent study of 14 nm Au nanoparticle uptake in fibroblast cells indicated that nanoparticles may begin to aggregate and locate to the perinuclear region in cells that are cultured for 1 to 3 hours after labelling.[168] As long as labels are internalised, their cellular location is not critical to cell tracking. However, it is notable that perinuclear localisation of nanoparticles would produce Au signals of shorter duration for *in vivo* studies, where there is further opportunity for aggregation, than for the images shown in Figure 3.2 and Figure 3.3.

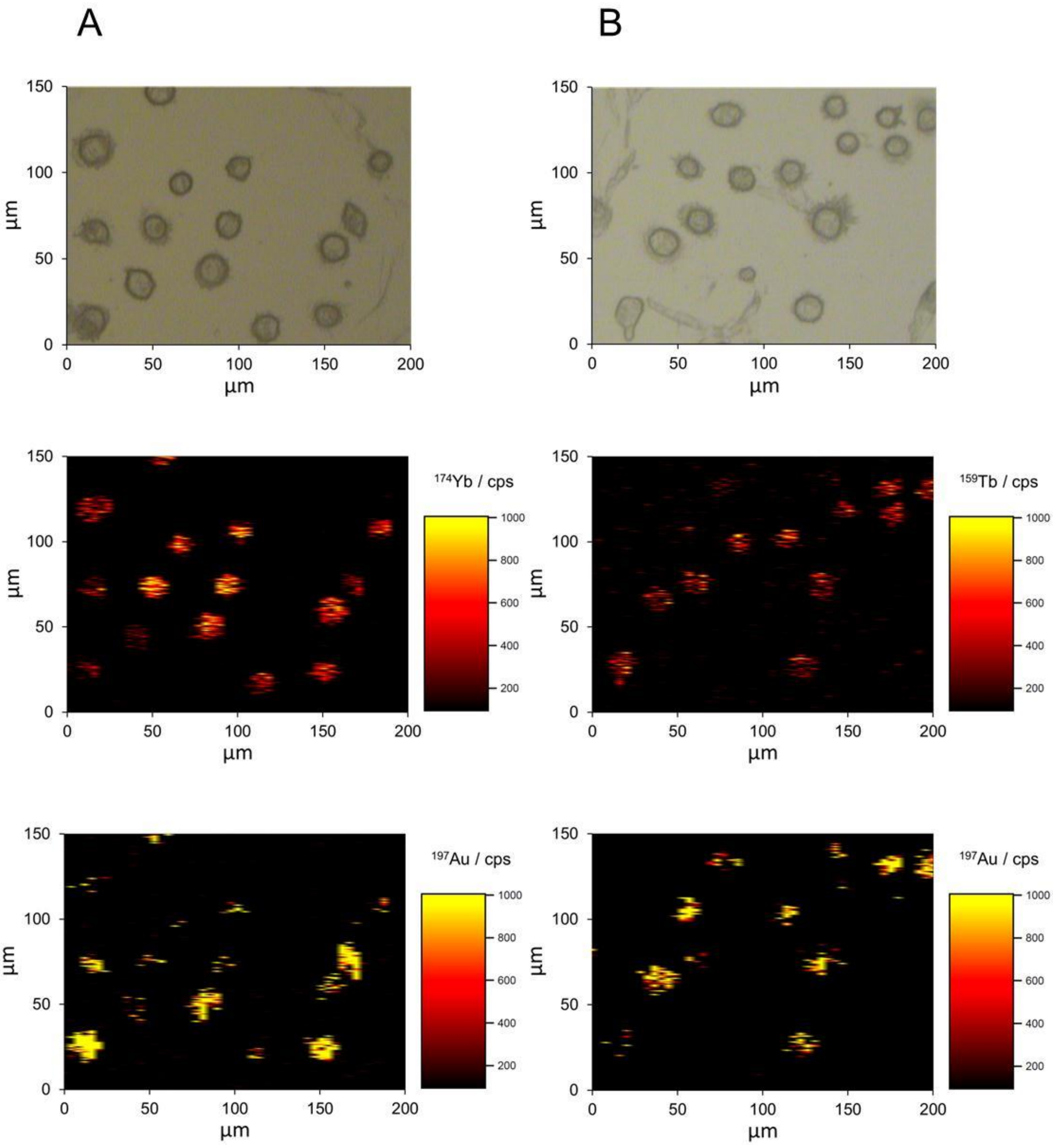

Figure 3.2 A: Microscopic image of a section of slide-mounted Au and anti-HLA-DR-^{174}Yb labelled Tol-DC (top). LA-ICP-MS image of the same section, showing the Yb (middle) and Au (bottom) distribution.
B: Microscopic image of a section of slide-mounted Au and anti-CD11c-^{159}Tb labelled Tol-DC (top). LA-ICP-MS image of the same section, showing the Tb (middle) and Au (bottom) distribution.

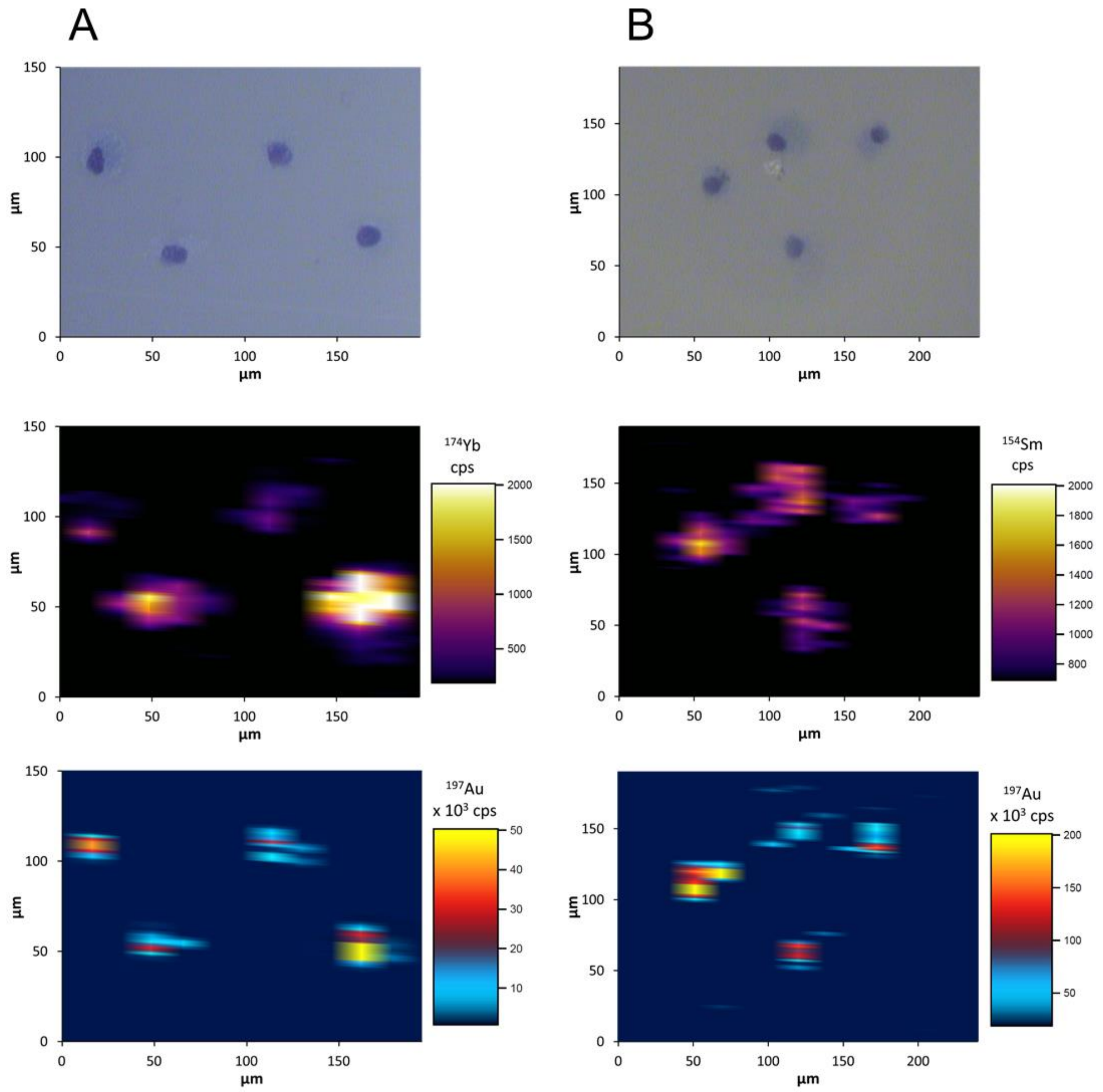

Figure 3.3 A: Microscopic image of a section of slide-mounted Au and anti-HLA-DR-^{174}Yb labelled Mregs (top). LA-ICP-MS image of the same section, showing the Yb (middle) and Au (bottom) distribution.

B: Microscopic image of a section of slide-mounted Au and anti-CD45-^{154}Sm labelled Mregs (top). LA-ICP-MS image of the same section, showing the Sm (middle) and Au (bottom) distribution.

3.3.4 *In vivo* mouse study

The distribution of cells after intravenous infusion reflects their active and passive migration and engraftment into tissues, as well as their death and elimination. In a previous tracking study, Hutchinson *et al*. used single photon emission computed tomography (SPECT) to analyse ^{111}In-oxine labelled Mregs in a transplanted human patient.[7] In this study, the ^{111}In-oxine label was predominately detected within the lungs during the first 2.5 hours after administration, but by 4.5 hours had begun spread to the liver and spleen via the blood.[7] However, due to radioisotope stability, the survival and fate of the Mregs could not be characterised beyond 30 hours using this method. In contrast, the use of Au nanoparticle labelling and LA-ICP-MS detection could provide valuable information on the trafficking of cells beyond this limit.

Gold labelled Mregs and Tol-DC were injected into NSG mice in two separate experiments. The presence of label in the major organs was assessed at day 1 and 7 post administration for Mregs and at days 3, 6 and 10 post-administration for Tol-DC. Figure 3.4 shows the amount of Au detected per organ for mice given labelled Mregs, compared to a non-labelled control. Gold was principally detected in the lungs, liver and spleen, with minor accumulation also observed in the kidney, heart, brain and intestine.

The distribution of label shown in Figure 3.4 is unsurprising, considering the route of cell administration used. High accumulation within the lungs is expected in the initial period after injection, since cells given intravenously are carried through the lungs by the blood and may become trapped in the pulmonary vasculature. Similarly, highly perfused organs, such as the liver, are expected to attract and accumulate cells. Interestingly, a SPECT study by Eggert *et al*. indicated that cells administered intravenously may show different migration patterns to those given subcutaneously or intraperitoneally.[169] Eggert observed that up to 55% of the cells injected into the peritoneum remained at the site of injection at 48 hours post-administration, which correlates with the findings of the Gd-labelled cell study, reported in Chapter 2, which used the intraperitoneal route.

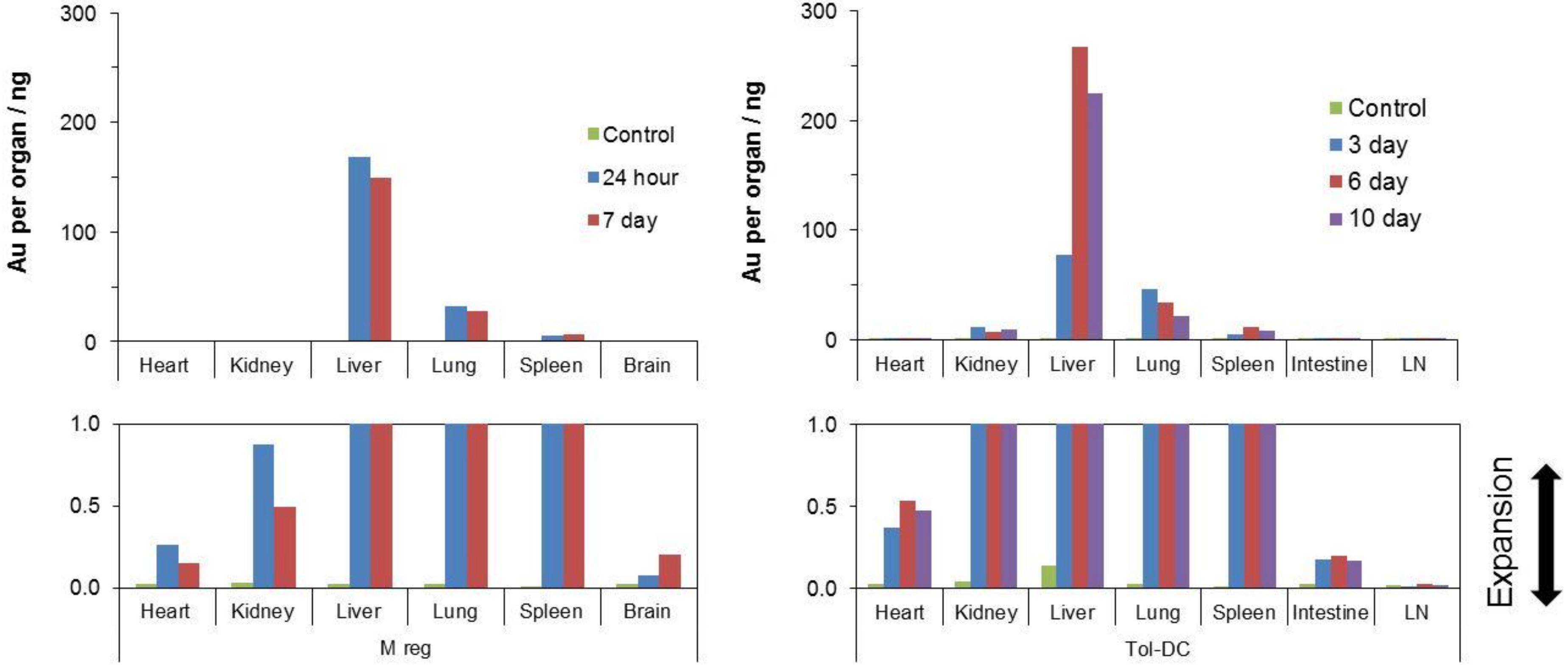

Figure 3.4 Tracking of Mregs and Tol-DC in immunodeficient mice using solution based ICP-MS analysis of digested organ samples. The proportion of gold detected within each organ, for samples taken at various time points after administration of Au labelled cells. Control animals given non-labelled cells are included for comparison. Graphs on the left hand side show the experiments involving Mregs (n=1), whilst the graphs on the right hand side show the average uptake for experiments involving Tol-DC (n=3). The lower panels show an expanded view of the scale between 0 and 1 ng Au per organ, to enable visualisation of the lower intensity data.

3.3.5 Laser ablation of tissue sections

Although the above ICP-MS study provided valuable information on the general localisation of administered cells, it offers very limited insight into the precise distribution of the cells within the tissues studied. To demonstrate the applicability of laser ablation sampling to provide spatially resolved information, paraffin embedded tissue sections from the above experiments were sectioned to a thickness of 6 μm. Investigations focussed on the liver, lung and spleen, which previously identified as the major sites of Au accumulation. Sampled areas were 320 x 245 μm in size, with two areas selected per tissue section. The results of this analysis are presented in Figure 3.5. As predicted by solution ICP-MS, label was detected in all three tissues. However, no pattern of signal distribution was perceived within the relatively small areas of tissue examined.

From Figure 3.5 it is difficult to verify whether the observed signals are from intact cells or from individual nanoparticles that may have been released through exocytosis or cell death. Concurrent detection of signals from cells pre-labelled with gold and post-labelled with metal-bound antibodies to HLA-DR would imply the presence of intact cells in mouse tissues. Unfortunately, sections of spleen that were counterstained with ^{174}Yb-conjugated anti-HLA-DR gave rise to high ^{174}Yb background signals, as shown in Figure 3.6. Therefore, no correlation between the distribution of ^{174}Yb and ^{197}Au signals could be established. It is possible that these metal-tagged antibodies are unsuitable for use on tissue sections, possibly owing to destruction of antigens during tissue fixation, or perhaps due to subsequent detachment of the label during storage, shipping or handling of the samples. It is equally possible that MAXPAR reagents have a greater propensity for non-specific binding to tissues than antibodies tagged with alternative labels. A previous publication by Waentig *et al*. noted high backgrounds for MAXPAR reagents in Western blot immunoassays, when compared to other reagents.[170] As the authors of this work pointed out, the MAXPAR reagents and their recommended protocols were optimised for single-cell analysis by mass cytometry. Post-labelling tissues with metal-labelled antibodies may require development of more suitable metal-conjugated antibodies, possibly labelled using different chemistries, as well as better histological methods to block non-specific binding of antibodies.

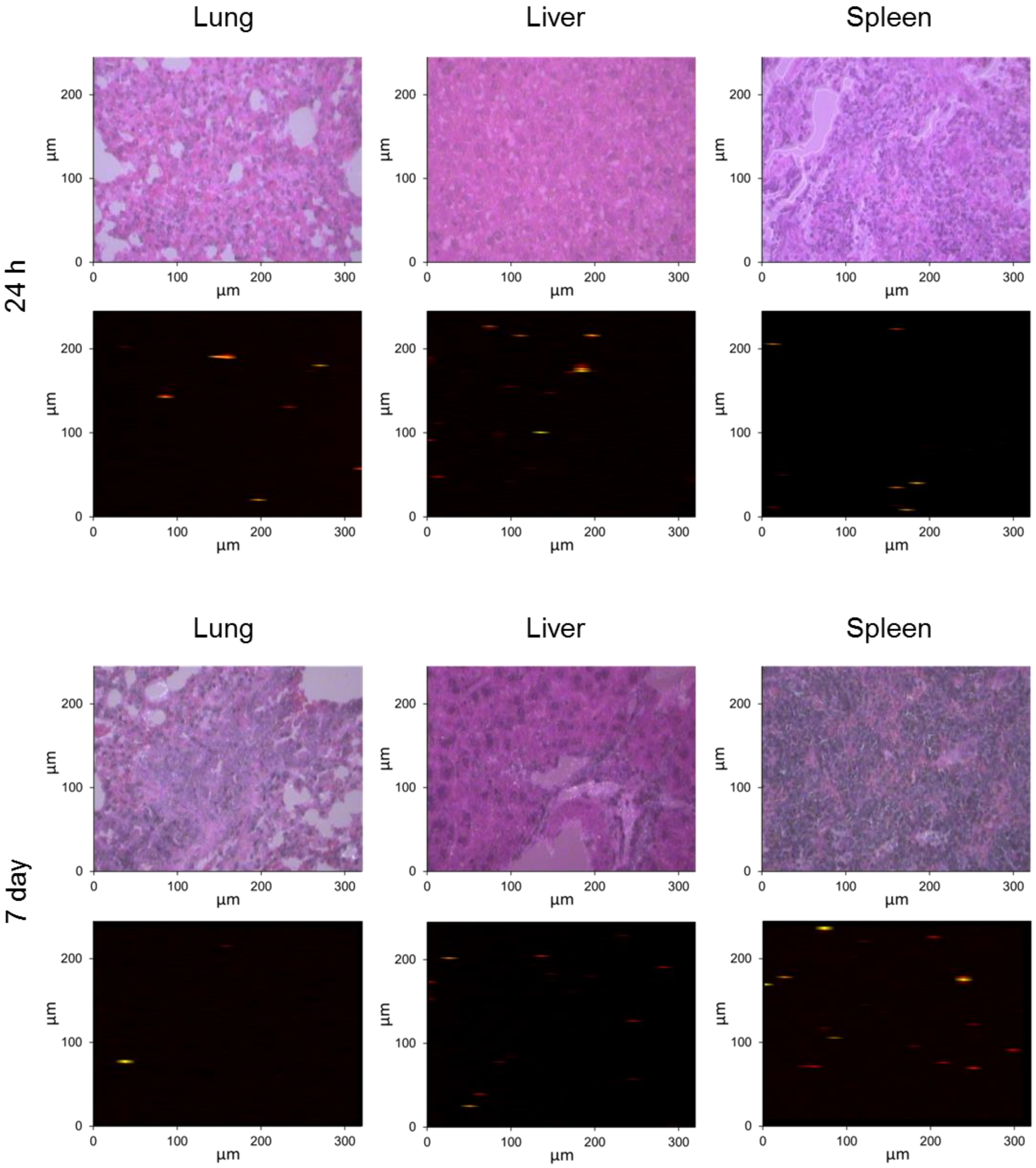

Figure 3.5 High resolution imaging of Au in small sections of mouse tissue. Optical images of mouse liver, lung and spleen tissue and the corresponding LA-ICP-MS images, showing the distribution of gold within each section. Regions of high gold intensity appear as coloured spots in the LA-ICP-MS images. It is likely that the broader spots correspond to cells, whilst the narrower streaks may indicate the presence of individual nanoparticles. Tissues were harvested at 24 hours (upper panels) and 7 days (lower panels) after administration of gold labelled Mregs, and were subsequently counterstained with H&E.

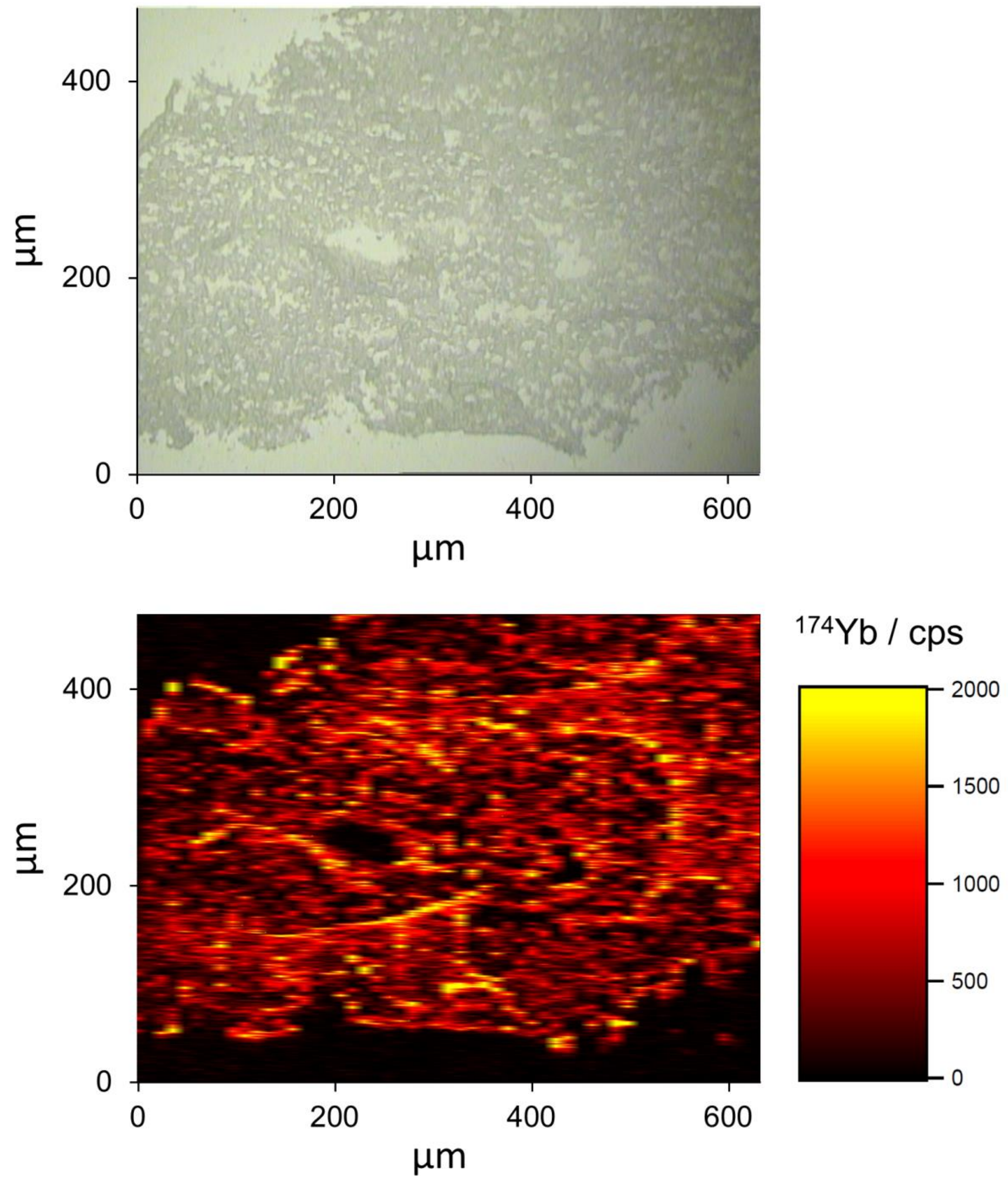

Figure 3.6 High resolution imaging of a section of mouse spleen tissue, which was counter-labelled with ^{174}Yb-tagged anti-HLA-DR. Top: Microscopic image of the 450 µm x 632 µm section of NSG mouse spleen tissue. Bottom: corresponding LA-ICP-MS image showing the ^{174}Yb distribution across the section.

3.4 Conclusion

This chapter reports the use of 50 nm sized gold nanoparticles to label regulatory macrophages and tolerogenic dendritic cells, which facilitated their detection by ICP-MS in *ex-vivo* mouse samples. Solution-based ICP-MS of the major organs identified the lungs, liver and spleen as the major sites of Au accumulation, at periods of up to 10 days after administration of the labelled cells. LA-ICP-MS of these tissues offered a unique combination of high sensitivity and spatial resolution and permitted longer tracking periods than were possible in previous experiments using SPECT detection. In addition, the use of non-radioisotopic tracers may be safer and more convenient than the ^{111}In-oxine labels, when manufacturing and administering cell based therapies. The only notable disadvantage of LA-ICP-MS compared to SPECT is its *ex-vivo* nature, which demands invasive sampling and precludes repeated measurements within a short timeframe.

Antibody-metal labels were successfully used to co-label isolated Tol-DC and Mregs with high specificity. LA-ICP-MS imaging revealed strong correlation of the antibody tags with gold signals, which has potential applications for the validation of Au tracking data. Unfortunately, the method could not be translated to the analysis of tissue sections, owing to high background levels of the rare earth metal in the tissue. This may be an indication of non-specific binding of the antibody labels used. The inability to identify co-labelled cells in tissue samples does not derive from the effectiveness of the LA-ICP-MS technique, but points instead to the limitations of current metal-tagged antibodies and histological methods. With the development of a new mass cytometry imaging platform expected in 2015,[171] there is likely to be considerable interest in developing new protocols and improved reagents for staining tissues with rare earth labels.

For phenotypic analysis of cells, it would be beneficial to measure many more parameters than studied here. The principal restriction on analysing a greater number of metal labels was the rate at which sector-field instruments detect each element, which they must do sequentially. Simultaneously detecting mass spectrometers, such as time-of-flight mass spectrometers, would enable concurrent, multi-channel measurements of a vast array of metals. However, TOF systems provide considerably lower sensitivity compared to sector-field mass spectrometers, or in the case of the CyTOF system,[61] have a limited mass range. Given the signal intensities observed for metal-tagged antibody labels, it appears that performing this analysis with commercially available LA and TOF systems may prove challenging. However, Wang *et al*. recently reported the development of a custom designed, high speed and high sensitivity laser ablation cell,[172] which was successfully coupled to a CyTOF to image an array of lanthanide-tagged antibodies.[173] Improvements of this nature to the core LA technology are of paramount importance to multi-parametric single cell analysis and hence will be discussed in more detail in Chapter 4.

4 Development of a High-speed LA-ICP-MS Interface for Bio-imaging

4.1 Introduction

Since the development of LA-ICP-MS imaging, there has been focus on improving the speed and sensitivity of the technique. Convolution of signals from consecutive laser pulses reduces the effective spatial resolution of images, so the degree of signal dispersion is considered the limiting factor for sampling speed. Commercially available systems have aerosol residence times of approximately a second; thus to image a 1 x 1 mm tissue biopsy at 10 µm resolution would take approximately 2.8 hours. Whilst this may be acceptable in the research setting, such lengthy analysis times preclude the application of LA-ICP-MS for routine clinical monitoring. Numerous groups have attempted to solve this problem by designing custom modifications to the existing systems.[172, 174-184] The interface between the laser and the mass spectrometer has attracted considerable interest here, particularly the dimensions of ablation cell/chamber, the position of the gas ports within it, and the transport conduit connecting the cell to the ICP.

4.1.1 The ablation cell/chamber

In order to accommodate a variety of sample formats, commercial LA cells typically have large inner volumes, which results in high aerosol dispersion. Consequently, there has been a drive to create low-volume, fast-washout cells for small samples,[131] whilst “open” cells, placed on top of the sample surface, are sometimes used for larger samples.[176, 177] An example of an open cell is the non-contact cell, which is suspended 200 µm above the sample surface and uses a curtain gas to exclude atmospheric gases from the site of ablation.[177] However, due to the complexity required to maintain an inert ablation atmosphere, the concept of open cells has not gained popularity.

More recently the focus has shifted to two-volume or cell-in-cell configurations. These typically include a low-volume inner sampling device, positioned above the ablation site, within a closed external cell. This enables the analysis of large format samples, such as gels or membranes, whilst maintaining a low effective volume within the ablated region. Furthermore, in systems where the inner cell maintains a consistent sampling position within the outer chamber, signal reproducibility is improved. Various inner sampling devices have been reported.[178-180] The laminar flow reactor (LFR) used a simple tube above the ablation site, and achieved washout times of 45 ms (to 10% peak maximum).[178] The volume-optional low-memory (VOLM) chamber used a 0.4 cm^3 cylindrical inner cell, producing washouts of 0.45 s (to 10% peak maximum).[179] Whilst the Laurin cell employed a ~1-2 cm^3 funnel shaped inner cell, yielding washouts of 1.5 s (to 1% peak maximum).[180]

4.1.2 Gas inlet/outlet ports

Expansion of the carrier gas as it enters the cell, and contraction as it exits, generates turbulent gas flows that can entrain ablated particles and increase their residence time.[181] Consequently, it is beneficial to arrange the gas ports in a geometry that will produce a laminar flow in the ablation region. This concept was integral to the single-volume designs reported by Gurvevich *et al*. and Monticelli *et al*., who achieved washouts of 30-40 ms (to 37% peak maximum) and 30 ms (to 10% peak maximum), respectively.[181, 182] In contrast to this, Bleiner and Altorfer's rotating nozzle inlet increased turbulent mixing, but this was beneficial as it reduced the dead volume within their large (30 cm^3) cell.[183] The rotating nozzle produced a two-fold higher "improvement factor" compared to their standard inlet, which was defined as signal intensity divided by point-to-point repeatability.[183]

4.1.3 The transport conduit

Another key area is the conduit connecting the ablation cell to the ICP torch. Many systems employ flexible polymer tubing, which is usually around 3-4 mm internal diameter and can be several metres in length. The flow path is usually intersected by a T- or Y-piece, for argon introduction, and may pass through a series of valves and other flow impedances. Flow modelling suggests that minimising these disruptions and maintaining a constant diameter conduit is beneficial to reduce signal dispersion.[185] This was confirmed experimentally in the aforementioned LFR cell, which used a tubing diameter equal to that of the injector tube, and included a custom, laminar flow connector for argon addition.[178] Wang *et al*. also developed a “tube cell” using this concept.[172] The ablation cell was adjoined below the tubing, such that the plume was lifted upwards by the helium flow, directly into the laminar argon flow, through an opening in the tubing. This removed the requirement for a conventional dispersive T-piece, producing signal widths of 30 ms at 1% peak maximum.

4.1.4 *In torch* ablation

Liu *et al*. designed an *in situ* laser ablation system for inductively coupled plasma - optical emission spectroscopy (ICP-OES), whereby ablation took place inside the ICP torch itself, removing the need for the LA cell or connecting tubing.[186] The sample was placed a millimetre below the plasma discharge, and the laser beam was directed through the plasma onto it. The resulting aerosol was transported into the plasma by the sample gas flow. Signals with a full width at half maximum (FWHM) of 0.7 ms were reported.[186] However, this arrangement was unsuitable for use with ICP-MS, as the MS interface, placed after the plasma, would have obstructed the laser beam.

Tanner *et al*. modified Liu’s *in torch* arrangement for use with mass spectrometry.[184] Instead of directing the laser beam through the plasma, it was focussed through a 10 x 10 mm hole in the top of the torch. The system produced signal durations with a FWHM of 4 ms when using a quadrupole mass analyser. However, the in torch system was impractical to implement, since it was limited to small samples and precise sample movement was impossible. Due to the high temperature of the sampling position, the system was also restricted to high melting point samples. Despite this, the speed of the *in torch* system can be regarded as the ultimate benchmark for the development and characterisation of new LA-ICP-MS interfaces.

4.1.5 The Loughborough system

Douglas *et al*. developed a new LA-ICP-MS interface that encompassed the key design areas outlined in sections 4.1.1 to 4.1.3.[187] The ablation cell used a two-volume arrangement, containing a 0.005 cm^3 internal volume “Sniffer” cell, sealed inside the lid of a standard UP-213 cell. This inner device, shown in Figure 4.1, sat approximately 100 μm above the sample surface and used a pressure gradient to efficiently capture the ablated plume, preventing its expansion into the outer cell.

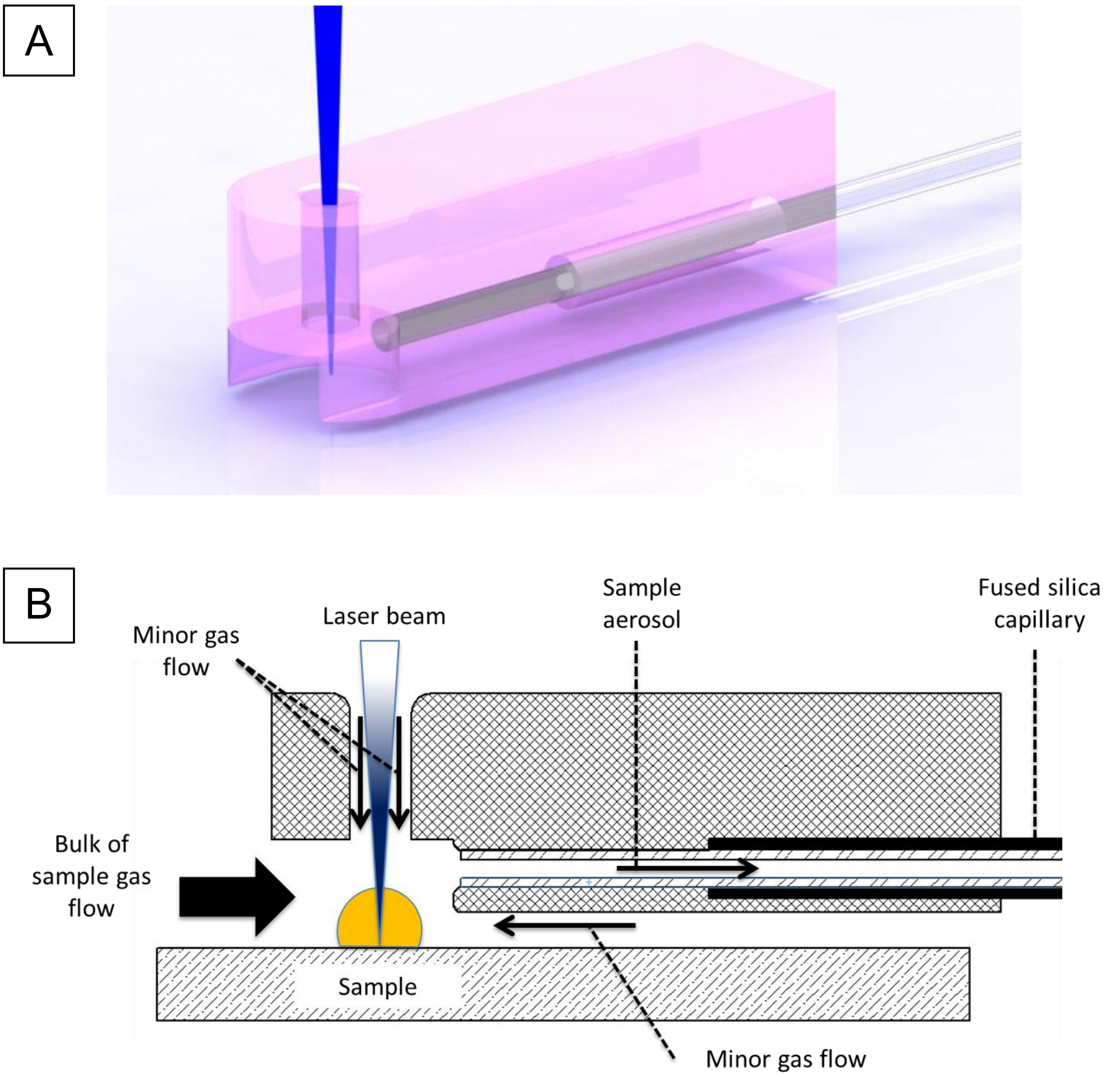

Figure 4.1 A) Semi-transparent rendered image and, B) cross-sectional view of the Sniffer. Image B reproduced with permission of David Douglas.

The Sniffer was integrated with a 250 μm i.d. fused silica capillary, which formed the central injector in a Dual Concentric Injector (DCI) ICP torch, shown in Figure 4.2 and Figure 4.3. The fused silica provided a short, constant diameter transport conduit, free from valves, T-pieces and other flow disruptions. The fused silica was held approximately concentric inside the outer injector by a Macor centring piece; thereby maintaining the sample flow on-axis with the orifice in the sampler and skimmer cones. Holes in the Macor allowed passage of the argon make-up gas; thus a stable central channel was formed through the plasma, independently of the helium flow. Moreover, the fused silica could be extended beyond the tip of the injector, past the turbulent recirculation region[188, 189] at the base of the plasma.

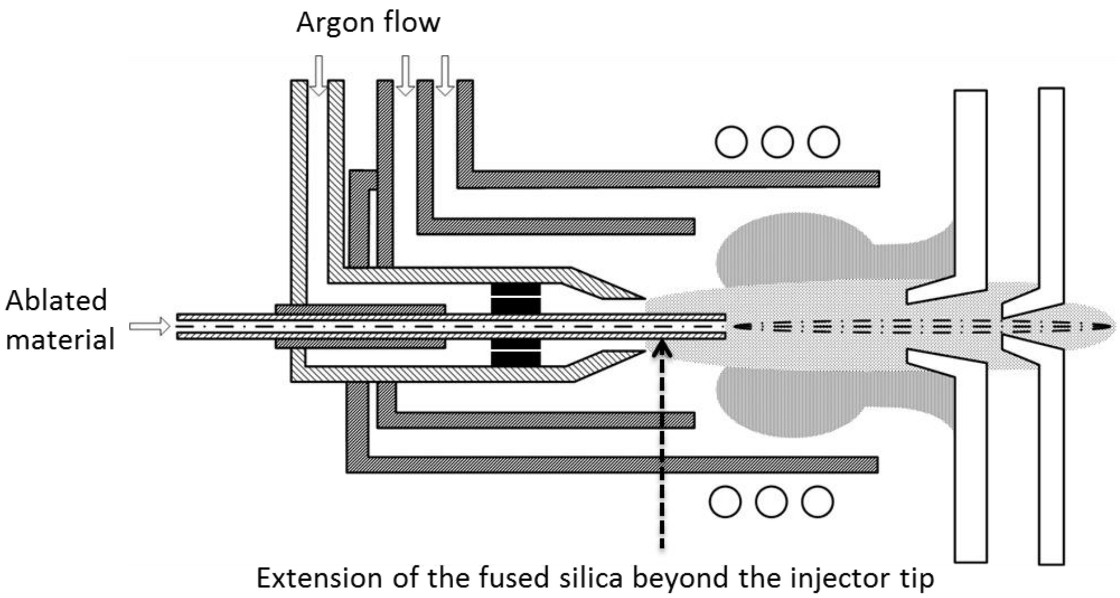

Figure 4.2 Cross sectional view of the Direct Concentric Injector (DCI) showing the extension of the fused silica tubing beyond the tip of the injector. Image reproduced with permission of David Douglas.

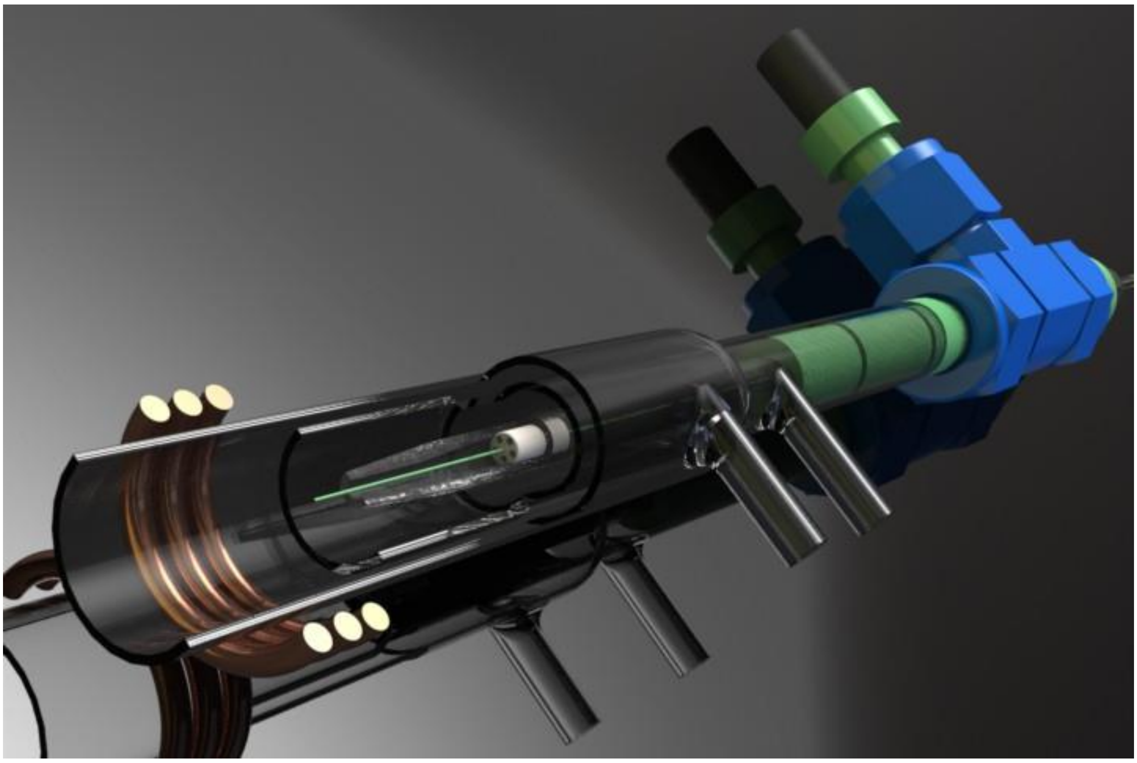

Figure 4.3 Rendered image of the Direct Concentric Injector. Image reproduced with permission of David Douglas.

When using the Sniffer with the DCI and standard UP213 cell, sub-100 ms single shot widths were achieved, leading to order of magnitude improvements in image analysis speed, and around a 10 fold improvement in peak area, compared to the standard system.[187]

The speed and sensitivity delivered by the DCI/Sniffer are key requirements for the acceptance of LA-ICP-MS as routine clinical monitoring technique. However, the Sniffer is a static device, so when used with a standard cell it is only capable of sampling at a single location per analysis. A modified arrangement is necessary to enable targeted imaging of tissue biopsies, blood smears or individual cells.

4.1.6 Aims for this thesis chapter

This section describes the development of a new outer cell, known as the Enterprise cell, for use with the Sniffer and DCI. Since the Sniffer is a stationary device, scanning across the sample surface must be accomplished using movement of the sample beneath the Sniffer. Two sample movement configurations are described. The first involved movement of the sample stage via a magnetic coupling between the sample holder and the existing UP213 2-axis movement stage. The second option involved direct contact between the sample holder and movement stage, through a hole in the base of the cell. These designs aimed to fulfil the following criteria:

1. Exclude atmospheric gases and maintain a pressurised inert ablation atmosphere.
2. Direct the gas flows in a way that is conducive to the capture and complete transport of ablated material by the Sniffer.
3. Retain a constant angular orientation of the sample in the cell.
4. Maintain a consistent distance between the base of the Sniffer and the sample surface.
5. Enable precision in sample movement, such that the sample can be reliably and consistently moved in 1 µm steps, with minimal lag.

Computational fluid dynamics (CFD) is a useful tool when designing and implementing any new fluid-based technology. It enables the user to optimise experimental designs prior to construction of a prototype, and offers insights into experimental results.

Numerical simulations have already been used in the field of ICP-MS for modelling gas flows within laser ablation cells, the transport tubing, spray chambers, and even the plasma itself.[185, 188-191] Here CFD was used to guide development of Enterprise cell, to examine the gas flows around the Sniffer region, and to monitor the trajectory of simulated particles through it.

4.2 Experimental

4.2.1 Materials

The Enterprise cell was designed to fit the UP-213 laser ablation system (Electro Scientific Industries, Cambridgeshire, UK). All custom delrin and aluminium parts were fabricated by Creative Machine, Washington, USA. The fused silica window was purchased from CVI Melles Griot, UK. All Macor parts were fabricated by Ceramic Substrates, Isle of Man, UK. The 3-axis manual movement stage was purchased from Edmund Optics, Yorkshire, UK. Dynamic seals were made from graphite filled PTFA and were purchased from Parker, USA. All static o-ring seals were made from Viton® material and were purchased from RS Components, Northamptonshire, UK. The ball race used for the magnetic coupling was also purchased from RS components. Compression fittings were purchased from Swagelok, Manchester, UK.

4.2.2 Design and construction of the basic Enterprise Cell

The design, shown in Figure 4.4 and Figure 4.5, was extensively refined within Solid Works before fabrication of the *Enterprise Cell*. The cell was constructed in a modular fashion, to allow cost effective modification and replacement of parts, as optimisation of the physical prototype progressed. The basic cell consisted of a delrin base, middle section, lid, optical window holder and positioning bar, with a 30 x 3 mm fused silica optical window. When assembled, the cylindrical cell had an internal volume of 118 cm^3. The Sniffer was glued into the bottom of the positioning bar, which was positioned above the sample holder, perpendicular to the sample gas inlet. At the default position, the Sniffer sat 100 µm above the sample surface. The use of removable washer shaped spacers below the positioning bar, or beneath the sample itself, allowed this distance to be adjusted as necessary. The cell incorporated four gas ports accessed through 1/8-27 NPT compression fittings. One of these gas ports was required for carrier gas entry, and another for exit of the fused silica tubing. The remaining two ports could be used for attachment of a pressure relief valve or for addition of a second ablation gas; although these were easily blanked off when these options were not required. The cell was attached to the UP213 system via a bracket, which incorporated a 3-axis manual micrometer movement stage, to enable alignment of the laser firing position with the 800 µm laser access hole in the Sniffer.

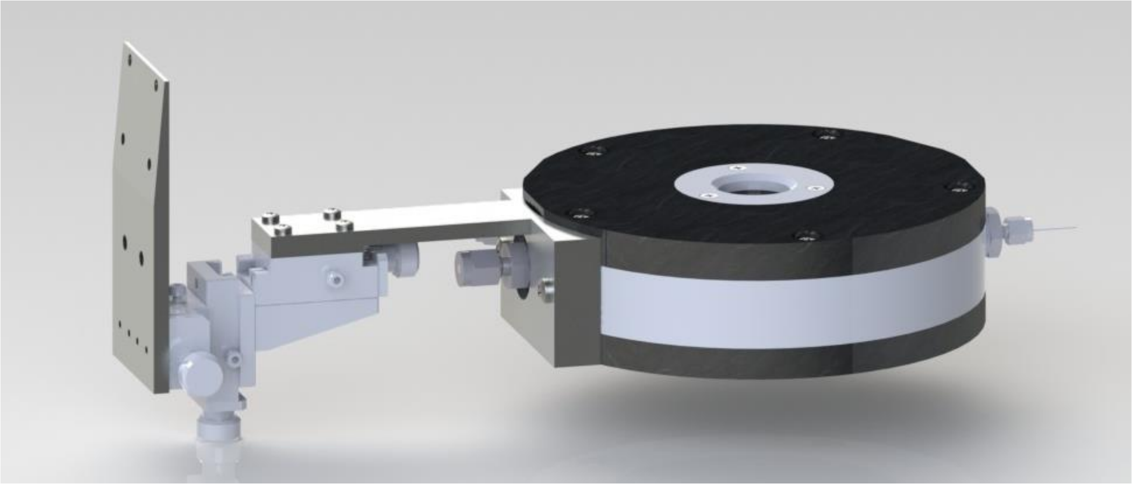

Figure 4.4 Rendered image of the closed Enterprise cell, showing the attachment bracket, incorporating a 3-axis manual micrometer movement stage.

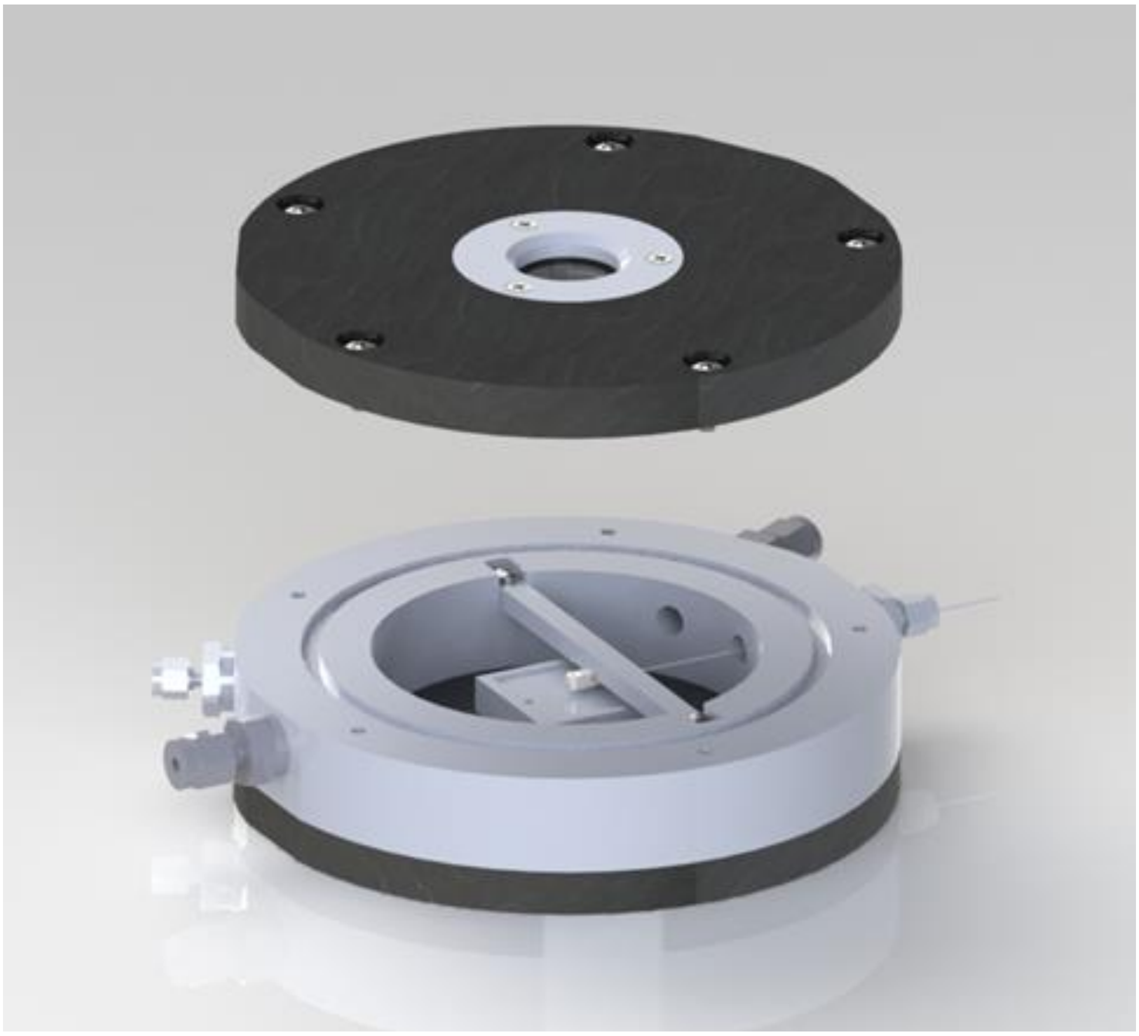

Figure 4.5 Rendered image of the open Enterprise cell.

4.2.3 Magnetic coupling

In this configuration, a set of magnets inside the sample holder were magnetically aligned to magnets in a positioning plate below the cell. This plate was connected to the existing UP213 2-axis movement stage, which is computer controlled. Two sets of magnets were required to ensure consistent alignment: the first positioned the sample holder, and the second prevented it from twisting during movement. The sample holder accommodated slides of up to 25 x 25 mm in size, and was mounted on a ball race, which ran along a Macor insert in the base of the cell. This insert had a 0.4-0.8 µm R_a surface finish, providing a smooth running surface for the ball race. A cross section of the magnetic coupling configuration is shown in Figure 4.6.

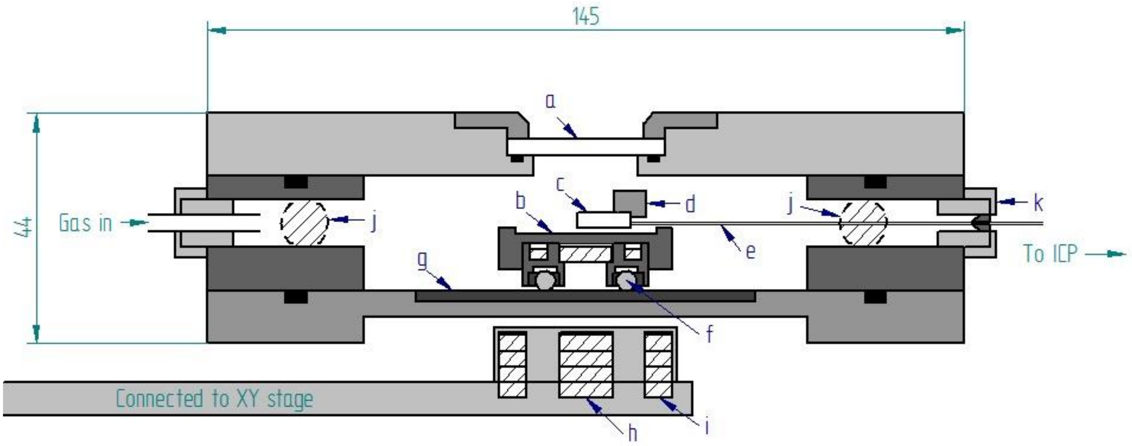

Figure 4.6 Cross section of the Enterprise cell, with the magnetic coupling, showing a) 25 x 3 mm optical window, b) sample position, c) Sniffer, d) positioning bar for the Sniffer, e) fused silica tube, f) acetal thrust race bearing, g) Macor insert, h) set of positioning magnets, i) set of aligning magnets, j) spare inlet/outlet ports, k) Swagelok 1/8 NPT connector. Dimensions are in mm. O-rings are shown in black.

4.2.4 Dynamic o-ring seal

As with the magnetic coupling, this configuration used a positioning plate attached to the 2-axis computer controlled movement stage. In this case the positioning plate was directly attached to the sample holder by means of a M4 screw, which fitted through a 25 mm hole in the base of the cell. To ensure the cell remained airtight, the gap was sealed with two dynamic seals, which were located between the sample holder and the inner base of the cell, and between the outer base of the cell and the movement plate. The movement plate incorporated a grease well, to reduce friction between the cell and movement plate, as necessary. A cross section of the o-ring seal configuration is shown in Figure 4.7.

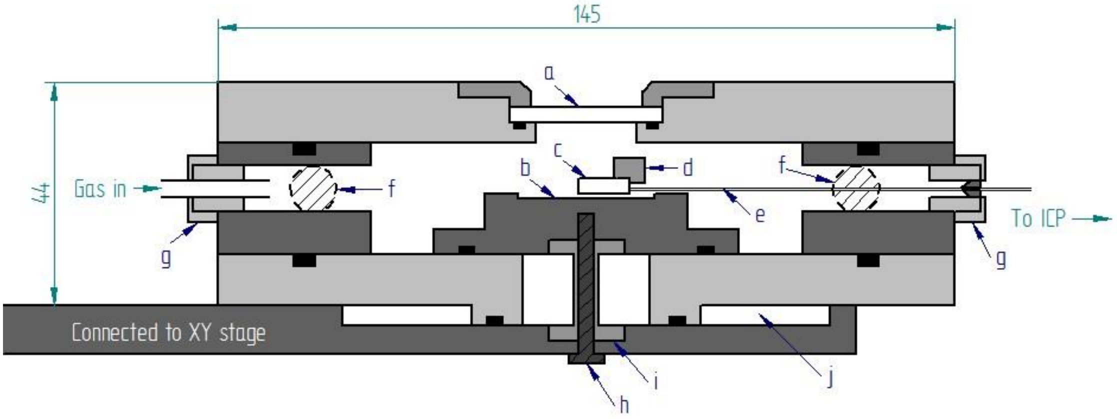

Figure 4.7 Cross section of Enterprise cell with dynamic o-ring seal movement, showing a) 25 x 3 mm optical window, b) sample position, c) Sniffer, d) positioning bar for the Sniffer, e) fused silica tube, f) spare inlet/outlet ports, g) Swagelok 1/8 NPT connector, h) M3 screw, i) metal support for the screw, j) grease well. Dimensions are in mm. O-rings are shown in black.

4.2.5 Flow simulation

Solid Works Flow Simulation 2011 SP5.0 (Dassault Systems, Massachusetts, USA) was used to model the gas flows within the Enterprise cell. Firstly, a three dimensional CAD model of the Enterprise cell was constructed within the Solid Works software. This model was set as the computational domain. The components were automatically selected by the software as the solid region and the volume within them was selected as the fluid region. The computational domain was then divided by a set of intersecting planes, forming a grid of control volumes, known as the initial mesh. This was set so that the lines of the mesh were spaced at 100 μm intervals. A higher level of refinement was required to accurately predict the flows around sharp edges and narrow channels, such as Sniffer and the gap between Sniffer and the sample surface, where the flow experiences a significant change in pressure and direction. Therefore, a finer refinement level, of 50 µm was set in these regions. This resulted in the formation of 1,410,611 sub-volumes within the fluid region, which are known as fluid cells, along with 1,591,687 volumes that cross both the solid and fluid region, known as partial cells.

The initial conditions were set so that the calculation began under atmospheric pressure at 298 K. Atmospheric pressure was also specified at the 250 µm i.d. fused silica outlet; although it is acknowledged that under experimental conditions the pressure in this region might not be exactly atmospheric. Helium was introduced into the cell through the main inlet port, at a flow rate of 125 ml/min. In dual flow simulations, argon was used as the major flow, at a flow rate of 100 ml/min, with He directed into a modified Sniffer through the second inlet port, at a flow rate of 25 ml/min. Following set-up, the software calculated the gas flows through the model using an iterative solver, which operates by calculating the Navier-Stokes equations for each fluid cell at the specified conditions.[192] Upon completion of the calculation, flow trajectories emanating from the inlet ports, and cut plots showing the gas velocity through the cell, were produced. Particle tracking studies were performed for an injection of 100 nm glass particles, originating from a sketch point 200 µm beneath the sniffer, concentric with the laser access hole. The average transit times for 100 particles to reach the outlet was taken as the computed wash-out time for the cell.

4.2.6 Demonstration for bio-analysis

The performance of the system was evaluated for single cell analysis of Gd labelled $CD4^{+}CD25^{+}CD127^{lo}$ nTreg. Cell labelling and preparation procedures were described previously in Chapter 2. The Enterprise was fitted to the UP-213 laser ablation system (Electro Scientific Industries, Cambridgeshire, UK) as outlined in section 4.2.2. The Sniffer was fabricated from Macor, a brilliant white material, which reflects illuminating light and impairs sample visualisation. Thus, cochineal food colouring (Dr Oetker, West Yorkshire, UK) was used to dye the Sniffer pink, prior to assembly. The Sniffer was then positioned 100 – 200 µm above the sample surface with the aid of feeler gauges. A 685 mm length of fused silica (250 µm i.d, 360 µm o.d.) was used to connect the Sniffer to the DCI. The DCI was then inserted into the semi-demountable torch on the Element XR (Thermo Scientific, Bremen, Germany). The fused silica was initially positioned within the DCI, such that the outlet was flush with the end of the injector tip. This was then extended towards the plasma at 1mm intervals. A pressure monitor was attached to the cell to monitor the pressure throughout the experiment. Typical operating parameters are given in Table 4.1.

Table 4.1 Laser and ICP-MS operating parameters when using the Enterprise cell.

Laser operating parameters	
Spot size	30 µm, round
Repetition frequency	1 Hz (single shot)
Laser power / fluence	42% / 6.40 J cm^{-2}
Helium flow rate	120 ml min^{-1}
Cell back pressure	11.62 psig
Sample to Sniffer distance	100 – 200 µm (approx.)
Fused silica length	685 mm
ICP-MS operating parameters	
Radio frequency (RF) power	1250 W
Cool gas flow rate	15.80 l min^{-1} Ar
Auxiliary gas flow rate	0.95 l min^{-1} Ar
Sample gas flow rate	1.45 l min^{-1} Ar
Torch x position	4.9 mm
Torch y position	2.9 mm
Torch z position	-2.0 mm

4.2.7 Peak characterisation

Instruments developed by different manufacturers employ unique software, and thus the terminology used to define the acquisition parameters varies considerably between systems. For clarity, a brief description of the key acquisition terminology used by the Element XR is outlined here. All data in this thesis was acquired using E Scan mode. When measuring one isotope using this mode, the magnetic field is set to a fixed value and the accelerating voltage and electric field are adjusted to repeatedly scan across a proportion of the mass peak, referred to as the mass window. The mass peak is split into a series of "samples" or measurement channels, which are described as the number of samples per peak. The user may define the time duration of each sample and the number of samples measured per peak. Conventionally, time resolved data is extracted from the ICP-MS in "FIN2" format, where the samples within each peak are averaged and the data is presented as the average signal acquired per time bin or "segment". The duration of these segments is a function of the mass window, the sample time and the number of samples per peak, plus the ~3 ms blind time of the duty cycle.

To determine the sensitivity improvement of the new ablation interface, an ICP method using 50 samples per peak, a sample time of 5 ms, and a mass window of 20% was used, which resulted in a segment duration of 50 ms. The data was extracted from the ICP in the conventional FIN2 format, such that the data points were spaced at 53 ms intervals. This method was chosen to maintain compatibility with the data presented previously in Chapters 2 and 3, which is typical for most single element LA applications. Processing of these signals was performed by summing the total signal corresponding to each ablation event, as described in previous chapters.

Since the peaks from the new interface were in the order of 10 ms, a finer time resolution was required for peak profiling. Thus, a second method using counting mode, a sample time of 0.1 ms, 1000 samples per peak and a mass window of 20% was used. For this, the individual ‘samples per peak’ (I.e. the raw data points), rather than the averaged data for each segment, were extracted directly from the inf file. This file format displays the data in a series of columns, with each column showing an individual scan across the mass window, and the rows in each column depicting the signals from each 0.1 ms measurement. Each sweep was then successively stitched together using an Excel macro, to provide 0.1 ms spaced, time resolved signal.

The time resolved data was transferred to IGOR Pro 6.22A (WaveMetrics Inc., Lake Oswego, USA) for calculation of the peak characteristics. A linear rise, plotted from the first data point to the peak top, was used to obtain the time at which the rising signal reached 50% of the peak maximum. An exponential decay curve was fitted from the peak top to the baseline using Equation 4.1. This was rearranged to Equation 4.2, to calculate the point at which the signal decayed to 50% of the peak maximum. The values were then subtracted to give the full width at half peak maximum (FWHM) in seconds. This process was repeated to calculate the full width at 10% peak maximum (FW0.1M) and full width at 1% peak maximum (FW0.01M) respectively.

$$y = y_0 + A.e^{\left(\frac{-(x-x_0)}{\tau}\right)}$$

Equation 4.1

$$x = -\left[ln\left(\frac{y - y_0}{A}\right).\tau\right] \qquad \textbf{Equation 4.2}$$

Where y and x are the signal and time variables y_0 and x_0 are constants, A is the fitted peak maximum and τ is the exponential decay constant.

4.2.8 Use of a fast data acquisition board

In later experiments, a P7882 dual-input photon counter board (FAST ComTec GmbH, Oberhaching, Germany) was connected to the ion detection board on the ICP-MS to improve the time resolution. To prevent data losses, the trip cable was disconnected from the ion detection board and ion beam deflection during ESA flyback was disabled. Signals were captured using the MCDWIN software supplied with the board, which displayed the signals as two dimensional arrays. The results were exported to IGOR Pro 6.22A in tab-delimited format, for further processing.

The above electrical connections were made after consultation with Thermo Fisher Scientific. To minimise the risk of instrument damage, or exposure to high voltages, users are strongly advised to obtain advice from the relevant instrument manufacturer before attempting to replicate these procedures.

4.3 Results and Discussion

4.3.1 Flow simulation

Flow simulations revealed that positioning the sample gas inlet collinear to the sample provided the most favourable gas flow dynamics. Examination of the individual flow trajectories revealed that the sample gas flowed around the outer chamber and converged upon the Sniffer region. The contour plot in Figure 4.8 displays the velocity profile across a horizontal cross section of the cell. It was shown that the computed gas flow accelerated considerably upon entering the Sniffer, from less than 0.5 m/s prior to the Sniffer entrance, to speeds of 70 m/s by the end of the fused silica tube. In dual-flow simulations the directed second flow entered the Sniffer at a higher speed than the main flow, and produced a gas velocity of nearly 80 m/s by the end of the exit tube.

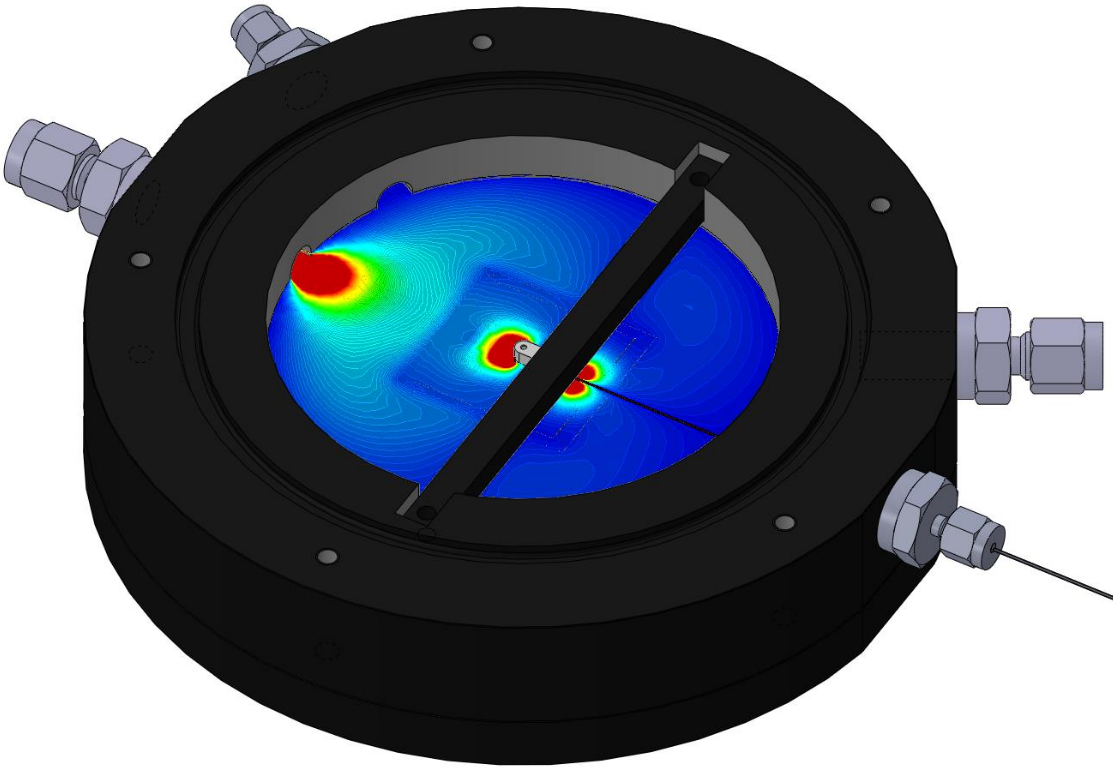

Figure 4.8 Cut plot showing the gas flows within the Enterprise cell as isolines and contours, with blue representing low velocity and red representing high velocity.

A detailed view of the flow pattern within the Sniffer region is shown in Figure 4.9. The bulk of the carrier gas flow entered through the cut out section at the front of the Sniffer, then swept across the sample surface, before entering the fused silica exit tube. A second gas flow entered the sniffer through the laser access hole. This flow may restrict the ablation plume and prevent escape of the ablated material into the outer cell. Minor gas pressure from behind the Sniffer was also present. This may help to lift the ablated material from the sample surface, assisting its entry into the fused silica exit tube. These flows are in accordance with flow modelling reported by Douglas for the modified UP-213 lid,[187] indicating that the use of a large volume outer chamber does not impact negatively on the gas flow dynamics within the Sniffer region.

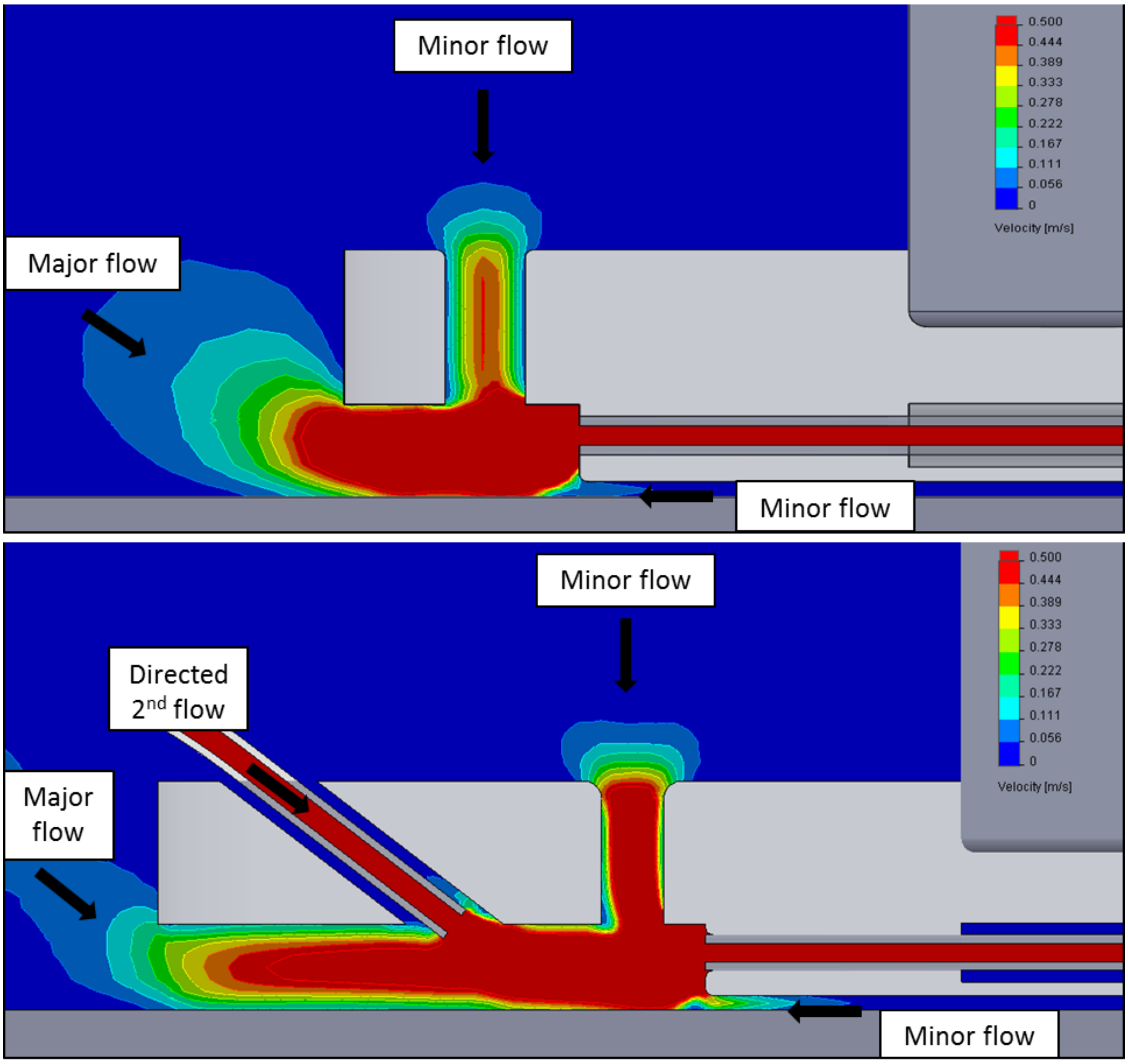

Figure 4.9 Simulation of the gas flows through the standard Sniffer (top) and Dual-flow Sniffer (bottom). Coloured bands represent the flow velocity, with blue signifying low speed and red signifying high speed (> 0.5 m/s). Black arrows have been inserted to indicate the flow direction.

Particle studies, using 100 nm glass particles, which originated from a location 200 µm beneath the Sniffer, concentric to the laser access hole, predicted that material ablated within the Sniffer cavity is efficiently captured by the Sniffer, and is conducted through the fused silica tubing towards the plasma. Residence times within the cell of 4 ms and 3.9 ms were calculated when using the Sniffer and Dual-flow Sniffer respectively. These results are indicative of a very fast washout system. However, it should be noted that the modelling did not account for the laser interaction, the spread of particulate within the ablation plume, or the plasma characteristics downstream of the ablation cell. Furthermore, the constructed model was based on an idealised setup, whereby the cell was perfectly sealed, the Sniffer was exactly parallel to the sample, and the fused silica connections provided an exact fit, with zero dead volume. These conditions can be difficult to achieve experimentally due to tolerance issues during manufacture, plus operator variation when constructing the cell. In addition, it is likely that edge effects will be introduced by the inclusion of variable sample shapes and sizes. For instance, sharp edges, such as those created during the cutting down of slides, will produce changes in flow direction and may introduce turbulence. Nevertheless, the flow modelling provided a positive indication of the flow characteristics within Enterprise cell, which supported construction of the prototype.

4.3.2 Evaluation of the two movement configurations

Pressure testing was initially performed off-line from the ICP-MS. A pressure monitor, placed prior to the cell, measured the back pressure at various sample gas flow rates. The magnetic coupling used an entirely enclosed outer cell; thus stable pressures were reached within a few minutes using this design, and were maintained stably for several hours, without adjustment of the gas flow. Cell pressure increased linearly with increasing increments of the sample gas flow in the range of 50 to 125 ml/ min, see Figure 4.10. Flow rates producing pressures above 12 psig were not investigated in this study due to safety concerns.

The magnetic coupling was capable of repositioning the sample beneath the Sniffer, but a significant amount of lag was observed between adjustments of the computer controlled stage and movement of the sample holder. Movements of the computer controlled stage of less than 100 µm were not registered by the sample holder, and larger movements at high speed were required to produce a response. Such movement is sufficient for single shot analysis, particularly on homogenous materials, where the aim is simply to shift to a different location on the sample surface. However, the ablation of lines or rasters, was not possible using the magnetic coupling.

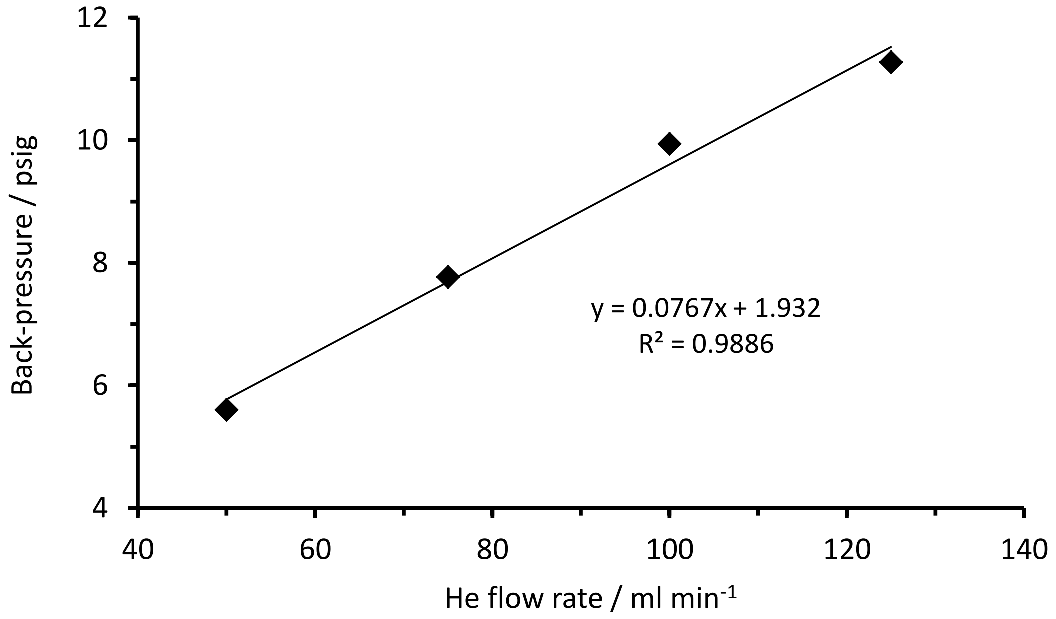

Figure 4.10 Back-pressure from the Enterprise cell at various He flow rates, when using the magnetic coupling.

The dynamic o-ring design used a hole in the cell base to enable direct contact and positioning of the sample tray. Atmospheric gases were excluded using two graphite c-seals, which were designed to operate with moving parts. Cell pressure was heavily dependent on the amount of compression applied to these seals, which was adjusted manually using the positioning stage on the cell bracket. Internal pressures of up to 8 psig were reached with this design. However, pressure was variable with the location of the sample tray. Adjustments to the sample position, for example when performing line scans, led to rapid decreases in the internal pressure, which was particularly evident when scanning at high speed.

The high level of c-seal compression required to maintain a consistent pressure within the cell compromised the sample movement capability. With high c-seal compression, friction between the moving components and the base of the cell caused drag of the sample holder. It is likely that an optimum degree of compression exists, which provides effective sample movement, whilst maintaining favourable gas flow dynamics. However, this optimum compression was difficult to reproducibly achieve using the prototype design developed here. Moreover, it is possible that friction observed during testing contributed to the overheating and subsequent failure of an electronics board on the UP-213 platform. The dynamic o-ring design was therefore abandoned at an early stage and the magnetic coupling was used for the demonstration experiments presented in section 4.3.3.

4.3.3 Demonstration for bio-analysis

The performance of the system was evaluated for single cell analysis of 98.5% pure CD4$^+$CD25$^+$CD127^{lo} nTreg, which were previously determined to contain an average Gd content of 5.08 x 10^7 atoms per cell, using solution-based ICP-MS. The peak characteristics for the Enterprise at various DCI extensions are shown in Table 4.2 and Figure 4.11. Peak widths were in the order of 3.5, 6 and 10 ms at full width 50%, 10% and 1% of the peak maximum respectively. However, slight signals above background were noted up to 20 ms after the peak had reached 1% maximum. These secondary signals were also observed by Van Malderen *et al*. when using a fast washout cell,[193] and thus may be a reflection of aerosol formation and transport processes previously masked at lower speeds.

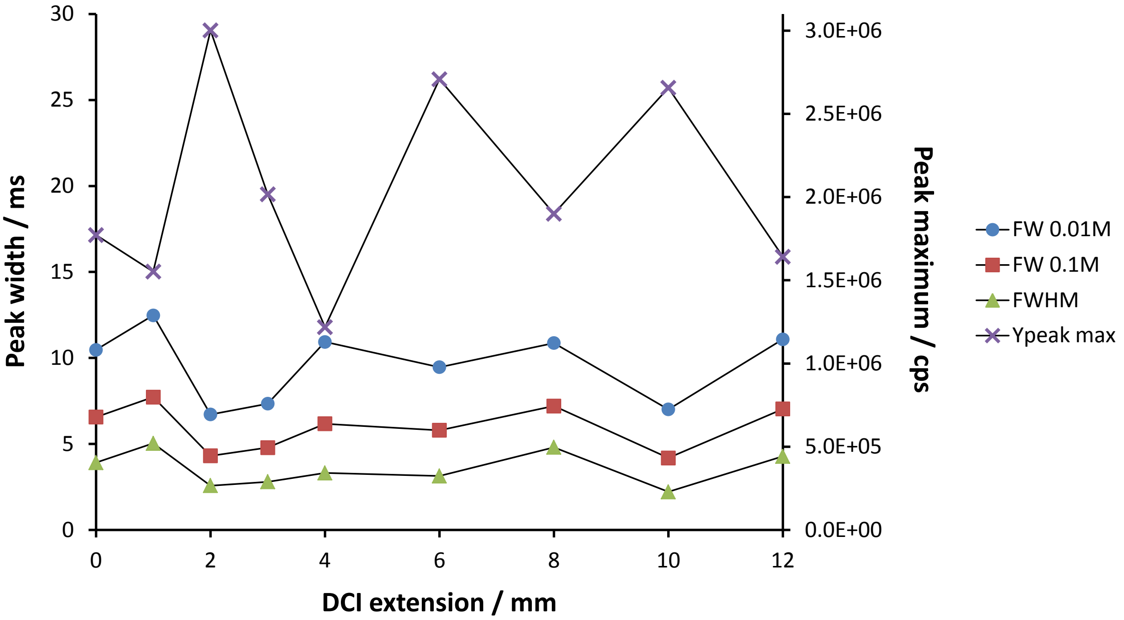

Figure 4.11 Average peak data for the ablation of 5 Gd labelled cells at each DCI extension. Note, peak maximum data is shown on the second axis.

Table 4.2 Average peak data for the ablation of 5 Gd labelled cells at each DCI extension.

Extension / mm	FW 0.01M / ms	FW 0.1M / ms	FWHM / ms	$Y_{peak\ max}$ / cps
0	10.47	6.56	3.91	1.77E+06
1	12.48	7.72	5.03	1.55E+06
2	6.72	4.31	2.57	3.00E+06
3	7.34	4.79	2.80	2.02E+06
4	10.93	6.17	3.31	1.22E+06
6	9.46	5.79	3.14	2.71E+06
8	10.87	7.21	4.80	1.90E+06
10	7.01	4.18	2.22	2.66E+06
12	11.11	7.04	4.28	1.64E+06

Figure 4.12 shows the peak profiles from five individual cells analysed at the 2 mm extension, which provided the narrowest signals at 1% peak maximum. These five individual peaks were then averaged to produce a typical peak profile, as shown in Figure 4.13. Peak profiles for the other DCI extensions are presented in Appendix 2. All peaks included a sharp linear rise, occurring over less than 10 data points, with an approximately exponential decay. However, the peak shape between these regions was variable, with a range of flat topped, sharp and split peaks occurring.

Split peaks were previously reported for in-torch ablation,[194] where the splitting was attributed to two overlapping Gaussian functions caused by particle separation during aerosol formation and expansion. It is likely that similar processes occurred within this system. For instance, the compressed nature of the plume within the Sniffer, when combined with the relatively small exit orifice, may have induced aggregational processes within the aerosol. A periodic 'chocking' effect is possible, in the sense that there may be insufficient pressure to maintain the velocity in the tube at very high mass flows. Differential transport within the plasma may also have contributed, since in practice it was difficult to implement a perfectly concentric dual injector. The fused silica is transported on a coil; thus even with the aid of a centring piece, it had the tendency to bend at the end. This may have led to some material entering the ICP off-axis, which was recently demonstrated to produce temporal shifts in signals.[195] The angle of the bend became more pronounced as the fused silica was extended further into the plasma, which may have contributed to the changing peak shape towards the longer extensions.

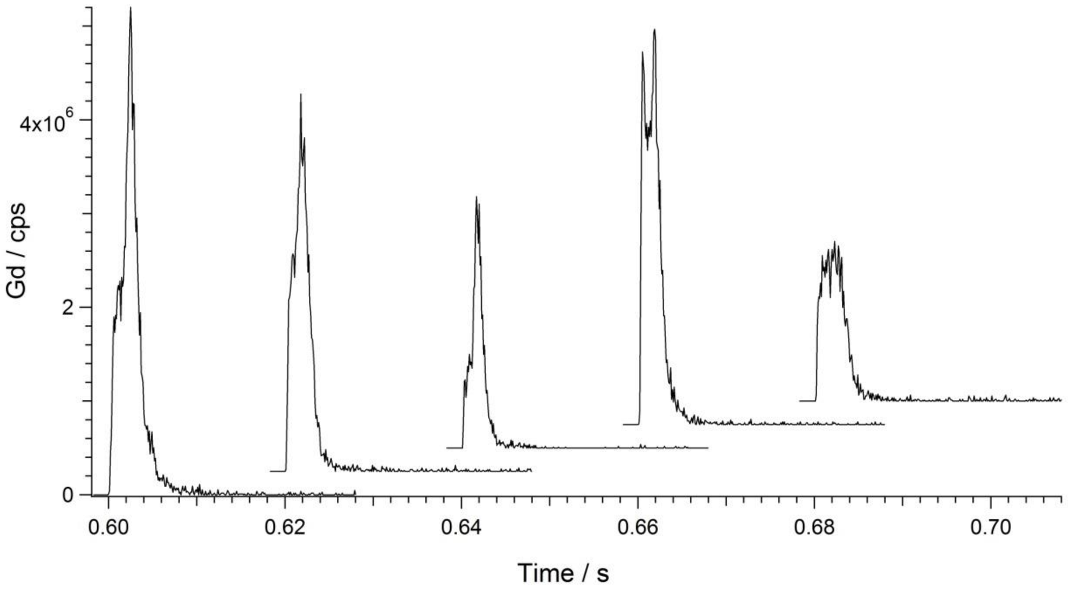

Figure 4.12 Peak profiles from of five individual Gd labelled cells when using the Enterprise cell, with the fused silica extended 2 mm past the tip of the injector. Signals are offset by 200 ms in the x direction and 2.5 x 10^5 cps in the y direction to aid comparison.

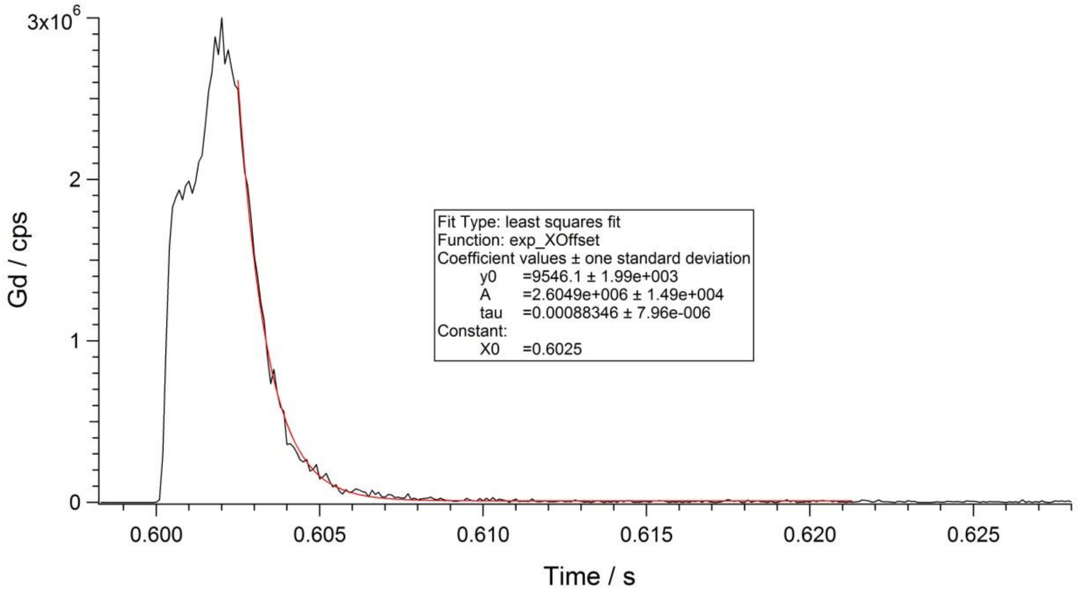

```
Fit Type: least squares fit
Function: exp_XOffset
Coefficient values ± one standard deviation
        y0    =9546.1 ± 1.99e+003
        A     =2.6049e+006 ± 1.49e+004
        tau   =0.00088346 ± 7.96e-006
Constant:
        X0    =0.6025
```

Figure 4.13 The averaged peak profile obtained for five Gd labelled cells using the Enterprise cell, with a fused silica extension of 2 mm past the tip of the injector.

It was hypothesised that, in addition to speed, the prototype technology would provide an increase in absolute sensitivity (integrated counts per unit mass) compared to conventional instrumentation. There are two potential factors that may contribute to this effect. The compression of the plume within the Sniffer region may reduce losses on the walls of the ablation chamber, whilst the use of an axial inner injector ensures more efficient ion sampling, through reduced deposition on the cones. To evaluate this hypothesis, the absolute sensitivity of the Enterprise system was compared to that of the tear-drop cell and standard injector used in Chapters 2 and 3. The tear drop cell, which has also been described as the Zircon cell, is a low, single-volume ablation cell, which was developed by Horstwood *et al.*[131] in response to aerosol transport experiments performed by Bleiner and Günther.[196] The cell provides sub 0.5 second peak widths for single shot work and produces greater sampling reproducibility than possible with the standard UP-213 cell.

The Enterprise was demonstrated to provide a significantly higher absolute sensitivity than the teardrop cell (one-tailed t-test, n=50, d.f. = 98, $P < 0.05$) at all DCI extensions tested. The effect was greatest at 6 mm extension, where the peak area was almost 6 times higher than obtained using the teardrop cell. Taking into account the average Gd loading of 5.08×10^{8} atoms per cell, this corresponds to an increase in detection efficiency from 4.24×10^{-5} to 2.35×10^{-4}, where detection efficiency is defined as the ratio of the ions reaching the detector to the number of atoms sampled by LA.

Robust statistics were used to evaluate the differences between each DCI extension. Robust statistics, such as Huber's H15 method, provide a more reliable estimation of the mean for data sets that include a small proportion of outliers.[197] Their use is particularly appropriate for this data set, which is normally distributed, but suffers from occasional high intensity outliers due to the 1.5% phagocytic monocyte contamination. Figure 4.12 shows the average signals at each extension, represented by the H15 mean. Error bars representing the H15 standard deviation indicate that there is no statistical difference between the various extensions, and this hypothesis was supported analysis of variance ($F_{8,441} = 1.43$, $P = 0.183$). However, it is likely that biological variation between samples and variability in laser fluence, along with concentricity problems of the inner injector, obscured any potential differences between these extensions.

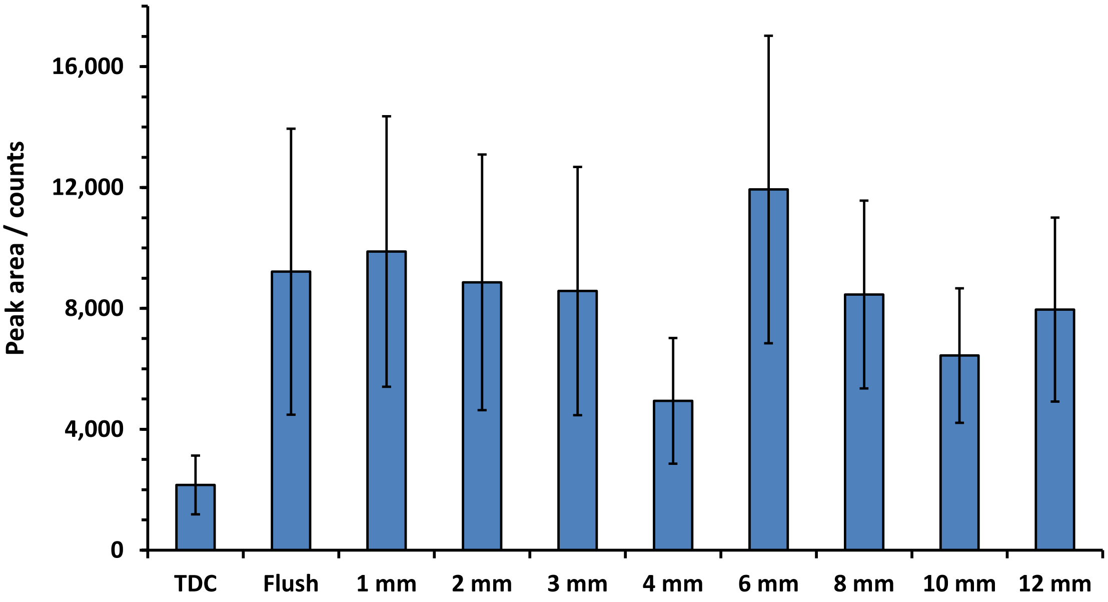

Figure 4.14 The H15 mean ^{157}Gd signal intensities for the ablation of 50 labelled T cells at various DCI extensions, compared to those obtained for the tear drop cell (TDC). Error bars depict the H15 standard deviation (n=50).

The current Enterprise cell does not include any provision for rapid sample exchange. Sample changeover required detaching the cell from the bracket via two screws, and removal of the cell lid via a further five screws. The narrow diameter of the fused silica outlet tube was beneficial during this process, since the cell lid could be opened with minimal air entrainment by the plasma. However, subsequent re-pressurisation of the cell was required before analysis. The total sample changeover process was accomplished in slightly under 10 minutes. This is considerably longer than for most commercial cells, but in the context of a 2 hour tissue biopsy analysis this time is not significant.

4.3.4 Limitations with ICP-MS data acquisition

ICP-MS was originally designed for the analysis of homogeneous solutions, where a continuous flow of analyte is nebulised, to produce a signal of constant average intensity. This form of analysis still represents the major proportion of all ICP-MS applications. However, the field has since expanded to include coupling to separation techniques and/or the use of alternative sample introduction strategies, which produce a time resolved transient signal profile. In many cases the software developed by ICP-

MS manufacturers has not sufficiently evolved to meet the new data acquisition requirements. This is most apparent when working with high speed sample introduction systems, such as the one developed here, where the capture of very short duration, temporally resolved signals is required. It is essential that the improved temporal resolution provided by high speed interfaces is not compromised by subsequent data grouping or averaging occurring within the software. Thus, when characterising the peaks in this chapter, it was necessary to extract the raw data points from the ICP-MS, rather than using the conventional data files. Significant time and computer processing power was required to convert the large number of raw data points into a 0.1 ms spaced, time resolved signal.

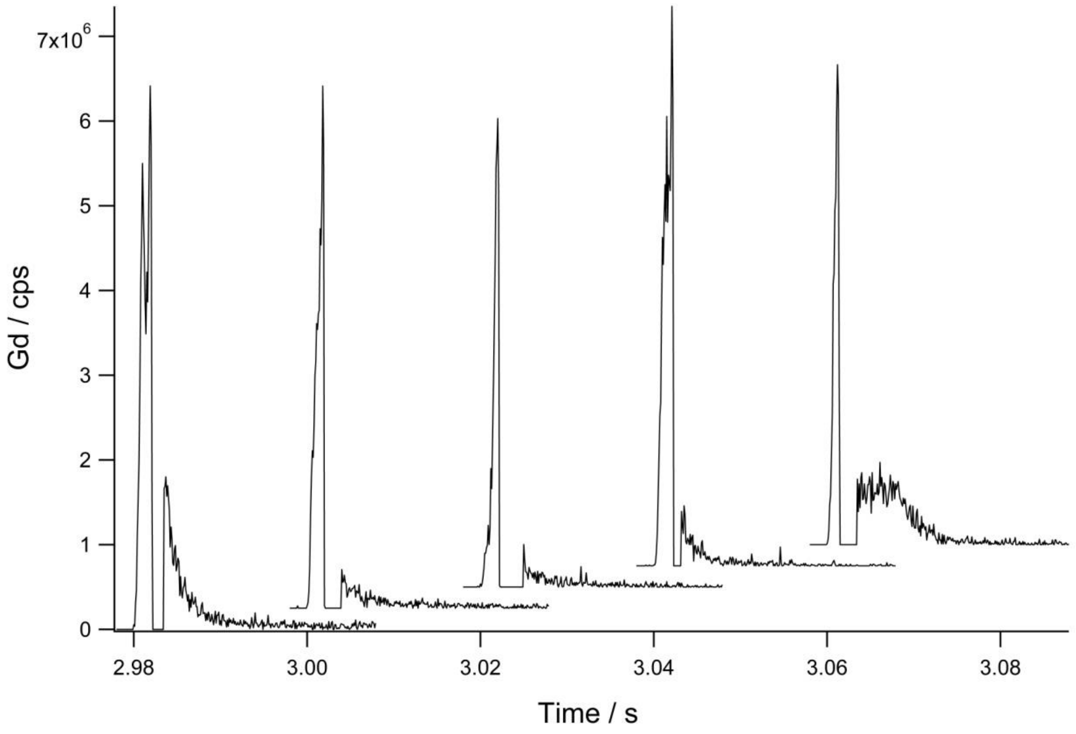

Figure 4.15 Signals from five individual peaks, showing detector trips and the associated data losses occurring when count rates exceed 5 x 10^6 cps.

Examination of the raw data highlighted further limitations with the data acquisition system on the Element XR. Methods using short sample durations suffer from high data losses, due to the electrostatic analyser (ESA) operation cycle. At the end of each sweep of the mass range the ion beam is deflected onto the wall of the electrical sector, whilst the ESA returns to the start mass to begin the next scan. This leads to loss of approximately 3 ms of data per sweep, which for the method used here amounted to approximately 15% of the duty cycle. Clearly, a 10 ms peak falling across the 3 ms gap cannot be accurately measured; thus nearly half of the data captured in the experiments above was unusable. Furthermore, working with small sample durations requires the detector to operate in counting mode. This mode is typically used for trace analysis, and accordingly the detector trips when the count rate exceeds 5 x 10^6 cps in two consecutive integrations. With such short, compressed signals it is easy to exceed this threshold with relatively low concentration samples, as demonstrated by the single cell data shown in Figure 4.15.

4.3.5 Use of a fast data acquisition board

To achieve faster data acquisition, some users have connected external devices to read out signals directly from the electron multiplier of quadrupole mass spectrometers. Examples include a digital oscilloscope connected to a Perkin Elmer ELAN 600,[194] which provided 20 µs time resolution, and an ion pulse counting unit connected to the Agilent 7500a via a function generator,[198] which produced 50 µs spaced data. An alternative approach combined a time-of-flight (TOF) mass analyser with the ICP and vacuum interface of a commercially available quadrupole instrument, enabling multi-element detection at 30 µs time resolution.[199, 200]

In this study, a multi-channel scaler board was used to read the TTL pulse output from the ion detection board on the Element XR. The board is similar to the type employed on TOF instrumentation and has a programmable time resolution, with a minimum bin width of 100 ns. Disabling ion deflection during the ESA flyback prevented the 3 ms data losses described above. In addition, disconnecting the detector trip cable enabled the analysis of the higher intensity signals associated with gold nanoparticle labelled macrophages. The signals produced from this analysis were of wider duration than reported previously, typically ranging between 20 and 50 ms (to 10% peak maximum), which could be a feature of the much higher count rate for the gold labelled cells.

Figure 4.16 shows signals from individual gold labelled macrophages, captured using bin widths of 10 and 100 µs, with magnified views of satellite signals occurring after the main peaks. It is assumed that these satellites correspond to free nanoparticles on the slide, which may have been ejected by the laser induced shockwave, possibly from locations outside of the Sniffer region. The 10 µs resolution appeared excessive for single cell analysis; however, it was shown to significantly enhance the profile of the nanoparticle signals. Indeed, the shape and duration of these signals is consistent with a recent paper, which reported peaks of 100-200 µs (FWHM) for Au nanoparticles that were introduced into an ICP-TOF-MS through a microdroplet generator.[201] It is hoped that the enhanced time resolution demonstrated here may pave the way for fundamental studies into the interaction of material with the Element XR.

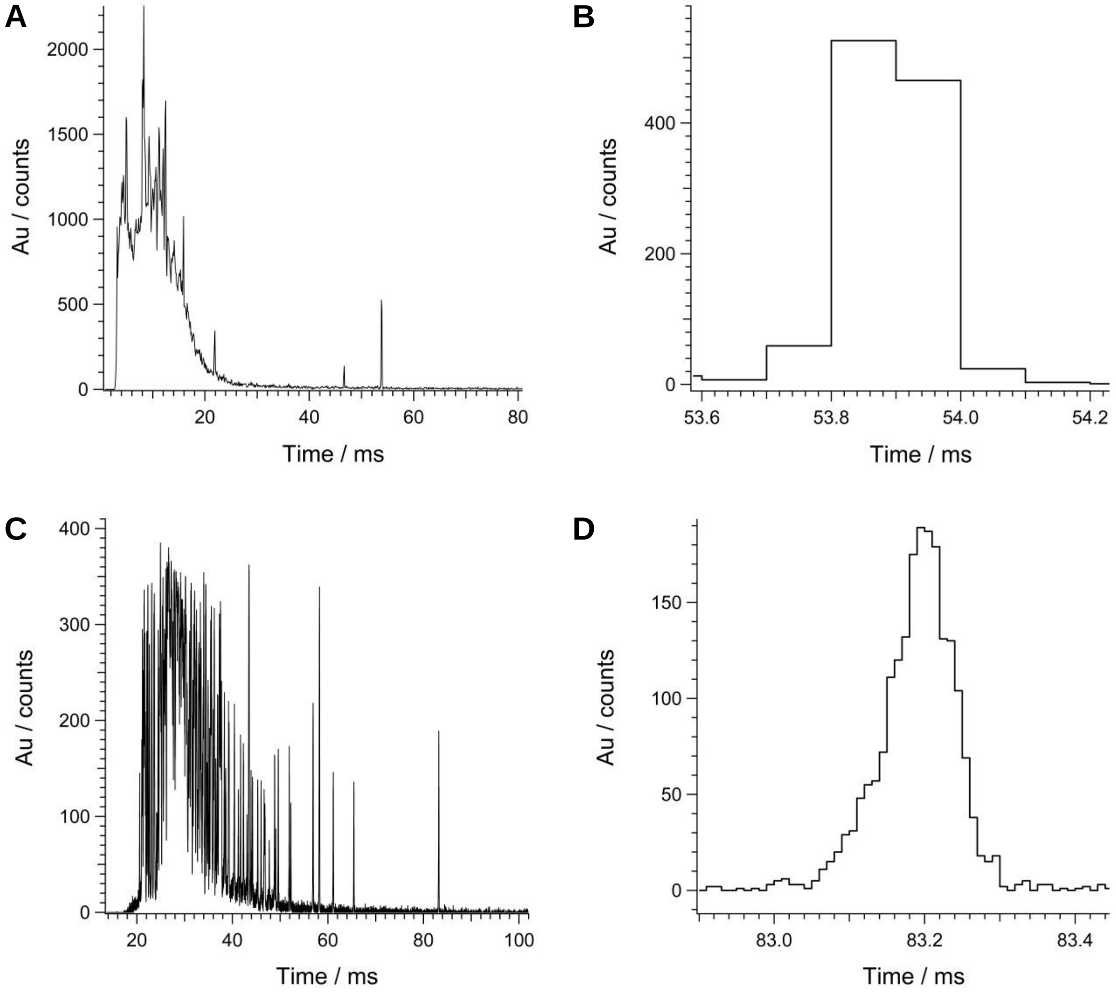

Figure 4.16 Signals observed for single cell LA-ICP-MS of individual gold labelled macrophages using the Enterprise cell and the fast data acquisition board. Signals were measured using bin widths of 100 (image A) and 10 μs (image C). Images B and D are magnifications of discrete events following the main peak in images A and C respectively, with each horizontal line representing the signal in an individual time bin. All data was acquired at 0 mm extension.

4.4 Conclusion

In this chapter, a prototype LA-ICP-MS interface was modified to enable the rapid analysis of Gd labelled cells at high sensitivity. There are no universally applied criteria to define the performance of laser ablation systems. However, the FW0.1M is perhaps the most significant criterion for cell tracking, since signals below 10% maximum are typically lower than the threshold value for identifying a labelled cell. Signals for this system were well below 10 ms at FW0.1M, which demonstrates that a sampling rate of 100 Hz is now feasible. This is expected to transform the analysis of a typical 1 x 1 mm biopsy, from several hours down to several minutes. The prototype system was also shown to provide a 6-fold increase in absolute sensitivity compared to the standard instrumentation. Assuming minimal label leakage, this will enable the analysis of cells after further 1 or 2 cell divisions than previously possible, which could potentially extend the therapeutic monitoring period. The prototype system therefore meets the demands of increased speed and sensitivity required by the ONE Study, which is critical if LA-ICP-MS is going to be adopted for routine analysis. Naturally, it follows that this level of performance will also benefit wider LA-ICP-MS applications than are described in this thesis.

The prototype technology reported here suffered from limitations imposed by financial, fabrication and assembly constraints. It is likely that the system did not precisely meet the concept of a perfectly straight and continuous flow path, with an inner injector exactly concentric with the outer injector. Indeed, to fully meet these criteria would likely require the manufacture of a combined laser ablation and ICP-MS system, sold as one integrated unit. At the time of writing, such a product is not on the market. There is also further scope for computational modelling of the plasma conditions, which would allow for increased understanding and optimisation of the system. For example, matching of the inner and outer injector flows could help to reduce turbulence within the plasma. Given the above, the preliminary data suggests that the underlying concepts are robust, but the system has further scope for improvement with a fully engineered version. This development task will now be undertaken by Electro Scientific Industries, who have filed a patent to protect the invention and intend to release a commercial version.[202]

5 Conclusion and Further Work

This thesis represents the first applications of LA-ICP-MS for single cell tracking of therapeutically administered cells. T cells, Mregs and Tol-DC were labelled with commercially available labelling reagents, in order to enable their discrimination from native cells. Uptake rates of up to 10^8 atoms per cell were achieved when labelling T cells with the MRI contrast agent Omniscan, whilst uptakes in the order of 10^9 atoms of Au per cell were observed when labelling Mregs and Tol-DC with 50 nm gold nanoparticles. Cells were examined on an individual basis, with close to 100% labelling and detection efficiency observed for all three cell types. The technique was validated using mixed preparations of labelled: non-labelled cells, and enabled enumeration of the labelled cells at close to the predicted ratio. Importantly, the cells retained sufficient label to remain detectable for up to 14 days following administration to immunodeficient mice.

The combination of laser sampling and mass spectrometric detection provided several advantages compared to other cell tracking techniques. Elemental detection does not rely on the stability of administered complexes; thus, labels could be detected at periods where detection by MRI or SPECT would be impossible. Furthermore, the exquisite detection capability of sector field ICP-MS allowed detection at levels of 10^7 atoms per cell and below, which is an order of magnitude improvement on molecular mass spectrometry.[124] Although ICP-MS requires *ex-vivo* samples, the technique is fairly versatile in terms of their format. A nebuliser and spray chamber interface enabled the analysis of digested organ samples, which provided a general overview of cell trafficking *in vivo*. Laser ablation then permitted high resolution imaging of Mregs and Tol-DC within tissue sections, as well as individual targeting of T cells that were extracted from the peritoneum. The laser instrumentation employed in this thesis can produce 2D images of 4 x 4 μm resolution, which compares favourably to MRI, which has a typical voxel size of 100 x 100 x 200 μm. LA sampling can therefore differentiate individual cells from cell clusters, and does not suffer from interfering artifacts, such as air pockets, which hinder detection when using alternative techniques. Incidentally, the major weakness of laser ablation, that is the lack of availability of matrix matched calibration standards, does not pose a limitation for this cell tracking application, since the analysis is purely qualitative.

The long-term goal of Work Package 2 was to develop technology and methods that could be applied to track cell products in the ONE Study human clinical trials. Consequently, only labelling agents that were both commercially available and had the potential to be licensed for human use were investigated. Due to the novelty of the LA-ICP-MS tracking approach, the labels used in this project had naturally been developed for other applications. Considerations taken into account when developing these labels were not necessarily aligned with those required for cell tracking by LA-ICP-MS. In MRI imaging, stability of the Gd chelates and their cellular localisation are prerequisites for image quality enhancement. Chelates located within endosomes lead to a reduction in MRI signal, as they are less able to interact with water molecules than those located in the cytoplasm.[125, 203] Therefore, ligand modifications that facilitate high endosomal uptake, although beneficial for LA-ICP-MS, may be disregarded in the early stages of MRI contrast agent development. If cell tracking by LA-ICP-MS gains popularity, then investment into the development of labelling complexes tailored exclusively to this technique is highly recommended.

Determining the fate of labels after cell death is vital to achieving reliable detection, since free label that has leaked from cells may be taken up by other phagocytes, providing a false positive signal. Co-labelling with two or more labels that are metabolised, degraded or excreted by different mechanisms is a suggested solution to this problem, since only live cells would carry both labels. Accordingly, the two labelling agents evaluated in this thesis have different primary routes of clearance, with Gd-DTPA-BMA excreted renally by glomerular filtration,[204] whilst Au nanoparticles (of above 8 μm diameter) are most likely removed through the hepatobilliary route.[205] A dual-labelling approach using these two reagents may be beneficial for future studies. An additional validation method could involve post-labelling the samples with metal-conjugated antibodies, to establish that cells bearing the tracer labels express the anticipated marker phenotype. In Chapter 3, three metal-tagged antibodies, ^{154}Sm-anti-CD45, ^{159}Tb-anti-CD11c and ^{174}Yb-anti-HLA-DR, were successfully detected in individual cells that had been counter-labelled in solution. However, non-specific binding of the antibody labels prevented their successful application in tissue sections. The development of additional metal-conjugated antibodies, as well as improved histological protocols to block non-specific binding, may improve this analysis.

LA-ICP-MS, as demonstrated in this thesis, is an exciting research tool, which has the potential to provide new insights into cellular therapy. However, improvements to the core technology are clearly necessary before the technique can be considered for routine clinical analysis. The data presented in Chapters 2 and 3 used a fairly standard LA-ICP-MS arrangement, which provided peak widths of around half a second and a detection efficiency of around 5 $x10^{-5}$, during the analysis of Gd labelled cells. Chapter 4 aimed to increase the throughput and absolute sensitivity of the analysis, through adaptation of an existing prototype interface [187] for bio-analysis. This interface formed a single diameter low-volume transport conduit from the point of ablation to the point introduction of the sample into the plasma, which minimised aerosol dispersion. Peak widths of less than 10 ms (full width at 10% peak maximum) were achieved for the analysis of single cells, which means that theoretically the analysis rate could be increased from its current rate of 2 cells per second, up to 100 cells per second, whilst maintaining individual cell resolution. This places the sampling speed of laser ablation within reach of solution based mass cytometry, which is reported to analyse 1000 cells per second, whilst LA retains the benefits of visualisation and selection of targets that the CyTOF cannot currently provide. The prototype interface was shown to provide a 5-6 fold increase in detection efficiency over the standard technology, which may prove critical for long term tracking of cells.

The intellectual property for the Loughborough technology has been purchased by Electro Scientific Industries, who have filed a patent to protect the invention,[202] and intend to incorporate the concepts into a commercial product. It is clear that this system will have wider applications than the studies reported in this thesis. In fact, another user has since coupled the prototype system to the Thermo Neptune and the Nu AttoM, for the analysis of sub-micron uranium particles.[206] Whilst the current "plug-and-play" interface is clearly applicable to a wide range of instruments, optimum performance could be achieved through the manufacture of an integrated LA and ICP-MS system, sold as a single instrument. The type of mass spectrometer best suited to this remains unclear. The work reported in this thesis used a sector-field ICP-MS, which delivered sufficient sensitivity for the applications described, but struggles to provide multi-parametric analysis due to the sequential mode of detection. A multi-collector sector-field instrument could enable simultaneous analysis of a greater number of closely spaced isotopes and would provide even higher detection efficiency, but these instruments suffer from relatively slow scan speeds, which would limit the benefits of the high-speed interface. Quadrupole mass analysers are perhaps the most common choice in current ICP-MS instruments. These instruments are relatively low cost and, although not simultaneous, they can rapidly scan through the mass range. However, they provide typically 10-fold lower sensitivity than sector-field instruments. Perhaps the most exciting option, in terms of multi-parametric capability, are TOF mass spectrometers, which simultaneously sample ions from the plasma and can provide ~30,000 spectra per second. Again, these are intrinsically less sensitive than sector-field instruments, with typically 10-50 fold lower sensitivity. Therefore, at present there is no commercially available ICP-MS instrument that satisfies the requirements of simultaneous measurement, high detection efficiency, and the necessary time resolution to take full advantage of the prototype technology.

It is acknowledged that software development may be also be required to handle the large and complex data sets that may be produced by a new system, particularly if the technology is to be used by medical technicians for clinical diagnosis. In the current arrangement, a significant proportion of time is spent individually selecting targets for ablation, hence automated cell recognition and selection software would be beneficial in a commercial instrument, to complement the increased analysis speed.

It can be concluded that the main requirements for cell tracking, namely high labelling and detection efficiency, label retention *in vivo*, and the absence of toxic effects, have been successfully demonstrated within the course of this thesis. If regulatory approval can be gained for use of labelled cells in patients, and the speed and sensitivity of the prototype LA technology can be incorporated into a commercial instrument, then LA-ICP-MS has great potential for the tracking of therapeutically administered cells in humans.

6 References

1. S. Sakaguchi, T. Yamaguchi, T. Nomura and M. Ono, "Regulatory T cells and immune tolerance", *Cell*, 2008, 133, 775-787.

2. A.N. McMurchy, A. Bushell, M.K. Levings and K.J. Wood, "Moving to tolerance: Clinical application of T regulatory cells", *Seminars in Immunology*, 2011, 23, 304-313.

3. K.J. Wood, A. Bushell and J. Hester, "Regulatory immune cells in transplantation", *Nature Reviews Immunology*, 2012, 12, 417-430.

4. H. Groux, A. Ogarra, M. Bigler, M. Rouleau, S. Antonenko, J.E. deVries and M.G. Roncarolo, "A CD4(+) T-cell subset inhibits antigen-specific T-cell responses and prevents colitis", *Nature*, 1997, 389, 737-742.

5. M. Battaglia, S. Gregori, R. Bacchetta and M.G. Roncarolo, "Tr1 cells: From discovery to their clinical application", *Seminars in Immunology*, 2006, 18, 120-127.

6. H. Peche, B. Trinite, B. Martinet and M.C. Cuturi, "Prolongation of heart allograft survival by immature dendritic cells generated from recipient type bone marrow progenitors", *American Journal of Transplantation*, 2005, 5, 255-267.

7. J.A. Hutchinson, P. Riquelme, B. Sawitzki, S. Tomiuk, P. Miqueu, M. Zuhayra, H.H. Oberg, A. Pascher, U. Lutzen, U. Janssen, C. Broichhausen, L. Renders, F. Thaiss, E. Scheuermann, E. Henze, H.D. Volk, L. Chatenoud, R.I. Lechler, K.J. Wood, D. Kabelitz, H.J. Schlitt, E.K. Geissler and F. Fandrich, "Cutting Edge: Immunological Consequences and Trafficking of Human Regulatory Macrophages Administered to Renal Transplant Recipients", *Journal of Immunology*, 2011, 187, 2072-2078.

8. P. Riquelme, S. Tomiuk, A. Kammler, F. Fandrich, H.J. Schlitt, E.K. Geissler and J.A. Hutchinson, "IFN-gamma-induced iNOS Expression in Mouse Regulatory Macrophages Prolongs Allograft Survival in Fully Immunocompetent Recipients", *Molecular Therapy*, 2013, 21, 409-422.

9. "*ONE Study research proposal*", 2010.

10. G. Digilio, V. Catanzaro, F. Fedeli, E. Gianolio, V. Menchise, R. Napolitano, C. Gringeria and S. Aime, "Targeting exofacial protein thiols with Gd-III complexes. An efficient procedure for MRI cell labelling", *Chemical Communications*, 2009, 893-895.

11. L. Ferreira, J. Karp, L. Nobre and R. Langer, "New Opportunities: The Use of Nanotechnologies to Manipulate and Track Stem Cells", *Cell Stem Cell*, 2008, 3, 136-146.

12. S.C. Rastogi, *Cell and Molecular Biology*, New Age International Ltd., New Delhi, 2nd edition, 2003.

13. S.D. Conner and S.L. Schmid, "Regulated portals of entry into the cell", *Nature*, 2003, 422, 37-44.

14. T.B. Huff, M.N. Hansen, Y. Zhao, J.X. Cheng and A. Wei, "Controlling the cellular uptake of gold nanorods", *Langmuir*, 2007, 23, 1596-1599.

15. M.R. Bernsen, A.D. Moelker, P.A. Wielopolski, S.T. Tiel and G.P. Krestin, "Labelling of mammalian cells for visualisation by MRI", *European Radiology*, 2009, 20, 255-274.

16. J. Guenoun, G.A. Koning, G. Doeswijk, L. Bosman, P.A. Wielopolski, G.P. Krestin and M.R. Bernsen, "Cationic Gd-DTPA liposomes for highly efficient labeling of mesenchymal stem cells and cell tracking with MRI", *Cell transplantation*, 2012, 21, 191-205.

17. A.B. Lyons, "Analysing cell division in vivo and in vitro using flow cytometric measurement of CFSE dye dilution", *Journal of Immunological Methods*, 2000, 243, 147-154.

18. T.D. Pollard and W.C. Earnshaw, *Cell Biology*, Elsevier Science, Philadelphia, 1st edition, 2002,

19. E.M. Winter, B. Hogers, L.M. van der Graaf, A.C. Gittenberger-de Groot, R.E. Poelmann and L. van der Weerd, "Cell Tracking Using Iron Oxide Fails to Distinguish Dead from Living Transplanted Cells in the Infarcted Heart", *Magnetic Resonance in Medicine*, 2010, 63, 817-821.

20. R.Z. Stodilka, K.J. Blackwood and F.S. Prato, "Tracking transplanted cells using dual-radionuclide SPECT", *Physics in Medicine and Biology*, 2006, 51, 2619-2632.

21. D. Hao, F.G. T. Ai, X. Hu, V.M. Runge and M. Tweedle, "MRI Contrast Agents: Basic Chemistry and Safety", *Journal of Magnetic Resonance Imaging*, 2012, 36, 1060-1071.

22. X.D. Zhang, D. Wu, X. Shen, P.X. Liu, N. Yang, B. Zhao, H. Zhang, Y.M. Sun, L.A. Zhang and F.Y. Fan, "Size-dependent *in vivo* toxicity of PEG-coated gold nanoparticles", *International Journal of Nanomedicine*, 2011, 6, 2071-2081.

23. A.M. Alkilany and C.J. Murphy, "Toxicity and cellular uptake of gold nanoparticles: what we have learned so far?", *Journal of Nanoparticle Research*, 2010, 12, 2313-2333.

24. E.E. Connor, J. Mwamuka, A. Gole, C.J. Murphy and M.D. Wyatt, "Gold nanoparticles are taken up by human cells but do not cause acute cytotoxicity", *Small*, 2005, 1, 325-327.

25. H.K. Patra, S. Banerjee, U. Chaudhuri, P. Lahiri and A.K. Dasgupta, "Cell selective response to gold nanoparticles", *Nanomedicine-Nanotechnology Biology and Medicine*, 2007, 3, 111-119.

26. M. Fritzsche and C.F. Mandenius, "Fluorescent cell-based sensing approaches for toxicity testing", *Analytical and Bioanalytical Chemistry*, 2010, 398, 181-191.

27. P. Bondza-Kibangou, C. Millot, J. Dufer and J.M. Millot, "Microspectrofluorometry of autofluorescence emission from human leukemic living cells under oxidative stress", *Biology of the Cell*, 2001, 93, 273-280.

28. S.J. Dodd, M. Williams, J.P. Suhan, D.S. Williams, A.P. Koretsky and C. Ho, "Detection of single mammalian cells by high-resolution magnetic resonance imaging", *Biophysical Journal*, 1999, 76, 103-109.

29. P. Foster-Gareau, C. Heyn, A. Alejski and B.K. Rutt, "Imaging single mammalian cells with a 1.5 T clinical MRI scanner", *Magnetic Resonance in Medicine*, 2003, 49, 968-971.

30. W.C. Shyu, C.P. Chen, S.Z. Lin, Y.J. Lee and H. Li, "Efficient tracking of non-iron-labeled mesenchymal stem cells with serial MRI in chronic stroke rats", *Stroke*, 2007, 38, 367-374.

31. M. Modo, D. Cash, K. Mellodew, S.C.R. Williams, S.E. Fraser, T.J. Meade, J. Price and H. Hodges, "Tracking transplanted stem cell migration using bifunctional, contrast agent-enhanced, magnetic resonance imaging", *Neuroimage*, 2002, 17, 803-811.

32. C. Heyn, J.A. Ronald, L.T. Mackenzie, I.C. MacDonald, A.F. Chambers, B.K. Rutt and P.J. Foster, "In vivo magnetic resonance imaging of single cells in mouse brain with optical validation", *Magnetic Resonance in Medicine*, 2006, 55, 23-29.

33. Y. Jin, H. Kong, R.Z. Stodilka, R.G. Wells, P. Zabel, P.A. Merrifield, J. Sykes and F.S. Prato, "Determining the minimum number of detectable cardiac-transplanted 111In-tropolone-labelled bone-marrow-derived mesenchymal stem cells by SPECT", *Physics in Medicine and Biology*, 2005, 50, 4445-4455.

34. K. Stojanov, E.F.J. de Vries, D. Hoekstra, A. van Waarde, R. Dierckx and I.S. Zuhorn, "F-18 FDG Labeling of Neural Stem Cells for In Vivo Cell Tracking with Positron Emission Tomography: Inhibition of Tracer Release by Phloretin", *Molecular Imaging*, 2012, 11, 1-12.

35. E. Sharif-Paghaleh, K. Sunassee, R. Tavare, K. Ratnasothy, A. Koers, N. Ali, R. Alhabbab, P.J. Blower, R.I. Lechler, L.A. Smyth, G.E. Mullen and G. Lombardi, "In Vivo SPECT Reporter Gene Imaging of Regulatory T Cells", *Plos One*, 2011, 6, e25857.

36. O. Ornatsky, D. Bandura, V. Baranov, M. Nitz, M.A. Winnik and S. Tanner, "Highly multiparametric analysis by mass cytometry", *Journal of Immunological Methods*, 2010, 361, 1-20.

37. J.S. Yoo, N. Won, H.B. Kim, J. Bang, S. Kim, S. Ahn and K.S. Soh, "In vivo imaging of cancer cells with electroporation of quantum dots and multispectral imaging", *Journal of Applied Physics*, 2010, 107,

38. E.J. Sutton, T.D. Henning, B.J. Pichler, C. Bremer and H.E. Daldrup-Link, "Cell tracking with optical imaging", *European Radiology*, 2008, 18, 2021-2032.

39. N. Kamaly, T. Kalber, G. Kenny, J. Bell, M. Jorgensen and A. Miller, "A novel bimodal lipidic contrast agent for cellular labelling and tumour MRI", *Organic and Biomolecular Chemistry*, 2010, 8, 201-211.

40. Z. Kotková, J. Kotek, D. Jirák, P. Jendelová, V. Herynek, Z. Berková, P. Hermann and I. Lukeš, "Cyclodextrin-based bimodal fluorescence/MRI contrast agents: An efficient approach to cellular imaging", *Chemistry - A European Journal*, 2010, 16, 10094-10102.

41. M.M. van Schooneveld, D.P. Cormode, R. Koole, J.T. van Wijngaarden, C. Calcagno, T. Skajaa, J. Hilhorst, D.C. t Hart, Z.A. Fayad, W.J.M. Mulder and A. Meijerink, "A fluorescent, paramagnetic and PEGylated gold/silica nanoparticle for MRI, CT and fluorescence imaging", *Contrast Media & Molecular Imaging*, 2010, 5, 231-236.

42. D.C. Macallan, C.A. Fullerton, R.A. Neese, K. Haddock, S.S. Park and M.K. Hellerstein, "Measurement of cell proliferation by labeling of DNA with stable isotope-labeled glucose: Studies in vitro, in animals, and in humans", *Proceedings of the National Academy of Sciences of the United States of America*, 1998, 95, 708-713.

43. M. Hellerstein, M.B. Hanley, D. Cesar, S. Siler, C. Papageorgopoulos, E. Wieder, D. Schmidt, R. Hoh, R. Neese, D. Macallan, S. Deeks and J.M. McCune, "Directly measured kinetics of circulating T lymphocytes in normal and HIV-1-infected humans", *Nature Medicine*, 1999, 5, 83-89.

44. D.C. Macallan, B. Asquith, A.J. Irvine, D.L. Wallace, A. Worth, H. Ghattas, Y. Zhang, G.E. Griffin, D.F. Tough and P.C. Beverley, "Measurement and modeling of human T cell kinetics", *European Journal of Immunology*, 2003, 33, 2316-2326.

45. M. Vukmanovic-Stejic, Y. Zhang, J.E. Cook, J.M. Fletcher, A. McQuaid, J.E. Masters, M.H.A. Rustin, L.S. Taams, P.C.L. Beverley, D.C. Macallan and A.N. Akbar, "Human CD4(+)CD25(hi)Foxp3(+) regulatory T cells are derived by rapid turnover of memory populations in vivo", *Journal of Clinical Investigation*, 2006, 116, 2423-2433.

46. D.E. Farthing, N.P. Buxbaum, C.V. Bare, S.M. Treadwell, V. Kapoor, K.M. Williams and R.E. Gress, "Sensitive GC-MS/MS Method to Measure Deuterium Labeled Deoxyadenosine in DNA from Limited Mouse Cell Populations", *Analytical Chemistry*, 2013, 85, 4613-4620.

47. S.D. Fox, R.A. Lempicki, D.A. Hosack, M.W. Baseler, J.A. Kovacs, H.C. Lane, T.D. Veenstra and H.J. Issaq, "A comparison of mu LC/electrospray ionization-MS and GC/MS for the measurement of stable isotope enrichment from a H-2(2) -glucose metabolic probe in T-cell genomic DNA", *Analytical Chemistry*, 2003, 75, 6517-6522.

48. X.Q. Cai, H.H. Chen, C.L. Wang, S.T. Chen, S.F. Lai, C.C. Chien, Y.Y. Chen, I.M. Kempson, Y. Hwu, C.S. Yang and G. Margaritondo, "Imaging the cellular uptake of tiopronin-modified gold nanoparticles", *Analytical and Bioanalytical Chemistry*, 2011, 401, 809-816.

49. T. Yamane, K. Hanaoka, Y. Muramatsu, K. Tamura, Y. Adachi, Y. Miyashita, Y. Hirata and T. Nagano, "Method for Enhancing Cell Penetration of Gd^{3+}-based

MRI Contrast Agents by Conjugation with Hydrophobic Fluorescent Dyes", *Bioconjugate Chemistry*, 2011, 22, 2227-2236.

50. L.M. Ricles, S.Y. Nam, K. Sokolov, S.Y. Emelianov and L.J. Suggs, "Function of mesenchymal stem cells following loading of gold nanotracers", *International Journal of Nanomedicine*, 2011, 6, 407-416.

51. Y.S. Zhang, Y. Wang, L.D. Wang, Y.C. Wang, X. Cai, C. Zhang, L.H.V. Wang and Y.N. Xia, "Labeling Human Mesenchymal Stem Cells with Gold Nanocages for in vitro and in vivo Tracking by Two-Photon Microscopy and Photoacoustic Microscopy", *Theranostics*, 2013, 3, 532-543.

52. S.R. Benhabbour, J.C. Luft, D. Kim, A. Jain, S. Wadhwa, M.C. Parrott, R.H. Liu, J.M. DeSimone and R.J. Mumper, "*In vitro* and *in vivo* assessment of targeting lipid-based nanoparticles to the epidermal growth factor-receptor (EGFR) using a novel Heptameric Z(EGFR) domain", *Journal of Controlled Release*, 2012, 158, 63-71.

53. L. Mueller, H. Traub, N. Jakubowski, D. Drescher, V.I. Baranov and J. Kneipp, "Trends in single-cell analysis by use of ICP-MS", *Analytical and Bioanalytical Chemistry*, 2014, 406, 6963-6977.

54. F.M. Li, D.W. Armstrong and R.S. Houk, "Behavior of bacteria in the inductively coupled plasma: Atomization and production of atomic ions for mass spectrometry", *Analytical Chemistry*, 2005, 77, 1407-1413.

55. K.S. Ho and W.T. Chan, "Time-resolved ICP-MS measurement for single-cell analysis and on-line cytometry", *Journal of Analytical Atomic Spectrometry*, 2010, 25, 1114-1122.

56. C.N. Tsang, K.S. Ho, H.Z. Sun and W.T. Chan, "Tracking Bismuth Antiulcer Drug Uptake in Single Helicobacter pylori cells", *Journal of the American Chemical Society*, 2011, 133, 7355-7357.

57. B. Franze, I. Strenge and C. Engelhard, "Single particle inductively coupled plasma mass spectrometry: evaluation of three different pneumatic and piezo-based sample introduction systems for the characterization of silver nanoparticles", *Journal of Analytical Atomic Spectrometry*, 2012, 27, 1074-1083.

58. S. Gschwind, L. Flamigni, J. Koch, O. Borovinskaya, S. Groh, K. Niemax and D. Gunther, "Capabilities of inductively coupled plasma mass spectrometry for the detection of nanoparticles carried by monodisperse microdroplets", *Journal of Analytical Atomic Spectrometry*, 2011, 26, 1166-1174.

59. K. Shigeta, G. Köllensperger, E. Rampler, H. Traub, L. Rottmann, U. Panne, A. Okino and N. Jakubowski, "Sample introduction of single selenized yeast cells (Saccharomyces cerevisiae) by micro droplet generation into an ICP-sector field mass spectrometer for label-free detection of trace elements", *Journal of Analytical Atomic Spectrometry*, 2013, 28, 637-645.

60. DVS Sciences, "*MAXPAR Antibody Labelling Kits*", 2011, Available: http://www.dvssciences.com/labeling-reagents.html, Last accessed: 12/09/2011.

61. D.R. Bandura, V.I. Baranov, O.I. Ornatsky, A. Antonov, R. Kinach, X.D. Lou, S. Pavlov, S. Vorobiev, J.E. Dick and S.D. Tanner, "Mass Cytometry: Technique

for Real Time Single Cell Multitarget Immunoassay Based on Inductively Coupled Plasma Time-of-Flight Mass Spectrometry", *Analytical Chemistry*, 2009, 81, 6813-6822.

62. "*CyTOF® Mass Cytometer*", 2013, Available: http://www.dvssciences.com/pdf/DVS_CyTOF_Brochure.PDF, Last accessed: 18/04/2013.

63. S.C. Bendall, E.F. Simonds, P. Qiu, E.A.D. Amir, P.O. Krutzik, R. Finck, R.V. Bruggner, R. Melamed, A. Trejo, O.I. Ornatsky, R.S. Balderas, S.K. Plevritis, K. Sachs, D. Pe'er, S.D. Tanner and G.P. Nolan, "Single-Cell Mass Cytometry of Differential Immune and Drug Responses Across a Human Hematopoietic Continuum", *Science*, 2011, 332, 687-696.

64. H.G. Fienberg, E.F. Simonds, W.J. Fantl, G.P. Nolan and B. Bodenmiller, "A platinum-based covalent viability reagent for single-cell mass cytometry", *Cytometry Part A*, 2012, 81A, 467-475.

65. J. Feldmann, A. Kindness and P. Ek, "Laser ablation of soft tissue using a cryogenically cooled ablation cell", *Journal of Analytical Atomic Spectrometry*, 2002, 17, 813-818.

66. A. Kindness, C.N. Sekaran and J. Feldmann, "Two-dimensional mapping of copper and zinc in liver sections by laser ablation-inductively coupled plasma mass spectrometry", *Clinical Chemistry*, 2003, 49, 1916-1923.

67. E. Moreno-Gordaliza, C. Giesen, A. Lazaro, D. Esteban-Fernandez, B. Humanes, B. Canas, U. Panne, A. Tejedor, N. Jakubowski and M.M. Gomez-Gomez, "Elemental Bioimaging in Kidney by LA-ICP-MS As a Tool to Study Nephrotoxicity and Renal Protective Strategies in Cisplatin Therapies", *Analytical Chemistry*, 2011, 83, 7933-7940.

68. B. Jackson, S. Harper, L. Smith and J. Flinn, "Elemental mapping and quantitative analysis of Cu, Zn, and Fe in rat brain sections by laser ablation ICP-MS", *Analytical and Bioanalytical Chemistry*, 2006, 384, 951-957.

69. M. Dehnhardt, M. Zoriy, Z. Khan, G. Reifenberger, T. Ekstrom, J.S. Becker, K. Zilles and A. Bauer, "Element distribution is altered in a zone surrounding human glioblastoma multiforme", *Journal of Trace Elements in Medicine and Biology*, 2008, 22, 17-23.

70. D. Hare, B. Reedy, R. Grimm, S. Wilkins, I. Volitakis, J.L. George, R.A. Cherny, A.I. Bush, D.I. Finkelstein and P. Doble, "Quantitative elemental bio-imaging of Mn, Fe, Cu and Zn in 6-hydroxydopamine induced Parkinsonism mouse models", *Metallomics*, 2009, 1, 53-58.

71. D.J. Hare, J.L. George, R. Grimm, S. Wilkins, P.A. Adlard, R.A. Cherny, A.I. Bush, D.I. Finkelstein and P. Doble, "Three-dimensional elemental bio-imaging of Fe, Zn, Cu, Mn and P in a 6-hydroxydopamine lesioned mouse brain", *Metallomics*, 2010, 2, 745-753.

72. A. Matusch, C. Depboylu, C. Palm, B. Wu, G.U. Hoglinger, M.K.H. Schafer and J.S. Becker, "Cerebral Bioimaging of Cu, Fe, Zn, and Mn in the MPTP Mouse Model of Parkinson's Disease Using Laser Ablation Inductively Coupled Plasma

Mass Spectrometry (LA-ICP-MS)", *Journal of the American Society for Mass Spectrometry*, 2010, 21, 161-171.

73. R.W. Hutchinson, A.G. Cox, C.W. McLeod, P.S. Marshall, A. Harper, E.L. Dawson and D.R. Howlett, "Imaging and spatial distribution of beta-amyloid peptide and metal ions in Alzheimer's plaques by laser ablation-inductively coupled plasma-mass spectrometry", *Analytical Biochemistry*, 2005, 346, 225-233.

74. S.H. Hu, S.C. Zhang, Z.C. Hu, Z. Xing and X.R. Zhang, "Detection of multiple proteins on one spot by laser ablation inductively coupled plasma mass spectrometry and application to immuno-microarray with element-tagged antibodies", *Analytical Chemistry*, 2007, 79, 923-929.

75. L. Waentig, P.H. Roos and N. Jakubowski, "Labelling of antibodies and detection by laser ablation inductively coupled plasma mass spectrometry : PART III. Optimization of antibody labelling for application in a Western blot procedure", *Journal of Analytical Atomic Spectrometry*, 2009, 24, 924-933.

76. T.C. de Bang, P. Pedas, J.K. Schjoerring, P.E. Jensen and S. Husted, "Multiplexed Quantification of Plant Thylakoid Proteins on Western Blots Using Lanthanide-Labeled Antibodies and Laser Ablation Inductively Coupled Plasma Mass Spectrometry (LA-ICP-MS)", *Analytical Chemistry*, 2013, 85, 5047-5054.

77. C. Giesen, L. Waentig, T. Mairinger, D. Drescher, J. Kneipp, P.H. Roos, U. Panne and N. Jakubowski, "Iodine as an elemental marker for imaging of single cells and tissue sections by laser ablation inductively coupled plasma mass spectrometry", *Journal of Analytical Atomic Spectrometry*, 2011, 26, 2160-2165.

78. D. Drescher, C. Giesen, H. Traub, U. Panne, J. Kneipp and N. Jakubowski, "Quantitative Imaging of Gold and Silver Nanoparticles in Single Eukaryotic Cells by Laser Ablation ICP-MS", *Analytical Chemistry*, 2012, 84, 9684-9688.

79. A.L. Gray, "Solid Sample Introduction by Laser Ablation for Inductively Coupled Plasma Source - Mass Spectrometry", *Analyst*, 1985, 110, 551-556.

80. I. Konz, B. Fernandez, M.L. Fernandez, R. Pereiro, H. Gonzalez-Iglesias, M. Coca-Prados and A. Sanz-Medel, "Quantitative bioimaging of trace elements in the human lens by LA-ICP-MS", *Analytical and Bioanalytical Chemistry*, 2014, 406, 2343-2348.

81. C. Austin, D. Hare, A.L. Rozelle, W.H. Robinson, R. Grimm and P. Doble, "Elemental bio-imaging of calcium phosphate crystal deposits in knee samples from arthritic patients", *Metallomics*, 2009, 1, 142-147.

82. D. Hare, F. Burger, C. Austin, F. Fryer, R. Grimm, B. Reedy, R.A. Scolyer, J.F. Thompson and P. Doble, "Elemental bio-imaging of melanoma in lymph node biopsies", *Analyst*, 2009, 134, 450-453.

83. R.E. Russo, X.L. Mao and S.S. Mao, "The physics of laser ablation in microchemical analysis", *Analytical Chemistry*, 2002, 74, 70A-77A.

84. B.L. Sharp and C. O'Connor, "Aerosol Generation and Sample Transport", in *Inductively Coupled Plasma Spectrometry and its Applications*, ed. S. J. Hill, Blackwell Publishing Ltd, Oxford, 2007, ch. 4, pp. 98-133.

85. R.E. Russo, X.L. Mao, H.C. Liu, J. Gonzalez and S.S. Mao, "Laser ablation in analytical chemistry - a review", *Talanta*, 2002, 57, 425-451.

86. R.E. Russo, X.L. Mao, J.J. Gonzalez, V. Zorba and J. Yoo, "Laser Ablation in Analytical Chemistry", *Analytical Chemistry*, 2013, 85, 6162-6177.

87. J. Koch and D. Gunther, "Review of the State-of-the-Art of Laser Ablation Inductively Coupled Plasma Mass Spectrometry", *Applied Spectroscopy*, 2011, 65, 155A-162A.

88. D. Gunther and B. Hattendorf, "Solid sample analysis using laser ablation inductively coupled plasma mass spectrometry", *Trac-Trends in Analytical Chemistry*, 2005, 24, 255-265.

89. I. Horn and F. von Blanckenburg, "Investigation on elemental and isotopic fractionation during 196 nm femtosecond laser ablation multiple collector inductively coupled plasma mass spectrometry", *Spectrochimica Acta Part B-Atomic Spectroscopy*, 2007, 62, 410-422.

90. H.R. Kuhn and D. Gunther, "Elemental fractionation studies in laser ablation inductively coupled plasma mass spectrometry on laser-induced brass aerosols", *Analytical Chemistry*, 2003, 75, 747-753.

91. E.F. Cromwell and P. Arrowsmith, "Semiquantitative analysis with laser ablation inductively coupled plasma mass spectrometry", *Analytical Chemistry*, 1995, 67, 131-138.

92. J. Koch, I. Feldmann, N. Jakubowski and K. Niemax, "Elemental composition of laser ablation aerosol particles deposited in the transport tube to an ICP", *Spectrochimica Acta Part B-Atomic Spectroscopy*, 2002, 57, 975-985.

93. H.R. Kuhn, M. Guillong and D. Gunther, "Size-related vaporisation and ionisation of laser-induced glass particles in the inductively coupled plasma", *Analytical and Bioanalytical Chemistry*, 2004, 378, 1069-1074.

94. C. O'Connor, M.R. Landon and B.L. Sharp, "Absorption coefficient modified pressed powders for calibration of laser ablation inductively coupled plasma mass spectrometry", *Journal of Analytical Atomic Spectrometry*, 2007, 22, 273-282.

95. J.A.T. Pugh, A.G. Cox, C.W. McLeod, J. Bunch, B. Whitby, B. Gordon, T. Kalber and E. White, "A novel calibration strategy for analysis and imaging of biological thin sections by laser ablation inductively coupled plasma mass spectrometry", *Journal of Analytical Atomic Spectrometry*, 2011, 26, 1667-1673.

96. D. Hare, C. Austin and P. Doble, "Quantification strategies for elemental imaging of biological samples using laser ablation-inductively coupled plasma-mass spectrometry", *Analyst*, 2012, 137, 1527-1537.

97. D.L. Andrews, *Lasers in Chemistry*, Springer, Berlin, 3rd edition, 1997,

98. M. Guillong, I. Horn and D. Gunther, "A comparison of 266 nm, 213 nm and 193 nm produced from a single solid state Nd : YAG laser for laser ablation ICP-MS", *Journal of Analytical Atomic Spectrometry*, 2003, 18, 1224-1230.

99. J.S. Becker, "Bioimaging of metals in brain tissue from micrometre to nanometre scale by laser ablation inductively coupled plasma mass spectrometry: State of the art and perspectives", *International Journal of Mass Spectrometry*, 2010, 289, 65-75.

100. R.E. Russo, X.L. Mao, J.J. Gonzalez and S.S. Mao, "Femtosecond laser ablation ICP-MS", *Journal of Analytical Atomic Spectrometry*, 2002, 17, 1072-1075.

101. I. Horn and D. Gunther, "The influence of ablation carrier gasses Ar, He and Ne on the particle size distribution and transport efficiencies of laser ablation-induced aerosols: implications for LA-ICP-MS", *Applied Surface Science*, 2003, 207, 144-157.

102. E.d. Hoffmann and V. Stroobant, *Mass Spectrometry: Principles and Applications*, John Wiley & Sons, Chichester, 3rd, 2007,

103. J.S. Becker and N. Jakubowski, "The synergy of elemental and biomolecular mass spectrometry: new analytical strategies in life sciences", *Chemical Society Reviews*, 2009, 38, 1969-1983.

104. C. Rappel and D. Schaumloffel, "Improved nanonebulizer design for the coupling of nanoHPLC with ICP-MS", *Journal of Analytical Atomic Spectrometry*, 2010, 25, 1963-1968.

105. J.A. Horner, S.A. Lehn and G.M. Hieftje, "Computerized simulation of aerosol-droplet desolvation in an inductively coupled plasma", *Spectrochimica Acta Part B-Atomic Spectroscopy*, 2002, 57, 1025-1042.

106. J.W. Olesik and J.C. Fister, "Incompletely desolvated droplets in argon inductively coupled plasmas - Their number, original size and effect on emission intensities", *Spectrochimica Acta Part B-Atomic Spectroscopy*, 1991, 46, 851-868.

107. J.W. Olesik and S.E. Hobbs, "Monodisperse Dried Microparticulate Injector - A new tool for studying fundamental processes in inductively-coupled plasmas", *Analytical Chemistry*, 1994, 66, 3371-3378.

108. B. Poulson, Personal Communication, Microdrop Technologies, Germany, 2012.

109. S.J. Hill, A. Fisher and M. Foulkes, "Basic Concepts and Instrumentation for Plasma Spectrometry", in *Inductively Coupled Plasma Spectrometry and its Applications*, ed. S. J. Hill, Blackwell Publishing Ltd, Oxford, 2007, ch. 3, pp. 61-97.

110. R. Thomas, "A Beginner's Guide to ICP-MS - Part IV: The Interface Region", *Spectroscopy*, 2001, 16, 26-34.

111. R. Thomas, "A Beginner's Guide to ICP-MS - Part V: The Ion Focusing System", *Spectroscopy*, 2001, 16, 38-44.

112. Element 2 Operator manual – Rev 2, Thermo Finnigan, 2001.

113. R. Thomas, "A Beginner’s Guide to ICP-MS - Part VII: Mass Separation Devices — Double-Focusing Magnetic-Sector Technology", *Spectroscopy*, 2001, 16, 22-27.

114. G. O’Connor and E.H. Evans, "Fundamental Aspects of Inductively Coupled Plasma – Mass Spectrometry (ICP-MS)", in *Inductively Coupled Plasma Spectrometry and its Applications*, ed. S. J. Hill, Blackwell Publishing Ltd, Oxford, 2007, ch. 5, pp. 134-159.

115. FinniganTM ELEMENT2/FinniganTM ELEMENT XR Hardware Manual, Revision A - 119 1410, 2005.

116. F.H. Khan, *Elements of Immunology*, Pearson Education India, Delhi, 1st edition, 2009, ch. 2, pp 25-57.

117. V.S. Gorantla, S. Schneeberger, G. Brandacher, R. Sucher, D. Zhang, W.P.A. Lee and X.X. Zheng, "T regulatory cells and transplantation tolerance", *Transplantation Reviews*, 2010, 24, 147-159.

118. N. Kamaly and A.D. Miller, "Paramagnetic Liposome Nanoparticles for Cellular and Tumour Imaging", *International Journal of Molecular Sciences*, 2010, 11, 1759-1776.

119. Y.K. Hsieh, P.S. Jiang, B.S. Yang, T.Y. Sun, H.H. Peng and C.F. Wang, "Using laser ablation/inductively coupled plasma mass spectrometry to bioimage multiple elements in mouse tumors after hyperthermia", *Analytical and Bioanalytical Chemistry*, 2011, 401, 909-915.

120. N. Kamaly, J.A. Pugh, T.L. Kalber, J. Bunch, A.D. Miller, C.W. McLeod and J.D. Bell, "Imaging of Gadolinium Spatial Distribution in Tumor Tissue by Laser Ablation Inductively Coupled Plasma Mass Spectrometry", *Molecular Imaging and Biology*, 2010, 12, 361-366.

121. J.A.T. Pugh, A.G. Cox, C.W. McLeod, J. Bunch, M.J. Writer, S.L. Hart, A. Bienemann, E. White and J. Bell, "Elemental imaging of MRI contrast agents: benchmarking of LA-ICP-MS to MRI", *Analytical and Bioanalytical Chemistry*, 2012, 403, 1641-1649.

122. J. Guenoun, A. Ruggiero, G. Doeswijk, R.C. Janssens, G.A. Koning, G. Kotek, G.P. Krestin and M.R. Bernsen, "*In vivo* quantitative assessment of cell viability of gadolinium or iron-labeled cells using MRI and bioluminescence imaging", *Contrast Media and Molecular Imaging*, 2013, 8, 165–174.

123. M. Port, J.M. Idee, C. Medina, C. Robic, M. Sabatou and C. Corot, "Efficiency, thermodynamic and kinetic stability of marketed gadolinium chelates and their possible clinical consequences: a critical review", *Biometals*, 2008, 21, 469-490.

124. E. Di Gregorio, E. Gianolio, R. Stefania, G. Barutello, G. Digilio and S. Aime, "On the Fate of MRI Gd-Based Contrast Agents in Cells. Evidence for Extensive Degradation of Linear Complexes upon Endosomal Internalization", *Analytical Chemistry*, 2013, 85, 5627-5631.

125. E. Terreno, S.G. Crich, S. Belfiore, L. Biancone, C. Cabella, G. Esposito, A.D. Manazza and S. Aime, "Effect of the intracellular localization of a Gd-based

imaging probe on the relaxation enhancement of water protons", *Magnetic Resonance in Medicine*, 2006, 55, 491-497.

126. M. Rudelius, H.E. Daldrup-Link, U. Heinzmann, G. Piontek, M. Settles, T.M. Link and J. Schlegel, "Highly efficient paramagnetic labelling of embryonic and neuronal stem cells", *European Journal of Nuclear Medicine and Molecular Imaging*, 2003, 30, 1038–1044.

127. M. Oliver, A. Ahmad, N. Kamaly, E. Perouzel, A. Caussin, M. Keller, A. Herlihy, J. Bell, A.D. Miller and M.R. Jorgensen, "MAGfect: a novel liposome formulation for MRI labelling and visualization of cells", *Organic & Biomolecular Chemistry*, 2006, 4, 3489-3497.

128. G. Digilio, V. Menchise, E. Gianolio, V. Catanzaro, C. Carrera, R. Napolitano, F. Fedeli and S. Aime, "Exofacial Protein Thiols as a Route for the Internalization of Gd(III)-Based Complexes for Magnetic Resonance Imaging Cell Labeling", *Journal of Medicinal Chemistry*, 2010, 53, 4877-4890.

129. T. Kalliokoski, E. Svedström, J. Saunavaara, A. Roivainen, M. Kankaanpää, H. Oivanen, P. Nuutila and O. Simell, "Imaging of Insulitis in NOD Mice with IL-2-Gd-DTPA and 1.5 T MRI", *Advances in Molecular Imaging*, 2011, 1, 43-49.

130. L.A. Tran, R. Krishnamurthy, R. Muthupillai, M.D. Cabreira-Hansen, J.T. Willerson, E.C. Perin and L.J. Wilson, "Gadonanotubes as magnetic nanolabels for stem cell detection", *Biomaterials*, 2010, 31, 9482-9491.

131. M.S.A. Horstwood, G.L. Foster, R.R. Parrish, S.R. Noble and G.M. Nowell, "Common-Pb corrected in situ U-Pb accessory mineral geochronology by LA-MC-ICP-MS", *Journal of Analytical Atomic Spectrometry*, 2003, 18, 837-846.

132. K. Yamada, N. Kato, A. Takagi, M. Koi and H. Hemmi, "One-milliliter wet-digestion for inductively coupled plasma mass spectrometry (ICP-MS): determination of platinum-DNA adducts in cells treated with platinum(II) complexes", *Analytical and Bioanalytical Chemistry*, 2005, 382, 1702-1707.

133. S.L. Kerr, "Enhancing nucleic acid detection using inductively coupled plasma mass spectrometry, by means of metal and nano-particle labelling", Ph.D. Thesis, Loughborough University, 2008.

134. A. Bushell, Personal Communication, University of Oxford, UK, 2014.

135. J.M. Idee, M. Port, C. Robic, C. Medina, M. Sabatou and C. Corot, "Role of Thermodynamic and Kinetic Parameters in Gadolinium Chelate Stability", *Journal of Magnetic Resonance Imaging*, 2009, 30, 1249-1258.

136. C. Robic, S. Catoen, D.M.-C. Goltstein, J.-M. Idee and M. Port, "The role of phosphate on Omniscan (R) dechelation: an in vitro relaxivity study at pH 7", *Biometals*, 2011, 24, 759-768.

137. Y. Cheng, H.Y. Yao, H.K. Lin, J.F. Lu, R.C. Li and K. Wang, "The events relating to lanthanide ions enhanced permeability of human erythrocyte membrane: binding, conformational change, phase transition, perforation and ion transport", *Chemico-Biological Interactions*, 1999, 121, 267-289.

138. A. Schmid, H. Kortmann, P.S. Dittrich and L.M. Blank, "Chemical and biological single cell analysis", *Current Opinion in Biotechnology*, 2010, 21, 12-20.

139. J.A. Kim, C. Åberg, A. Salvati and K.A. Dawson, "Role of cell cycle on the cellular uptake and dilution of nanoparticles in a cell population", *Nature Nanotechnology*, 2012, 7, 62-68.

140. A. Akl, N.D. Jones, N. Rogers, M.A. Bakr, A.Mostafa, E.L.M.E. Shehawy, M.A. Ghoneim and K.J. Wood, "An investigation to assess the potential of $CD25^{high}CD4^{+}$ T cells to regulate responses to donor alloantigens in clinically stable renal transplant recipients", *Transplantation International*, 2008, 21, 65-73.

141. M. Martínez-Llordella, I. Puig-Pey, G. Orlando, M. Ramoni, G. Tisone, A. Rimola, J. Lerut, D. Latinne, C. Margarit, I. Bilbao, S. Brouard, M. Hernández-Fuentes, J.-P. Soulillou and A. Sánchez-Fueyo, "Multiparameter Immune Profiling of Operational Tolerance in Liver Transplantation", *American Journal of Transplantation*, 2007, 7, 309–319.

142. Y. Zhai and J.W. Kupiec-Weglinski, "What is the role of regulatory T cells in transplantation tolerance? ", *Current Opinion in Immunology*, 1999, 11, 497–503.

143. S.N. Nadig, J. Wieckiewicz, D.C. Wu, G. Warnecke, W. Zhang, S. Luo, A. Schiopu, D.P. Taggart and K.J. Wood, "In vivo prevention of transplant arteriosclerosis by ex vivo-expanded human regulatory T cells", *Nature Medicine*, 2010, 16, 809-U112.

144. Y. Li, X. Zhao, D. Cheng, H. Haga, T. Tsuruyama, K. Wood, S. Sakaguchi, K. Tanaka, S. Uemoto and T. Koshiba, "The Presence of Foxp3 Expressing T Cells Within Grafts of Tolerant Human Liver Transplant Recipients", *Trransplantation*, 2008, 86, 1837- 1843.

145. L. Graca, S.P. Cobbold and H. Waldmann, "Identification of Regulatory T Cells in Tolerated Allografts", *Journal of Experimental Medicine*, 2002, 195, 1641–1646.

146. S. Qin, S.P. Cobbold, H. Pope, J. Elliott, D. Kioussis, J. Davies and H. Waldmann, ""Infectious" Transplantation Tolerance", *Science*, 1993, 259, 974-977.

147. C.D. Surh and J.Sprent, "Homeostatic T Cell Proliferation: How Far Can T Cells Be Activated to Self-Ligands?", *Journal of Experimental Medicine*, 2000, 192, F9-F14.

148. S.E. Cowper, H.S. Robin, S.M. Steinberg, L.D. Su, S. Gupta and P.E. LeBoit, "Scleromyxoedema-like cutaneous diseases in renal-dialysis patients", *Lancet*, 2000, 356, 1000-1001.

149. T. Grobner, "Gadolinium - a specific trigger for the development of nephrogenic fibrosing dermopathy and nephrogenic systemic fibrosis?", *Nephrology Dialysis Transplantation*, 2006, 21, 1104-1108.

150. P. Marckmann, L. Skov, K. Rossen, A. Dupont, M.B. Damholt, J.G. Heaf and H.S. Thomsen, "Nephrogenic systemic fibrosis: Suspected causative role of

gadodiamide used for contrast-enhanced magnetic resonance imaging", *Journal of the American Society of Nephrology*, 2006, 17, 2359-2362.

151. P. Riquelme, E.K. Geissler and J.A. Hutchinson, "Alternative approaches to myeloid suppressor cell therapy in transplantation: comparing regulatory macrophages to tolerogenic DCs and MDSCs", *Transplantation Research*, 2012, 1, 17.

152. A. Moreau, E. Varey, L. Bouchet-Delbos and M.-C. Cuturi, "Cell therapy using tolerogenic dendritic cells in transplantation", *Transplantation Research*, 2012, 1, 13.

153. J. Song, J. Zhou and H. Duan, "Self-Assembled Plasmonic Vesicles of SERS-Encoded Amphiphilic Gold Nanoparticles for Cancer Cell Targeting and Traceable Intracellular Drug Delivery", *Journal of the American Chemical Society*, 2012, 134, 13458−13469.

154. T. Stuchinskaya, M. Moreno, M.J. Cook, D.R. Edwards and D.A. Russell, "Targeted photodynamic therapy of breast cancer cells using antibody-phthalocyanine-gold nanoparticle conjugates", *Photochemical & Photobiological Sciences*, 2011, 10, 822-831.

155. B.D. Chithrani, A.A. Ghazani and W.C.W. Chan, "Determining the size and shape dependence of gold nanoparticle uptake into mammalian cells", *Nano Letters*, 2006, 6, 662-668.

156. D.B. Chithrani, M. Dunne, J. Stewart, C. Allen and D.A. Jaffray, "Cellular uptake and transport of gold nanoparticles incorporated in a liposomal carrier'", *Nanomedicine-Nanotechnology Biology and Medicine*, 2010, 6, 161-169.

157. S.D. Perrault and W.C.W. Chan, "Synthesis and Surface Modification of Highly Monodispersed, Spherical Gold Nanoparticles of 50-200 nm", *Journal of the American Chemical Society*, 2009, 131, 17042-17043.

158. X.C. Ye, L.H. Jin, H. Caglayan, J. Chen, G.Z. Xing, C. Zheng, V. Doan-Nguyen, Y.J. Kang, N. Engheta, C.R. Kagan and C.B. Murray, "Improved Size-Tunable Synthesis of Monodisperse Gold Nanorods through the Use of Aromatic Additives", *ACS Nano*, 2012, 6, 2804-2817.

159. N. Elbialy, N. Mohamed and A.S. Monem, "Synthesis, characterization and application of gold nanoshells using mesoporous silica core", *Microporous and Mesoporous Materials*, 2014, 190, 197-207.

160. J.Y. Chen, J.M. McLellan, A. Siekkinen, Y.J. Xiong, Z.Y. Li and Y.N. Xia, "Facile synthesis of gold-silver nanocages with controllable pores on the surface", *Journal of the American Chemical Society*, 2006, 128, 14776-14777.

161. R. Thomas, "A Beginner's Guide to ICP-MS - Part XII: A Review of Interferences", *Spectroscopy*, 2002, 17, 24-31.

162. H. Tapiero and K.D. Tew, "Trace elements in human physiology and pathology: zinc and metallothioneins", *Biomedicine & Pharmacotherapy*, 2003, 57, 399-411.

163. J.A. Hutchinson, P. Riquelme, E.K. Geissler and F. Fändrich, "Human regulatory macrophages", *Methods in Molecular Biology*, 2011, 677, 181–192.

164. M. Segovia, M.-C. Cuturi and M. Hill, "Preparation of mouse bone marrow-derived dendritic cells with immunoregulatory properties", *Methods in Molecular Biology*, 2011, 677, 161-168.

165. A. Albanese and W.C.W. Chan, "Effect of Gold Nanoparticle Aggregation on Cell Uptake and Toxicity", *ACS Nano*, 2011, 5, 5478–5489.

166. M. Wang, L.-N. Zheng, B. Wang, H.-Q. Chen, Y.-L. Zhao, Z.-F. Chai, H.J. Reid, B.L. Sharp and W.-Y. Feng, "Quantitative Analysis of Gold Nanoparticles in Single Cells by Laser Ablation Inductively Coupled Plasma-Mass Spectrometry", *Analytical Chemistry*, 2014, 86, 10252−10256.

167. K. Kawamura, K. Iyonaga, H. Ichiyasu, J. Nagano, M. Suga and Y. Sasaki, "Differentiation, maturation, and survival of dendritic cells by osteopontin regulation", *Clinical and Diagnostic Laboratory Immunology*, 2005, 12, 206-212.

168. T. Büchner, D. Drescher, H. Traub, P. Schrader, S. Bachmann, N. Jakubowski and J. Kneipp, "Relating surface-enhanced Raman scattering signals of cells to gold nanoparticle aggregation as determined by LA-ICP-MS micromapping", *Analytical and Bioanalytical Chemistry*, 2014, 406, 7003-7014.

169. A.A.O. Eggert, M.W.J. Schreurs, O.C. Boerman, W.J.C. Oyen, A.J. de Boer, C.J.A. Punt, C.G. Figdor and G.J. Adema, "Biodistribution and vaccine efficiency of murine dendritic cells are dependent on the route of administration", *Cancer Research*, 1999, 59, 3340-3345.

170. L. Waentig, N. Jakubowski, S. Hardt, C. Scheler, P.H. Roos and M.W. Linscheid, "Comparison of different chelates for lanthanide labeling of antibodies and application in a Western blot immunoassay combined with detection by laser ablation (LA-)ICP-MS", *Journal of Analytical Atomic Spectrometry*, 2012, 27, 1311-1320.

171. Fluidigm Corporation, "*Early Access Program for New Imaging Mass Cytometry Platform*", 2014, Available: http://www.fluidigm.com/press/july-31-2014, Last accessed: 10/09/14.

172. H.A.O. Wang, D. Grolimund, C. Giesen, C.N. Borca, J.R.H. Shaw-Stewart, B. Bodenmiller and D. Gunther, "Fast Chemical Imaging at High Spatial Resolution by Laser Ablation Inductively Coupled Plasma Mass Spectrometry", *Analytical Chemistry*, 2013, 85, 10107-10116.

173. C. Giesen, H.A.O. Wang, D. Schapiro, N. Zivanovic, A. Jacobs, B. Hattendorf, P.J. Schüffler, D. Grolimund, J.M. Buhmann, S. Brandt, Z. Varga, P.J. Wild, D. Günther and B. Bodenmiller, "Highly multiplexed imaging of tumor tissues with subcellular resolution by mass cytometry", *Nature Methods*, 2014, 11, 417-425.

174. I. Feldmann, C.U. Koehler, P.H. Roos and N. Jakubowski, "Optimisation of a laser ablation cell for detection of hetero-elements in proteins blotted onto membranes by use of inductively coupled plasma mass spectrometry", *Journal of Analytical Atomic Spectrometry*, 2006, 21, 1006-1015.

175. M.B. Fricker, D. Kutscher, B. Aeschlimann, J. Frommer, R. Dietiker, J. Bettmer and D. Gunther, "High spatial resolution trace element analysis by LA-ICP-MS using a novel ablation cell for multiple or large samples", *International Journal of Mass Spectrometry*, 2011, 307, 39-45.

176. J. Pisonero, D. Fliegel and D. Gunther, "High efficiency aerosol dispersion cell for laser ablation-ICP-MS", *Journal of Analytical Atomic Spectrometry*, 2006, 21, 922-931.

177. D. Asogan, B.L. Sharp, C.J.P. O'Connor, D.A. Green and R.W. Hutchinson, "An open, non-contact cell for laser ablation-inductively coupled plasma-mass spectrometry", *Journal of Analytical Atomic Spectrometry*, 2009, 24, 917-923.

178. H. Lindner, D. Autrique, C.C. Garcia, K. Niemax and A. Bogaerts, "Optimized Transport Setup for High Repetition Rate Pulse-Separated Analysis in Laser Ablation-Inductively Coupled Plasma Mass Spectrometry", *Analytical Chemistry*, 2009, 81, 4241-4248.

179. Y.S. Liu, Z.C. Hu, H.L. Yuan, S.H. Hu and H.H. Cheng, "Volume-optional and low-memory (VOLM) chamber for laser ablation-ICP-MS: application to fiber analyses", *Journal of Analytical Atomic Spectrometry*, 2007, 22, 582-585.

180. W. Muller, M. Shelley, P. Miller and S. Broude, "Initial performance metrics of a new custom-designed ArF excimer LA-ICPMS system coupled to a two-volume laser-ablation cell", *Journal of Analytical Atomic Spectrometry*, 2009, 24, 209-214.

181. E.L. Gurevich and R. Hergenroder, "A simple laser ICP-MS ablation cell with wash-out time less than 100 ms", *Journal of Analytical Atomic Spectrometry*, 2007, 22, 1043-1050.

182. D. Monticelli, E.L. Gurevich and R. Hergenroder, "Design and performances of a cyclonic flux cell for laser ablation", *Journal of Analytical Atomic Spectrometry*, 2009, 24, 328-335.

183. D. Bleiner and H. Altorfer, "A novel gas inlet system for improved aerosol entrainment in laser ablation inductively coupled plasma mass spectrometry", *Journal of Analytical Atomic Spectrometry*, 2005, 20, 754-756.

184. M. Tanner and D. Günther, "In torch laser ablation sampling for inductively coupled plasma mass spectrometry", *Journal of Analytical Atomic Spectrometry*, 2005, 20, 987-989.

185. D. Autrique, A. Bogaerts, H. Lindner, C.C. Garcia and K. Niemax, "Design analysis of a laser ablation cell for inductively coupled plasma mass spectrometry by numerical simulation", *Spectrochimica Acta Part B-Atomic Spectroscopy*, 2008, 63, 257-270.

186. X.R. Liu and G. Horlick, "In-situ laser ablation sampling for inductively coupled plasma atomic emission spectrometry", *Spectrochimica Acta Part B-Atomic Spectroscopy*, 1995, 50, 537-548.

187. D. Douglas, "Development of a high speed, high efficiency LA-ICP-MS interface", Ph.D. Thesis, Loughborough University, 2013.

188. H. Lindner, A. Murtazin, S. Groh, K. Niemax and A. Bogaerts, "Simulation and Experimental Studies on Plasma Temperature, Flow Velocity, and Injector Diameter Effects for an Inductively Coupled Plasma", *Analytical Chemistry*, 2011, 83, 9260-9266.

189. M. Aghaei, L. Flamigni, H. Lindner, D. Gunther and A. Bogaerts, "Occurrence of gas flow rotational motion inside the ICP torch: a computational and experimental study", *Journal of Analytical Atomic Spectrometry*, 2014, 29, 249-261.

190. D. Asogan, B.L. Sharp, C.J.P. O'Connor, D.A. Green and J. Wilkins, "Numerical simulations of gas flows through an open, non-contact cell for LA-ICP-MS", *Journal of Analytical Atomic Spectrometry*, 2011, 26, 631-634.

191. D. Bleiner and A. Bogaerts, "Computer simulations of sample chambers for laser ablation-inductively coupled plasma spectrometry", *Spectrochimica Acta Part B-Atomic Spectroscopy*, 2007, 62, 155-168.

192. DSS, Solid Works Flow Simulation 2011: Technical Reference, Dassault Systems, 2011.

193. S.J.M. Van Malderen, J.T. van Elteren and F. Vanhaecke, "Development of a fast laser ablation-inductively coupled plasma-mass spectrometry cell for sub-µm scanning of layered materials", *Journal of Analytical Atomic Spectrometry*, 2014, DOI: 10.1039/c4ja00137k.

194. M. Tanner and D. Günther, "Signal acquisition in µs time resolution for in-torch LA-ICP-MS", *Journal of Analytical Atomic Spectrometry*, 2007, 22, 1189-1192.

195. O. Borovinskaya, M. Aghaei, L. Flamigni, B. Hattendorf, M. Tanner, A. Bogaerts and D. Günther, "Diffusion- and velocity-driven spatial separation of analytes from single droplets entering an ICP off-axis", *Journal of Analytical Atomic Spectrometry*, 2014, 29, 262-271.

196. D. Bleiner and D. Gunther, "Theoretical description and experimental observation of aerosol transport processes in laser ablation inductively coupled plasma mass spectrometry", *Journal of Analytical Atomic Spectrometry*, 2001, 16, 449-456.

197. Analytical Methods Committee, "*Robust statistics: a method of coping with outliers*", 2001, Available: www.rsc.org/images/robust-statistics-technical-brief-6_tcm18-214850.pdf, Last accessed: 07/11/13.

198. S.-i. Miyashita, A.S. Groombridge, S.-i. Fujii, A. Minoda, A. Takatsu, A. Hioki, K. Chiba and K. Inagaki, "Highly efficient single-cell analysis of microbial cells by time-resolved inductively-coupled plasma mass spectrometry", *Journal of Analytical Atomic Spectrometry*, 2014, 29, 1598-1606.

199. M. Tanner and D. Günther, "A new ICP-TOFMS. Measurement and readout of mass spectra with 30 µs time resolution, applied to in-torch LA-ICP-MS", *Analytical and Bioanalytical Chemistry*, 2008, 391, 1211-1220.

200. O. Borovinskaya, B. Hattendorf, M. Tanner, S. Gschwind and D. Günther, "A prototype of a new inductively coupled plasma time-of-flight mass spectrometer providing temporally resolved, multi-element detection of short signals

generated by single particles and droplets", *Journal of Analytical Atomic Spectrometry*, 2013, 28, 226-233.

201. O. Borovinskaya, S. Gschwind, B. Hattendorf, M. Tanner and D. Günther, "Simultaneous Mass Quantification of Nanoparticles of Different Composition in a Mixture by Microdroplet Generator-ICPTOFMS", *Analytical Chemistry*, 2014, 86, 8142-8148.

202. B.L. Sharp, D.N. Douglas and A.J. Managh, Electro Scientific Industries Inc., "Laser ablation cell and torch system for a compositional analysis system", World patent, 2014, WO 2014/127034 A1.

203. C. Cabella, S.G. Crich, D. Corpillo, A. Barge, C. Ghirelli, E. Bruno, V. Lorusso, F. Uggeri and S. Aime, "Cellular labeling with Gd(III) chelates: only high thermodynamic stabilities prevent the cells acting as 'sponges' of Gd3+ ions", *Contrast Media & Molecular Imaging*, 2006, 1, 23-29.

204. S. Aime and P. Caravan, "Biodistribution of Gadolinium-Based Contrast Agents, Including Gadolinium Deposition", *Journal of Magnetic Resonance Imaging*, 2009, 30, 1259–1267.

205. M. Longmire, P.L. Choyke and H. Kobayashi, "Clearance Properties of Nano-sized Particles and Molecules as Imaging Agents: Considerations and Caveats", *Nanomedicine*, 2008, 3, 703–717.

206. G. Craig, M.S.A. Horstwood, H.J. Reid, R.R. Parrish and B.L. Sharp, "Isotope ratio analysis of sub-micron uranium particles with an ultrafast washout laser ablation cell coupled to MC-ICP-MS", Paper presented at the 12th European Workshop on Laser Ablation, London, UK, 8-11th July, 2014.

7 Appendix

7.1 Appendix 1 – Supplementary FACS data for Chapter 2

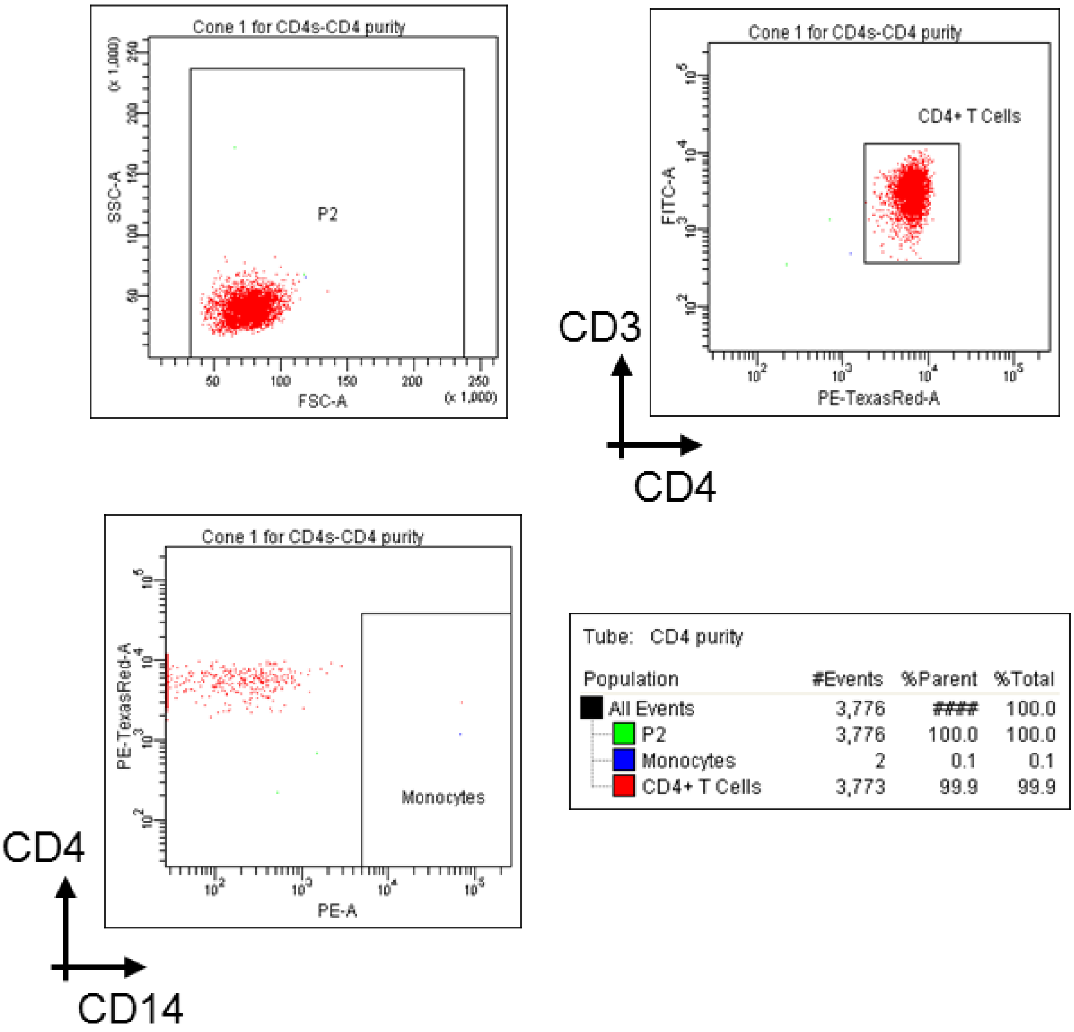

Tube: CD4 purity

Population	#Events	%Parent	%Total
■ All Events	3,776	####	100.0
🟩 P2	3,776	100.0	100.0
🟦 Monocytes	2	0.1	0.1
🟥 CD4+ T Cells	3,773	99.9	99.9

Figure 7.1 Example FACS plots obtained prior to labelling CD4+ T cells with Omniscan. Human CD4$^+$ cells were isolated to high purity by flow sorting and analysed for final CD3+CD4+ T cell purity and CD14 monocyte contamination. Monocytes represented approximately 0.1% of the cells subjected to gadolinium solution analysis. Data shown are representative of isolations from three individual cell donors. Figure courtesy of Andrew Bushell.

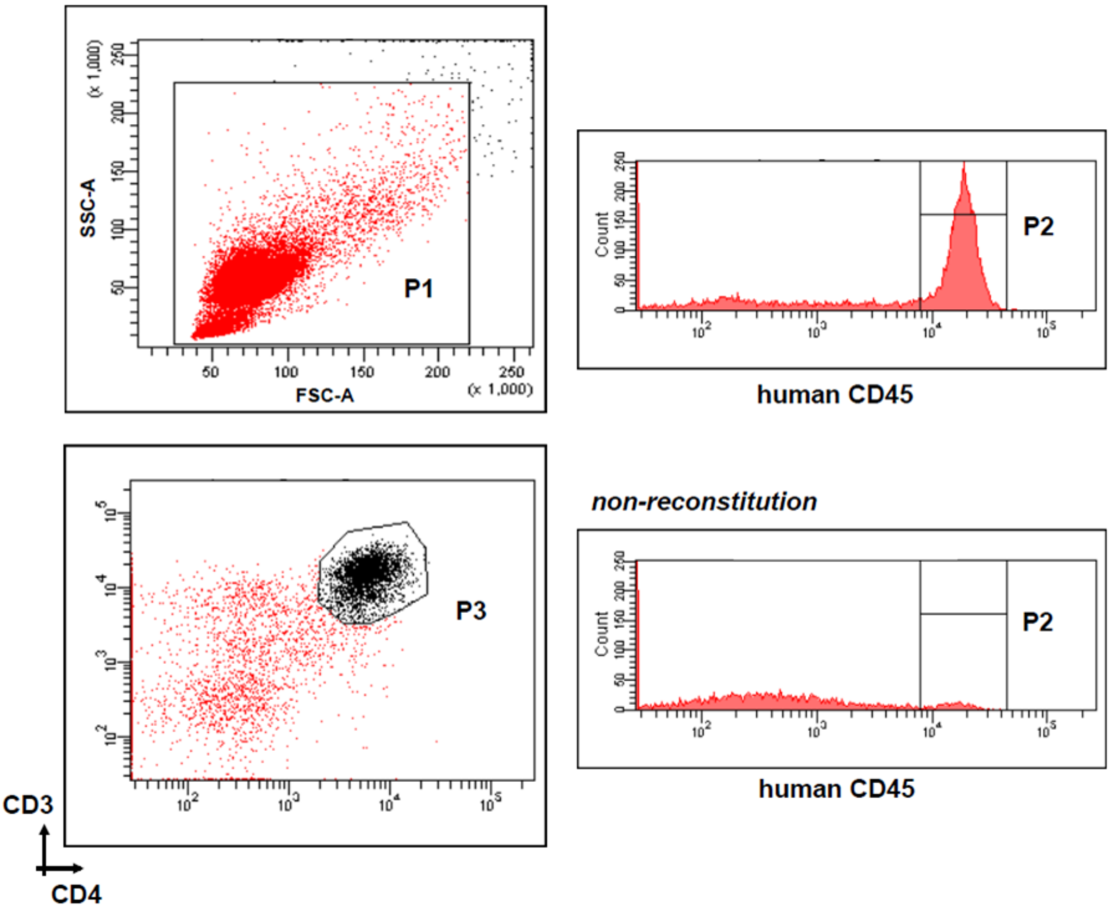

Figure 7.2 Example FACS plots from the in vivo mouse studies reported in Chapter 2. Human CD4$^+$ T cells were labelled with Omniscan, washed extensively and administered intraperitonealy (2x10^6) to BALB/c immunodeficient mice, together with 3x10^6 autologous PBMC. Peritoneal lavage samples were collected for flow cytometry (see above) and LA-ICP-MS (see Chapter 2) analysis.
Day 6 lavage data: one of three mice shown. Top left panel: leucocyte gate. Top right panel: readily detected human CD45$^+$ cells (P2 gate). Bottom left panel: human CD3$^+$CD4$^+$ T cells within the gated CD45$^+$ population confirming CD4$^+$ T cell reconstitution. For comparison, the bottom right panel shows another of the three mice with no evidence of human cell reconstitution. Figure courtesy of Andrew Bushell.

7.2 Appendix 2 – Supplementary Figures for Chapter 4

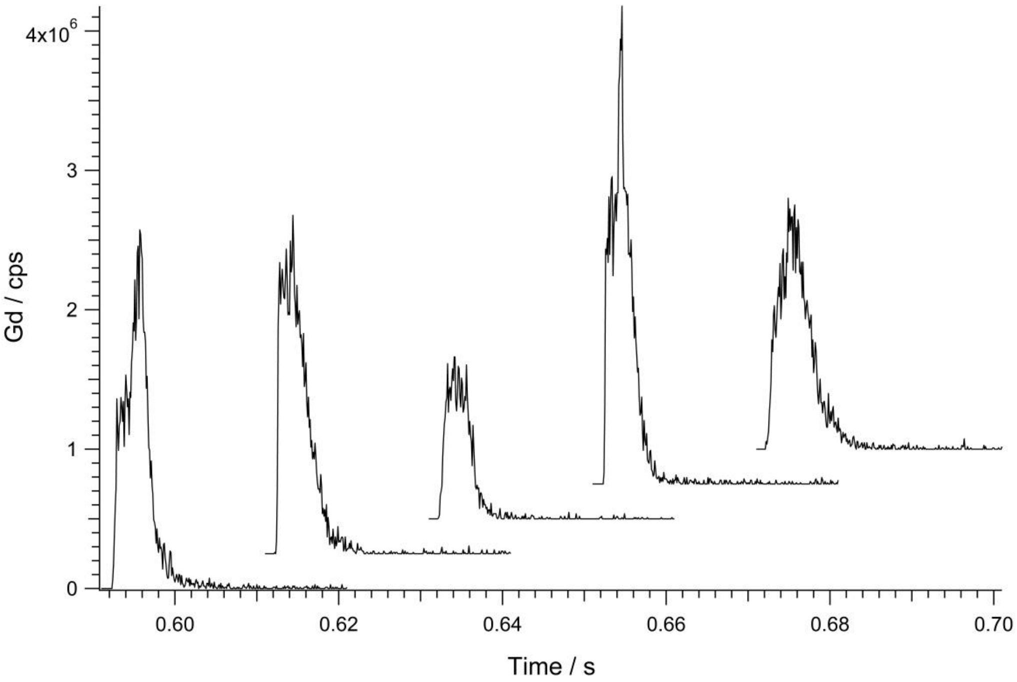

Figure 7.3 Peak profiles from of 5 individual Gd labelled cells that were ablated using the Enterprise cell, with the fused silica outlet level with the tip of the injector. Signals are offset by 200 ms in the x direction and 2.5 x 10^5 cps in the y direction.

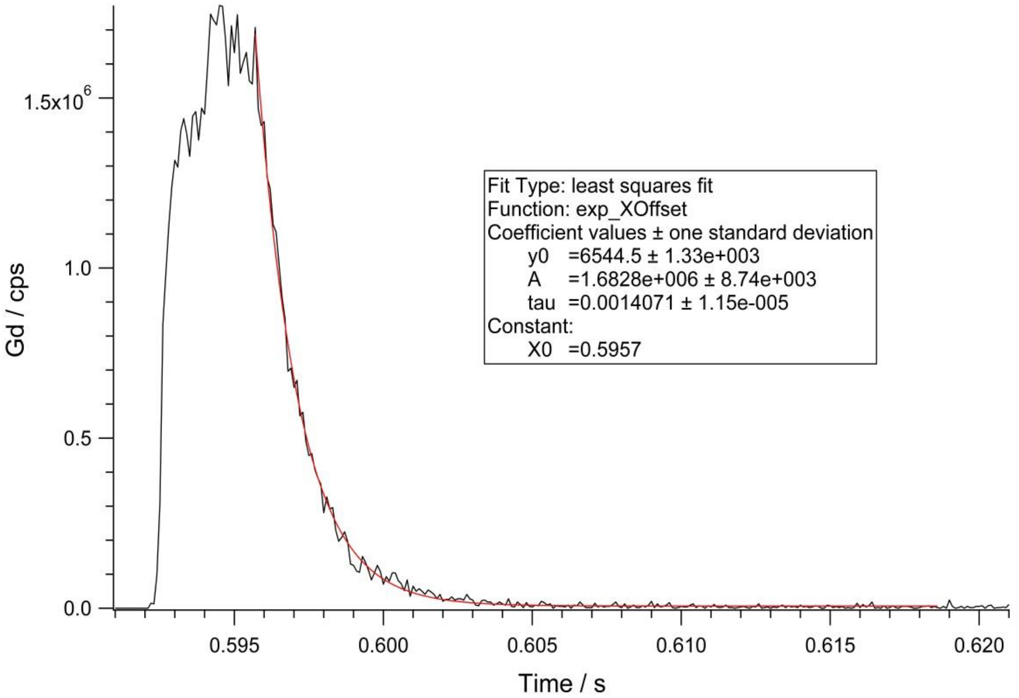

Figure 7.4 The averaged peak profile obtained for five Gd labelled cells using the Enterprise cell, with the fused silica outlet level with the tip of the injector.

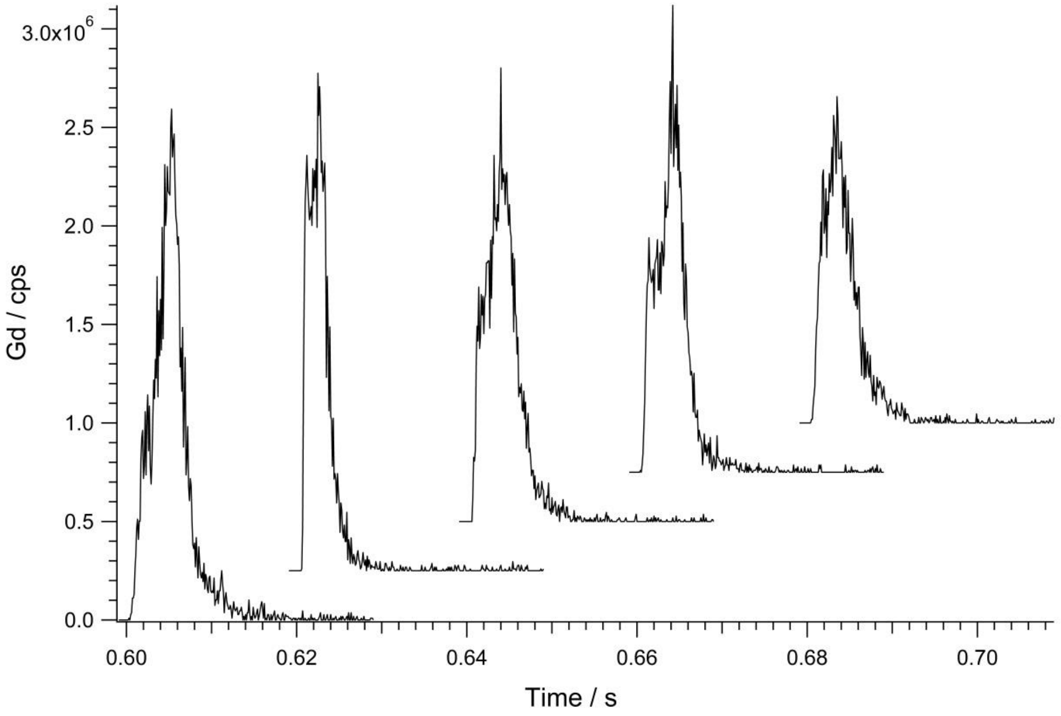

Figure 7.5 Peak profiles from of 5 individual Gd labelled cells that were ablated using the Enterprise cell, with the fused silica extended 1 mm past the tip of the injector. Signals are offset by 200 ms in the x direction and 2.5 x 10^5 cps in the y direction to aid comparison.

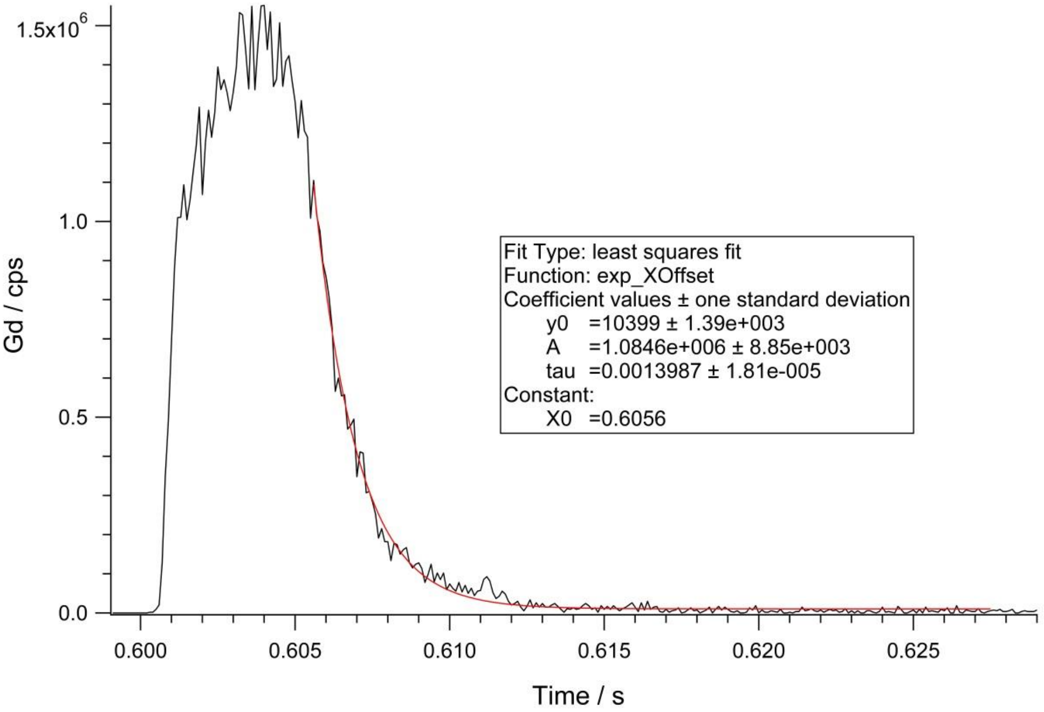

Figure 7.6 The averaged peak profile obtained for five Gd labelled cells using the Enterprise cell, with a fused silica extension of 1 mm past the tip of the injector.

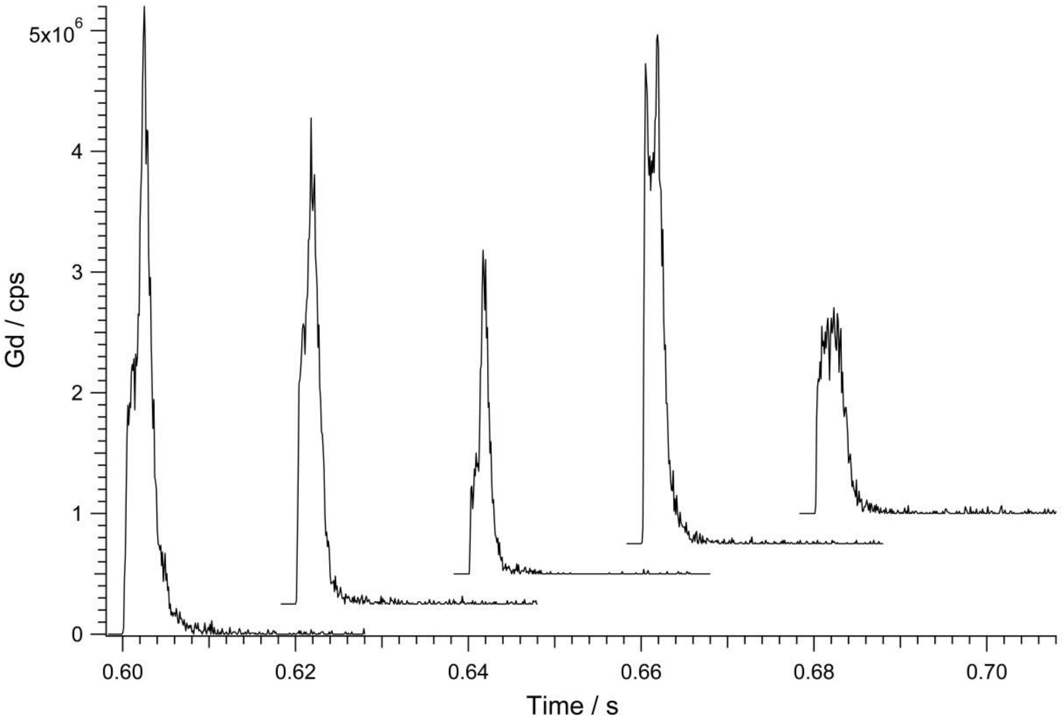

Figure 7.7 Peak profiles from of five individual Gd labelled cells that were ablated using the Enterprise cell, with the fused silica extended 2 mm past the tip of the injector. Signals are offset by 200 ms in the x direction and 2.5 x 10^5 cps in the y direction to aid comparison.

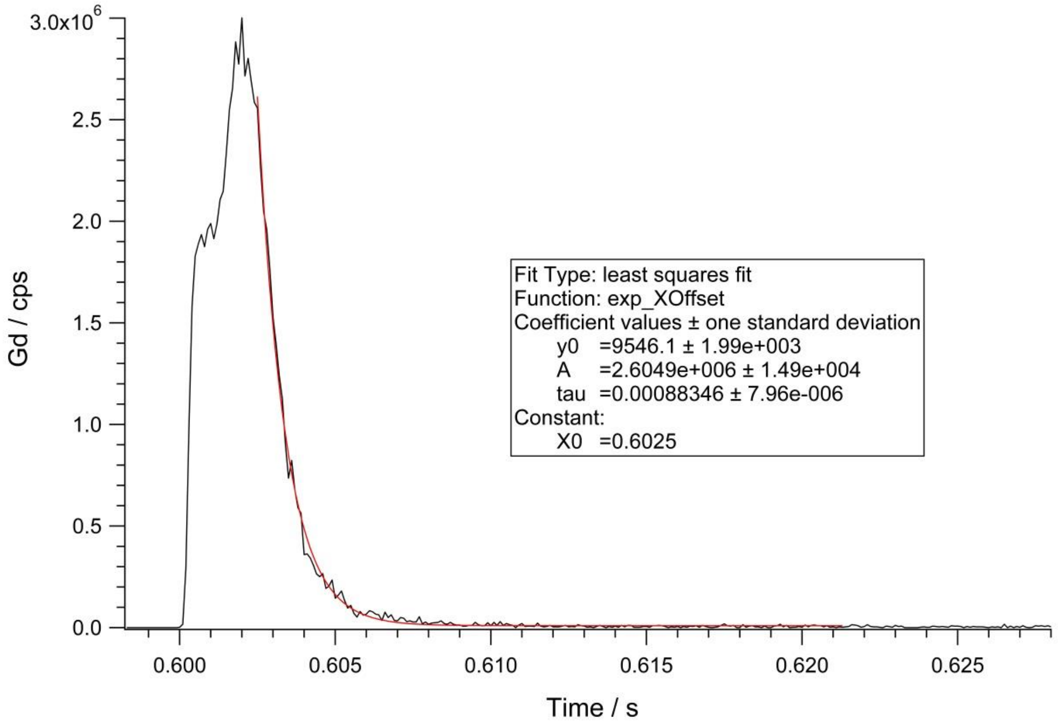

Figure 7.8 The averaged peak profile obtained for five Gd labelled cells using the Enterprise cell, with a fused silica extension of 2 mm past the tip of the injector.

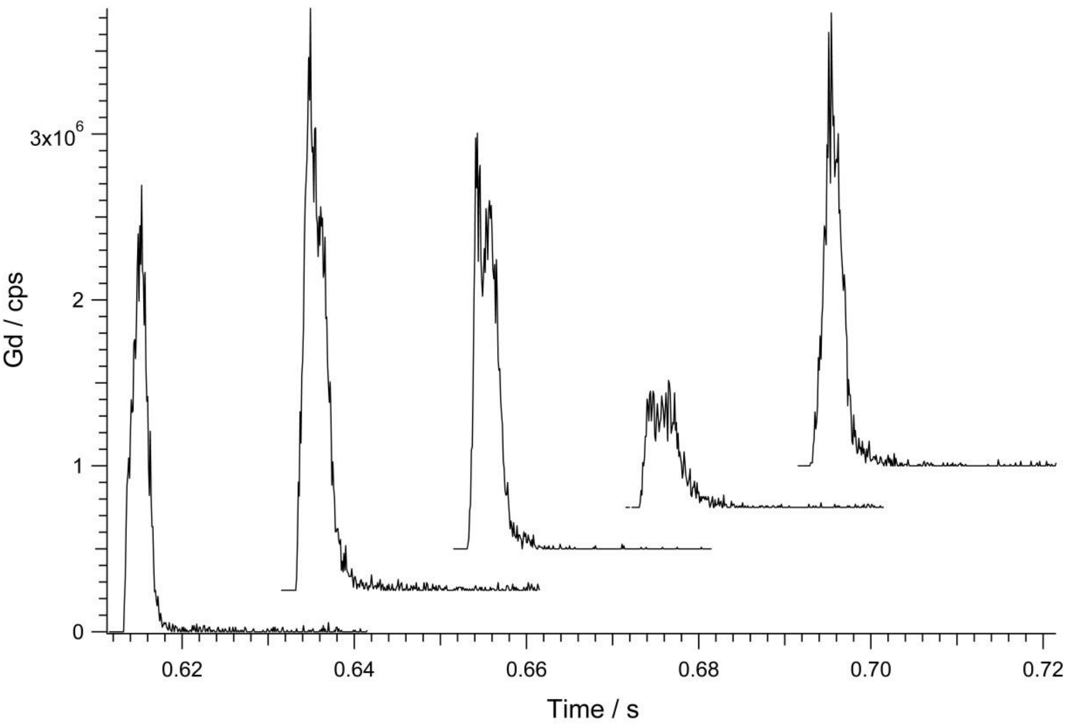

Figure 7.9 Peak profiles from of five individual Gd labelled cells that were ablated using the Enterprise cell, with the fused silica extended 3 mm past the tip of the injector. Signals are offset by 200 ms in the x direction and 2.5 x 10^5 cps in the y direction to aid comparison.

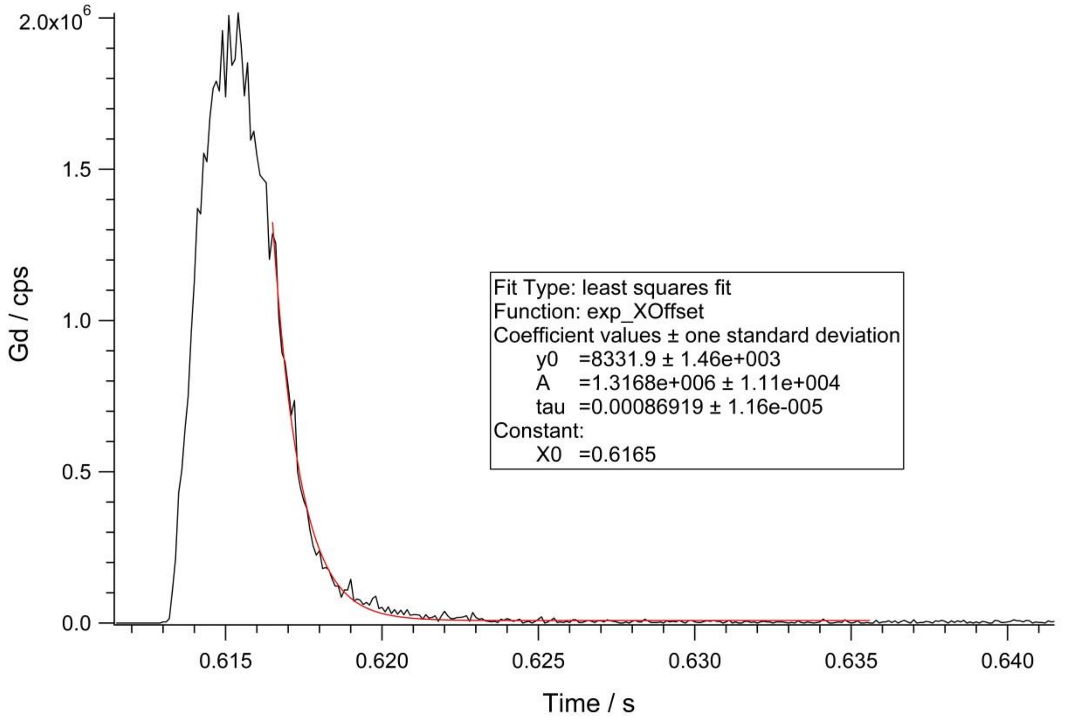

```
Fit Type: least squares fit
Function: exp_XOffset
Coefficient values ± one standard deviation
      y0   =8331.9 ± 1.46e+003
      A    =1.3168e+006 ± 1.11e+004
      tau  =0.00086919 ± 1.16e-005
Constant:
      X0   =0.6165
```

Figure 7.10 The averaged peak profile obtained for five Gd labelled cells using the Enterprise cell, with a fused silica extension of 3 mm past the tip of the injector.

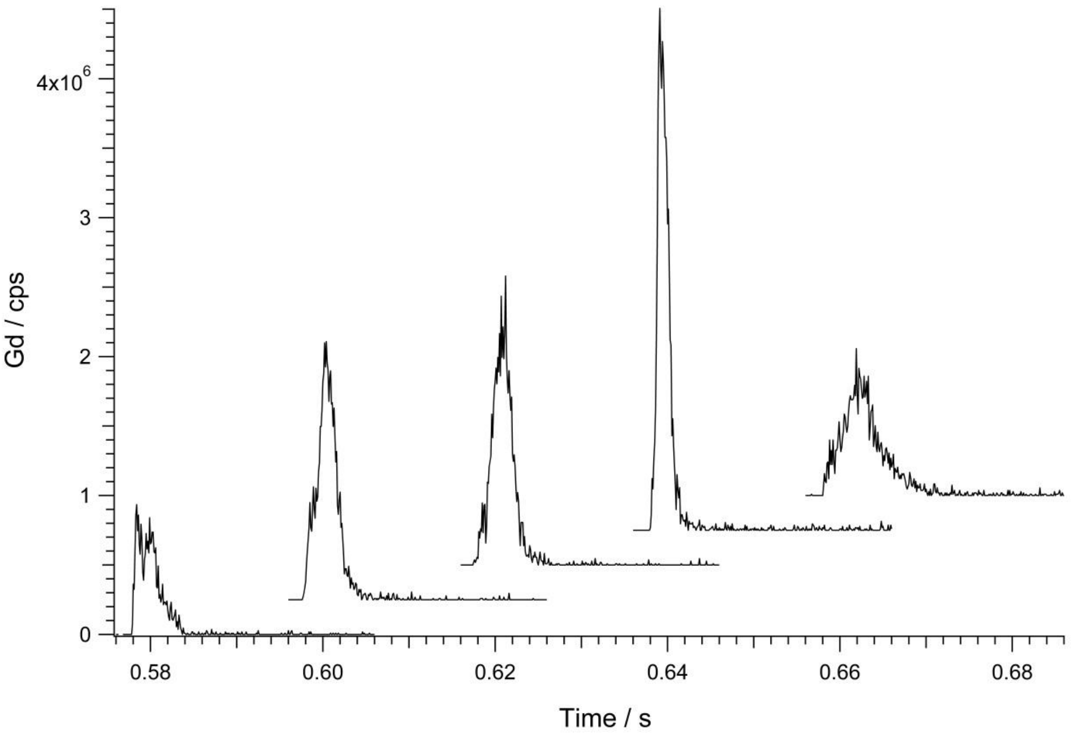

Figure 7.11 Peak profiles from of five individual Gd labelled cells that were ablated using the Enterprise cell, with the fused silica extended 4 mm past the tip of the injector. Signals are offset by 200 ms in the x direction and 2.5 x 10^5 cps in the y direction to aid comparison.

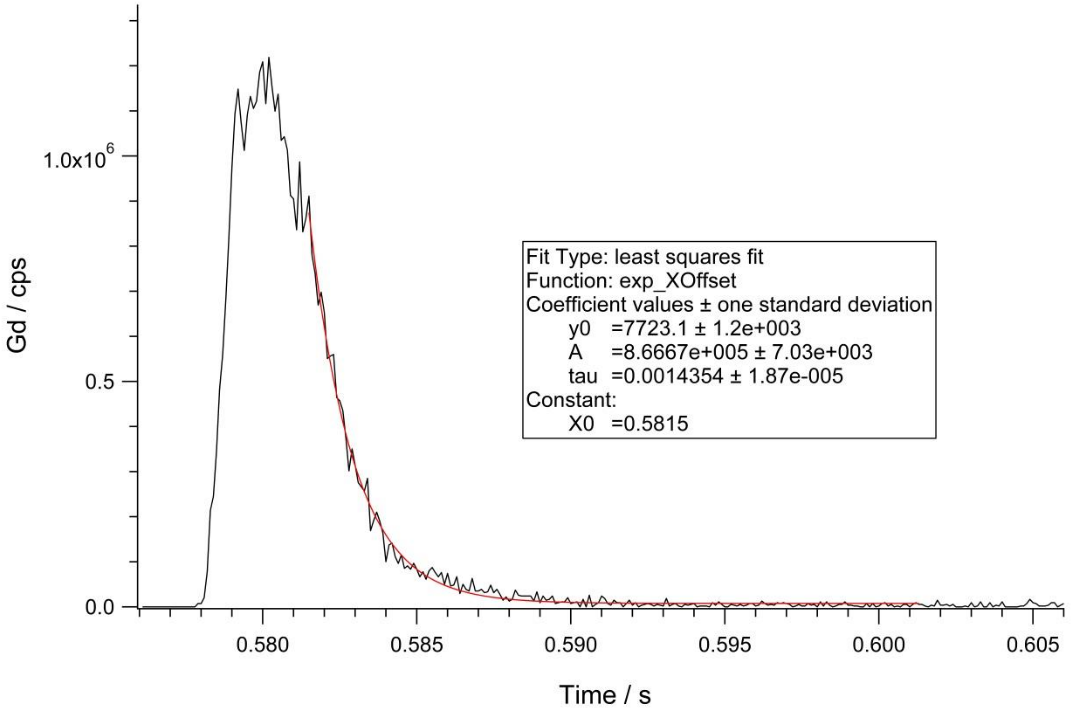

Fit Type: least squares fit
Function: exp_XOffset
Coefficient values ± one standard deviation
y0 =7723.1 ± 1.2e+003
A =8.6667e+005 ± 7.03e+003
tau =0.0014354 ± 1.87e-005
Constant:
X0 =0.5815

Figure 7.12 The averaged peak profile obtained for five Gd labelled cells using the Enterprise cell, with a fused silica extension of 4 mm past the tip of the injector.

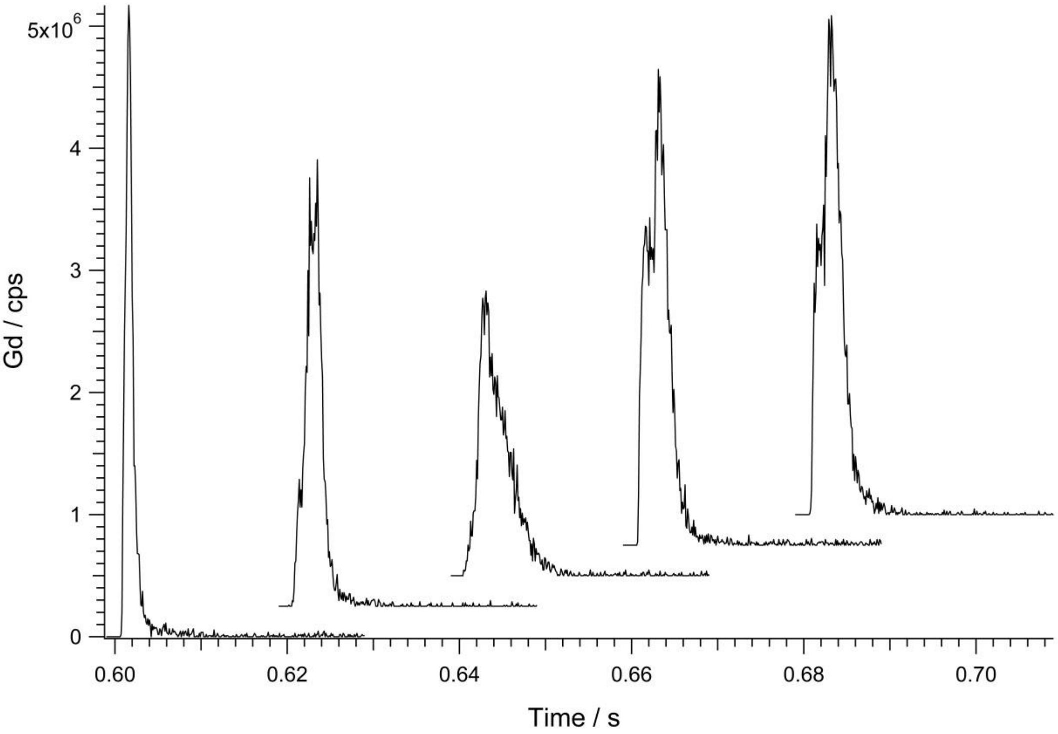

Figure 7.13 Peak profiles from of five individual Gd labelled cells that were ablated using the Enterprise cell, with the fused silica extended 6 mm past the tip of the injector. Signals are offset by 200 ms in the x direction and 2.5 x 10^5 cps in the y direction to aid comparison.

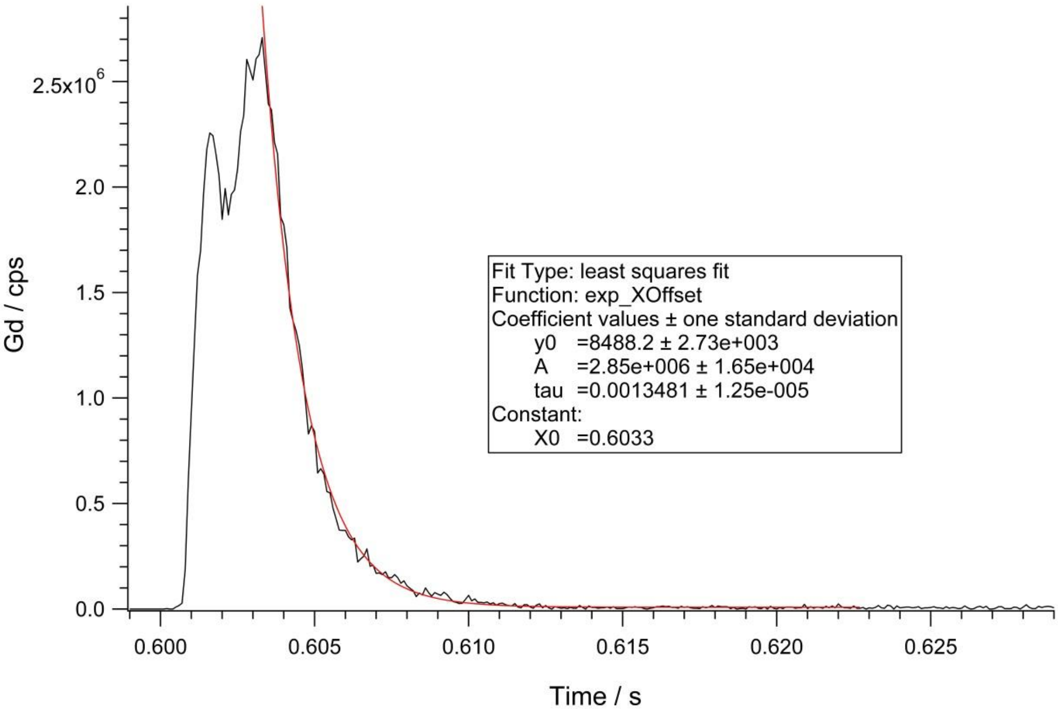

Figure 7.14 The averaged peak profile obtained for five Gd labelled cells using the Enterprise cell, with a fused silica extension of 6 mm past the tip of the injector.

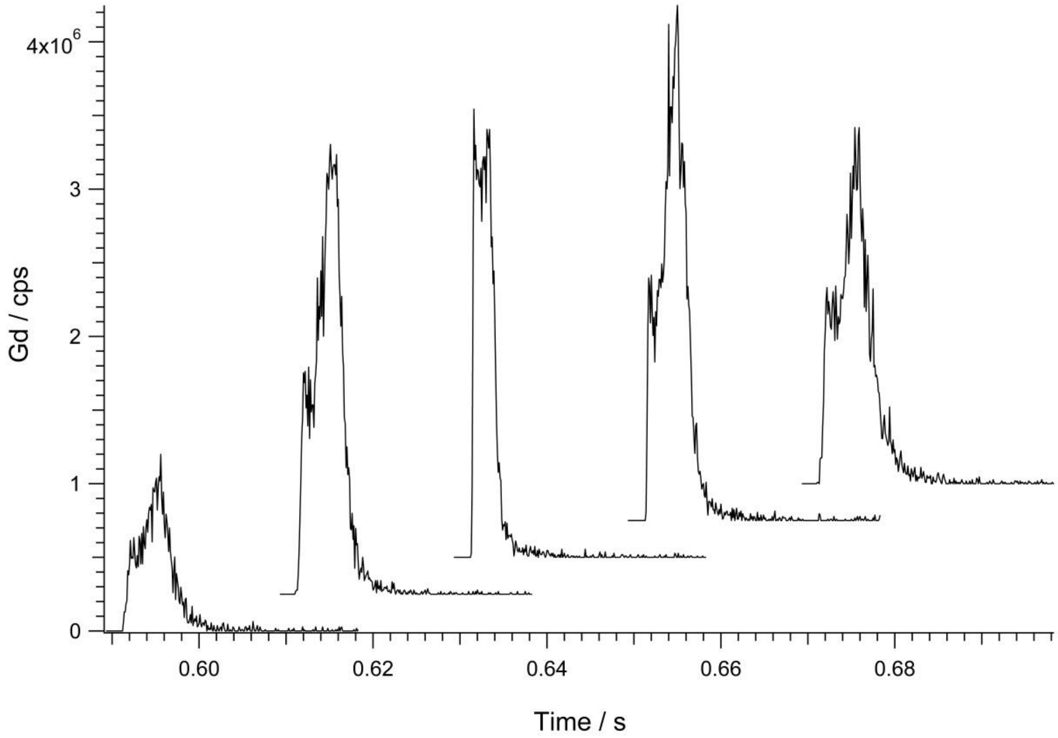

Figure 7.15 Peak profiles from of five individual Gd labelled cells that were ablated using the Enterprise cell, with the fused silica extended 8 mm past the tip of the injector. Signals are offset by 200 ms in the x direction and 2.5 x 10^5 cps in the y direction to aid comparison.

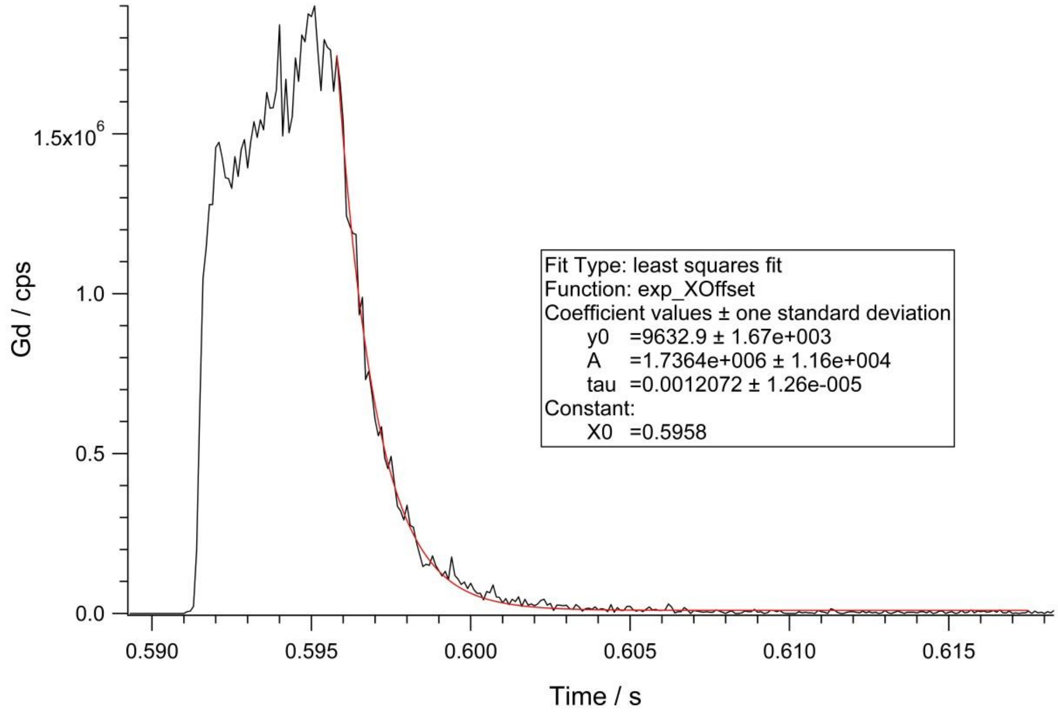

Figure 7.16 The averaged peak profile obtained for five Gd labelled cells using the Enterprise cell, with a fused silica extension of 8 mm past the tip of the injector.

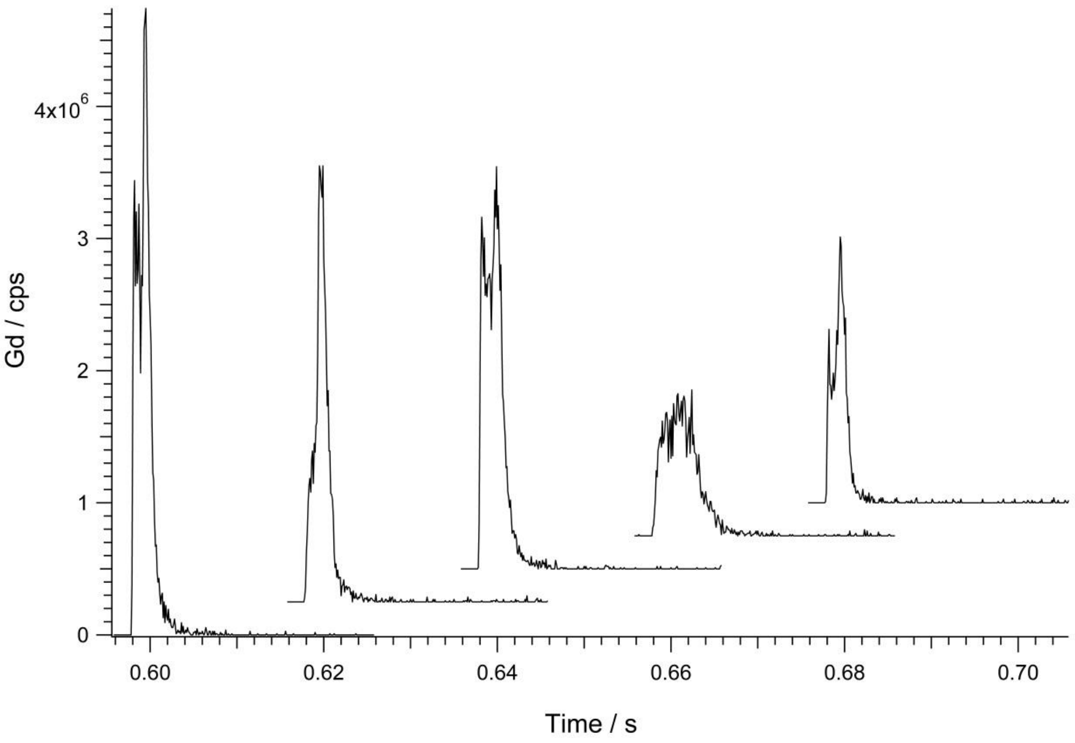

Figure 7.17 Peak profiles from of five individual Gd labelled cells that were ablated using the Enterprise cell, with the fused silica extended 10 mm past the tip of the injector. Signals are offset by 200 ms in the x direction and 2.5 x 10^5 cps in the y direction to aid comparison.

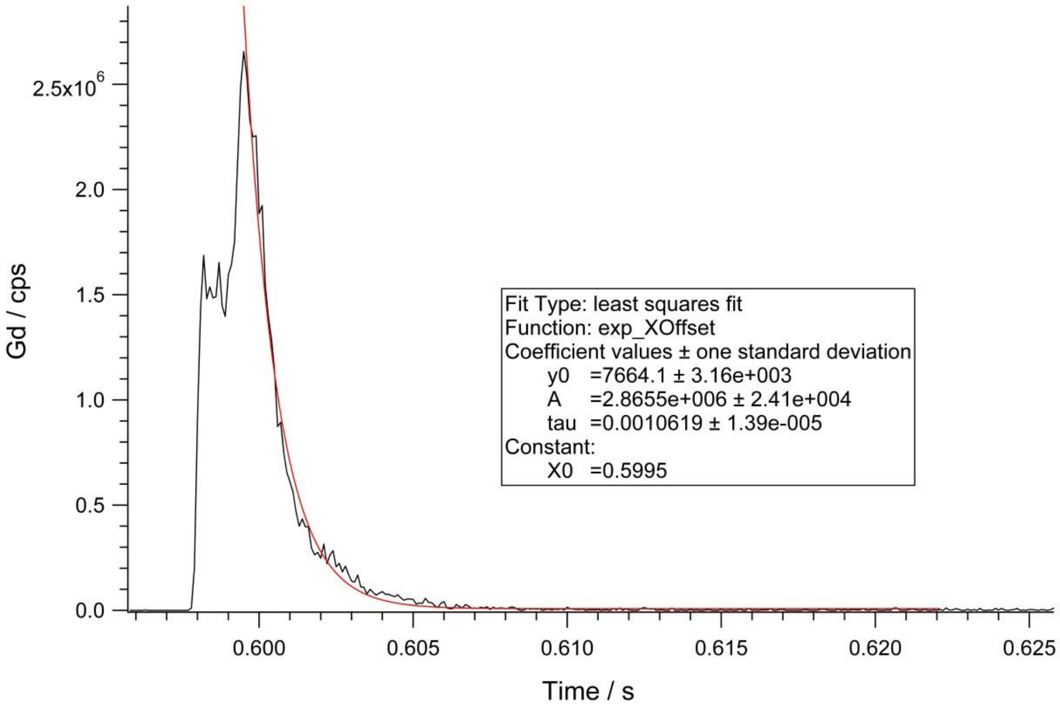

Figure 7.18 The averaged peak profile obtained for five Gd labelled cells using the Enterprise cell, with a fused silica extension of 10 mm past the tip of the injector.

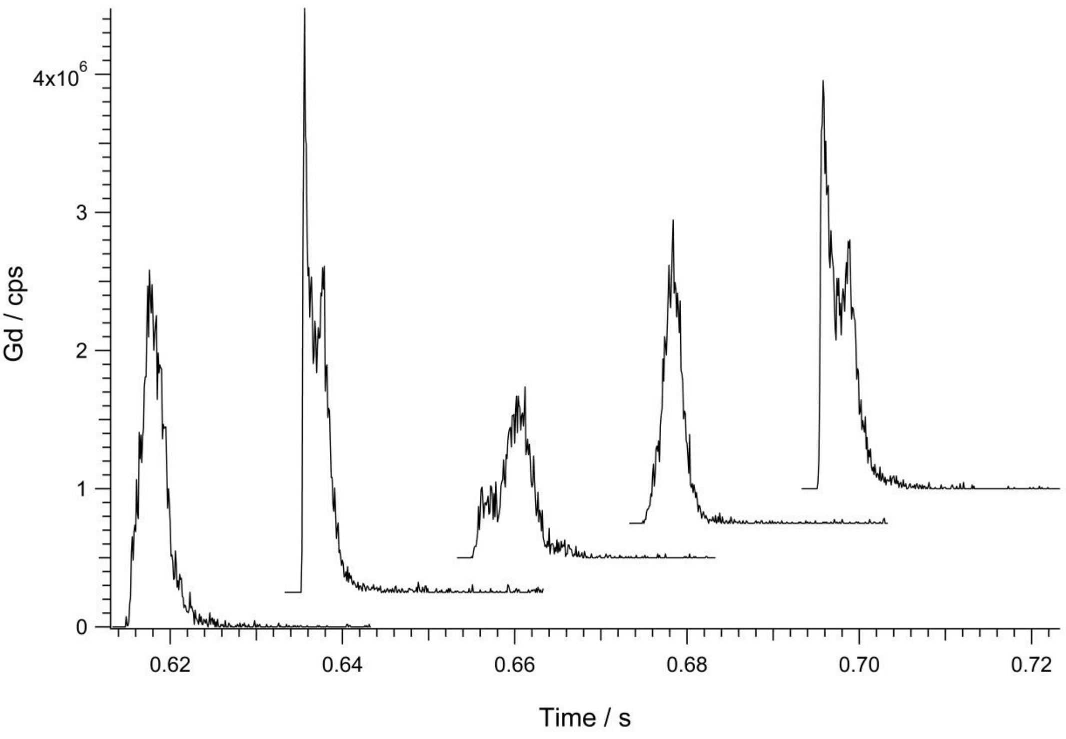

Figure 7.19 Peak profiles from of five individual Gd labelled cells that were ablated using the Enterprise cell, with the fused silica extended 12 mm past the tip of the injector. Signals are offset by 200 ms in the x direction and 2.5 x 10^5 cps in the y direction to aid comparison.

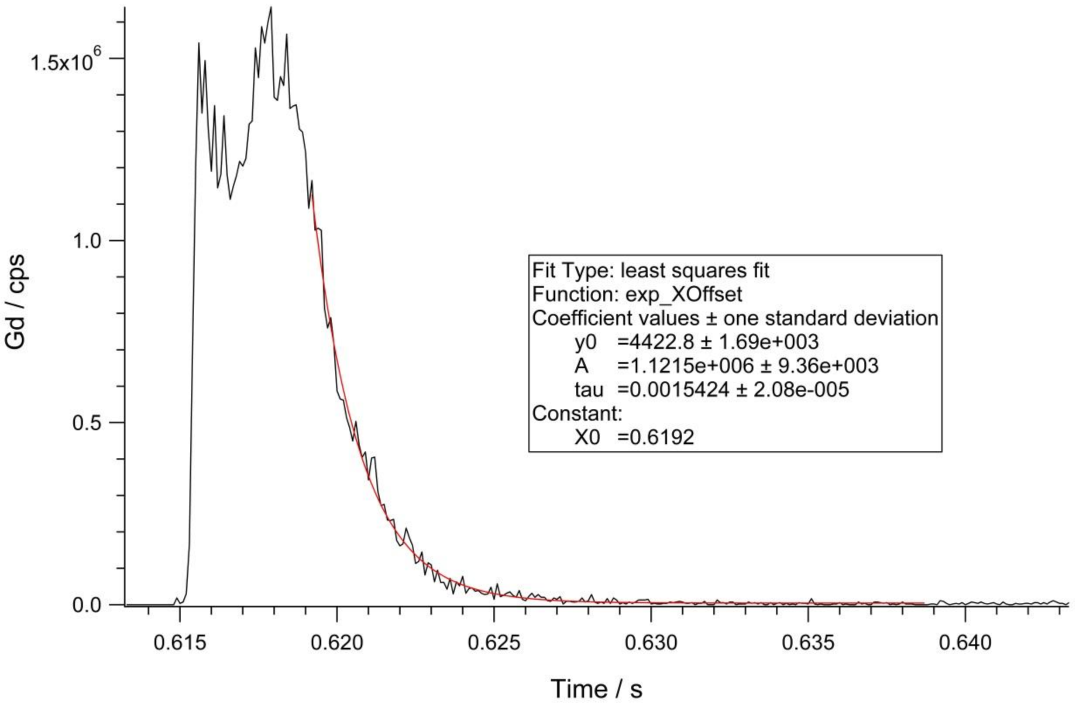

```
Fit Type: least squares fit
Function: exp_XOffset
Coefficient values ± one standard deviation
      y0   =4422.8 ± 1.69e+003
      A    =1.1215e+006 ± 9.36e+003
      tau  =0.0015424 ± 2.08e-005
Constant:
      X0   =0.6192
```

Figure 7.20 The averaged peak profile obtained for five Gd labelled cells using the Enterprise cell, with a fused silica extension of 12 mm past the tip of the injector.

7.3 Appendix 3 – Supplementary CAD drawings for Chapter 4

The technical drawings for the components used to construct the Enterprise cell are listed below and provided in the following pages.

	Technical drawing	Purpose of component	Page
Basic cell	Optical window holder	To lock the optical window securely in place	151
	Top of the cell	To maintain pressure inside the cell and exclude atmospheric gases.	152
	Middle of the cell	To maintain pressure inside the cell, exclude atmospheric gases and to allow entry of the carrier gas and exit of the ablated material.	154
	Bar for Sniffer	To support the Sniffer parallel to the sample and at a fixed distance above its surface.	157
	Bracket	To connect the cell to the UP-213 (via a 3-axis manual movement stage).	158
	Bracket	To connect the cell to the UP-213 (via a 3-axis manual movement stage).	159
Magnetic coupling	Sample holder	To accommodate 1 mm thick slides of up to 25 x 25 mm in size.	161
	Cage for rotary bearing	To accommodate a set of magnets (for movement of the sample) and to connect the rotary bearing to the sample holder (for smoothness in movement).	162
	Base of the cell	To maintain pressure inside the cell, exclude atmospheric gases and to provide a smooth running surface for the rotary bearing.	164
	Lower magnet holder	To accommodate a set of magnets, which align with those inside the cell to enable sample movement.	166
	Magnet attachment plate	To connect the magnet holder to the 2-axis movement stage on the UP-213 and hence enable computer controlled movement of the sample.	167
O-ring design	Base of the cell	To maintain pressure inside the cell and exclude atmospheric gases, whilst enabling physical coupling to a 2-axis movement stage located outside of the cell.	168
	Sample holder	To accommodate 1 mm thick slides of up to 25 x 25 mm in size, and to provide a gas tight seal onto the base of the cell.	170
	Supporting block	To prevent the joining screw from flexing during movement.	171
	Movement plate	To connect the sample holder to the 2-axis movement stage on the UP-213 and to lubricate the o-rings, in order to enable computer controlled sample movement with low friction.	172

ITEM NO.	PART NUMBER	QTY.
1	Optical window holder	1
2	30 x 3 mm optical window	1
3	Top of the cell	1
4	Middle of the cell	1
5	Bar for sniffer	1
6	Sniffer V9.2	1
7	0.5 mm o.d. fused silica tube	1
8	Male 1/16" Connector (O-seal Straight Thread 5/16-24UNF1/16")	2
9	Male 1/8" Connector (O-seal Straight Thread 5/16-24UNF1/16")	2
10	Sample holder	1
11	Cage for bearing	1
12	Macor running plate	1
13	Base of the cell	1
14	xyz stage to UP213 bracket	1
15	xyz axis to cell bracket	1
16	Magnet holder	1
17	Magnet attachment plate	1

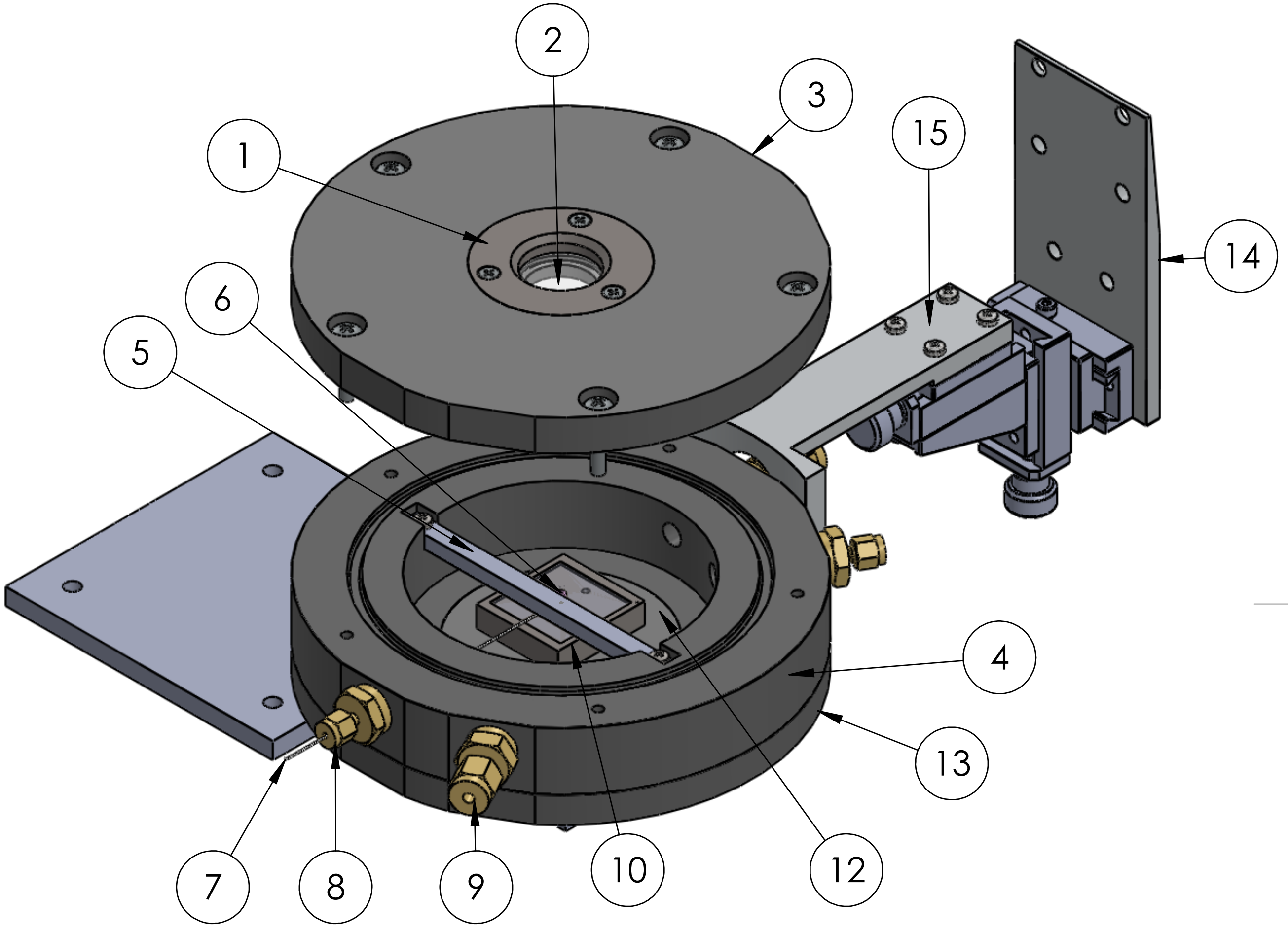

UNLESS OTHERWISE SPECIFIED:
DIMENSIONS ARE IN MILLIMETERS
SURFACE FINISH:
TOLERANCES:
LINEAR:
ANGULAR:

FINISH:

DEBUR AND
BREAK SHARP
EDGES

DO NOT SCALE DRAWING

REVISION

Loughborough University

	NAME	SIGNATURE	DATE
DRAWN	Amy Managh		29/02/12
CHK'D			
APPV'D			
MFG			
Q.A			

TITLE:

Enterprise cell assembly

MATERIAL:

DWG NO.

A4

WEIGHT:

SCALE:1:5

SHEET 1 OF 1

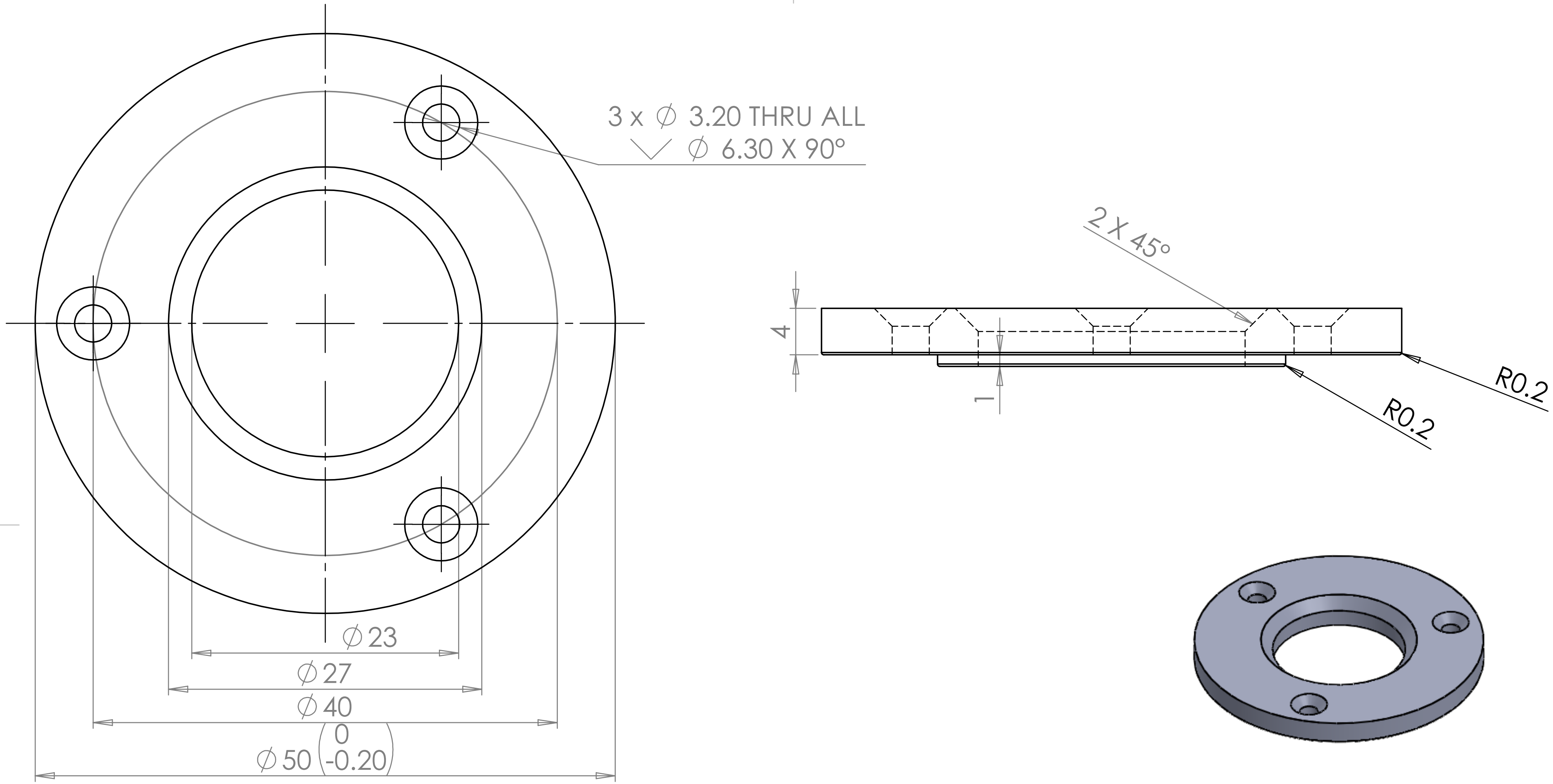

UNLESS OTHERWISE SPECIFIED: DIMENSIONS ARE IN MILLIMETERS SURFACE FINISH: TOLERANCES (UNLESS STATED): LINEAR: ±0.2 ANGULAR: ±0.1°	FINISH:		DEBUR AND BREAK SHARP EDGES	DO NOT SCALE DRAWING	REVISION
	NAME	SIGNATURE	DATE	Loughborough University	
DRAWN	Amy Managh		28/02/12	TITLE:	
CHK'D				Optical window holder	
APPV'D					
MFG					
Q.A			MATERIAL: Delrin	DWG NO.	A4
			WEIGHT:	SCALE: 2:1	SHEET 1 OF 1

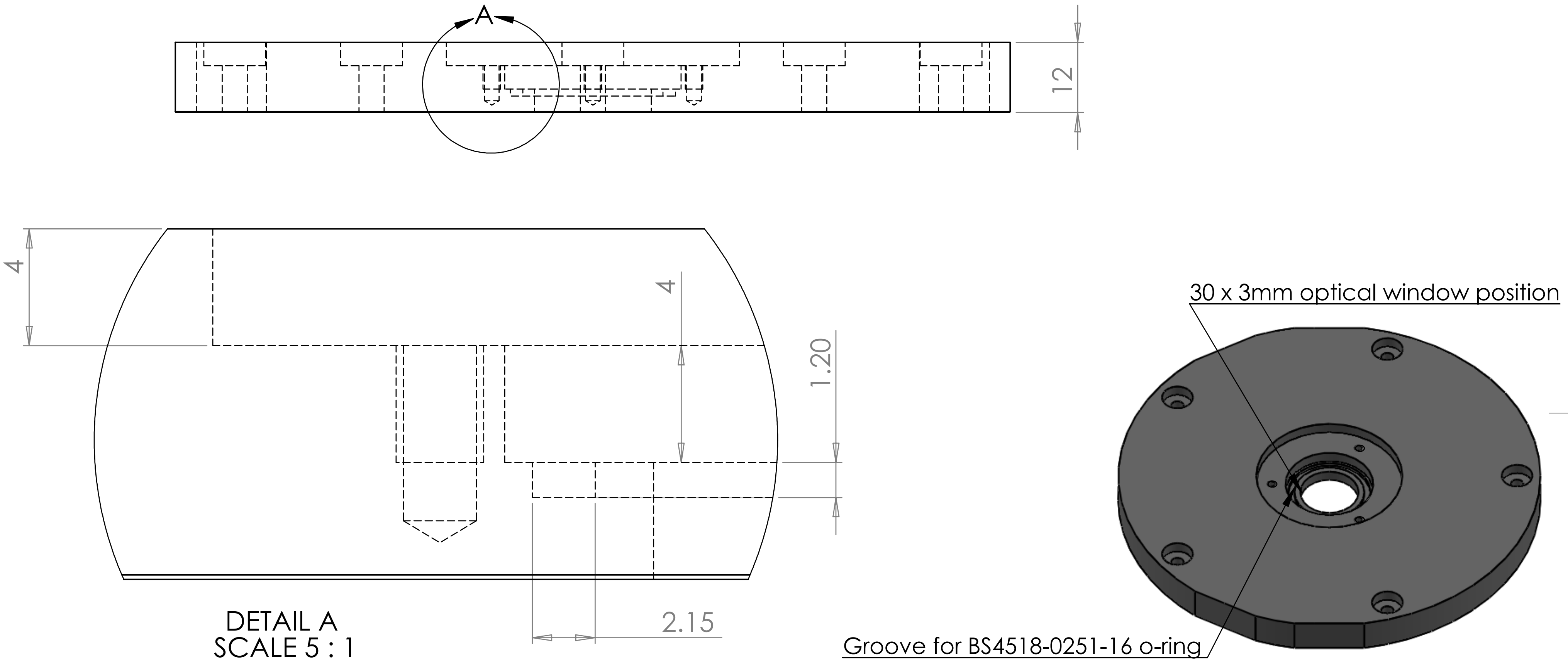

UNLESS OTHERWISE SPECIFIED: DIMENSIONS ARE IN MILLIMETERS SURFACE FINISH: TOLERANCES (UNLESS STATED): LINEAR: ±0.2 ANGULAR: ±0.1°	FINISH:	DEBUR AND BREAK SHARP EDGES	DO NOT SCALE DRAWING	REVISION
			Loughborough University	

	NAME	SIGNATURE	DATE
DRAWN	Amy Managh		28/02/12
CHK'D			
APPV'D			
MFG			
Q.A			

TITLE:

Top of the cell

MATERIAL: Delrin

DWG NO.

A4

WEIGHT:

SCALE: 1:1

SHEET 1 OF 2

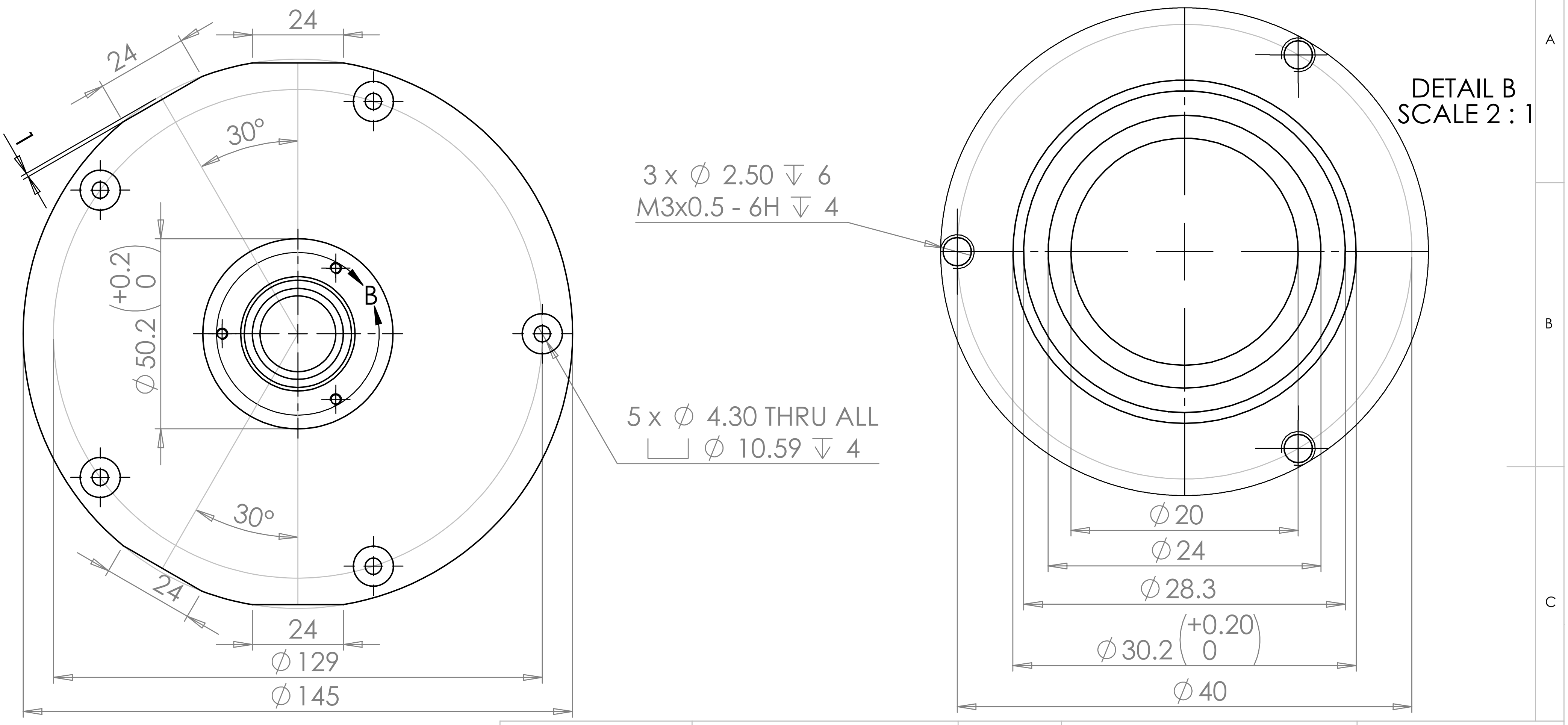

UNLESS OTHERWISE SPECIFIED: DIMENSIONS ARE IN MILLIMETERS SURFACE FINISH: TOLERANCES (UNLESS STATED): LINEAR: ±0.2 ANGULAR: ±0.1°	FINISH:		DEBUR AND BREAK SHARP EDGES	DO NOT SCALE DRAWING / REVISION Loughborough University
	NAME	SIGNATURE	DATE	TITLE:
DRAWN	Amy Managh		28/02/12	Top of the cell
CHK'D				
APPV'D				
MFG				
Q.A			MATERIAL: Delrin	DWG NO. A4
			WEIGHT:	SCALE: 2:1 / SHEET 2 OF 2

SolidWorks Educational Edition.
For Instructional Use Only.

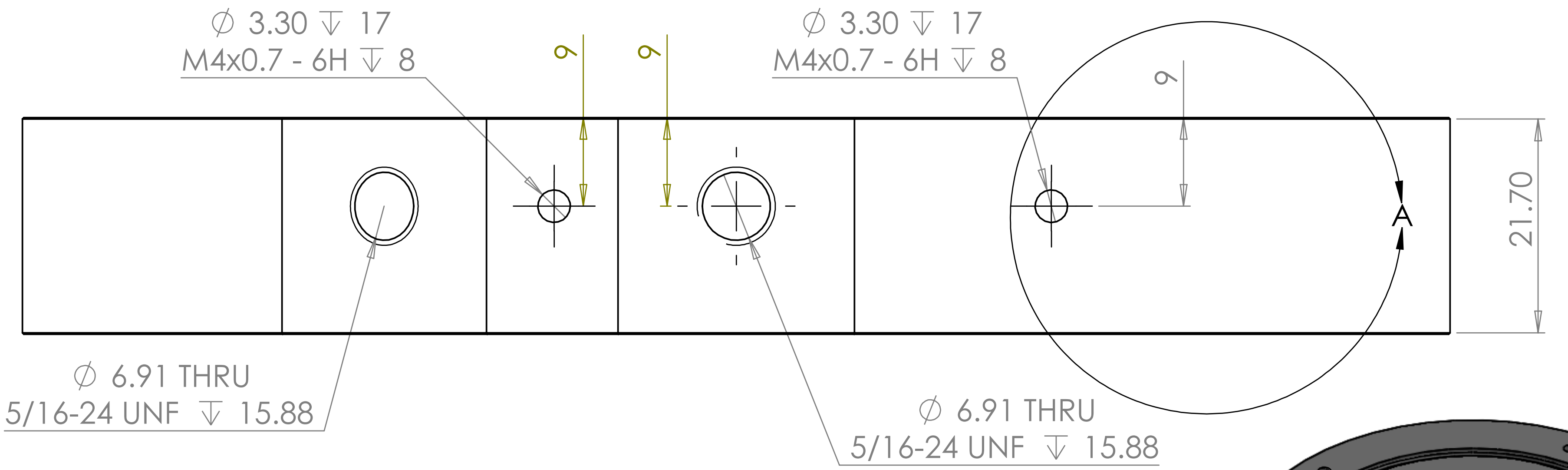

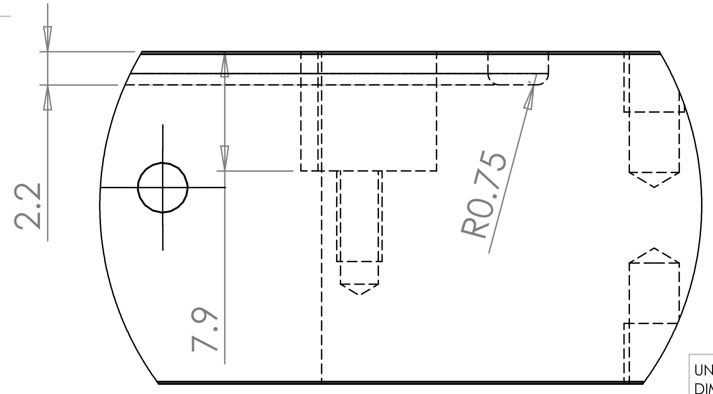

DETAIL A
SCALE 2 : 1

SolidWorks Educational Edition.
For Instructional Use Only.

UNLESS OTHERWISE SPECIFIED:
DIMENSIONS ARE IN MILLIMETERS
SURFACE FINISH:
TOLERANCES (UNLESS STATED):
LINEAR: ±0.2
ANGULAR: ±0.1°

FINISH:

DEBUR AND BREAK SHARP EDGES

DO NOT SCALE DRAWING

REVISION

Loughborough University

TITLE:

Middle of the cell

	NAME	SIGNATURE	DATE
DRAWN	Amy Managh		28/02/12
CHK'D			
APPV'D			
MFG			
Q.A			

MATERIAL:
Delrin

WEIGHT:

DWG NO.

A4

SCALE: 1.5:1

SHEET 1 OF 3

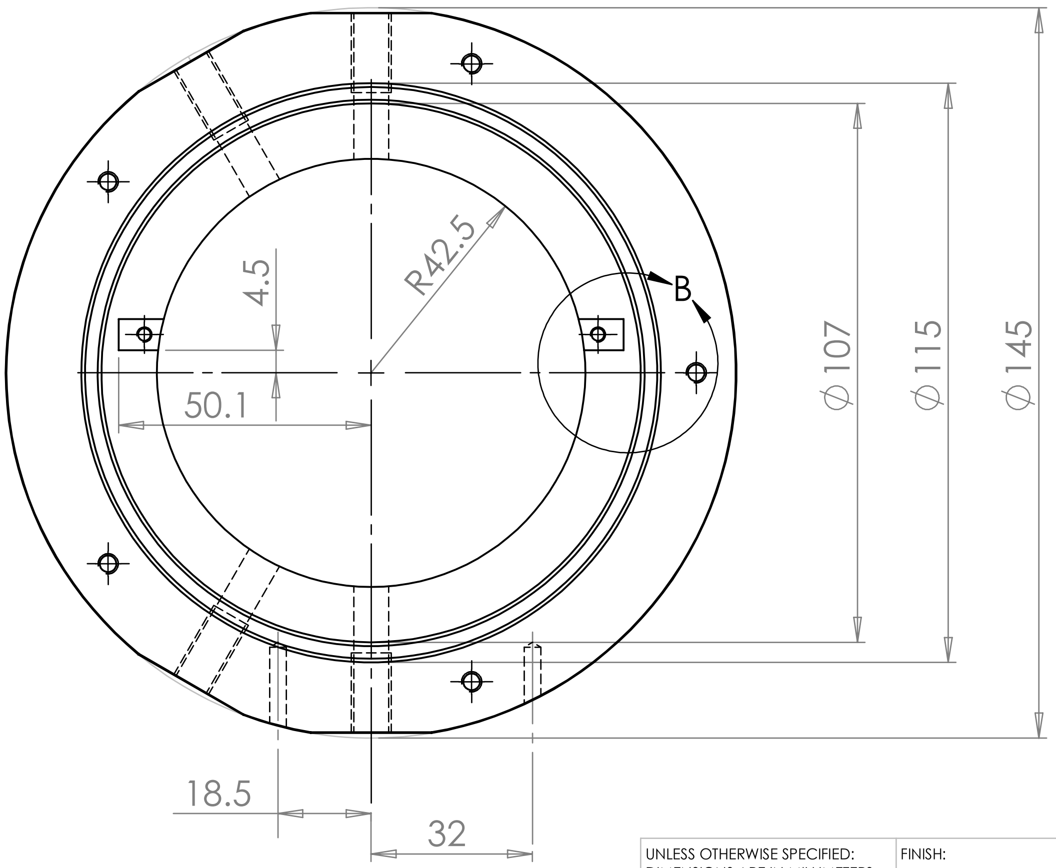

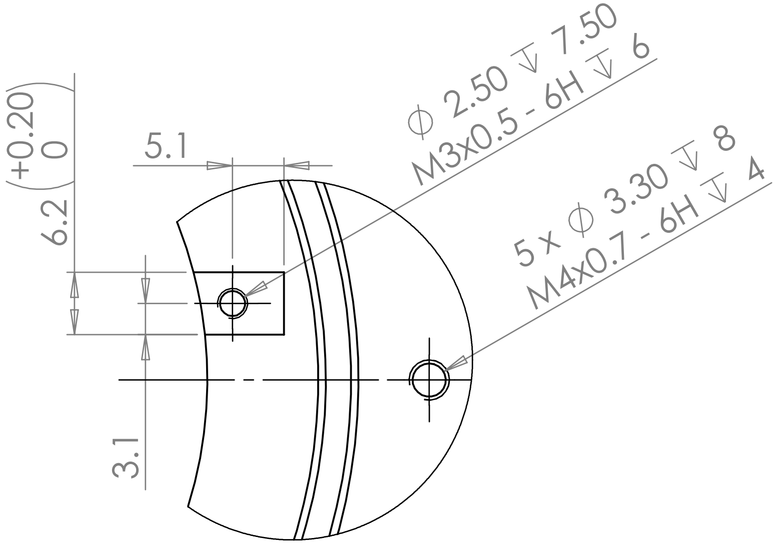

DETAIL B
SCALE 2 : 1.5

UNLESS OTHERWISE SPECIFIED:
DIMENSIONS ARE IN MILLIMETERS
SURFACE FINISH:
TOLERANCES (UNLESS STATED):
LINEAR: ±0.2
ANGULAR: ±0.1°

FINISH:

DEBUR AND
BREAK SHARP
EDGES

DO NOT SCALE DRAWING

REVISION

Loughborough University

	NAME	SIGNATURE	DATE
DRAWN	Amy Managh		28/02/12
CHK'D			
APPV'D			
MFG			
Q.A			

TITLE:

Middle of the cell

MATERIAL:
Delrin

DWG NO.

A4

WEIGHT:

SCALE: 1:1.5

SHEET 2 OF 3

SolidWorks Educational Edition.
For Instructional Use Only.

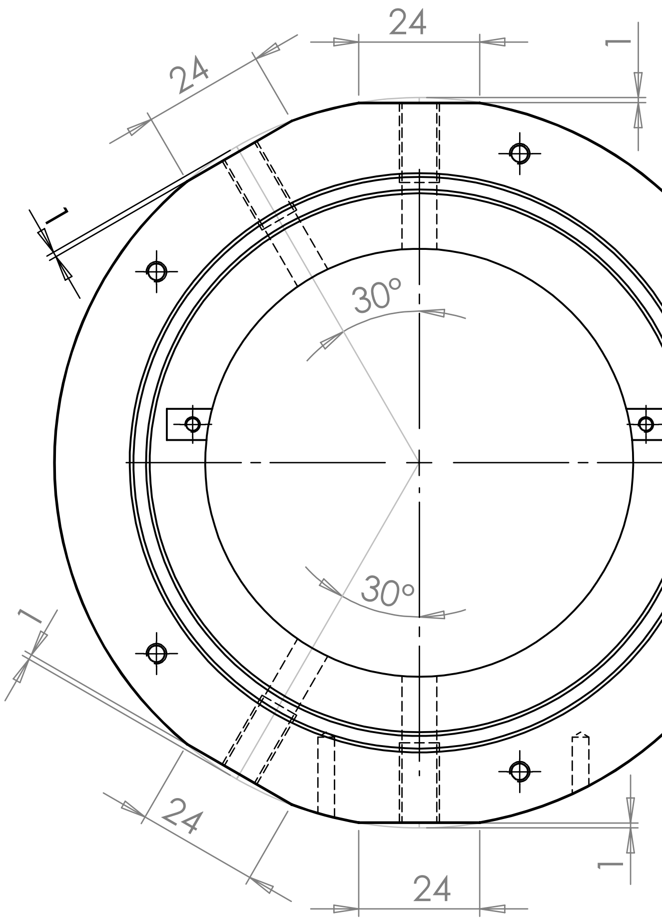

UNLESS OTHERWISE SPECIFIED:
DIMENSIONS ARE IN MILLIMETERS
SURFACE FINISH:
TOLERANCES (UNLESS STATED):
LINEAR: ±0.2
ANGULAR: ±0.1°

FINISH:

DEBUR AND
BREAK SHARP
EDGES

DO NOT SCALE DRAWING

REVISION

Loughborough University

	NAME	SIGNATURE	DATE
DRAWN	Amy Managh		28/02/12
CHK'D			
APPV'D			
MFG			
Q.A			

TITLE:

Middle of the cell

MATERIAL:
Delrin

DWG NO.

A4

WEIGHT:

SCALE: 1:1.5

SHEET 3 OF 3

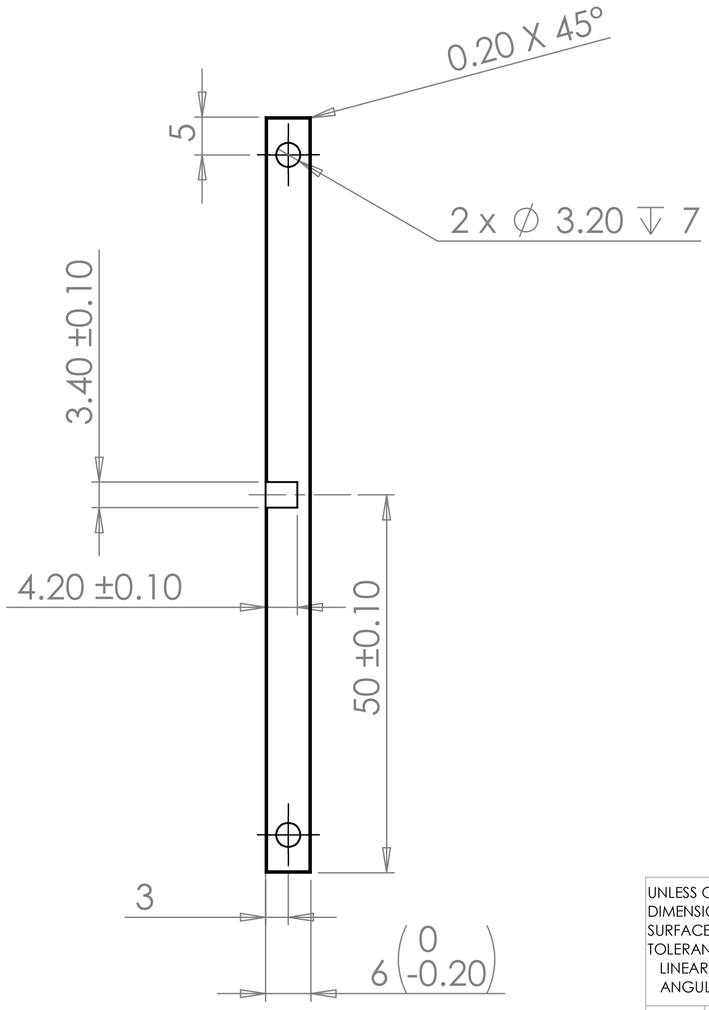

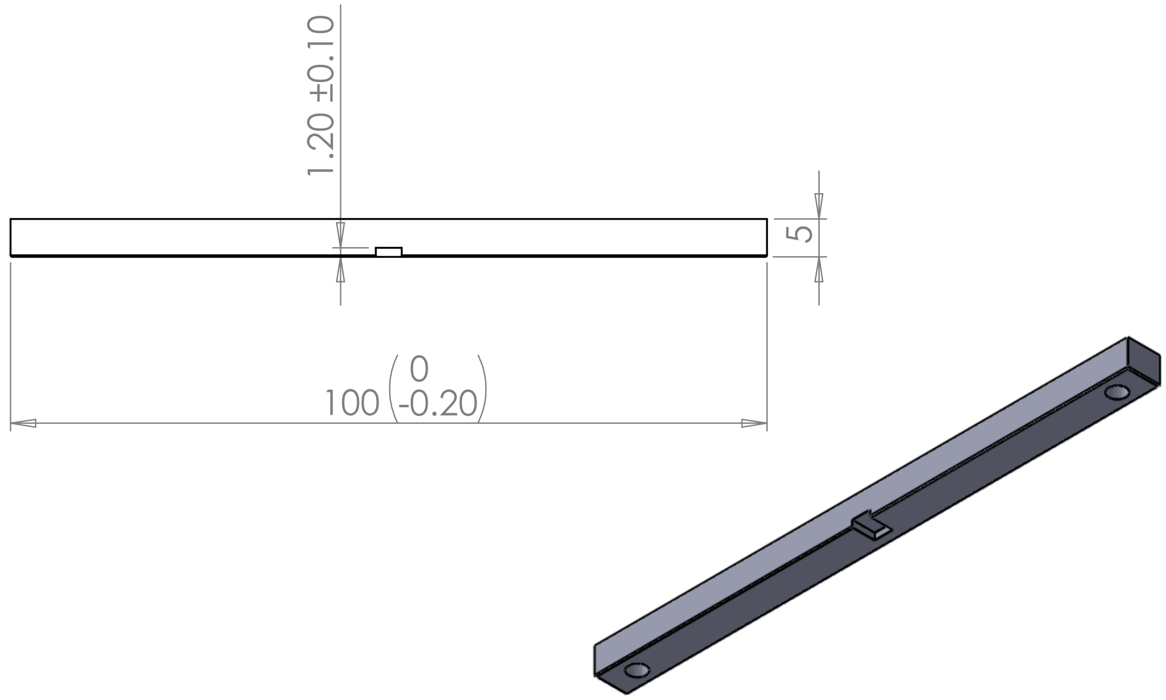

UNLESS OTHERWISE SPECIFIED:
DIMENSIONS ARE IN MILLIMETERS
SURFACE FINISH:
TOLERANCES (UNLESS STATED):
LINEAR: ± 0.2
ANGULAR: ± 0.1°

FINISH:

DEBUR AND BREAK SHARP EDGES

DO NOT SCALE DRAWING

REVISION

Loughborough University

	NAME	SIGNATURE	DATE
DRAWN	Amy Managh		28/02/12
CHK'D			
APPV'D			
MFG			
Q.A			

TITLE:

Bar for sniffer

MATERIAL:
Delrin

DWG NO.

A4

WEIGHT:

SCALE:1:1

SHEET 1 OF 1

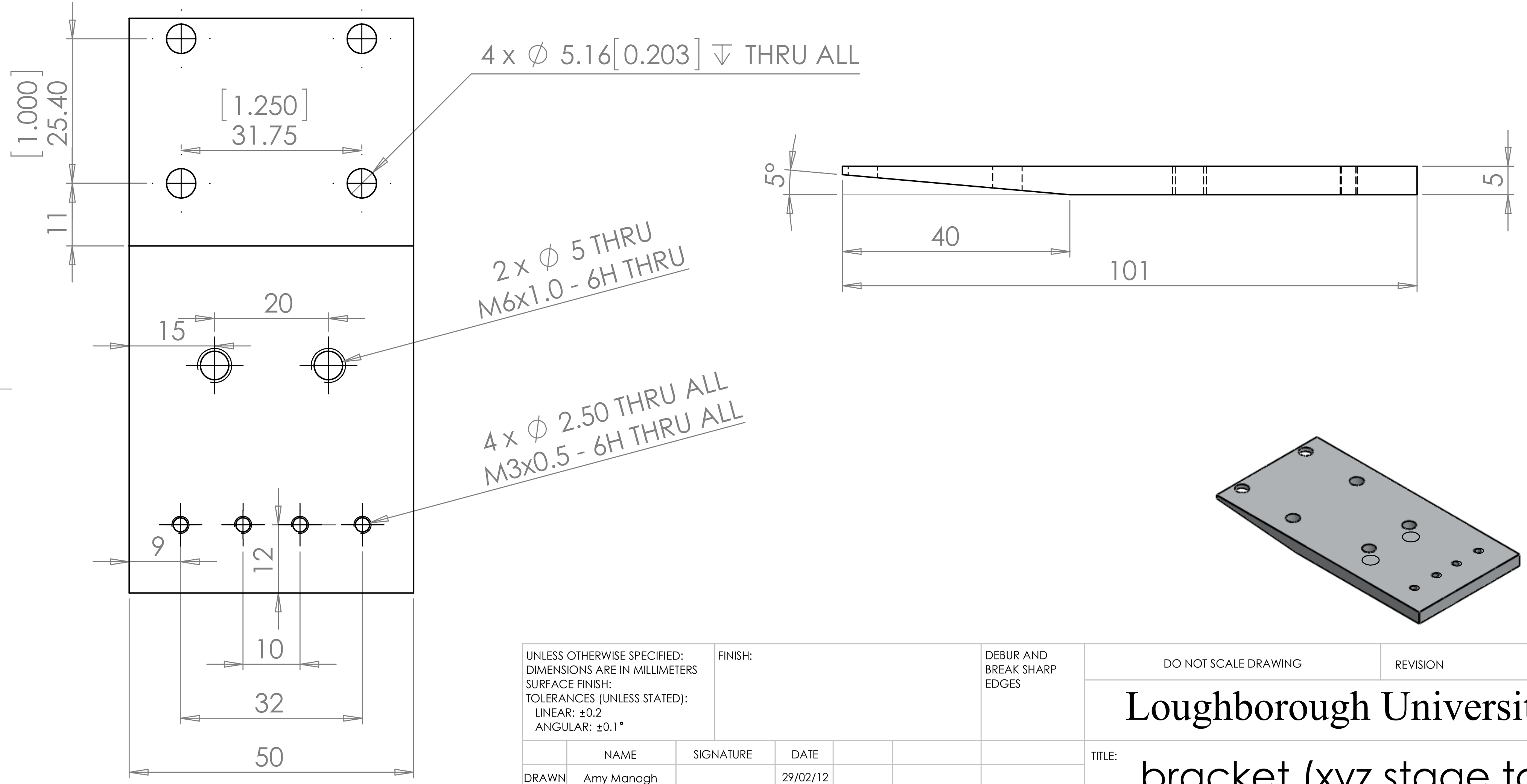

UNLESS OTHERWISE SPECIFIED:
DIMENSIONS ARE IN MILLIMETERS
SURFACE FINISH:
TOLERANCES (UNLESS STATED):
LINEAR: ±0.2
ANGULAR: ±0.1°

FINISH:

DEBUR AND BREAK SHARP EDGES

DO NOT SCALE DRAWING

REVISION

Loughborough University

	NAME	SIGNATURE	DATE
DRAWN	Amy Managh		29/02/12
CHK'D			
APPV'D			
MFG			
Q.A			

TITLE:

bracket (xyz stage to UP213)

MATERIAL:
Aluminium

DWG NO.

A4

WEIGHT:

SCALE:1:1

SHEET 1 OF 1

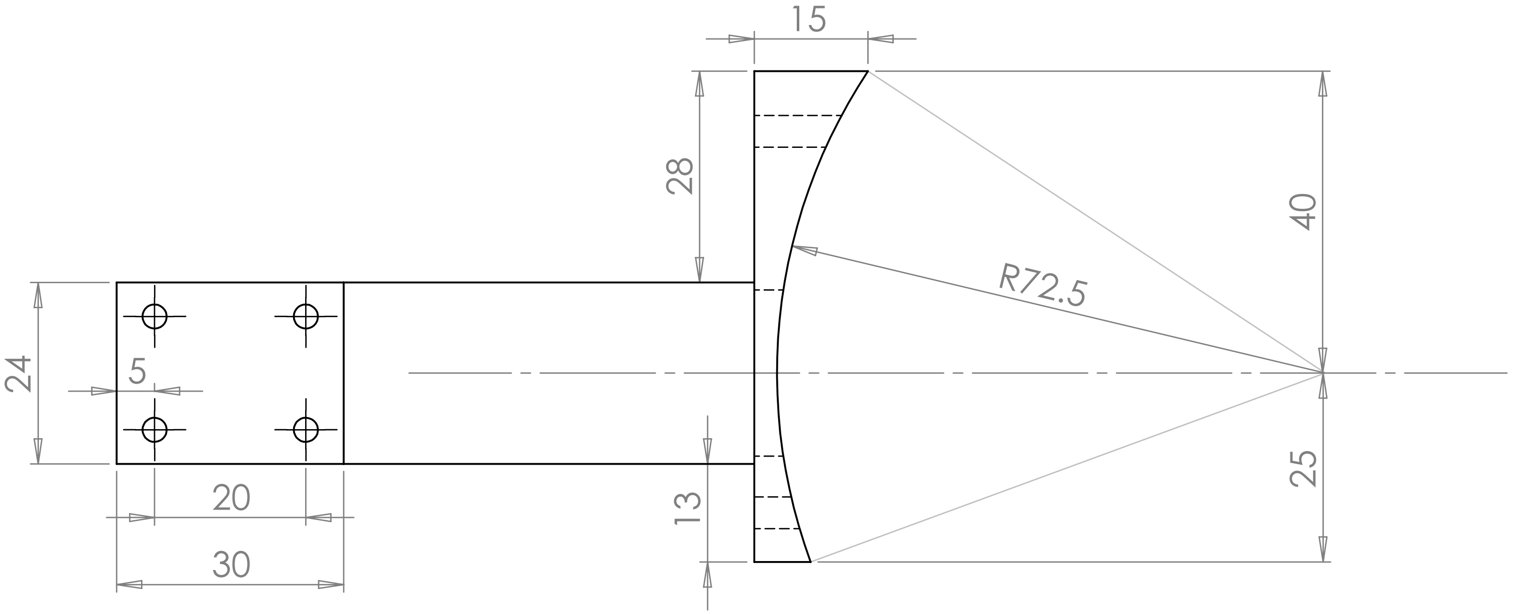

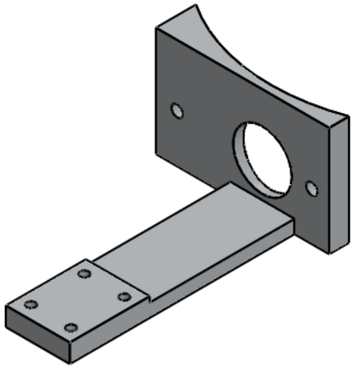

UNLESS OTHERWISE SPECIFIED:
DIMENSIONS ARE IN MILLIMETERS
SURFACE FINISH:
TOLERANCES (UNLESS STATED):
LINEAR: ±0.2
ANGULAR: ±0.1°

FINISH:

DEBUR AND
BREAK SHARP
EDGES

DO NOT SCALE DRAWING

REVISION

Loughborough University

	NAME	SIGNATURE	DATE
DRAWN	Amy Managh		29/02/12
CHK'D			
APPV'D			
MFG			
Q.A			

TITLE:

Bracket (xyz stage to cell)

MATERIAL:
Aluminium

DWG NO.

A4

WEIGHT:

SCALE: 1:1

SHEET 1 OF 2

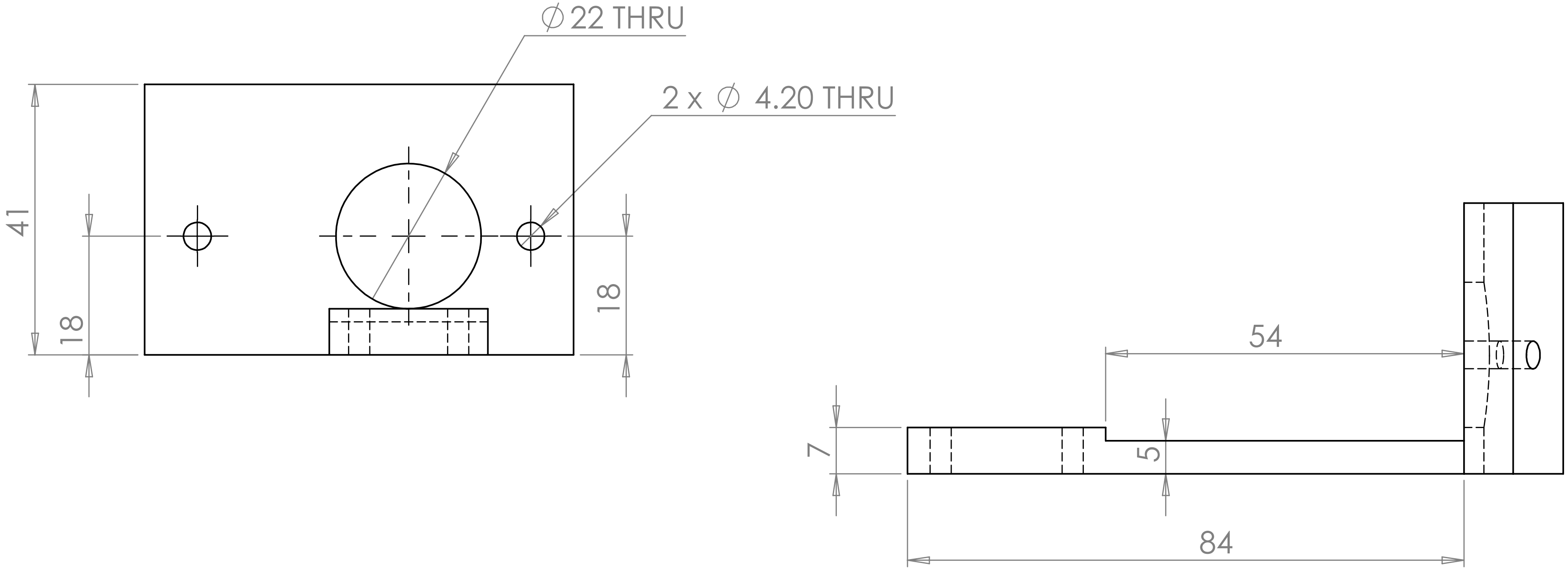

UNLESS OTHERWISE SPECIFIED:
DIMENSIONS ARE IN MILLIMETERS
SURFACE FINISH:
TOLERANCES (UNLESS STATED):
LINEAR: ±0.2
ANGULAR: ±0.1°

FINISH:

DEBUR AND
BREAK SHARP
EDGES

DO NOT SCALE DRAWING

REVISION

Loughborough University

	NAME	SIGNATURE	DATE
DRAWN	Amy Managh		29/02/12
CHK'D			
APPV'D			
MFG			
Q.A			

TITLE:

Bracket (xyz stage to cell)

MATERIAL:
Aluminium

DWG NO.

A4

WEIGHT:

SCALE: 1:1

SHEET 2 OF 2

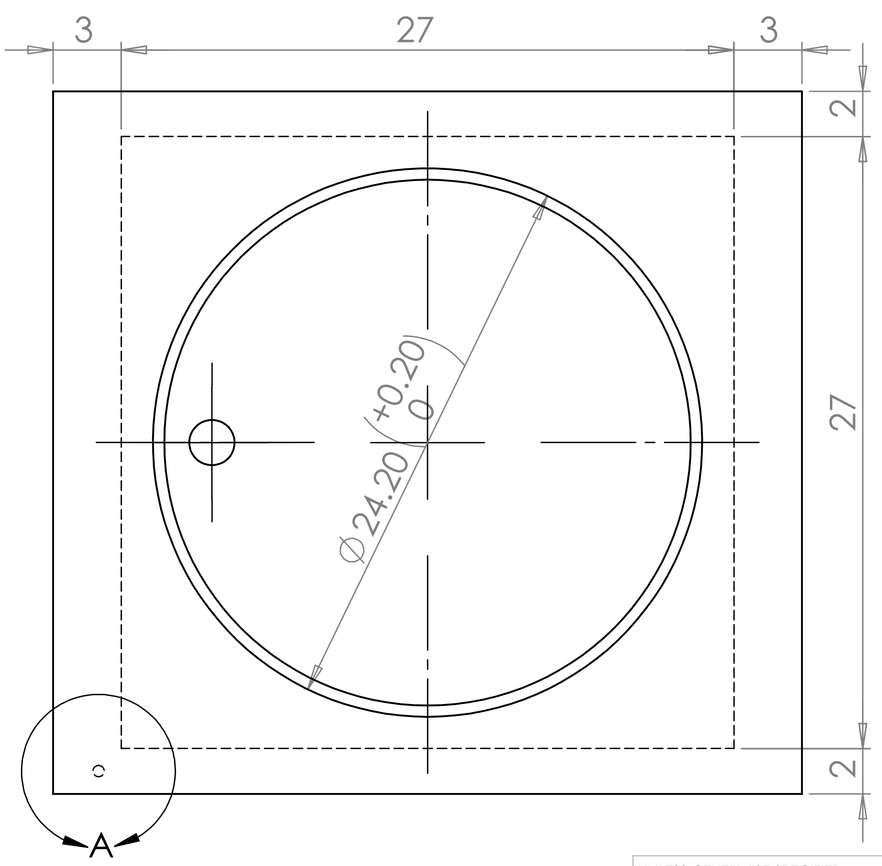

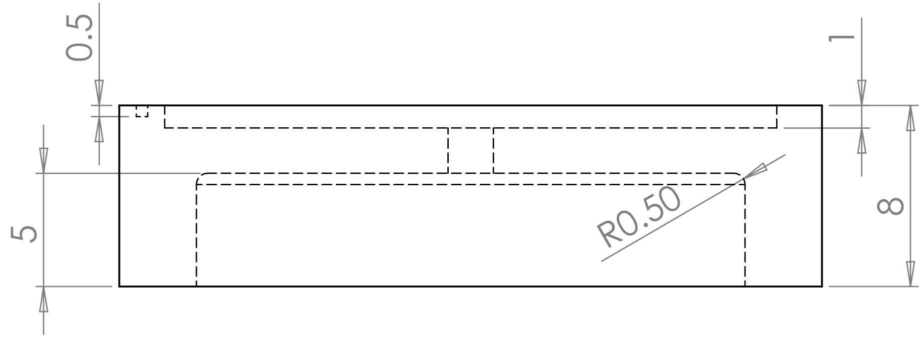

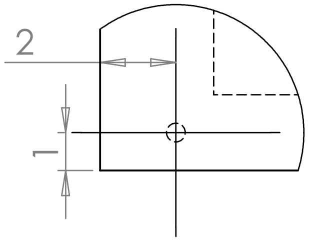

DETAIL A
SCALE 5 : 1

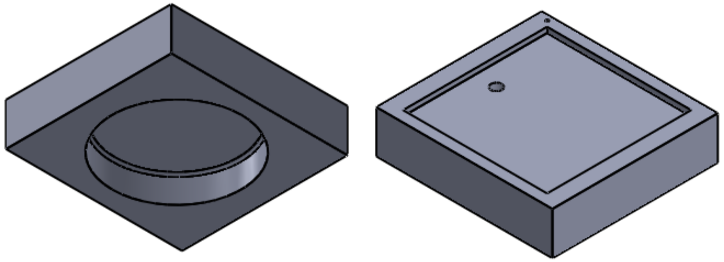

UNLESS OTHERWISE SPECIFIED: DIMENSIONS ARE IN MILLIMETERS SURFACE FINISH: TOLERANCES (UNLESS STATED): LINEAR: ±0.2 ANGULAR: ±0.1°	FINISH:		DEBUR AND BREAK SHARP EDGES	DO NOT SCALE DRAWING
				REVISION
	NAME	SIGNATURE	DATE	TITLE:
DRAWN	Amy Managh		28/02/12	
CHK'D				
APPV'D				
MFG				
Q.A			MATERIAL: Delrin	DWG NO.
			WEIGHT:	SCALE: 3:1

Loughborough University

Sample holder

A4

SHEET 1 OF 1

SolidWorks Educational Edition.
For Instructional Use Only.

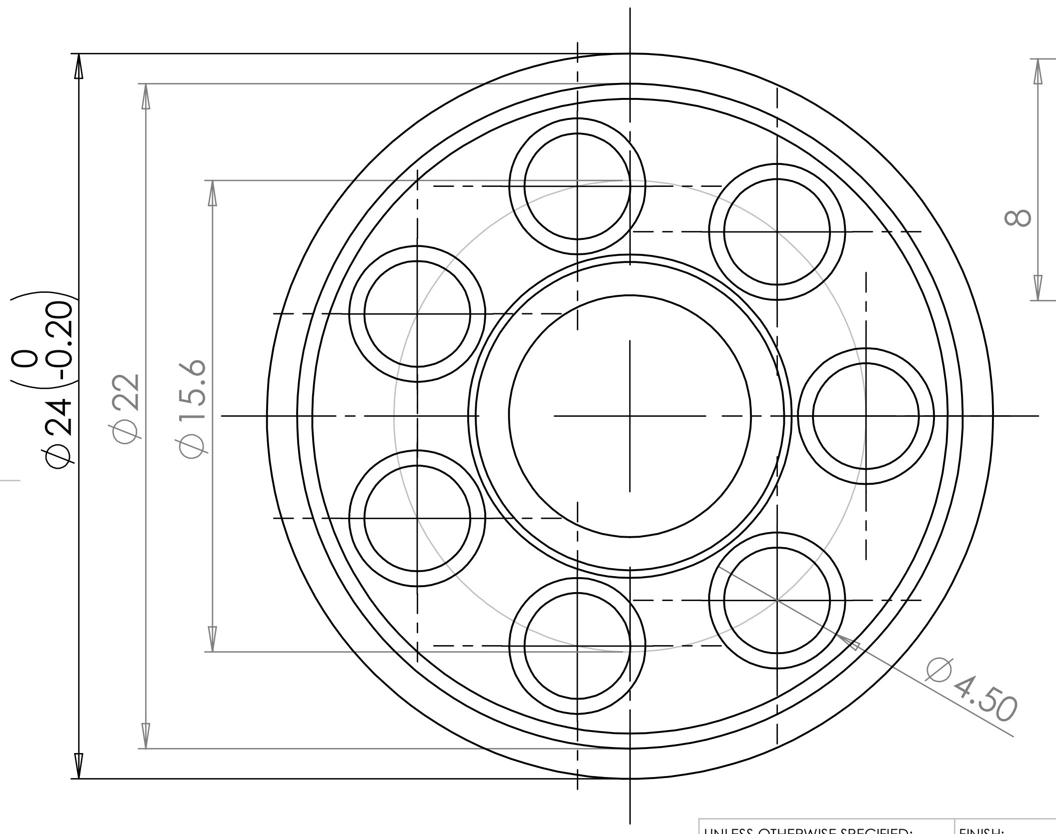

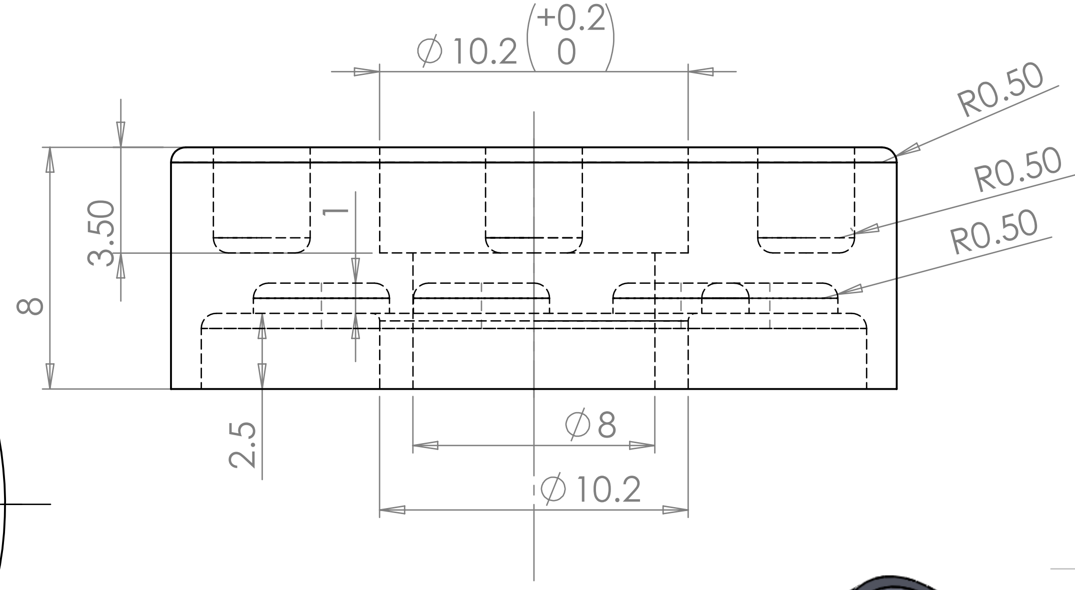

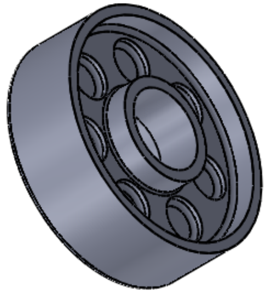

SolidWorks Educational Edition.
For Instructional Use Only.

UNLESS OTHERWISE SPECIFIED:
DIMENSIONS ARE IN MILLIMETERS
SURFACE FINISH:
TOLERANCES (UNLESS STATED):
LINEAR: ±0.2
ANGULAR: ±0.1°

FINISH:

DEBUR AND
BREAK SHARP
EDGES

DO NOT SCALE DRAWING

REVISION

Loughborough University

	NAME	SIGNATURE	DATE
DRAWN	Amy Managh		28/02/12
CHK'D			
APPV'D			
MFG			
Q.A			

TITLE:

Cage for rotary bearing

MATERIAL:
Delrin

DWG NO.

A4

WEIGHT:

SCALE: 4:1

SHEET 1 OF 2

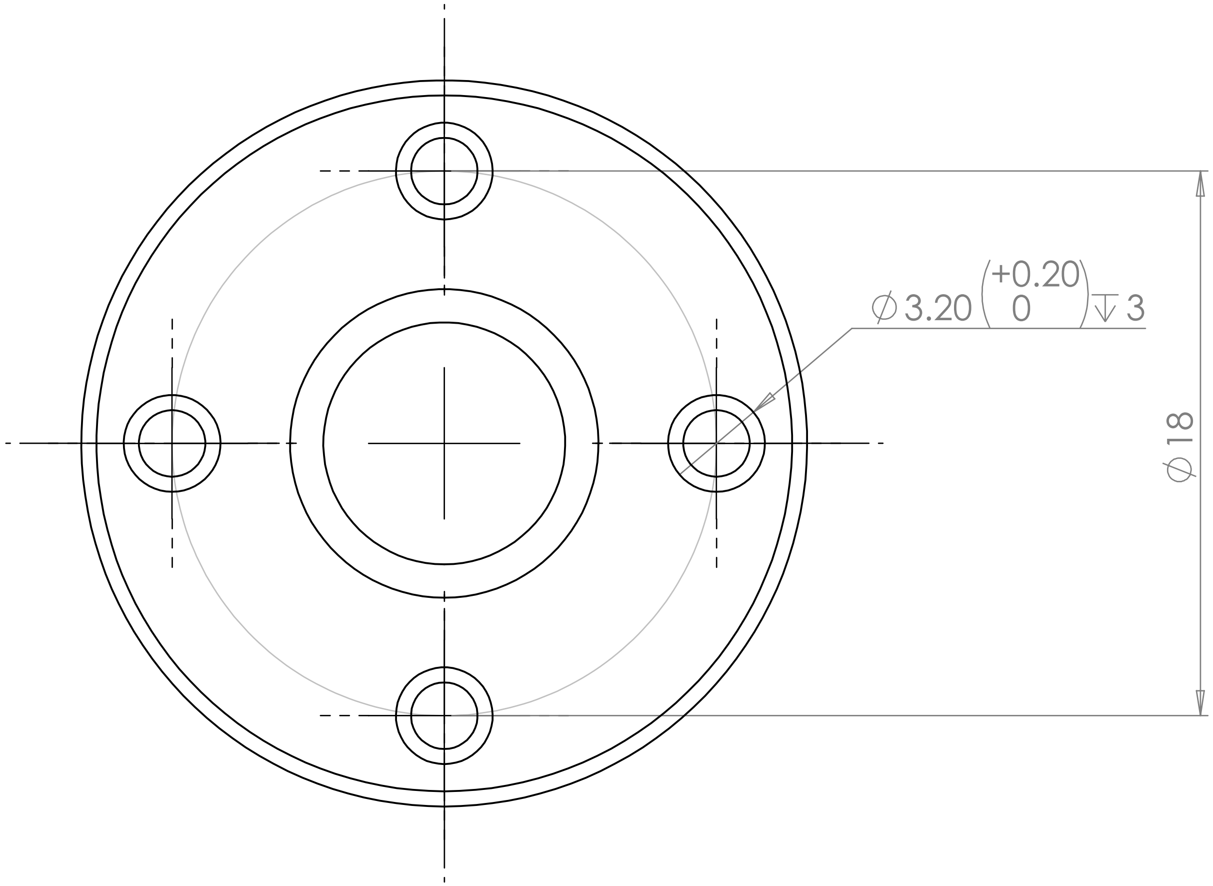

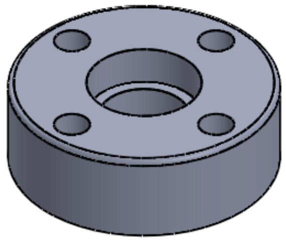

UNLESS OTHERWISE SPECIFIED:
DIMENSIONS ARE IN MILLIMETERS
SURFACE FINISH:
TOLERANCES (UNLESS STATED):
LINEAR: ±0.2
ANGULAR: ±0.1°

FINISH:

DEBUR AND BREAK SHARP EDGES

DO NOT SCALE DRAWING

REVISION

Loughborough University

	NAME	SIGNATURE	DATE
DRAWN	Amy Managh		28/02/12
CHK'D			
APPV'D			
MFG			
Q.A			

TITLE:

Cage for rotary bearing

MATERIAL: Delrin

WEIGHT:

DWG NO.

A4

SCALE: 4:1

SHEET 2 OF 2

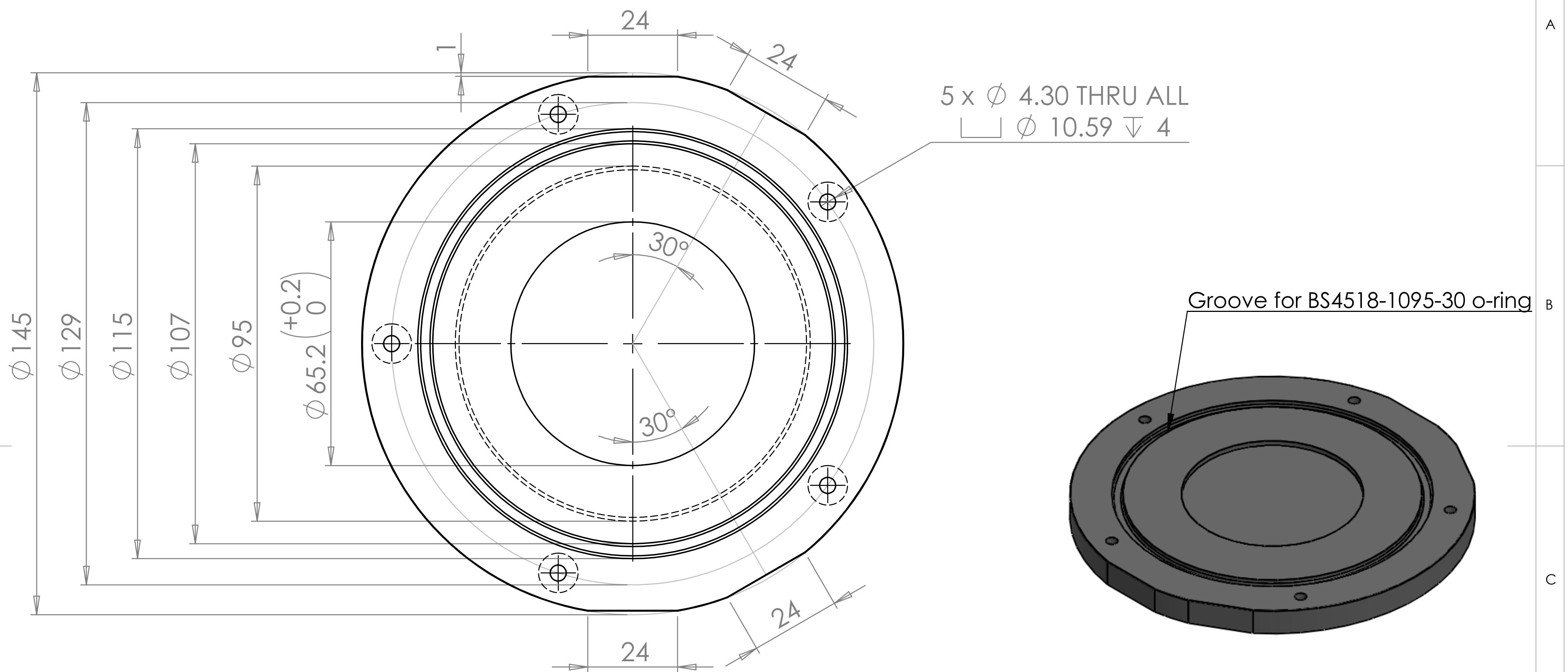

UNLESS OTHERWISE SPECIFIED: DIMENSIONS ARE IN MILLIMETERS SURFACE FINISH: TOLERANCES (UNLESS STATED): LINEAR: ±0.2 ANGULAR: ±0.1°		FINISH:				DEBUR AND BREAK SHARP EDGES	DO NOT SCALE DRAWING Loughborough University	REVISION
	NAME	SIGNATURE	DATE				TITLE: Base of the cell	
DRAWN	Amy Managh		28/02/12					
CHK'D								
APPV'D								
MFG								
Q.A				MATERIAL: Delrin			DWG NO.	A4
				WEIGHT:			SCALE: 1:1.5	SHEET 1 OF 2

SolidWorks Educational Edition.
For Instructional Use Only.

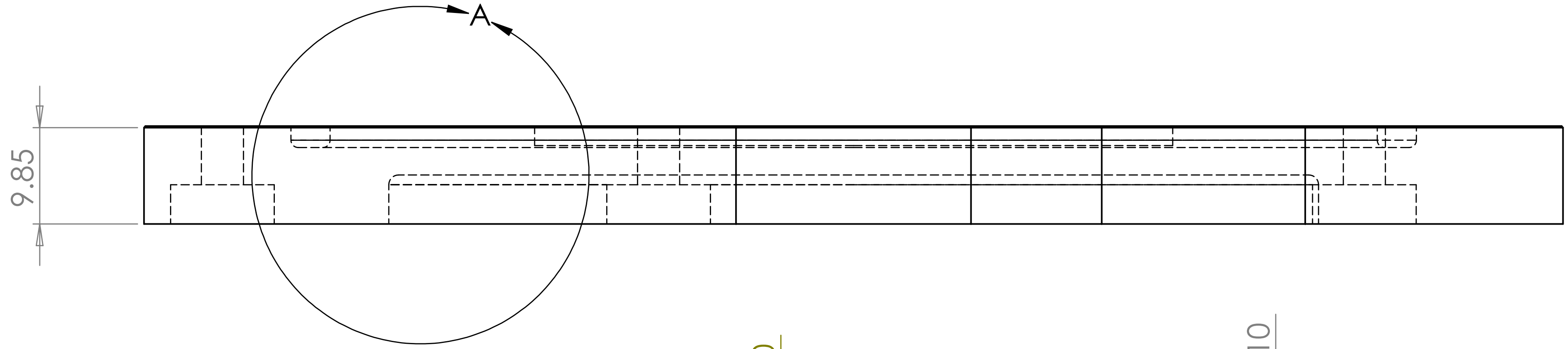

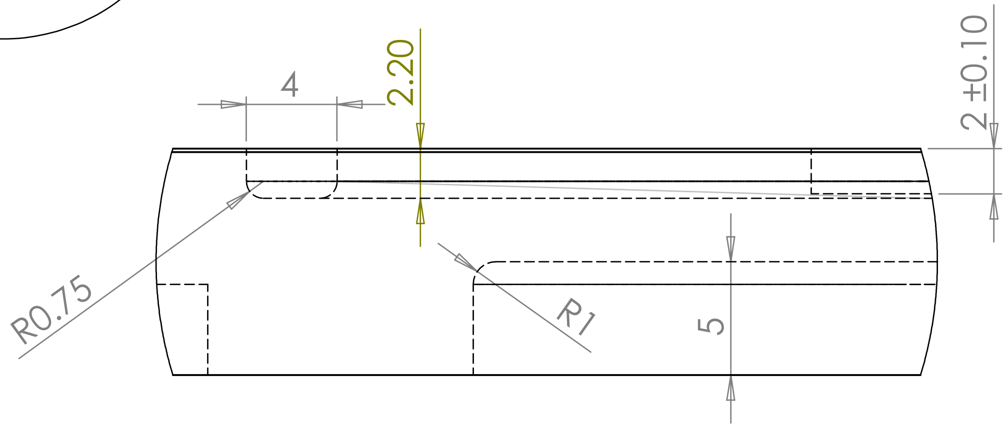

DETAIL A
SCALE 3 : 1

UNLESS OTHERWISE SPECIFIED: DIMENSIONS ARE IN MILLIMETERS SURFACE FINISH: TOLERANCES (UNLESS STATED): LINEAR: ±0.2 ANGULAR: ±0.1°	FINISH:	DEBUR AND BREAK SHARP EDGES	DO NOT SCALE DRAWING	REVISION

Loughborough University

	NAME	SIGNATURE	DATE
DRAWN	Amy Managh		28/02/12
CHK'D			
APPV'D			
MFG			
Q.A			

TITLE:

Base of the cell

MATERIAL: Delrin

DWG NO.

A4

WEIGHT:

SCALE: 1:1.5

SHEET 2 OF 2

SolidWorks Educational Edition.
For Instructional Use Only.

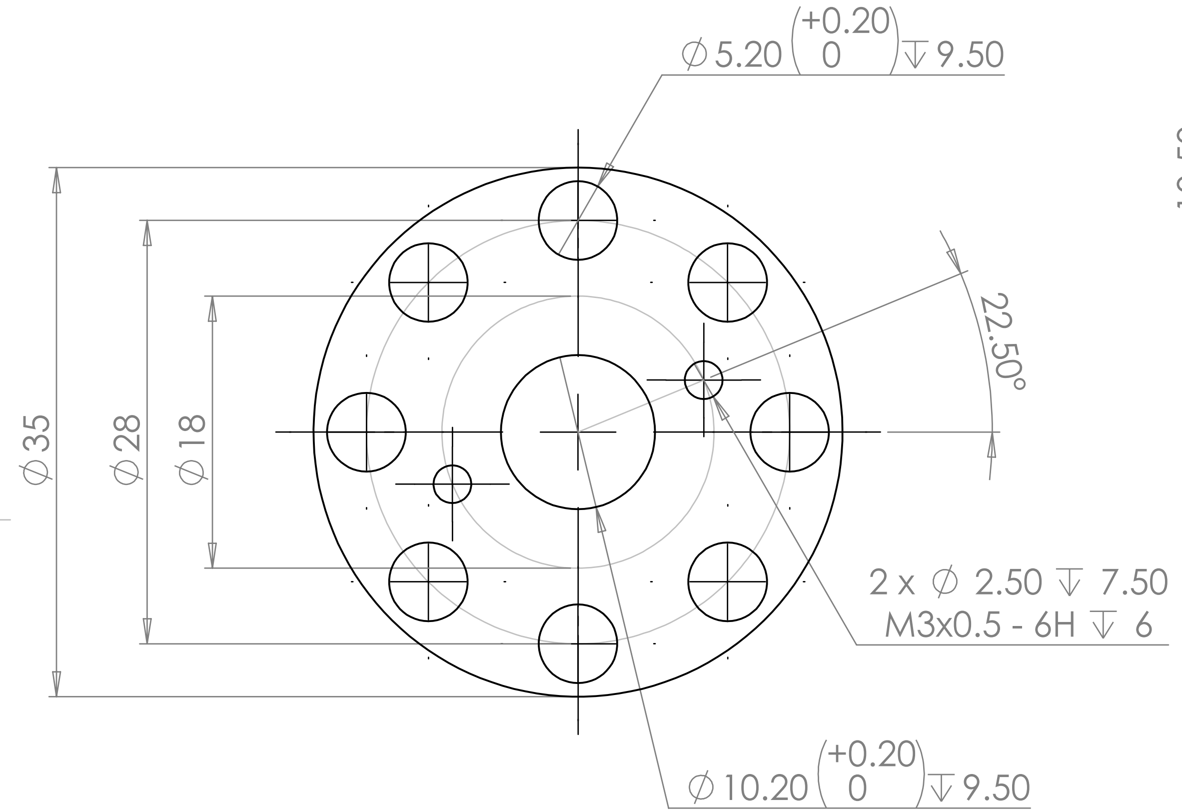

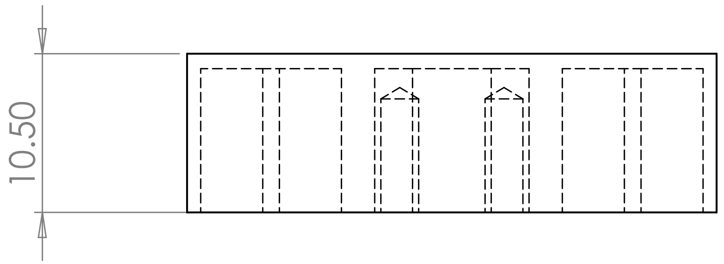

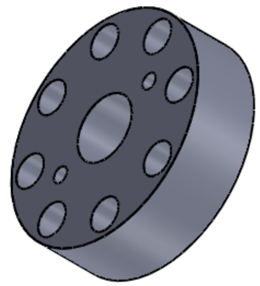

UNLESS OTHERWISE SPECIFIED: DIMENSIONS ARE IN MILLIMETERS SURFACE FINISH: TOLERANCES (UNLESS STATED): LINEAR: ± 0.2 ANGULAR: ± 0.1°	FINISH:		DEBUR AND BREAK SHARP EDGES		DO NOT SCALE DRAWING	REVISION
	NAME	SIGNATURE	DATE		Loughborough University	
DRAWN	Amy Managh		29/02/12		TITLE:	
CHK'D					Lower magnet holder	
APPV'D						
MFG						
Q.A			MATERIAL: Delrin		DWG NO.	A4
			WEIGHT:		SCALE:2:1	SHEET 1 OF 1

SolidWorks Educational Edition.
For Instructional Use Only.

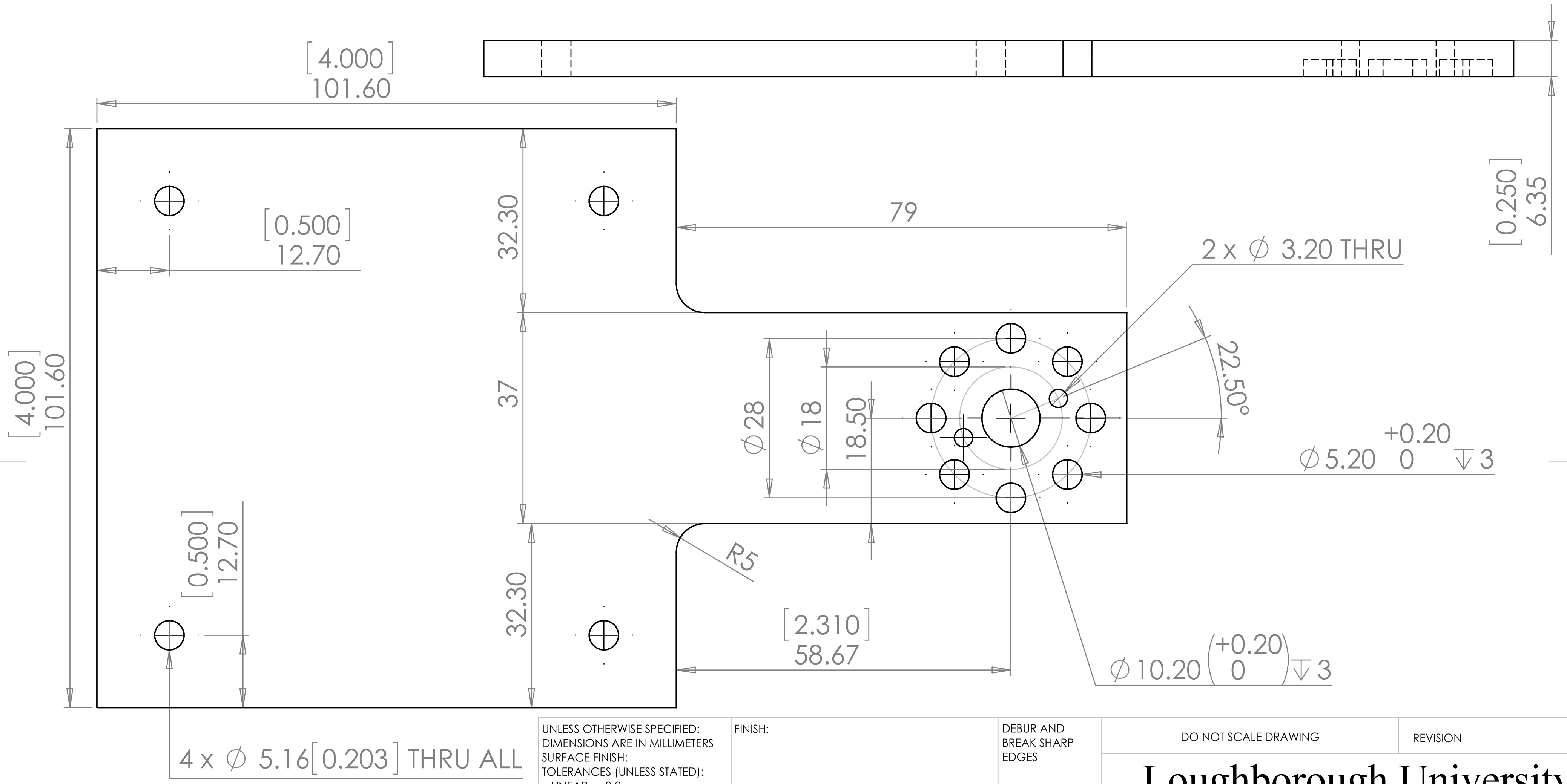

UNLESS OTHERWISE SPECIFIED:
DIMENSIONS ARE IN MILLIMETERS
SURFACE FINISH:
TOLERANCES (UNLESS STATED):
LINEAR: ± 0.2
ANGULAR: ± 0.1°

FINISH:

DEBUR AND BREAK SHARP EDGES

DO NOT SCALE DRAWING

REVISION

Loughborough University

TITLE:

Magnet attachment plate

	NAME	SIGNATURE	DATE
DRAWN	Amy Managh		29/02/12
CHK'D			
APPV'D			
MFG			
Q.A			

MATERIAL:
Delrin

DWG NO.

A4

WEIGHT:

SCALE: 1:1

SHEET 1 OF 1

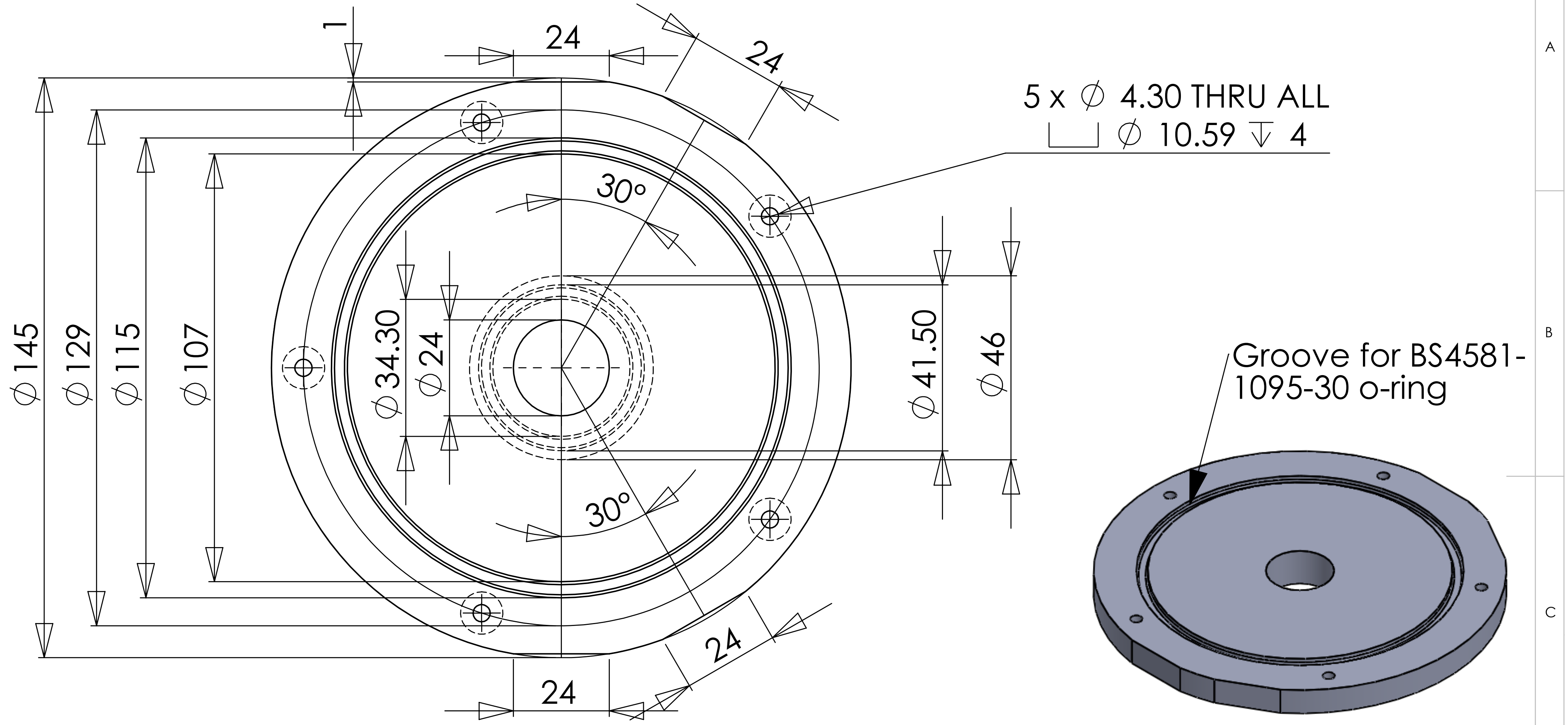

UNLESS OTHERWISE SPECIFIED:
DIMENSIONS ARE IN MILLIMETERS
SURFACE FINISH:
TOLERANCES:
LINEAR: ± 0.2
ANGULAR: ± 0.1°

FINISH:

DEBUR AND BREAK SHARP EDGES

DO NOT SCALE DRAWING

REVISION

Loughborough University

TITLE:

Base of the cell for o-ring seal

	NAME	SIGNATURE	DATE
DRAWN	Amy Managh		18/07/12
CHK'D			
APPV'D			
MFG			
Q.A			

MATERIAL:
Delrin

DWG NO.

A4

WEIGHT:

SCALE: 0.7:1

SHEET 1 OF 2

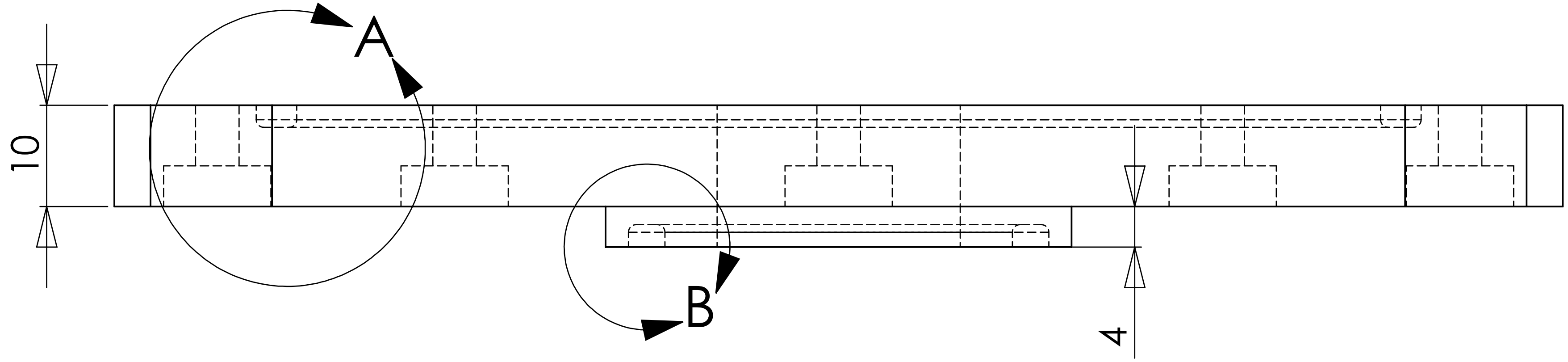

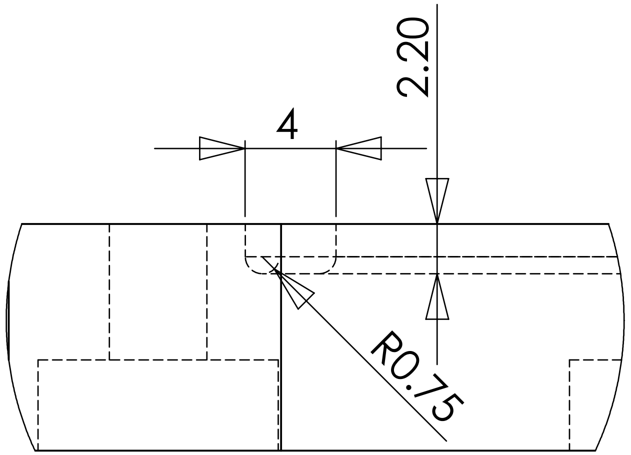

DETAIL A
SCALE 3 : 1

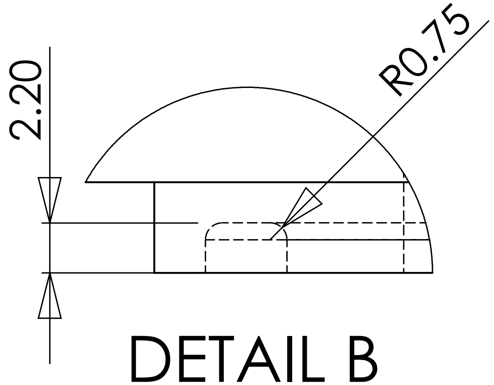

DETAIL B
SCALE 3 : 1

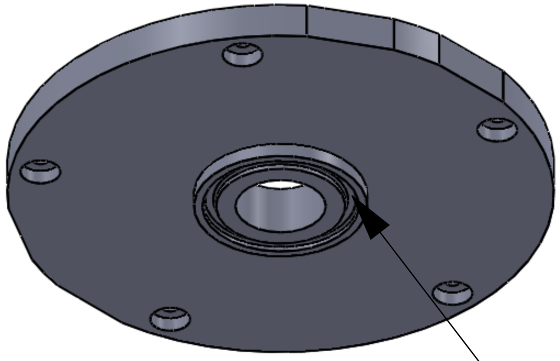

Groove for BS1806-127 o-ring

UNLESS OTHERWISE SPECIFIED: DIMENSIONS ARE IN MILLIMETERS SURFACE FINISH: TOLERANCES: LINEAR: ± 0.2 ANGULAR: ± 0.1°	FINISH:	DEBUR AND BREAK SHARP EDGES	
	NAME	SIGNATURE	DATE
DRAWN	Amy Managh		18/07/12
CHK'D			
APPV'D			
MFG			
Q.A			

MATERIAL: Delrin

WEIGHT:

DO NOT SCALE DRAWING

REVISION

Loughborough University

TITLE:

Base of the cell for o-ring seal

DWG NO.

A4

SCALE: 1.5:1

SHEET 2 OF 2

SolidWorks Student Edition.
For Academic Use Only.

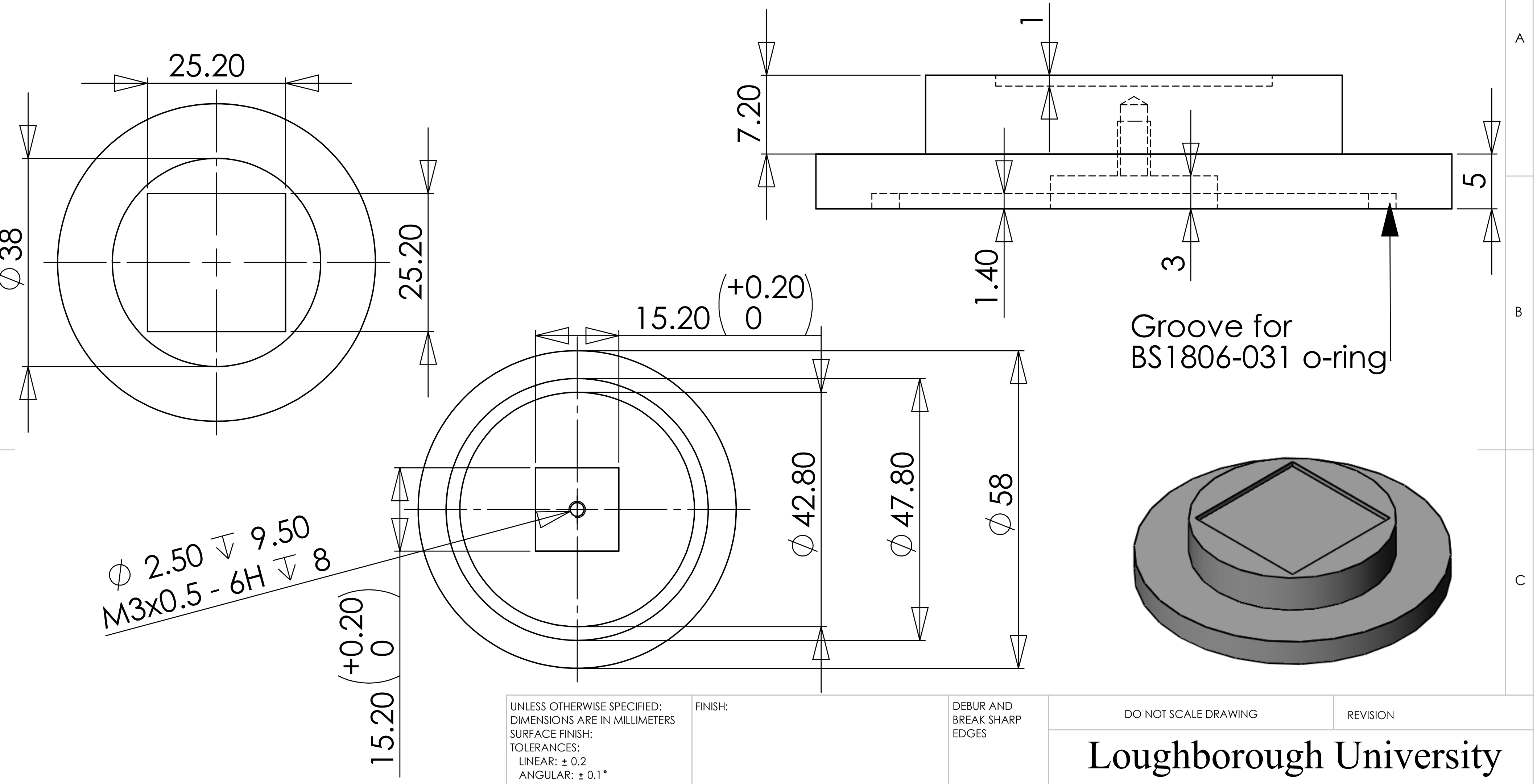

UNLESS OTHERWISE SPECIFIED:
DIMENSIONS ARE IN MILLIMETERS
SURFACE FINISH:
TOLERANCES:
LINEAR: ± 0.2
ANGULAR: ± 0.1°

FINISH:

DEBUR AND
BREAK SHARP
EDGES

DO NOT SCALE DRAWING

REVISION

Loughborough University

	NAME	SIGNATURE	DATE
DRAWN	Amy Managh		18/07/12
CHK'D			
APPV'D			
MFG			
Q.A			

TITLE:

Sample holder for o-ring seal

MATERIAL:
Delrin

WEIGHT:

DWG NO.

A4

SCALE:1:1

SHEET 1 OF 1

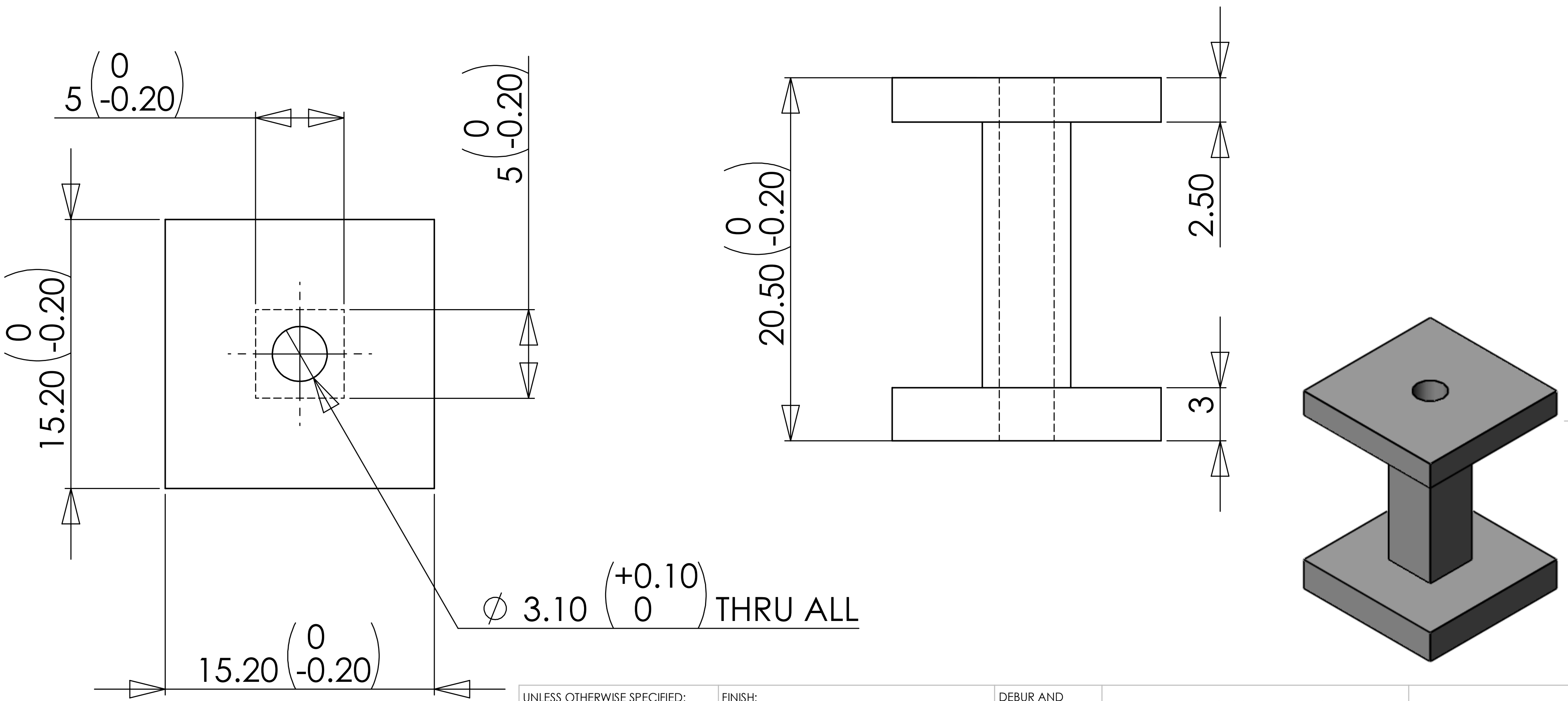

UNLESS OTHERWISE SPECIFIED:
DIMENSIONS ARE IN MILLIMETERS
SURFACE FINISH:
TOLERANCES:
LINEAR: ± 0.2
ANGULAR: ± 0.1°

FINISH:

DEBUR AND
BREAK SHARP
EDGES

DO NOT SCALE DRAWING

REVISION

Loughborough University

	NAME	SIGNATURE	DATE
DRAWN	Amy Managh		20/07/12
CHK'D			
APPV'D			
MFG			
Q.A			

TITLE:

Supporting block

MATERIAL:
Aluminium

DWG NO.

A4

WEIGHT:

SCALE: 3:1

SHEET 1 OF 1

SolidWorks Student Edition.
For Academic Use Only.

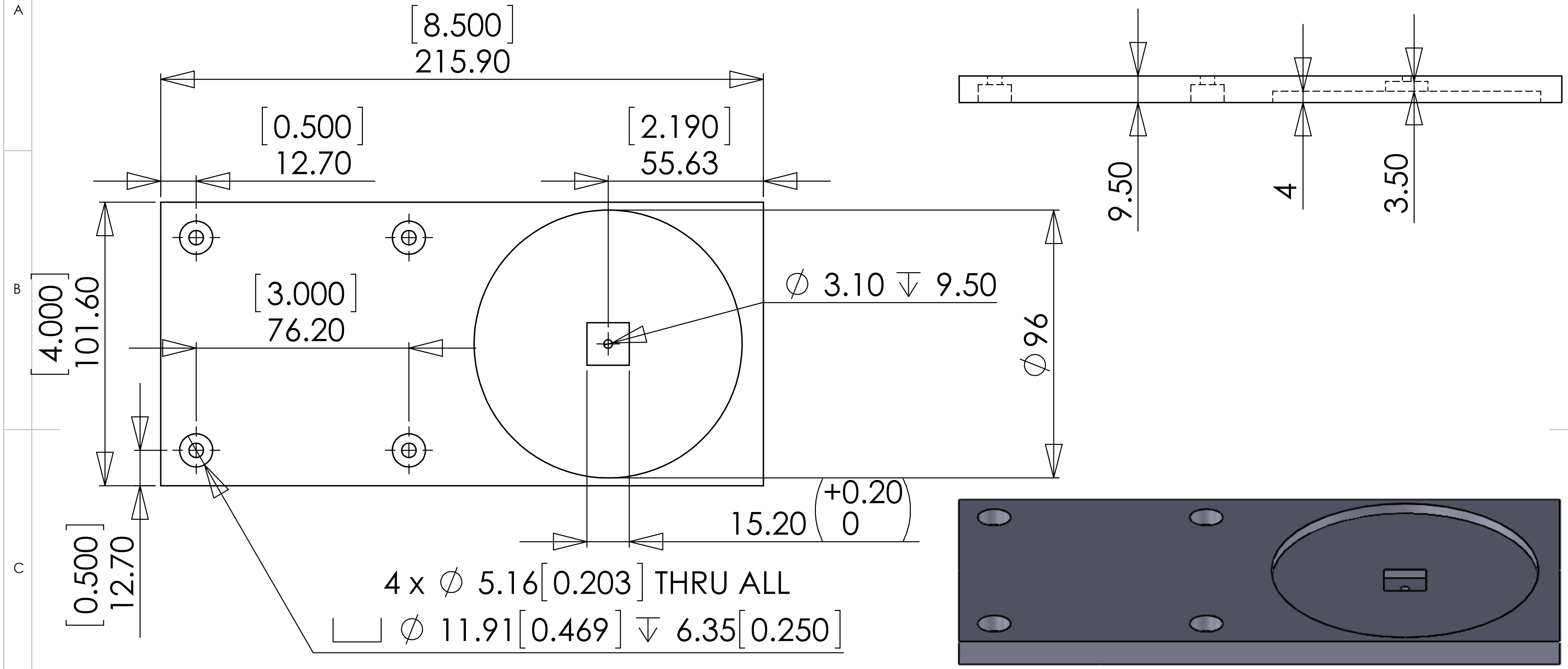

UNLESS OTHERWISE SPECIFIED: DIMENSIONS ARE IN MILLIMETERS SURFACE FINISH: TOLERANCES: LINEAR: ± 0.2 ANGULAR: ± 0.1°	FINISH:			DEBUR AND BREAK SHARP EDGES	DO NOT SCALE DRAWING	REVISION
					Loughborough University	
	NAME	SIGNATURE	DATE		TITLE:	
DRAWN	Amy Managh		23/01/13		Movement plate for o-ring seal	
CHK'D						
APPV'D						
MFG						
Q.A				MATERIAL: Aluminium	DWG NO.	A4
				WEIGHT:	SCALE:1:2	SHEET 1 OF 1

7.4 Appendix 4 – Publications and Conference Attendance

7.4.1 Publications

Two journal articles were produced from the research described in this thesis. The first paper describes tracking of gadolinium labelled T cells, as outlined in Chapter 2, and was targeted towards the Analytical Chemistry community. The paper was classified as an editor's highlight and featured on the front cover of the November 2013 issue of *Analytical Chemistry*. The second publication was targeted towards an immunological audience and focussed on tracking gold nanoparticle labelled Mregs, as covered in Chapter 3. A further publication covering the work on the LA-ICP-MS interface, presented in Chapter 4, is currently in preparation and a patent has been filed to cover this invention. The citation information for the published outputs is provided below.

A.J. Managh, S.L. Edwards, A. Bushell, K.J. Wood, E.K. Geissler, J.A. Hutchinson, R.W. Hutchinson, H.J. Reid and B.L. Sharp, "Single cell tracking of gadolinium labeled CD4+ T cells by laser ablation inductively coupled plasma mass spectrometry", *Analytical Chemistry,* 2013, 85, 10627-10634.

A.J. Managh, R.W. Hutchinson, P. Riquelme, C. Broichhausen, A. Wege, U. Ritter, N. Ahrens, G. Köhl, L. Walter, H.J. Schlitt, H.J. Reid, E.K. Geissler, B.L. Sharp and J.A. Hutchinson, "Laser ablation – inductively coupled plasma mass spectrometry: An emerging technology for detecting rare cells in tissue sections", *Journal of Immunology*, 2014, 193, 2600-2608.

B.L. Sharp, D.N. Douglas, **A.J. Managh**, "Laser ablation cell and injector system for a compositional analysis system", Electro Scientific Industries Inc., 2014, US patent, US 2014/0224775 (A1).

7.4.2 Presentations

The work contained within this thesis has been presented in both oral and poster format to audiences from a diverse range scientific backgrounds. This includes presentations at scientific conferences, presentations at annual meetings of the ONE Study consortium, as well as smaller departmental talks. The highlights are listed below:

Oral: Work Package 2: Tracking administered cells, ONE Study Annual Meeting 2012, Regensburg, Germany, 28/11/12 – 30/11/12.

Oral: Work Package 2: Tracking Administered cells, ONE Study Annual Meeting 2013, Regensburg, Germany, 20/11/13 - 22/11/13.

Poster: Single cell tracking by laser ablation ICP-MS, Winter Conference on Plasma Spectrochemistry, Amelia Island, Florida, USA, 06/01/14 – 11/01/14.

Oral: Single cell tracking of therapeutic cells by laser ablation ICP-MS, Loughborough University Research Network Meeting, Loughborough, UK, 21/05/14.

Oral: Single cell analysis using a fast-washout LA-ICP-MS interface, European Workshop on Laser Ablation, London, UK, 08/07/14 – 11/07/14. *Awarded the prize for the best oral presentation.*

7.4.3 Training

A list of the Loughborough University lectures, staff development courses, workshops and seminars attended during the course of the PhD is provided below:

Lectures: Atomic and Molecular Spectroscopy	26 & 28/10/10
Lectures: Mass Spectrometry and Associated Techniques	16, 23 & 30/11/10

Workshop: 9th East Midlands Proteomics Workshop	03/11/10
Workshop: Health and Life Sciences Conference	14/03/11
Workshop: 10th East Midlands Proteomics Workshop	02/11/11
Workshop: New advances in laser ablation (BGS, Keyworth)	20/04/12

Training course: Postgraduate Research Students Induction	02/11/10

Training course: Teaching skills: Preparing to teach	29/11/10
Training course: Teaching skills: Promoting learning	06/12/10
Training course: Teaching Skills: Supervising practical activities	08/02/11
Training course: Influencing: how to get out of your own way	18/03/11
Training course: Getting the most from the skills development programme	03/03/11
Training course: Getting the most out of supervision	28/03/11
Training course: Introduction to University laser safety	30/03/11
Training course: Designing and producing conference posters	07/04/11
Training course: Excel 2007 – Tables and lookup functions	18/05/11
Training course: Excel 2007 – Pivot tables and pivot charts	25/05/11
Training course: Networking skills: attending conferences	02/06/11
Training course: Speed reading for research students	07/06/11
Training course: Blood borne viruses and other pathogens	12/01/12
Training course: Copyright and your thesis	09/05/12
Training course: Introduction to the design of multi-factor experiments	30/05/12
Training course: Working effectively with outside organisations	17/10/12
Training course: Writing up your PhD thesis	24/04/13
Training course: VIVA – what happens?	14/05/13
Training course: Public engagement and research	22/05/13
Training course: Successful interviews	11/06/13
Training course: Academic job applications	12/11/13
Training course: Introduction to the job of lecturer for postgraduates and RA’s	19/11/13

Safety seminar: Good Laboratory Practice (Paul Thomas)	22/02/12
Safety seminar: Flammable materials (Anish Patel)	14/03/12
Safety seminar: Fire safety/extinguisher training (Rod Harrison)	16/04/12
Safety seminar: Liquefied gases, cryogenics (Claire Camp)	18/04/12
Safety seminar: Corrosive materials (Paul O’Hara)	23/05/12
Safety seminar: Pressurised gases (Shuo Kang)	06/06/12
Safety seminar: Electrical hazards (Iain Kirkpatrick)	05/07/12
Safety seminar: Radioactive materials and ionising radiation (Monica Felipe-Sotelo)	25/10/12
Safety seminar: Waste disposal (Nolwenn Derrien)	16/01/13

Research seminar: From Laboratory to Clinic - Analytical Chemistry in Action (Barry Sharp)	08/02/12
Research seminar: Mass spectrometry simplified: ambient ionization and miniature mass spectrometers (R. Graham Cooks)	23/02/12
Research seminar: Molecular recognition using functionalised nanoparticles (David Russell)	07/03/12
Research seminar: Semi-integration and electrochemistry (Keith Oldham)	27/03/12
Research seminar: From the electronics of molecules to molecular electronics (Paul Low)	30/05/12
Research seminar: Surface Mobility, Structure Modulation and Host-Guest Effects in Supramolecules (Jon Hill)	07/06/12
Research seminar: Dye-sensitised solar cells and thermoelectrics (Jorge Garcia-Cañadas)	21/09/12
Research seminar: Recent Advances in Total Synthesis and Asymmetric Catalysis (Patrick Guiry)	24/10/12
Research seminar: Novel Diagnostics and Sensors for Fuel Cells (Dan Brett)	23/01/13
Research seminar: Solid oxide fuel cells (John Irvine)	06/03/13
Research seminar: Managing the UK's Radioactive Waste Legacy (Francis Livens)	13/03/13

analytical chemistry

Editors' Highlight

pubs.acs.org/ac

Single Cell Tracking of Gadolinium Labeled CD4$^+$ T Cells by Laser Ablation Inductively Coupled Plasma Mass Spectrometry

Amy J. Managh,[†] Sheldon L. Edwards,[‡] Andrew Bushell,[‡] Kathryn J. Wood,[‡] Edward K. Geissler,[§] James A. Hutchinson,[§] Robert W. Hutchinson,[⊥] Helen J. Reid,[†] and Barry L. Sharp*,[†]

[†]Centre for Analytical Science, Department of Chemistry, Loughborough University, Loughborough, Leicestershire, LE11 3TU, United Kingdom

[‡]Nuffield Department of Surgical Sciences, University of Oxford, John Radcliffe Hospital, Headington, Oxford, OX3 9DU, United Kingdom

[§]Division of Experimental Surgery, Department of Surgery, University Hospital Regensburg, Regensburg, Bavaria, 93053, Germany

[⊥]Electro Scientific Industries, 8 Avro Court, Ermine Business Park, Huntingdon, Cambridgeshire, PE29 6XS, United Kingdom

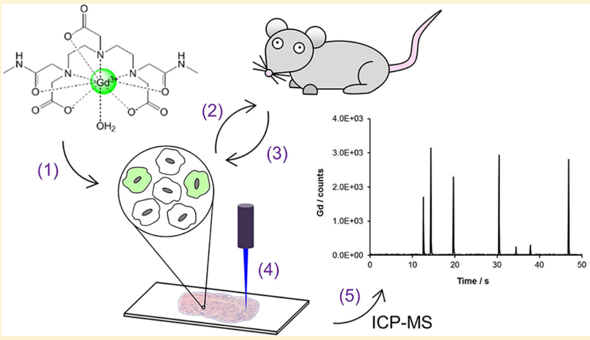

ABSTRACT: Cellular therapy is emerging as a promising alternative to conventional immunosuppression in the fields of hematopoietic stem cell (HSC) transplantation, autoimmune disease, and solid organ transplantation. Determining the persistence of cell-based therapies in vivo is crucial to understanding their regulatory function and requires the combination of an extremely sensitive detection technique and a stable, long-lifetime cell labeling agent. This paper reports the first application of laser ablation inductively coupled plasma mass spectrometry (LA-ICP-MS) to perform single cell detection of T cell populations relevant to cellular immunotherapy. Purified human CD4$^+$ T cells were labeled with commercially available Gd-based magnetic resonance imaging (MRI) contrast agents, Omniscan and Dotarem, which enabled passive loading of up to 10^8 Gd atoms per cell. In mixed preparations of labeled and unlabeled cells, LA-ICP-MS was capable of enumerating labeled cells at close to the predicted ratio. More importantly, LA-ICP-MS single cell analysis demonstrated that the cells retained a sufficient label to remain detectable for up to 10 days post-labeling both in vitro and in vivo in an immunodeficient mouse model.

Cellular therapy with defined populations of regulatory immune cells is emerging as a clinically viable strategy to augment or replace conventional immunosuppression in the fields of hematopoietic stem cell (HSC) transplantation, autoimmune disease, and solid organ transplantation where the major driver is improved therapy and a reduction in drug toxicities. Much of the optimism surrounding these approaches is based on data from a large number of diverse animal models which show unequivocally that cellular therapy can take advantage of endogenous regulatory mechanisms in the mammalian immune system.

Phase I/II clinical trials have evaluated naturally occurring regulatory T cells (nTreg), in the context of graft-versus-host-disease (GVHD), a life-threatening complication of HSC transplantation[1−3] and in pediatric patients with new-onset Type 1 diabetes.[4] In solid-organ transplantation, an international consortium is currently seeking regulatory approval for the evaluation of several types of regulatory immune cells in living-donor kidney transplantation. Cell types under investigation in this study will include nTreg,[5−7] Tr1 cells,[8,9] dendritic cells,[10] and macrophages.[11,12]

Determining the persistence and tissue distribution of the administered cells is essential for assessing their immunoregulatory effects in vivo, but tracking therapeutic cells presents two significant challenges. First, in the majority of cases, the cellular therapy will be derived from the transplant donor in HSC transplantation or from the recipient in the case of kidney transplantation. Thus, in most cases, the cells will be autologous with the immune system of the transplant recipient and therefore invisible to normal phenotypic methods of detection such as flow cytometry. Second, at current planned doses, the administered cells will represent a small fraction of the recipient's endogenous regulatory immune cells adding further to the problem of detection. A solution to these two related problems would be the development of clinically acceptable (GMP) cell labeling techniques combined with a sensitive detection method, capable of detection of single cells and at very high cell detection efficiency.

Contrast agents (CA) are frequently used in conjunction with clinical magnetic resonance imaging (MRI) to enhance the quality of images. These agents typically consist of a

Received: July 23, 2013
Accepted: September 30, 2013
Published: September 30, 2013

dx.doi.org/10.1021/ac4022715 | *Anal. Chem.* 2013, 85, 10627−10634

paramagnetic metal ion, such as Gd^{3+} or Fe^{2+}/Fe^{3+}, associated with a strong chelating ligand.[13] Gadolinium-based contrast agents are a particularly attractive option for cell labeling, due to their low background levels in the human body, and indeed several studies have reported their use as cellular labels for MRI tracking studies.[14−16] However, while MRI is undoubtedly valuable for bulk imaging, the technique is currently incapable of providing the necessary sensitivity and spatial resolution for single cell monitoring.

Laser ablation inductively coupled plasma mass spectrometry (LA-ICP-MS) is a sensitive analytical technique, widely used for mapping the distribution of elements in complex biological samples.[17] Examples include the analysis of copper and zinc in liver and kidney sections,[18,19] the mapping of copper, zinc, iron, and manganese in sections of brain tissue,[20−24] and the quantification of metal binding proteins in gels following electrophoretic separation of blood serum.[25] Recently, the technique has been applied to image the distribution of iodine, silver, and gold in single fibroblast cells, following labeling in vitro with KI_3 and gold and silver nanoparticles, respectively.[26,27] Studies have also reported the detection of gadolinium-based contrast agents in tumor and tissue samples.[28−30] Two of these investigations involved a direct comparison between LA-ICP-MS and MRI and demonstrated the enhanced sensitivity and spatial resolution achievable when using LA-ICP-MS.[29,30]

Although LA-ICP-MS clearly has remarkable sensitivity, application of this technique to cellular therapy depends upon cell labeling techniques that are likely to be approved for clinical use. In the current study, purified human $CD4^+$ T cells were labeled with the contrast agents, Omniscan (gadolinium diethylenetriaminepentaacetic acid bismethylamide, Gd-DTPA-BMA) or Dotarem (gadolinium 1,4,7,10-tetraazacyclododecane-1,4,7,10-tetracarboxylic acid, Gd-DOTA), that are both in routine clinical use in magnetic resonance imaging. We demonstrate that human $CD4^+$ T cells and highly purified naturally occurring regulatory T cells can be labeled efficiently with Gd-chelates and that the cells can then be readily detected in mixed populations using LA-ICP-MS. Importantly, both in vitro and in vivo, the cells retain a detectable label for at least 10 days. To the authors' knowledge, this is the first application of LA-ICP-MS to track single gadolinium labeled human T cells.

■ EXPERIMENTAL SECTION

Instrumentation and Operating Parameters. Analyses were performed on a sector-field ICP-MS instrument (Element 2XR, Thermo Scientific, Bremen, Germany). For solution analyses, the instrument was fitted with a cyclonic spray chamber (Glass Expansion, Victoria, Australia), a conical glass concentric nebulizer (Glass Expansion, Victoria, Australia), and a 0.25 mm I.D. probe (Elemental Scientific, Omaha, USA). For laser ablation, a UP-213 laser ablation system (Electro Scientific Industries, Cambridgeshire, UK) was coupled to the sector-field ICP-MS instrument. The laser system was fitted with a low-volume, tear-drop shaped cell, which has been described elsewhere.[31] Helium was used as an ablation gas, at a typical flow rate of 0.6 L/min, with argon introduced through a Y-piece, at a flow rate of 0.8 L/min, after the ablation cell. The system was tuned for maximum ^{238}U signal intensity, while keeping the Th/U ratio to approximately 1, during the ablation of NIST 611 glass. Typical operating conditions are given in Table 1.

Table 1. Typical Operating Conditions for ICP-MS and LA-ICP-MS Analyses

parameters	ICP-MS	LA-ICP-MS
ICP radio frequency (RF) power, W	1215	1260
cool gas flow rate, L min^{-1}	15.50	15.50
auxiliary gas flow rate, L min^{-1}	0.95	0.95
sample gas flow rate, L min^{-1}	0.90	0.80
sample uptake rate, μL min^{-1}	~70	
torch x position, mm	3.9	5.2
torch y position, mm	3.0	2.9
torch z position, mm	−2.5	−1.9
ablation gas flow, L min^{-1}		He, 0.60
laser spot size, μm		25−30
repetition frequency, Hz		1 (single shot)
laser power setting, %		50
laser fluence, J cm^{-2}		8.97

Cell Culture and Labeling. Human peripheral blood mononuclear cells (PBMC) were isolated from a leukocyte cone obtained from a local blood bank. Leukocytes were enriched by Ficoll density gradient centrifugation, and $CD4^+$ cells were isolated (~95−98% purity) by MACS positive selection (Miltenyi Biotec). To isolate defined populations to >98% purity, cells were labeled with anti-CD4 (Beckman-Coulter clone SFCI2T4D11), anti-CD25 (BD Biosciences clone M-A251), and anti-CD127 (BD Biosciences clone hIL-7R-M21) antibodies and flow-sorted on a BD FACSAria (BD Biosciences). After isolation, cells were plated at a density of 1 × 10^6 cells per well in 2 mL of RPMI 1640 medium, supplemented with 10% human albumin, penicillin, streptomycin, and glutamine, plus 1 × 10^5 U/mL human recombinant IL-2 (Proleukin, Novartis). Each well also received a volume of either Gd-DTPA-BMA (Omniscan, GE Healthcare, UK) or Gd-DOTA (Dotarem, Guerbet Laboratories, France). The cells were incubated overnight (~16 h) at 37 °C in 95% air/5% CO_2. Following the incubation period, the cells were washed extensively in PBS/2% FCS to remove any unbound label. Cell viability was determined using a trypan blue assay.

Optimization of the Labeling Dose and Incubation Time. Labeling optimization experiments for Gd-DOTA and Gd-DTPA were carried out in parallel using cells from the same donor. Cell culture and sample preparation were performed in accordance with the procedure detailed above. Quantification of label uptake by the cell population was determined using solution-based ICP-MS. For this, cells were spun down into pellets and then digested according to the method proposed by Yamada et al.[32] and modified by Kerr.[33] Briefly, this involved addition of 67% HNO_3 (100 μL per 1 × 10^6 cells) and heating at 70 °C for 1 h, followed by addition of 30% H_2O_2 (100 μL per 1 × 10^6 cells) and heating at 70 °C for a further 4 h. The samples were then evaporated to dryness under a stream of nitrogen and reconstituted in 2% HNO_3. A range of calibration standards were prepared by dilution of a 10 ppm elemental standard solution (SPEX Certiprep Ltd., Middlesex, UK).

For the dose optimization study, doses of 5, 10, 20, 50, 100, and 200 μL of either Omniscan or Dotarem were added to each well, prior to incubation overnight. This corresponds to 0.19, 0.38, 0.75, 1.86, 3.63, and 6.72 mg Gd/mL and 0.20, 0.39, 0.78, 1.92, 3.74, and 7.15 mg of Gd/mL, for the Omniscan and Dotarem wells, respectively. A total of three replicates were performed for each dose. In addition, three control wells containing cells without contrast agent were prepared.

Following dose optimization, the incubation time was varied using the optimum dose. Incubation times of 0, 1, 2, 4, 8, and 16 h were assessed in triplicate. The optimum dose and incubation time were then carried forward to subsequent experiments.

Laser Ablation of Single Cells. For laser ablation-ICP-MS, labeled cells were plated onto slides (Thermo Superfrost, Thermo Scientific, UK) using a CytoSpin (Shandon Cytospin, Thermo Scientific, UK). This was to ensure removal of the cell culture media and provide an even distribution of the cells across the slide, enabling single cell targeting. In addition to the slides containing labeled cells, control slides containing non-labeled CD4$^+$ cells were also prepared. Each slide held approximately 50 000 cells. Single cell identification was demonstrated by ablating 25 μm diameter areas at locations corresponding to cells. This size was chosen to ensure sampling of the complete cell, while minimizing the chance of overlap onto neighboring cells. Only single cells were targeted; cells present in clusters or closer than 25 μm apart were disregarded. The presence or absence of label was determined from the ^{157}Gd signal.

To simulate biological samples, where labeled cells are present among a background of non-labeled cells, slides containing mixed labeled and non-labeled cells were prepared. For these, the relevant dilutions were made in solution before fixing the cells onto slides. Ratios of 1:1, 1:10, and 1:100 were prepared as known samples, and a replicate of each was provided as a blind sample. Blind samples were randomized and identified with a nondescriptive character. The expected ratios of these were not disclosed to the analyst until after the analysis was completed.

In Vivo and in Vitro Label Retention. In order to demonstrate cellular retention of the label and assess its potential for cell tracking studies, a 10 day in vivo mouse study was conducted. All mouse experiments were conducted in accordance with the Animals (Scientific Procedures) Act 1986. Human peripheral blood mononuclear cells (PBMC) were isolated from leukocyte cones. The CD4$^+$ component was isolated using the procedure described above, and these cells were labeled using the optimized labeling procedure. Following labeling, the Gd-CD4$^+$ cells were washed extensively and recombined with the non-CD4$^+$ PBMC component. Remixing with the unlabeled PMBC component was found to be necessary to ensure viability of the cells in the host. The recombined cells were then injected intraperitoneally into BALB/C Rag-/-common-γ chain mice, at a level of 5 million cells per mouse. At 3, 6, and 10 days post infusion, the spleen and blood were harvested and a peritoneal lavage was performed. The extracted cells were plated onto slides for LA-ICP-MS analysis, using the CytoSpin method described above. Flow cytometry (BD FACSCanto, BD Biosciences) was used to determine the extent of human cell reconstitution.

To estimate the degree of signal loss caused by label leakage, an in vitro label retention study was performed in parallel to the in vivo mouse experiments, using cells from the same donor. For this, the cells were washed extensively after labeling and cultured for a further period in vitro before rewashing and plating onto slides.

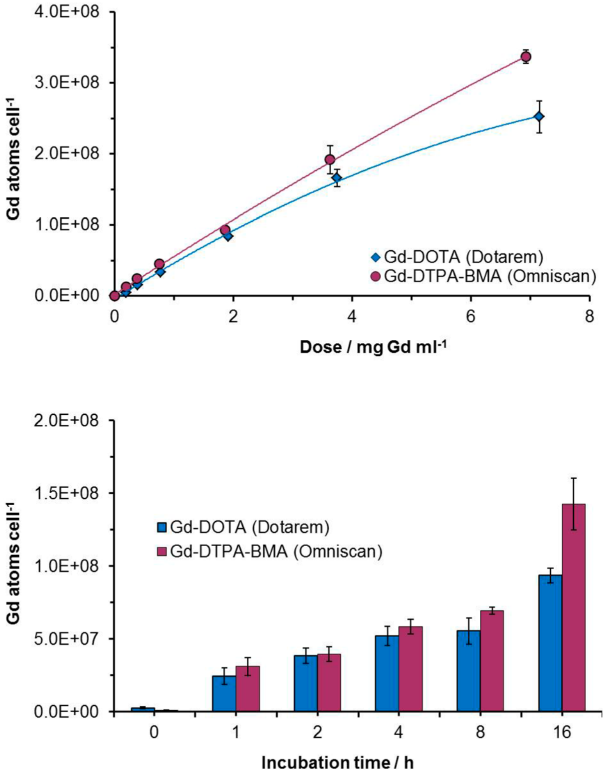

Figure 1. Relationship between the dose of Gd-DOTA and Gd-DTPA-BMA (top) and the incubation time (bottom) on the uptake of Gd atoms by human CD4$^+$ T cells. Uptake was determined using solution-based ICP-MS. Error bars show the standard error of the mean (n = 3).

■ RESULTS AND DISCUSSION

Label Uptake and Optimization. Figure 1 shows the impact of increasing the dose of gadolinium chelate on the uptake of Gd by human CD4$^+$ cells. Uptake of Gd increased in a dose-dependent manner. A quadratic fit with a low second order term fitted the data; however, no plateau was reached in the dose range examined. Despite the higher uptake at 100 and 200 μL, a dose of 50 μL was chosen as the optimum (this corresponds to 1.86 and 1.96 mg Gd/mL for Omniscan and Dotarem, respectively). Volumes higher than 50 μL occupied a significant portion of the 2 mL culture medium, which could potentially cause osmotic effects. However, it should be pointed out that the cell viability was 96% or above for all doses tested.

Gadolinium uptake also increased as a function of incubation time for both complexes, as shown in Figure 1. The highest uptake was observed after 16 h, which was used as the standard incubation time in all subsequent experiments. Longer incubation times were not tested on the grounds that they might have a detrimental effect on cell viability. As shown later, the labeling levels achieved were more than adequate for achieving ~100% detection efficiency. A 0 h time point was included in the study as a measure of the efficiency of the cell washing process. For this, the Gd complex was added to the well and the cells were washed immediately, thereby allowing insufficient time for label internalization. Consequently, any Gd found in these samples was taken to be from incomplete removal of the non-internalized complex and thus represents the background in the assay. The Gd content of the 0 h samples ranged between 5 and 20 times larger than that in the non-labeled controls. However, this figure represents only 0.7% and 3% of the final uptake achieved using the optimized labeling conditions for Gd-DTPA-BMA and Gd-DOTA, respectively. The cell washing procedure was therefore considered sufficient to enable quantification of label uptake. The optimization experiments, shown in Figure 1, indicated that Gd-DTPA-BMA provides higher net Gd loading than Gd-DOTA, with an average loading of 1.43×10^8 atoms per cell observed for Gd-DTPA-BMA compared to only 9.36×10^7 atoms per cell for Gd-DOTA at the optimized conditions. Therefore, Gd-DTPA-BMA was used in all subsequent experiments.

It is likely that uptake of the Gd complexes occurred predominately by pinocytosis, as has been reported for other cell lines.[34,35] Gadolinium internalized via this route is known to localize to endosomes within the perinuclear region of the cell,[34] where subsequent detachment of Gd^{3+} from its chelate may occur.[35] Dechelation is expected to be more prevalent for Omniscan than Dotarem. As shown in Figure 2, the DTPA-BMA chelate is non-ionic and has an open chain structure, hence providing less stable binding to Gd^{3+} than the macrocylic, ionic DOTA chelate.[36] Dechelation is accelerated in the presence of phosphate or competing cations,[37] both of which are constituents of the cell culture media. Thus, it is likely that, by the 16 h time point, a portion of the Gd in the culture media was also present as free rather than complexed Gd. Free Gd^{3+} ions may be subject to a different route of uptake than the complexed form. In 1999, Cheng et al. conducted a comprehensive study into the uptake of lanthanide 3+ ions by erythrocytes.[38] Gd^{3+} was found to bind initially to membrane phospholipids, followed by a transfer to membrane proteins. This process induced conformational changes in the membrane, which resulted in the formation of pores, facilitating the entry of Gd^{3+}. It is possible that this mechanism may have provided an additional route for Gd uptake. Since Gd-DTPA-BMA is known to be more unstable than Gd-DOTA, this additional route may account for the differences between Gd uptake for the two chelates, particularly at the 16 h time point.

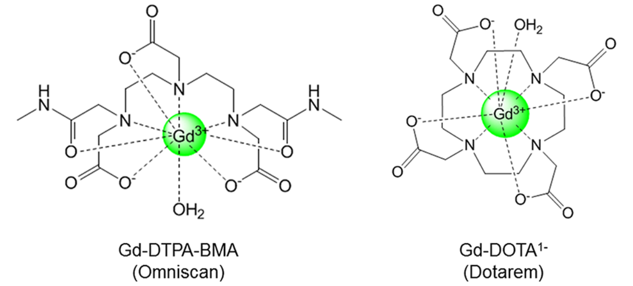

Figure 2. Structures of the commercially available contrast agents used for cell labeling.

The data shown in Figure 1 was obtained using cells isolated from human PBMC by magnetic negative selection of $CD19^+$ B cells and $CD14^+$ monocytes followed by CD4 positive selection. Phenotypic analysis showed that the resultant populations were between 95% and 98% $CD4^+$ T cells, but they also contained ~2−5% monocytes due to low level monocyte expression of CD4. In view of the fact that these cells are known to have very active phagocytic and pinocytic pathways, the possibility that the Gd labeling seen was due to preferential monocyte uptake could not be ruled out. To address this question, human $CD4^+$ T cells were purified by flow sorting to purities exceeding 99%, containing <0.2% $CD14^+$ monocytes (data not shown). The resultant populations were then labeled using the optimized Gd-DTPA-BMA protocol described above. Subsequent analysis showed a gadolinium uptake of 4.53×10^7 atoms per cell for 99.6% pure $CD4^+$ T cells, compared with the 1.43×10^8 atoms per cell seen for the lower purity (~95−98%) $CD4^+$ T cells.

Most of the initial focus on regulatory immune cellular therapy has been and will continue to be on naturally occurring Treg (nTreg).[5−7] Although these cells represent only ~5−10% of $CD4^+$ T cells in human peripheral blood, the actual proportion and function varies considerably between individuals. To determine the likely variability in Gd labeling of functional nTreg, human $CD4^+CD25^+CD127^{lo}$ T cells were flow sorted from three different individuals using a sort strategy known to isolate nTreg with high functional activity both in vitro and in humanized mouse models.[39,40] The resultant populations (purity 97.9%, 98.5%, and 98.1%, donors 1−3, respectively) were then labeled with the optimized Gd-DTPA-BMA protocol and analyzed as described. The labeling of these nTreg showed remarkable consistency with 5.06×10^7, 5.08×10^7, and 5.88×10^7 Gd atoms per cell detected from donors 1−3, respectively.

The above data show unequivocally that populations of non-phagocytic human T cells being considered for cellular therapy can be labeled with gadolinium chelates, thus offering a potential approach for therapeutic T cell tracking. However, determining the persistence of gadolinium-labeled T cells in accessible tissues such as the peripheral blood is potentially compromised by the presence of highly phagocytic cells such as granulocytes, neutrophils, and monocytes. Positive selection on the basis of CD4 would allow enrichment of populations likely to contain administered nTreg but, as described above, monocytes would present a problem since they might phagocytose gadolinium from dying circulating T cells, thereby giving false positives. Although flow sorting to >99% T cell homogeneity is a valuable research approach, cell losses would preclude this as a diagnostic strategy. Therefore, laser ablation-ICP-MS was evaluated for the ability to identify labeled targets at a single cell level where the ablation of specific, individual cells could provide a key advantage not available from solution analysis.

Laser Ablation of Single Cells. Human $CD4^+$ T cells were purified by positive selection (final purity, 97.2%) and labeled with Gd-DTPA-BMA as described. Unlabeled cells cultured for 16 h in the presence of IL-2 served as a negative control. Figure 3 shows the ^{157}Gd signal intensities for the ablation of 25 individual labeled cells (A) and 25 individual unlabeled cells (B) after deposition onto slides by centrifugation. Distinct signals were observed for the ablation of the labeled cells, compared to only background noise for their non-labeled counterparts. The 25 μm spot size and ~9 J cm^{-2} fluence used in these experiments ensured complete ablation of each ~10 μm cell in less than a second; see Figure 4. Therefore, each signal observed can be regarded as representative of the total amount of Gd per individual cell. Figure 5 is a histogram showing the variation in label uptake observed when ablating 1000 individual labeled cells taken from the same labeled population as used in Figure 3. For this, the ^{157}Gd signal intensities were grouped into classes, with the number of occurrences for each class plotted on the y-axis. Of the 1000 cells ablated, 998 gave clear signals, confirming uptake of Gd by human $CD4^+$ T cells. In the range of $0−1.5 \times 10^4$ counts, the distribution of signals was approximately Gaussian, with a RSD of 39%. A small percentage (1.6%) of signals occurred outside this region. These higher signals are likely to correspond to the ablation of monocytes. Accordingly, the number of high signals

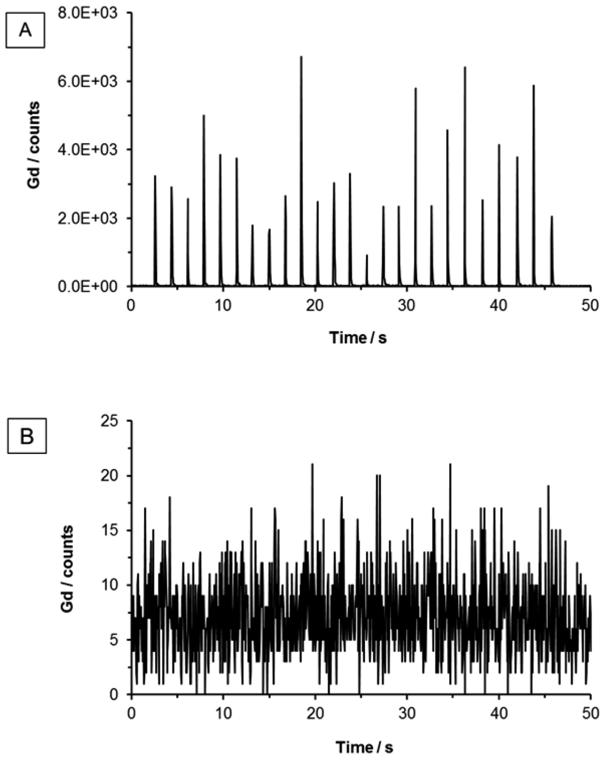

Figure 3. Signal intensities obtained when performing LA-ICP-MS on (A) 25 single Gd-DTPA-BMA labeled human CD4$^+$ T cells and (B) 25 single non-labeled human CD4$^+$ T cells.

observed matches closely with the proportion of contaminating CD14$^+$ monocytes (2.8%) in the input cell population.

Application of the technique to cell tracking requires discrimination of labeled cells from a background of non-labeled cells. In a demonstration experiment, labeled CD4$^+$ T cells were mixed with non-labeled CD4$^+$ T cells in various ratios, prior to analysis by LA-ICP-MS. As shown in Table 2, the percentage labeled as determined by LA-ICP-MS matched approximately with the prepared ratios, with differences accounted for by a combination of incomplete mixing and pipetting errors. As a further test of the technique, blind ratios of labeled and unlabeled CD4$^+$ T cells were prepared and the blinding was only revealed after LA-ICP-MS analysis. As shown in Table 2, ratios observed from the blind experiments corresponded with the expected ratios, adding further confirmation to the reliability of the technique.

In Vivo and in Vitro Label Retention. In addition to detection, a second key characteristic for any label considered for in vivo cell tracking is label retention. Therefore, Gd-DTPA-BMA labeled CD4$^+$ T cells were cultured in vitro in gadolinium-free T cell growth medium containing IL-2 and samples taken daily for LA-ICP-MS analysis. As shown in Table 3, although the average signal intensities fell with time, reaching roughly 50% of the day 1 value after 10 days, the label remained detectable at all time points examined, with 98.8% of cells retaining sufficient Gd for detection up to 10 days in culture. In view of the low background signals observed for non-labeled cells, it seems likely that Gd labeled cells should be detectable for periods well beyond 10 days.

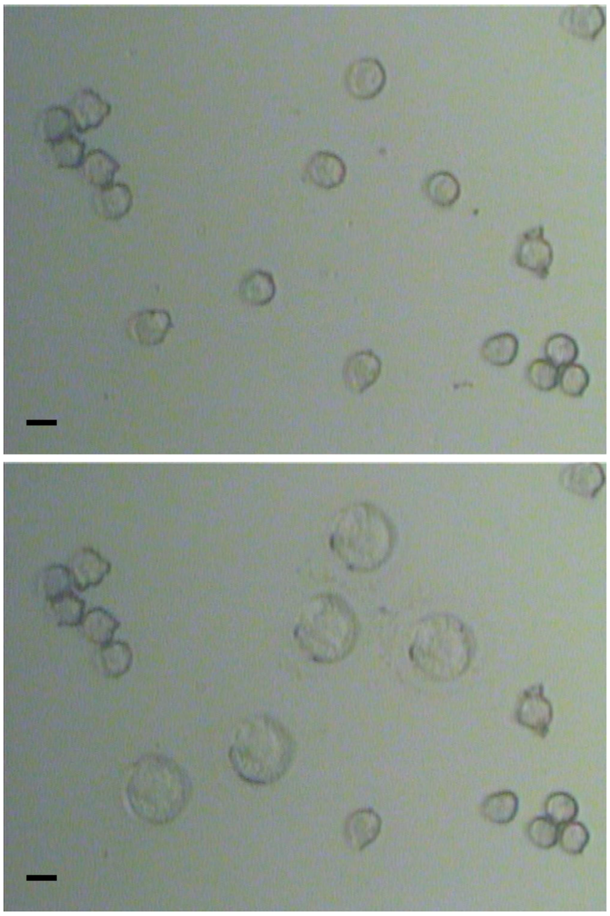

Figure 4. Images showing slide mounted cells before (top) and after (bottom) the ablation of five single cells. The scale bar is 10 μm.

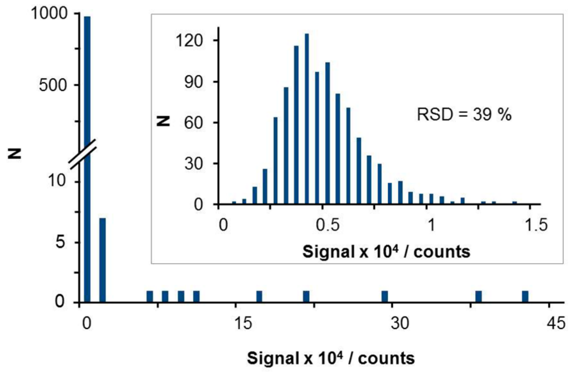

Figure 5. Histogram showing the distribution of ^{157}Gd signal intensities for the ablation of 1000 Gd labeled cells. It is speculated that the human CD4+ cells (97.2% pure in the total cell population) are present within the first peak, with signals outside this range (1.6% of the signals observed) corresponding to the ablation of phagocytic monocytes. The inset shows the expanded view of the distribution within the first peak.

Although in vitro label retention is encouraging, a more important question with respect to cellular therapy is whether cells retain a gadolinium signal in vivo. To address this question, we took advantage of a well characterized humanized mouse model in which immunodeficient BALB/c mice lacking T cells, B cells, and functional NK cells are reconstituted with defined populations of human immune cells.[39] These double knockout (DKO) mice were reconstituted intraperitoneally with 2 × 10^6 Gd-DTPA-BMA labeled CD4$^+$ T cells together with 3 × 10^6 autologous PBMC which aid T cell reconstitution by providing essential T cell growth and survival factors. At 3, 6,

Table 2. Percentage of Gd Labeled Cells Observed When Performing Single Cell LA-ICP-MS on Slides Containing Various Ratios of Gd Labeled to Non-labeled Human CD4$^+$ T Cells[a]

	labeled/non-labeled ratio	% labeled cells identified	% labeled cells expected
known	1:0	99.8	100
	1:1	39.6	50
	1:10	5.5	9.1
	1:100	0.6	1
	0:1	0.1	0
blind	1:1	39.1	50
	1:10	5.2	9.1
	1:100	0.7	1

[a] Labeled cells were identified on the basis of their ^{157}Gd signal. 1000 cells were ablated per sample.

Table 3. Number of Gd Labeled Human CD4$^+$ Cells Observed after Various Periods of in Vitro Culture, Following Labeling with the Gd Chelate Omniscan[a]

day	% Gd labeled cells observed	average signal/counts
1	100	4118
2	100	3296
3	100	2901
4	99.6	2959
5	100	2744
6	100	2473
7	99.6	2220
10	98.8	2014

[a] Individual cells (250 per sample) were analysed by LA-ICP-MS. Labeled cells were identified on the basis of their ^{157}Gd signal.

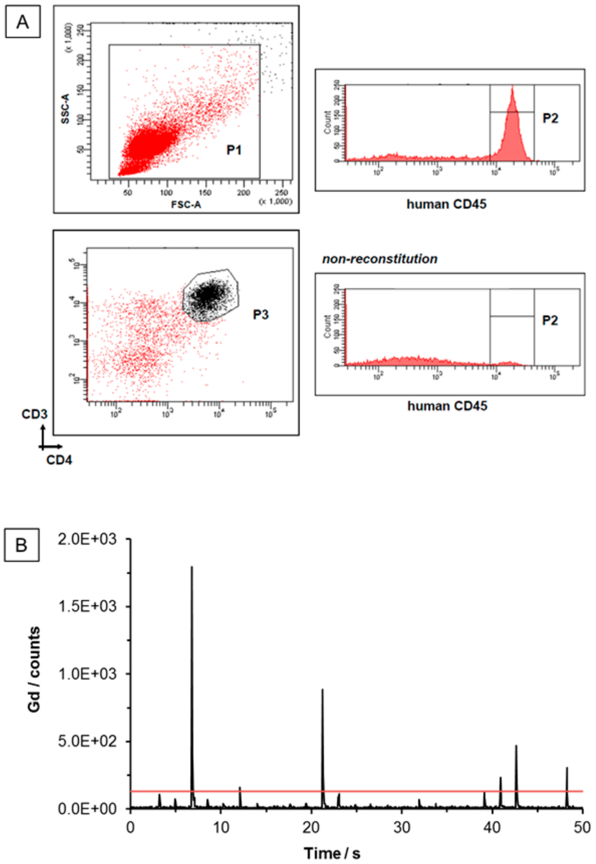

Figure 6. Human CD4$^+$ T cells (purity 97.2%) were labeled with Gd-DTPA-BMA, washed extensively, and administered intraperitoneally (2 × 10^6) to BALB/c immunodeficient mice together with 3 × 10^6 autologous PBMC. Peritoneal lavage samples were collected for flow cytometry (A) and LA-ICP-MS analysis (B). (A) Day 6 lavage data: one of three mice shown; upper left panel: leucocyte gate; upper right panel: readily detected human CD45$^+$ cells (P2 gate); lower left panel: human CD3$^+$CD4$^+$ T cells within the gated CD45$^+$ population confirming CD4$^+$ T cell reconstitution. For comparison, lower right panel shows another of the three mice with no evidence of human cell reconstitution. (B) Example data from the reconstituted lavage shown in (A) (day 6, mouse 5 lavage), showing the presence of 6 Gd labeled cells. Small peaks below the threshold value (red line) were not included in the % labeled count.

and 10 days after reconstitution, the mice were killed for recovery of the peritoneal lavage, spleen, and blood. Reconstitution in this model is defined as >1% human CD45$^+$ cells in the leucocyte gate as determined by flow cytometry.[39] In agreement with previous experience of this model which showed that reconstitution of spleen and blood lags behind that of the peritoneal lavage, human cells were not found in the spleen or blood up to day 10 (not shown). However, human CD45$^+$ cells were readily detected in the peritoneal lavage. Example data for one of three mice harvested 6 days after cell administration is shown in Figure 6A. For comparison, the lower histogram shows an example of non-reconstitution. As shown in the lower dot plot, region P3 confirms the presence of human CD4$^+$ T cells within the human CD45$^+$ gate.

Aliquots of each lavage sample were plated without cell purification onto slides for LA-ICP-MS analysis. Figure 6B shows an LA-ICP-MS plot from the lavage sample in Figure 6A showing identification of 5 gadolinium labeled cells. It is notable that, while cells analyzed after in vitro culture were relatively uniform in size, those examined from the lavage samples contained significant numbers of blasting cells possibly representing T cells mounting a xenogeneic graft-versus-host response. To accommodate the larger cell diameters, the ablation spot size was increased from 25 to 30 μm. However, increasing the spot size made the selection of single cells more challenging and it is possible that some of the low signals in Figure 6B were caused by slight overlap of the ablated region with the edges of neighboring labeled cells. To account for the low signals, a threshold value was set at 5% of the average signal intensity of the corresponding in vitro sample. Signals below this threshold were not included in the % labeled count.

Table 4 summarizes the in vivo Gd retention data for day 3, day 6, and day 10 following the administration of labeled CD4$^+$ T cells and shows the percentage of labeled cells found in the mouse lavage samples. In each case, the detection of Gd labeled cells by LA-ICP-MS correlated with the presence of human CD4$^+$ T cells in the lavage. Furthermore, at the last time point examined when only two mice were available (day 10), both showed clear reconstitution and gadolinium positive cells were unambiguously detected (Table 4). Thus, both the in vitro and the in vivo data indicate that, when labeled with Gd-DTPA-BMA, human CD4$^+$ T cells retain a detectable gadolinium level for at least 10 days.

Nephrogenic Systemic Fibrosis. The potential use of gadolinium labeling for tracking immune cellular therapies would depend on a favorable toxicity profile for the label itself and while Gd-chelates are widely used in clinical MRI, one significant complication of in vivo gadolinium administration is

Table 4. Percentage of Gd Labeled Cells in Ex Vivo Mouse Lavage Samples, Following Infusion of 5 Million Gd Labeled Human CD4$^+$ Cells[a]

mouse	day	% Gd positive cells (by LA-ICP-MS)	human cell reconstitution (by flow cytometry)
1	3	13.2	not detected
2	3	66.4	positive
3	3	14.0	not detected
4	6	2.0	not detected
5	6	35.6	positive
6	6	48.4	positive
7	10	20.4	positive
8	10	49.2	positive

[a] Individual cells (250 per sample) were analysed by LA-ICP-MS. Labeled cells were identified on the basis of their ^{157}Gd signal. Human cell reconstitution was determined by flow cytometry (BD FACSCanto, BD Biosciences).

nephrogenic systemic fibrosis (NSF). Although rare, this condition is potentially fatal and is characterized by "extensive thickening and hardening of the skin".[41] Studies on patients with impaired renal function have found a link between the intravenous administration of gadolinium chelates and the onset of NSF.[42,43] Consequently, the administration of gadolinium contrast agents for MRI imaging is contra-indicated in patients with renal impairment. Thus, any proposed use of gadolinium labeling should be treated with caution, particularly since regulatory approval is currently being sought for cellular therapy in renal transplant patients.[44] However, it is important to note that, at the anticipated cell doses used in this study (3×10^6/kg patient body weight), the Gd exposure from the proposed labeling method is dramatically lower than that received during a typical MRI scan. When taking into account the average cell uptake shown in the current study of ~27 fg and the anticipated cell dose, the likely Gd exposure from cell labeling is ~81 ng/kg. This is over 100,000 times lower than the 15.2 mg/kg dose employed for MRI imaging. (Omniscan is typically administered at a level of 0.2 mL per kg patient weight; the formulation contains 287 mg/mL Gd-DTPA-BMA, which equates to 76.1 mg/mL Gd.) The risk is further minimized due to the route of administration, since for cell labeling, the gadolinium chelates are essentially compartmentalized inside the cells rather than being introduced into the systemic circulation.

CONCLUSION

This paper represents the first application of LA-ICP-MS to perform single cell tracking of therapeutically administered cells. The technique was demonstrated on an immunodeficient mouse model, where the Gd-DTPA-BMA label allowed discrimination of human CD4$^+$ cells for up to 10 days post-administration. A working dose of 50 μL of Omniscan/2 mL well (1.86 mg Gd/ml) was used for cell labeling, which was based on sufficiency for cell tracking. However, since Gd cell content decreases with each cell division, it may be beneficial to increase this dose when performing longer term tracking experiments. Doses of up to 200 μL of Omniscan (6.72 mg Gd/ml) were utilized during the solution study without noticeable impact on cell viability. Assessment of the effect of Gd-DTPA-BMA on the regulatory function of T cells will be the subject of a future study.

The LA-ICP-MS detection method has several advantages over other cell tracking techniques. First, elemental detection does not rely on stable binding of Gd^{3+} to the chelate; thus, the label can be detected at periods where its enhancement on MRI relaxation would be lost. Second, the use of laser ablation allows single cell targeting, removing interferences from other artifacts, and also has the potential to track cells in tissue biopsies. Third, the superior detection capability of sector field ICP-MS allows detection at levels of 10^7 atoms per cell and below, compared to the value of 10^8 atoms per cell recently reported for molecular mass spectrometry.[35] With improved instrumentation, which will be described in another paper, and the use of higher efficiency mass spectrometers, it should be possible to improve this detection limit by 2–3 orders of magnitude. A further advantage of the technique is that, if combined with fluorescently labeled antibody staining, it would be possible to target ablation to specific and defined cell subsets in a sample of peripheral blood or tissue biopsy and provide semi-quantitative data. If applied to the tracking of Gd-labeled CD4$^+$CD25$^+$ nTreg in vivo, it would thus be possible to define the proportion of cell therapy nTreg within the total CD4$^+$ T cell compartment. If immune cellular therapy is to progress beyond the current phase I/II trials, such quantification will probably prove to be essential.

LA-ICP-MS, as demonstrated here, is an exciting research tool, which has the potential to provide new insights into cellular therapy, and will be a key enabling technique for the development of the field of single cell metallomics. However, improvements to increase throughput are necessary before the technique can be considered for routine analysis in the clinical setting. Current LA-ICP-MS instrumentation has a data rate of approximately 1–5 pixels per second, limited by the LA cell–mass spectrometer interface. Developments to improve the efficiency of this region, and hence increase the speed of data acquisition, will be reported in a subsequent paper.

AUTHOR INFORMATION

Corresponding Author

*E-mail: B.L.Sharp@lboro.ac.uk.

Notes

The authors declare no competing financial interest.

ACKNOWLEDGMENTS

Support received from the ONE Study, a European Commission Seventh Framework Program funded project (EU FP7-HEALTH "The ONE Study", Project reference 260687), and the British Heart Foundation PG 10/62/28504 is gratefully acknowledged.

REFERENCES

(1) Trzonkowski, P.; Bieniaszewska, M.; Juscinska, J.; Dobyszuk, A.; Krzystyniak, A.; Marek, N.; Mysliwska, J.; Hellmann, A. *Clin. Immunol.* **2009**, *133*, 22–26.

(2) Brunstein, C. G.; Miller, J. S.; Cao, Q.; McKenna, D. H.; Hippen, K. L.; Curtsinger, J.; DeFor, T.; Levine, B. L.; June, C. H.; Rubinstein, P.; McGlave, P. B.; Blazar, B. R.; Wagner, J. E. *Blood* **2011**, *117*, 1061–1070.

(3) Di Ianni, M.; Falzetti, F.; Carotti, A.; Terenzi, A.; Castellino, F.; Bonifacio, E.; Del Papa, B.; Zei, T.; Ostini, R. I.; Cecchini, D.; Aloisi, T.; Perruccio, K.; Ruggeri, L.; Balucani, C.; Pierini, A.; Sportoletti, P.; Aristei, C.; Falini, B.; Reisner, Y.; Velardi, A.; Aversa, F.; Martelli, M. F. *Blood* **2011**, *117*, 3921–3928.

(4) Marek-Trzonkowska, N.; Mysliwiec, M.; Dobyszuk, A.; Grabowska, M.; Techmanska, I.; Juscinska, J.; Wujtewicz, M. A.;

Witkowski, P.; Mlynarski, W.; Balcerska, A.; Myslinwska, J.; Trzonkowski, P. *Diabetes Care* **2012**, *35*, 1817−1820.

(5) Sakaguchi, S.; Yamaguchi, T.; Nomura, T.; Ono, M. *Cell* **2008**, *133*, 775−787.

(6) McMurchy, A. N.; Bushell, A.; Levings, M. K.; Wood, K. J. *Semin. Immunol.* **2011**, *23*, 304−313.

(7) Wood, K. J.; Bushell, A.; Hester, J. *Nat. Rev. Immunol.* **2012**, *12*, 417−430.

(8) Groux, H.; Ogarra, A.; Bigler, M.; Rouleau, M.; Antonenko, S.; deVries, J. E.; Roncarolo, M. G. *Nature* **1997**, *389*, 737−742.

(9) Battaglia, M.; Gregori, S.; Bacchetta, R.; Roncarolo, M. G. *Semin. Immunol.* **2006**, *18*, 120−127.

(10) Peche, H.; Trinite, B.; Martinet, B.; Cuturi, M. C. *Am. J. Transplant.* **2005**, *5*, 255−267.

(11) Hutchinson, J. A.; Riquelme, P.; Sawitzki, B.; Tomiuk, S.; Miqueu, P.; Zuhayra, M.; Oberg, H. H.; Pascher, A.; Lutzen, U.; Janssen, U.; Broichhausen, C.; Renders, L.; Thaiss, F.; Scheuermann, E.; Henze, E.; Volk, H. D.; Chatenoud, L.; Lechler, R. I.; Wood, K. J.; Kabelitz, D.; Schlitt, H. J.; Geissler, E. K.; Fandrich, F. *J. Immunol.* **2011**, *187*, 2072−2078.

(12) Riquelme, P.; Tomiuk, S.; Kammler, A.; Fandrich, F.; Schlitt, H. J.; Geissler, E. K.; Hutchinson, J. A. *Mol. Ther.* **2013**, *21*, 409−422.

(13) Kamaly, N.; Miller, A. D. *Int. J. Mol. Sci.* **2010**, *11*, 1759−1776.

(14) Shyu, W. C.; Chen, C. P.; Lin, S. Z.; Lee, Y. J.; Li, H. *Stroke* **2007**, *38*, 367−374.

(15) Guenoun, J.; Koning, G. A.; Doeswijk, G.; Bosman, L.; Wielopolski, P. A.; Krestin, G. P.; Bernsen, M. R. *Cell Transplant.* **2012**, *21*, 191−205.

(16) Kalliokoski, T.; Svedström, E.; Saunavaara, J.; Roivainen, A.; Kankaanpää, M.; Oivanen, H.; Nuutila, P.; Simell, O. *Adv. Mol. Imaging* **2011**, *1*, 43−49.

(17) Becker, J. S.; Zoriy, M.; Matusch, A.; Wu, B.; Salber, D.; Palm, C. *Mass Spectrom. Rev.* **2010**, *29*, 156−175.

(18) Feldmann, J.; Kindness, A.; Ek, P. *J. Anal. At. Spectrom.* **2002**, *17*, 813−818.

(19) Kindness, A.; Sekaran, C. N.; Feldmann, J. *Clin. Chem.* **2003**, *49*, 1916−1923.

(20) Jackson, B.; Harper, S.; Smith, L.; Flinn, J. *Anal. Bioanal. Chem.* **2006**, *384*, 951−957.

(21) Dehnhardt, M.; Zoriy, M.; Khan, Z.; Reifenberger, G.; Ekstrom, T.; Becker, J. S.; Zilles, K.; Bauer, A. *J. Trace Elem. Med. Biol.* **2008**, *22*, 17−23.

(22) Hare, D.; Reedy, B.; Grimm, R.; Wilkins, S.; Volitakis, I.; George, J. L.; Cherny, R. A.; Bush, A. I.; Finkelstein, D. I.; Doble, P. *Metallomics* **2009**, *1*, 53−58.

(23) Hare, D. J.; George, J. L.; Grimm, R.; Wilkins, S.; Adlard, P. A.; Cherny, R. A.; Bush, A. I.; Finkelstein, D. I.; Doble, P. *Metallomics* **2010**, *2*, 745−753.

(24) Matusch, A.; Depboylu, C.; Palm, C.; Wu, B.; Hoglinger, G. U.; Schafer, M. K. H.; Becker, J. S. *J. Am. Soc. Mass Spectrom.* **2010**, *21*, 161−171.

(25) Neilsen, J. L.; Abildtrup, A.; Christensen, J.; Watson, P.; Cox, A.; McLeod, C. W. *Spectrochim. Acta, Part B: At. Spectrosc.* **1998**, *53*, 339−345.

(26) Giesen, C.; Waentig, L.; Mairinger, T.; Drescher, D.; Kneipp, J.; Roos, P. H.; Panne, U.; Jakubowski, N. *J. Anal. At. Spectrom.* **2011**, *26*, 2160−2165.

(27) Drescher, D.; Giesen, C.; Traub, H.; Panne, U.; Kneipp, J.; Jakubowski, N. *Anal. Chem.* **2012**, *84*, 9684−9688.

(28) Hsieh, Y. K.; Jiang, P. S.; Yang, B. S.; Sun, T. Y.; Peng, H. H.; Wang, C. F. *Anal. Bioanal. Chem.* **2011**, *401*, 909−915.

(29) Kamaly, N.; Pugh, J. A.; Kalber, T. L.; Bunch, J.; Miller, A. D.; McLeod, C. W.; Bell, J. D. *Mol. Imaging Biol.* **2010**, *12*, 361−366.

(30) Pugh, J. A. T.; Cox, A. G.; McLeod, C. W.; Bunch, J.; Writer, M. J.; Hart, S. L.; Bienemann, A.; White, E.; Bell, J. *Anal. Bioanal. Chem.* **2012**, *403*, 1641−1649.

(31) Horstwood, M. S. A.; Foster, G. L.; Parrish, R. R.; Noble, S. R.; Nowell, G. M. *J. Anal. At. Spectrom.* **2003**, *18*, 837−846.

(32) Yamada, K.; Kato, N.; Takagi, A.; Koi, M.; Hemmi, H. *Anal. Bioanal. Chem.* **2005**, *382*, 1702−1707.

(33) Kerr, S. L. Ph.D. Thesis, Loughborough University, 2008.

(34) Terreno, E.; Crich, S. G.; Belfiore, S.; Biancone, L.; Cabella, C.; Esposito, G.; Manazza, A. D.; Aime, S. *Magn. Reson. Med.* **2006**, *55*, 491−497.

(35) Di Gregorio, E.; Gianolio, E.; Stefania, R.; Barutello, G.; Digilio, G.; Aime, S. *Anal. Chem.* **2013**, DOI: 10.1021/ac400973q.

(36) Idee, J. M.; Port, M.; Robic, C.; Medina, C.; Sabatou, M.; Corot, C. *J. Magn. Reson. Imaging* **2009**, *30*, 1249−1258.

(37) Robic, C.; Catoen, S.; Goltstein, D. M.-C.; Idee, J.-M.; Port, M. *Biometals* **2011**, *24*, 759−768.

(38) Cheng, Y.; Yao, H. Y.; Lin, H. K.; Lu, J. F.; Li, R. C.; Wang, K. *Chem.-Biol. Interact.* **1999**, *121*, 267−289.

(39) Nadig, S. N.; Wieckiewicz, J.; Wu, D. C.; Warnecke, G.; Zhang, W.; Luo, S.; Schiopu, A.; Taggart, D. P.; Wood, K. J. *Nat. Med.* **2010**, *16*, 809−U112.

(40) Issa, F.; Hester, J.; Goto, R.; Nadig, S. N.; Goodacre, T. E.; Wood, K. *Transplantation* **2010**, *90*, 1321−1327.

(41) Cowper, S. E.; Robin, H. S.; Steinberg, S. M.; Su, L. D.; Gupta, S.; LeBoit, P. E. *Lancet* **2000**, *356*, 1000−1001.

(42) Grobner, T. *Nephrol., Dial., Transplant.* **2006**, *21*, 1104−1108.

(43) Marckmann, P.; Skov, L.; Rossen, K.; Dupont, A.; Damholt, M. B.; Heaf, J. G.; Thomsen, H. S. *J. Am. Soc. Nephrol.* **2006**, *17*, 2359−2362.

(44) www.onestudy.org (accessed 04/05/12).

■ NOTE ADDED AFTER ASAP PUBLICATION

After this paper was published ASAP on October 3, 2013, a correction was made to the funding information in the Acknowledgment. The corrected version was reposted November 19, 2013.

Laser Ablation–Inductively Coupled Plasma Mass Spectrometry: An Emerging Technology for Detecting Rare Cells in Tissue Sections

Amy J. Managh,* Robert W. Hutchinson,[†] Paloma Riquelme,[‡] Christiane Broichhausen,[‡] Anja K. Wege,[§] Uwe Ritter,[¶] Norbert Ahrens,[‖] Gudrun E. Koehl,[‡] Lisa Walter,[‡] Christian Florian,[‡] Hans J. Schlitt,[‡] Helen J. Reid,* Edward K. Geissler,[‡] Barry L. Sharp,* and James A. Hutchinson[‡]

Administering immunoregulatory cells to patients as medicinal agents is a potentially revolutionary approach to the treatment of immunologically mediated diseases. Presently, there are no satisfactory, clinically applicable methods of tracking human cells in patients with adequate spatial resolution and target cell specificity over a sufficient period of time. Laser ablation–inductively coupled plasma mass spectrometry (LA-ICP-MS) represents a potential solution to the problem of detecting very rare cells in tissues. In this article, this exquisitely sensitive technique is applied to the tracking of gold-labeled human regulatory macrophages (Mregs) in immunodeficient mice. Optimal conditions for labeling Mregs with 50-nm gold particles were investigated by exposing Mregs in culture to variable concentrations of label: Mregs incubated with 3.5×10^9 particles/ml for 1 h incorporated an average of 3.39×10^8 Au atoms/cell without loss of cell viability. Analysis of single, gold-labeled Mregs by LA-ICP-MS registered an average of 1.9×10^5 counts/cell. Under these conditions, 100% labeling efficiency was achieved, and label was retained by Mregs for ≥36 h. Gold-labeled Mregs adhered to glass surfaces; after 24 h of culture, it was possible to colabel these cells with human-specific ^{154}Sm-tagged anti–HLA-DR or ^{174}Yb-tagged anti-CD45 mAbs. Following injection into immunodeficient mice, signals from gold-labeled human Mregs could be detected in mouse lung, liver, and spleen for at least 7 d by solution-based inductively coupled plasma mass spectrometry and LA-ICP-MS. These promising results indicate that LA-ICP-MS tissue imaging has great potential as an analytical technique in immunology. ***The Journal of Immunology*, 2014, 193: 000–000.**

Administration of regulatory or suppressor cell populations to nontolerant recipients as a means of establishing tolerance is a well-known technique in experimental immunology, but its clinical application is only now being seriously investigated (1). In principle, a broad spectrum of immunological conditions might be amenable to treatment with cell-based immunoregulatory therapies, including T cell–mediated autoimmune diseases (2, 3), chronic inflammatory conditions (4), graft-versus-host disease (5), and solid organ transplant rejection (6). In such conditions, cell-based immunoregulatory therapies might reduce or obviate the need for conventional immunosuppressive therapy, sparing patients its attendant complications. Moreover, because tolerance achieved through peripheral regulation (as opposed to purely deletional mechanisms or immunological ignorance) is dominant and self-sustaining, there exists the staggering possibility that cell-based immunotherapy might offer curative treatments for diseases that would otherwise require long-term general immunosuppressive therapy (7).

Several immunoregulatory cell types are now reaching the point of preclinical development that would allow them to be investigated as immunosuppressive agents in early-phase clinical trials (8–11). One particularly promising candidate cell type for use as an adjunct immunosuppressive agent in transplantation is the regulatory macrophage (Mreg) (12). The Mreg reflects a unique state of macrophage differentiation, distinguished from macrophages in other activation states by its mode of derivation, robust phenotype, and potent T cell suppressor function (13). Mregs potently suppress mitogen-stimulated T cell proliferation in vitro, which can be attributed to IFN-γ–induced IDO activity, as well as contact-dependent deletion of activated T cells. In addition, Mregs drive the development of activated induced regulatory T cells that, in turn, suppress the proliferation of effector T cells and inhibit the maturation of monocyte-derived dendritic cells in response to TNF-α (14). Therefore, it is thought that when Mregs are administered to an allogeneic recipient they can initiate a feed-forward loop of immunological regulation, potentially leading to the long-term acceptance of a foreign transplant (15).

To use any therapeutic agent safely and effectively, clinicians must be able to predict its effectiveness and safety in individual patients (16). An important determinant of the biological effect and safety of any therapeutic cell product is its pharmacokinetics

---

*Centre for Analytical Science, Department of Chemistry, Loughborough University, Loughborough, Leicestershire LE11 3TU, United Kingdom; [†]Electro Scientific Industries, Huntingdon, Cambridgeshire PE29 6XS, United Kingdom; [‡]Division of Experimental Surgery, Department of Surgery, University Hospital Regensburg, Regensburg 93053, Germany; [§]Department of Obstetrics and Gynaecology, University Hospital Regensburg, Regensburg 93053, Germany; [¶]Institute for Immunology, University of Regensburg, Regensburg 93053, Germany; and [‖]Department of Transfusion Medicine, University Hospital Regensburg, Regensburg 93053, Germany

Received for publication April 3, 2014. Accepted for publication June 22, 2014.

This work was supported by the European Union 7th Framework Programme through The ONE Study initiative (Award 260687) and the Regensburger Centrum für Interventionelle Immunologie.

Address correspondence and reprint requests to Dr. James A. Hutchinson, Department of Surgery, University Hospital Regensburg, Franz-Josef-Strauss-Allee 11, 93053 Regensburg, Germany. E-mail address: james.hutchinson@ukr.de

The online version of this article contains supplemental material.

Abbreviations used in this article: DPBS, Dulbecco's PBS; LA-ICP-MS, laser ablation–inductively coupled plasma mass spectrometry; Mreg, regulatory macrophage.

www.jimmunol.org/cgi/doi/10.4049/jimmunol.1400869

(i.e., its distribution, survival, and fate in the recipient). Typically, pharmacokinetic studies in humans are performed as part of the early clinical pharmaceutical development process; however, in the case of Mregs, and cell-based medicinal products in general, adequate methods for reliably detecting infused cells in tissues over days or weeks after transfer are not available (17). In a previous study, we used single-photon emission computed tomography to track ^{111}In oxine-labeled allogeneic human Mregs in one patient: Mregs given by central venous infusion were first concentrated in the pulmonary vasculature but by 3 h postinfusion had migrated to the liver, spleen, and hematopoietically active bone marrow via the blood (13). Although this radiological tracing study provided valuable information, it tells us very little about the precise distribution of Mregs within tissues, and, owing to the short half-life of ~~[~~^{111}In~~]~~, the survival and fate of Mregs after 30 h postinfusion could not be characterized.

Cell tracking in patients presents a number of substantial obstacles (18). To identify cells after administration to a recipient, it is necessary that they are specifically and durably labeled. A variety of cell labeling reagents and corresponding detection technologies exist, notably radioisotopic labeling (19), stable isotope labeling (e.g., deuterium), nuclear magnetic resonance labels (20), nanoparticles (21), and luminescent dyes (22); however, to some degree, each of these approaches is limited by detection sensitivity, signal nonspecificity, and the impermanence or toxicity of labels. Thus, there is an unfulfilled need for a cell labeling and cell detection technology capable of reliably quantifying very low-frequency cells (perhaps as few as 1 in 10^7 cells) in tissues with a very low false-positive detection rate. Most importantly, none of the existing cell-tracking techniques are capable of reliable single-cell detection at a suitable level of resolution to identify single cells and their microanatomical context. Judged by these performance requirements, existing technologies are not suitably sensitive or specific, so alternative approaches must be considered.

Laser ablation–inductively coupled plasma mass spectrometry (LA-ICP-MS) is an analytical technique that is predominantly used in earth and material sciences, but it is also beginning to be applied to analysis of biological samples (23). In principle, LA-ICP-MS entails vaporizing small parts of a sample using a focused pulse of laser energy. The elemental composition of this vaporized material is analyzed by mass spectrometry, which provides exquisitely sensitive detection. By taking contiguous samples across a specimen, a map of the distribution of elements within a complex sample can be constructed. This strategy has been used to visualize endogenous elements in biological tissues (24), and elemental tagging prior to LA-ICP-MS enables specific tissue features, such as amyloid deposits in brain tissue (25), to be distinguished. Applications of this remarkable technique to the problem of tracking rare cells would overcome many of the limitations associated with other methodologies: A "microscope" that used LA-ICP-MS to map tissue components labeled with rare earth metals would be incredibly sensitive and specific, because most rare earth metals are completely absent from tissues. Hence, the objective of the work presented in this article was to develop an LA-ICP-MS method for identifying labeled human Mregs in tissues specimens.

Materials and Methods

Experiments in animals

Animal experiments were performed in accordance with permission Nr. 54-2532.1-10/12 granted by the Regierung von Oberbayern. NSG (NOD.Cg-*Prkdc*^{scid} *Il2rg*^{tm1Wjl}/SzJ) mice were bred in-house. Animals were kept in individually ventilated cages and fed a conventional diet.

Generation and gold labeling of human Mregs

Human Mregs were generated as previously described (26). Briefly, CD14$^+$ monocytes were isolated from Ficoll-prepared PBMCs by positive selection using anti-CD14 MicroBeads (Miltenyi Biotec, Bergisch Gladbach, Germany). Monocytes were plated in six-well Cell+ plates (Sarstedt, Nümbrecht, Germany) at 10^6 cells/well in RPMI 1640 (Lonza, Cologne, Germany) containing 10% heat-inactivated human AB serum (Lonza), 2 mM GlutaMAX (Invitrogen, Karlsruhe, Germany), 100 U/ml penicillin (Lonza), 100 μg/ml streptomycin (Lonza), and recombinant human M-CSF (R&D Systems, Wiesbaden-Nordenstadt, Germany) at 25 ng/ml carried on 0.1% human albumin (CSL-Behring, Hattersheim-am-Main, Germany). On day 6 of culture, cells were stimulated for 18 h with 25 ng/ml recombinant human IFN-γ (Chemicon, Billerica, MA). To label Mregs with 50-nm gold nanoparticles (Sigma, Munich, Germany), human Mregs were harvested, washed twice in Dulbecco's PBS (DPBS), and resuspended at 10^6 cells/ml in prewarmed X-Vivo 10 (Lonza) containing 3.5×10^9 gold nanoparticles/ml. The cell suspension was incubated at 37°C for 1 h in a closed 15-ml tube with end-over-end rotation. Thereafter, the cells were washed three times in DPBS before further processing.

Flow cytometry

Cell surface staining was performed at 4°C in DPBS/1% BSA/0.02% NaN$_3$/10% FcR-block (Miltenyi Biotec), as described elsewhere (13). Dead cells were excluded with 7-aminoactinomycin D (BD Biosciences, Heidelberg, Germany). Data were collected using a FACSCanto II cytometer (BD Biosciences), and the proportion of live Mregs, gated by physical characteristics, was analyzed using FlowJo v7.6.5 software. To assess the T cell–suppressive capacity of Mregs, allogeneic PHA-stimulated CFSE-labeled CD3$^+$ T cells and Mregs were set in direct 1:1 coculture for 5 d. Subsequently, T cell proliferation was quantified by flow cytometry, as previously described (26).

Culture of gold-labeled Mregs in chamber slides

Mregs were resuspended in Mreg-generation medium (as above) before replating into chamber slides (BD Falcon, Heidelberg, Germany) at a density of 10^6 viable Mregs/ml. Cells replated in chamber slides were allowed to adhere over 24 h. For counterstaining, adherent Mregs were washed three times in ice-cold DPBS, air dried, and stained with Diff-Quik Giemsa reagents (Medion Diagnostics, Munich, Germany).

Administration of gold-labeled human Mregs to NSG mice and tissue preparation

Immediately prior to injection, the concentration of gold-labeled Mregs was adjusted to 5×10^6 viable cells/ml in DPBS, without Ca^{2+} or Mg^{2+}, supplemented with 60 IU/ml heparin. Cell suspensions were injected through a 27-gauge needle into the tail vein of recipient NSG mice over 30–180 s. For solution-based ICP-MS and LA-ICP-MS analyses, organs were harvested at 24 h or 7 d postinfusion by postmortem dissection. Tissues for analysis by LA-ICP-MS were fixed in paraformaldehyde and embedded in paraffin wax, and 6-μm sections were cut. Sections were mounted on SuperFrost glass microscope slides (Thermo Fisher Scientific, Schwerte, Germany) and stored in a dry environment at 37°C for several days prior to further processing. Sections were dewaxed with Roti-Histol (Carl Roth, Karlsruhe, Germany) and progressively rehydrated in increasingly dilute ethanol. Following conventional immunohistochemical techniques, tissues were blocked with 5% normal mouse serum in TBS for 1 h. Tissues were stained overnight at 4°C using primary metal-tagged MaxPar Abs (Fluidigm Sciences, Sunnyvale, CA) diluted in TBS + 5% normal mouse serum, according to the manufacturer's recommendations. Specifically, tissues were stained with ^{154}Sm-tagged anti-CD45 (clone HI30) or ^{174}Yb-tagged anti–HLA-DR (clone L243). Sections were counterstained with H&E before progressive dehydration in alcohol and air drying.

Solution-based ICP-MS

Analyses were performed on a sector-field ICP-MS instrument (Element 2XR; Thermo Scientific, Bremen, Germany). The instrument was fitted with a cyclonic spray chamber, a conical glass concentric nebulizer (both from Glass Expansion, West Melbourne, VIC, Australia), and a 0.25-mm inner diameter probe (Elemental Scientific, Omaha, NE). Prior to analysis, the samples were digested in small volumes of concentrated acid using the procedure reported previously by our group (23). Following evaporation of the acid, a 5% aqua regia solution was used to reconstitute the samples. Gold is known to have a high affinity for the surfaces of the sample introduction system (27). Therefore, to minimize memory effects, solutions of 5% aqua regia and 10 mM cysteine were aspirated between samples.

LA-ICP-MS

Analyses were performed on a laser ablation system (UP-213, Nd:YAG, λ 213 nm; ElectroScientific Industries) coupled to a sector-field ICP-MS instrument (Element 2XR; Thermo Scientific) in external trigger mode. The laser ablation system was fitted with a low-volume, teardrop-shaped ablation cell, which was described elsewhere (28). Helium was used as the ablation gas, at a typical flow rate of 0.6 l/min, with an argon make-up flow introduced, at a flow rate of 0.8 l/min, after the ablation cell. Single-cell identification was demonstrated by ablating 55-μm-diameter areas at locations corresponding to individual cells. Only single cells were targeted; cells present in clusters or <55 μm apart were discounted. The presence of label was determined from the time-resolved ^{197}Au signal-intensity profile. Imaging of the cells and tissue sections was accomplished by performing adjacent line scans over sections of the slide, while measuring ^{197}Au, ^{154}Sm, or ^{174}Yb in time-resolved mode. Images were constructed using Iolite version 2.15 (Melbourne Isotope Group, Melbourne, VIC, Australia), a freeware data deconvolution package that runs on the IGOR-Pro 6.22A platform (WaveMetrics, Lake Oswego, OR). The software converts each raw data point into a color-coded pixel; thus, the color profile of the resulting image depicts the distribution of the respective elements across the sampled region.

Results

Labeling of human Mregs for detection by LA-ICP-MS

From an analytical chemistry perspective, most d-block and f-block elements can be equally easily quantified by LA-ICP-MS. Metal labels can be incorporated into living cells by various biological processes, including phagocytosis, pinocytosis, receptor-mediated endocytosis, or cell surface labeling. Retention of a metal label may be passive or active, and it may or may not require reaction of the metal with cellular constituents. The choice of metal label, its chemical form, and the mechanisms by which it is taken up and retained by living cells determine its properties as a tracer label. From a biological perspective, the qualities that we expect of a useful living cell label for in vivo tracking studies are durability, biological inertness, and specificity; hence, absence of label from normal tissues. Omniscan, a gadolinium-based nuclear magnetic resonance contrast agent, was shown to be a suitable reagent for labeling human regulatory T cells, which presumably acquired label by fluid-phase pinocytosis (23).

In the current study, 50-nm gold particles were selected as a label because Mregs are known to be highly phagocytic (15). Optimal conditions for labeling were determined by incubating Mregs with gold particles at a range of concentrations for various periods prior to measuring cellular gold content by solution-based ICP-MS (Table I). Label uptake was time and concentration dependent and did not reach saturation within the range of tested conditions; nevertheless, gold incorporation after 1 h of incubation with 3.5×10^9 particles/ml was >500-fold the lower limit of detection. To ascertain whether gold labeling had any effect on Mreg viability, cell surface phenotype, or in vitro function, gold-labeled and unlabeled Mregs were analyzed by flow cytometry and suppression assays (Fig. 1). After labeling, no differences in dead cell frequency, marker phenotype, or suppressor activity were observed. Accordingly, gold nanoparticles at concentrations of 3.5×10^9 particles/ml are suitable for labeling human Mregs without obvious toxic effects.

Laser ablation of single Mregs

To assess the uptake of gold label by individual cells, gold-labeled Mregs were washed extensively after labeling and replated in chamber slides. The majority of replated Mregs readhered to the vessel surface within 1 h and acquired typical Mreg morphology (Fig. 2A). After 1 h, the adherent cells were washed extensively and Giemsa stained prior to analysis by LA-ICP-MS. Single Mregs were ablated with single shots of a 55-μm-diameter laser. This beam size ensured complete ablation of an individual cell, while reducing the chance of inadvertently ablating neighboring cells. LA-ICP-MS of the labeled cells yielded an average signal intensity of 1.9×10^5 counts/cell (77% relative SD). Each signal was clearly distinguishable from the low background signal ~0–10 counts (Fig. 2B). No signals above background were observed for the ablation of nonlabeled cells or from control areas of the slide containing no cells (Fig. 2C). This demonstrated that labeled cells can be rapidly and reliably distinguished from their nonlabeled counterparts, a point that was subsequently confirmed during the analysis of mixed populations of labeled/nonlabeled cells (Table II). To prove that gold nanoparticles are retained by living Mregs, labeled cells were cultured for 36 h in chamber slides before LA-ICP-MS analysis. Clear signals, with an average signal intensity of 1.6×10^5 counts/cell (69% relative SD), were obtained for this analysis (Fig. 2D). Therefore, it is concluded that living, adherent Mregs can be labeled with 100% labeling efficiency and retain gold nanoparticles for ≥36 h after labeling.

The above experiments sampled entire cells to demonstrate 100% cell labeling and detection capability. For tissue imaging, it is clearly beneficial to decrease the diameter of the laser spot to less than the size of the cell and, hence, increase the resolution of the image. To demonstrate that the cells internalize sufficient label for high-resolution imaging, 8-μm-wide line scans were performed across a cluster of labeled cells (Fig. 3). The count rates remained sufficient to enable detection of the cells, whereas the 8-μm spot size was sufficient to discriminate between the signals from individual cells.

Gold-labeled Mregs can be dual labeled with ^{154}Sm-tagged or ^{174}Yb-tagged Abs

When gold-labeled Mregs are administered to a recipient, release of gold nanoparticles and subsequent reuptake by recipient phagocytes could lead to misidentification of those recipient cells as Mregs. One solution to this problem is to establish that cells bearing the tracer label express the anticipated marker phenotype by immunohistochemical "postlabeling" using metal-conjugated Abs.

Table I. Optimizing conditions for labeling human Mregs with 50-nm gold particles

Gold Concentration (particles/ml)	Incubation Time		
	10 s	1 h	2 h
0	Not detected	Not detected	Not detected
3.50×10^7	Not detected	1.79E+06	1.75E+06
1.75×10^8	Not detected	1.06E+07	9.52E+06
3.50×10^8	1.54E+06	3.09E+07	3.76E+07
1.75×10^9	1.05E+07	1.71E+08	3.64E+08
3.50×10^9	1.51E+07	3.39E+08	4.36E+08

Human Mregs were incubated with various concentrations of gold nanoparticles, and their gold uptake was determined by ICP-MS. Data are the average number of gold atoms internalized/cell for each labeling condition.

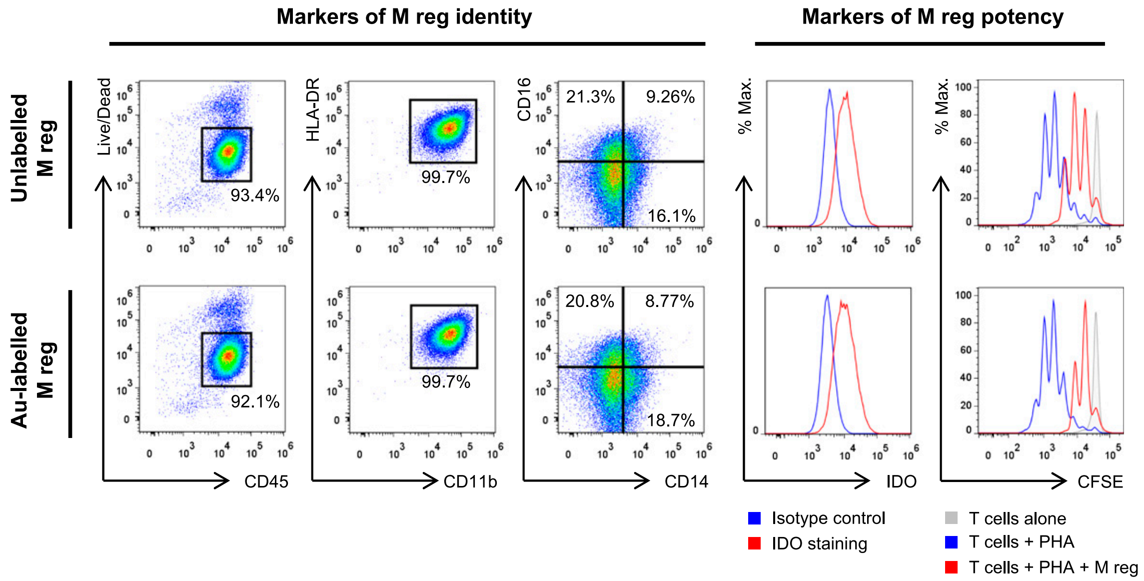

FIGURE 1. Labeling human Mregs with 50-nm gold nanoparticles did not affect their viability, phenotype, or suppressor function. Human Mregs were incubated for 1 h in the presence or absence of 3.5×10^9 gold nanoparticles/ml. Subsequently, the phenotype and viability of unlabeled and gold-labeled Mregs were assessed by flow cytometry. Data are representative of $n = 3$ independent allogeneic pairs. No difference was observed in the viability of gold-labeled Mregs compared with unlabeled Mregs. Likewise, no differences were observed between gold-labeled and unlabeled Mregs in the expression of CD11b, HLA-DR, CD14, or CD16. Both gold-labeled and unlabeled Mregs expressed similar levels of IDO, which is indispensible for the T cell–suppressive function of human Mregs. Accordingly, gold labeling of Mregs did not affect their capacity to suppress polyclonal proliferation of CFSE-labeled, PHA-stimulated allogeneic $CD4^+$ T cells in direct 1:1 cocultures.

Therefore, we examined the technical feasibility of codetecting Mregs labeled with gold and ^{174}Yb-tagged anti–HLA-DR (Fig. 4A) or ^{154}Sm-tagged anti-CD45 (Fig. 4B) Abs. Mregs were labeled with gold nanoparticles prior to overnight culture in chamber slides. Unfixed, adherent Mregs were counterlabeled by incubation with metal-conjugated Abs. After extensive washing, the dual-labeled Mregs were analyzed by LA-ICP-MS. Coextensive signals were obtained for gold labeling and the postlabels, proving that this method could, in principle, be used to detect dual labeling of cells in tissues.

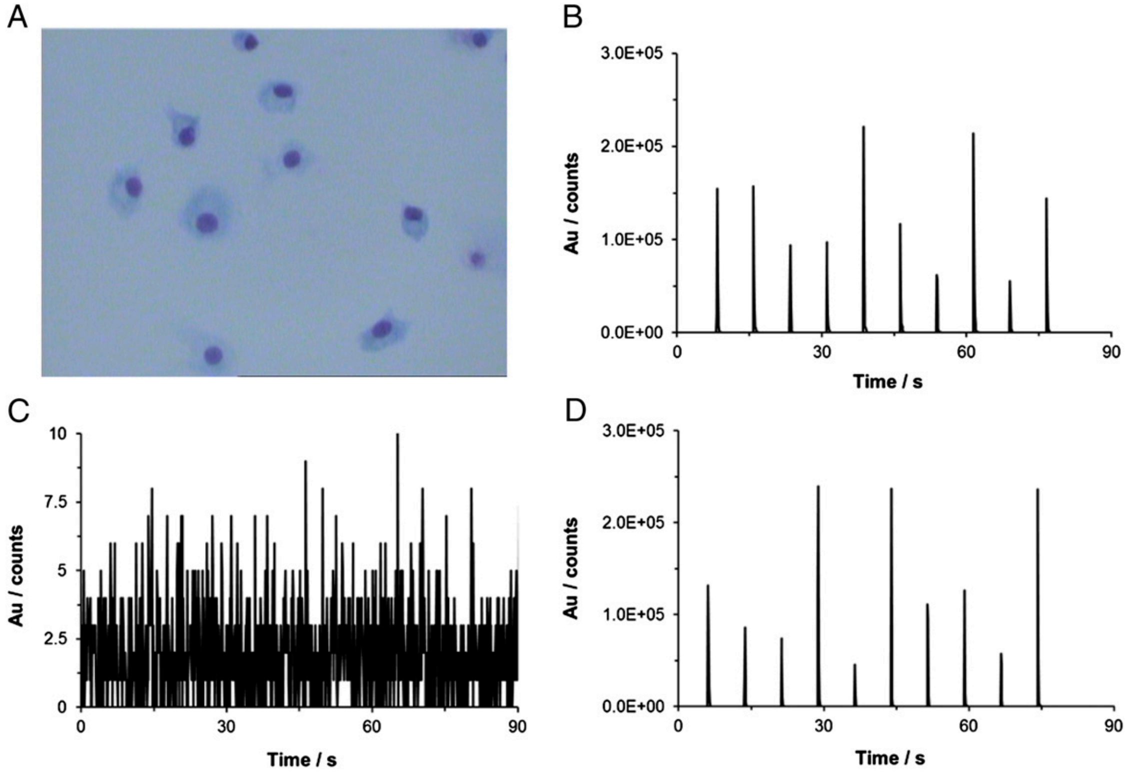

FIGURE 2. One hundred percent labeling efficiency was achieved when Mregs were incubated with 3.5×10^9 gold nanoparticles/ml for 1 h. (**A**) After labeling with gold nanoparticles, Mregs were able to readhere to a plastic tissue culture surface. Cells were visualized using a Giemsa counterstain. (**B**) Single gold-labeled Mregs were ablated with single shots of a 55-μm-diameter laser, yielding an average signal intensity of 1.9×10^5 counts/cell (77% relative SD). (**C**) No signals above background were observed when unlabeled Mregs were ablated. (**D**) Labeled Mregs retained gold for ≥36 h after labeling.

Table II. Specificity of ^{197}Au labeling of human Mregs

Ratio of Labeled/Nonlabeled Cells	Culture Time after Labeling (h)	No. of Cells Ablated	No. of Labeled Cells Detected
1:0	1	100	100
0:1	1	100	0
1:1	1	100	45
1:0	36	100	100
0:1	36	100	0
1:1	36	100	43

Various proportions of gold-labeled Mregs were plated in chamber slides and allowed to adhere for 1 or 36 h. The relative numbers of labeled and unlabeled Mregs were assessed by LA-ICP-MS. Labeled and unlabeled Mregs were clearly discriminable. There was no significant transfer of gold label from labeled to unlabeled Mregs over the 36-h incubation period.

Tracking of human Mregs in NSG mice

The eventual anatomical distribution of Mregs after i.v. infusion reflects their passive and active migration and engraftment into different tissues, as well as their death and elimination. To track the survival and tissue distribution of Mregs in vivo, gold-labeled human Mregs were injected into NSG mice. The presence of label in brain, heart, kidney, liver, spleen, small intestine, large intestine, skeletal muscle, and tail skin was assessed on days 1 and 7 postinjection by solution-based ICP-MS (Table III). At both time points, gold label was principally detected in lung, liver, and spleen (although above-background signal was also detected in kidney, heart, brain, and intestine), which is consistent with previous results from flow cytometry experiments that showed transient engraftment of Mregs in these tissues (28).

To investigate whether LA-ICP-MS permits detection of individual gold-labeled cells in tissues, recipient tissues were harvested at day 1 or 7 postinjection of gold-labeled Mregs. These tissues were fixed with paraformaldehyde and embedded in paraffin. Six-micron sections of lung, liver, and spleen were conventionally counterstained with H&E prior to analysis by LA-ICP-MS. Sampled areas were 320 × 245 μm in size, with two sampled areas selected per tissue section. As predicted by solution-based ICP-MS, label was detected in all three tissues at 1 and 7 d postinjection (Fig. 5). Within the relatively small areas of tissue examined, no particular pattern of signal distribution was perceived.

Discussion

Faced with the problem of detecting very rare cells in tissues, the aim of this work was to demonstrate that LA-ICP-MS can be used to identify metal-labeled cells in tissue samples with high sensitivity and specificity. In principle, this objective has been realized;

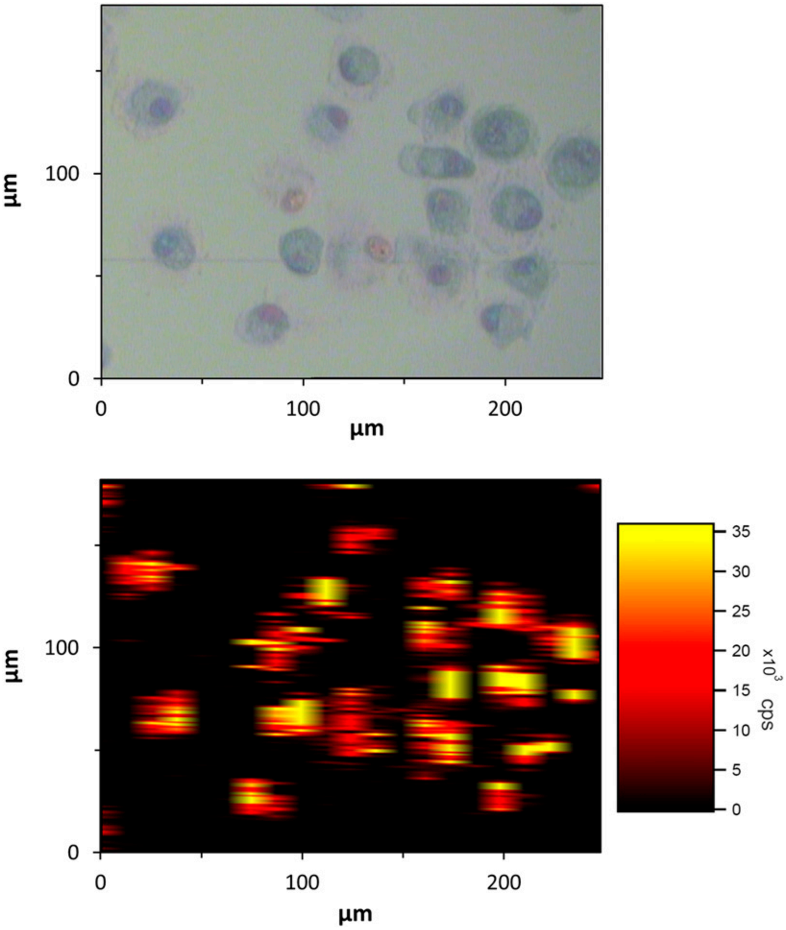

FIGURE 3. An 8-μm laser spot–size is sufficient to allow detection of gold-labeled Mregs. Eight-micrometer– line scans were made across a group of gold-labeled, Giemsa-counterstained Mregs. Count rates were adequate to detect labeled cells, whereas the spot size was small enough to allow spatial resolution of adjacent cells. The *upper panel* shows optical images and the *lower panel* shows the distribution of gold label.

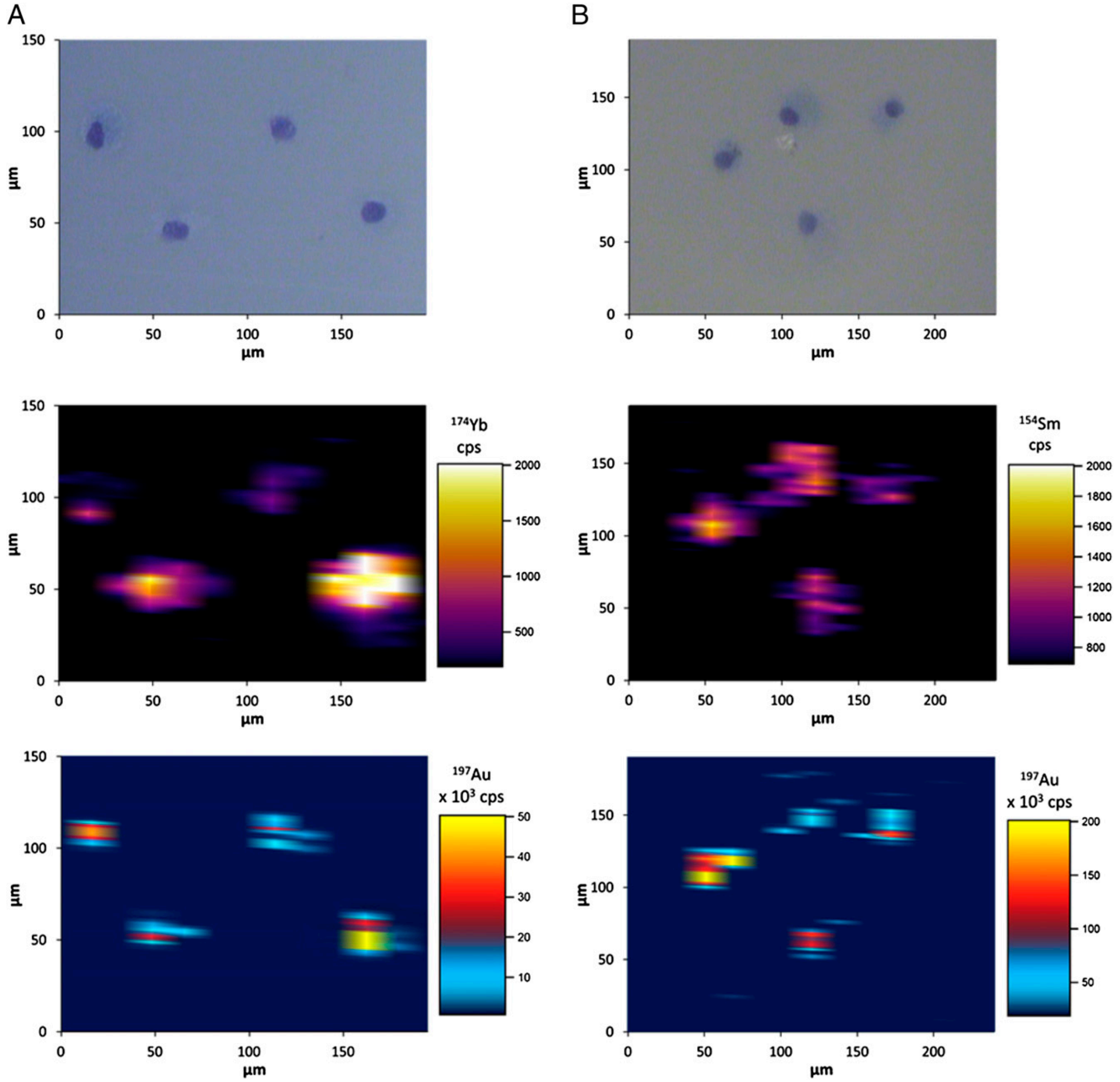

FIGURE 4. Gold-labeled Mregs can be dual labeled with ^{174}Yb-tagged or ^{154}Sm-tagged Abs. Gold-labeled Mregs were cultured overnight in chamber slides prior to postlabeling with either ^{174}Yb-conjugated anti–HLA-DR (**A**) or ^{154}Sm-conjugated anti-CD45 (**B**) mAbs. After extensive washing, the dual-labeled Mregs were counterstained with Giemsa and subjected to LA-ICP-MS analysis.

in practice, the technology is not ready to be commonly used in immunological research. Nevertheless, the results presented in this article indicate the enormous future potential of LA-ICP-MS in imaging biological specimens at a level of resolution suitable for identifying individual cells. Although this study focused on the narrow application of this approach to detecting gold-labeled Mregs, clearly LA-ICP-MS tissue imaging could be useful for a much broader range of applications. Therefore, we must ask ourselves how the current system might be improved to better serve the needs of biologists.

The resolution of images generated by LA-ICP-MS is dictated primarily by laser parameters (e.g., laser spot diameter, line spacing, repetition frequency, and scanning speed). Finer resolution is necessarily better when imaging histological specimens. In the current study, a beam width of 8 µm and scan speed of 8 µm/s were used for the analysis of tissue sections, which provided sufficient resolution to identify single cells. In principle, the resolution of images could be increased to ≤1 µm. However, the choice of laser parameters must take into account additional factors, such as the instrument sensitivity and the required analysis speed.

Presently, the speed of analyzing specimens is slow: to image an area of 1 mm^2 using an 8-µm spot diameter and 8-µm/s scan speed takes ~4.5 h. The speed of analysis is largely limited by the washout time of the laser ablation chamber, which determines the duration of the signal from each laser pulse. Commercially available systems typically provide washout times in the order of a few seconds; however, with custom modifications, many users have reduced this time, in some cases to <100 ms. With improved instrumentation, washout times might be reduced to ~10 ms, which would drastically improve both the sensitivity and the speed of analysis.

Using our current LA-ICP-MS system, it was possible to detect two labels on cultured cells; however, for many applications it

Table III. Presence of ^{197}Au-labeled human Mregs in tissues of recipient mice on days 1 and 7 postinjection by solution-based ICP-MS

	Day 1		Day 7	
Tissue	Au-Labeled Mregs	Unlabeled Mregs	Au-Labeled Mregs	Unlabeled Mregs
Lung	251.40 ± 13	0.15[a]	122.47 ± 9	0.09[a]
Spleen	147.85 ± 12	0.04[a]	181.25 ± 11	0.07[a]
Liver	120.46 ± 26	0.02[a]	132.15 ± 29	0.02[a]
Kidney	8.23 ± 12	0.23[a]	2.56 ± 3	0.12[a]
Heart	3.27 ± 56	0.23[a]	1.09 ± 124	0.12[a]
Skeletal muscle	0.48[a]	0.12[a]	0.49 ± 97	0.21[a]
Brain	1.46 ± 22	0.04[a]	0.06[a]	0.07[a]
Tail skin	35.70 ± 134	2.10[a]	0.47 ± 24	nt
Large intestine	0.67[a]	0.06[a]	0.63 ± 44	0.45[a]
Small intestine	1.90 ± 58	0.43[a]	0.86 ± 47	0.50[a]

Data are pg Au/mg tissue ± % RSD; $n = 3$/group.

[a] Below the limit of detection.

nt, not tested; RSD, relative SD.

would be useful to measure many more parameters. In principle, this could be achieved by combining the existing LA-ICP-MS with conventional fluorescence microscopy or by developing the system to detect multiple metal labels. The principal restriction on analyzing a greater number of metal labels is the rate at which sector field mass spectrometers detect each element, which they must do sequentially. Therefore, the capability of the current system to detect multiple metal labels could be improved by using a simultaneously detecting mass spectrometer, such as a time-of-flight mass spectrometer.

In this study, we applied LA-ICP-MS to the real-world biological problem of identifying rare cells in tissues. In doing so, we demonstrated the potential usefulness and power of this method in biological research. The technology presented in this article allowed detection of gold-labeled cells in tissues with very high specificity and sensitivity, as well as revealing their microanatomical relationship to recipient tissue structures. The specificity of LA-ICP-MS tissue imaging reflects the large signal-to-background ratio afforded by using rare earth metals or biologically inert nanoparticles as labels. The sensitivity of LA-ICP-MS tissue imaging (i.e., the ability to reliably detect very rare cells) is a reflection of the incredible sensitivity of mass spectrometry as an analytical technique. Unsurprisingly, there is now great interest in exploiting mass spectrometry as a specific and sensitive detection method in various biological applications, most notably in flow cytometry (30). A commercially available device known as the CyTOF is being adopted by many groups interested in clinical immune monitoring, with ~~to~~ astonishing results (31, 32). The coupling of laser ablation with ICP-MS–based detection presented in this article takes this technology to a new level by combining detection of specific Ags with spatial resolution, allowing accurate, sensitive, and specific mapping of Ag distribution within tissues.

Concurrent detection of signals from Mregs prelabeled with gold and postlabeled with metal-tagged Abs would imply the presence of intact human Mregs in mouse tissues. Dual labeling and LA-ICP-MS detection of gold-labeled Mregs grown on chamber slides with either ^{174}Yb-tagged anti–HLA-DR or ^{154}Sm-tagged anti-CD45 was successful. Unfortunately, when sections of spleen from mice that had received gold-labeled Mregs were counterstained with the ^{174}Yb-conjugated anti–HLA-DR Ab before being analyzed at low resolution by LA-ICP-MS, very high and spatially diverse background signals for ^{174}Yb were detected (Supplemental Fig. 1). Therefore, no correlation in the distribution of ^{174}Yb and ^{197}Au signals could be established. We are unable to explain this nonspecific staining in mouse tissues. One possibility is that our metal-tagged mAbs are unsuitable for use on tissue sections, possibly owing to the destruction of Ags during tissue fixation. Also, we cannot discount the possibility that MaxPar reagents have a greater propensity for nonspecific binding to tissues than do Abs with alternative labels. Because of the very high sensitivity of LA-ICP-MS, postlabeling with rare earth metal–labeled Abs might require development of more suitable metal-conjugated Abs, possibly labeled using different chemistries, as well as better histological techniques to block nonspecific binding of Abs. Importantly, our inability to identify colabeled Mregs does not detract from the potential usefulness of LA-ICP-MS in detecting colabeled cells in tissues; rather, it speaks to the current limitations of our metal-labeled Abs and histological techniques, which are ultimately soluble issues.

Albeit a niche application of LA-ICP-MS tissue imaging, characterizing the distribution, survival, and fate of therapeutic cells in patients will be critical to their future development as pharmaceutical agents (29, 33). LA-ICP-MS offers an unrivaled combination of sensitivity, specificity, and spatial resolution, which makes it an especially suitable method for cell tracking. Moreover, using LA-ICP-MS as a detection method makes available a variety of nonradioisotopic tracers, which may be safer and more convenient than currently available labels in the manufacture and application of cell-based therapies. Another exciting possibility of LA-ICP-MS cell tracking is that colabeling cells with two or more metal-containing compounds that are metabolized, degraded, or excreted by different mechanisms might make discrimination of live and dead cells possible, because only live cells would carry both labels. This article is proof-of-concept that gold-labeled Mreg can be detected in tissues for at least 7 d after infusion. Serious consideration is being given to the feasibility and clinical safety of labeling Mreg with gold nanoparticles for infusion into patients; indeed, clinical translation of cell tracking by LA-ICP-MS is a key objective of The ONE Study initiative (www.onestudy.org).

We conclude that, although LA-ICP-MS tissue imaging is a nascent technology, it has the potential to be a very powerful analytical technique in biology. If the present limitations of resolution and number of labels can be overcome, then LA-ICP-MS–based tissue imaging has a bright future.

Acknowledgments

We thank Yvonne Lukas, Anke Hofmann, and Joachim Schweimer for outstanding technical support.

Disclosures

The authors have no financial conflicts of interest.

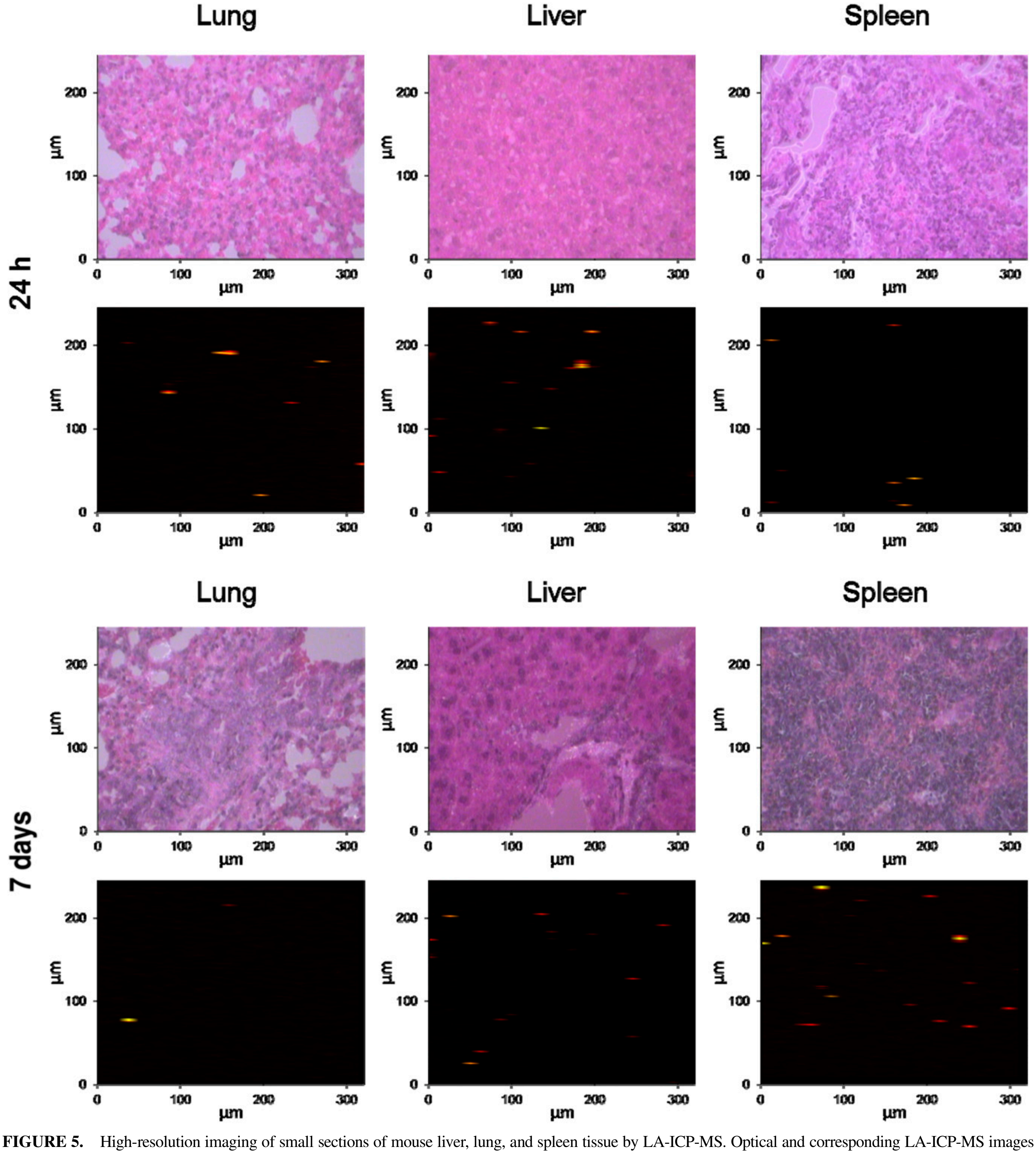

FIGURE 5. High-resolution imaging of small sections of mouse liver, lung, and spleen tissue by LA-ICP-MS. Optical and corresponding LA-ICP-MS images of mouse liver, lung, and spleen show the distribution of gold within each tissue. Regions of high gold intensity appear as colored spots in the LA-ICP-MS images. Tissues were harvested at 24 h (*upper panels*) and 7 d (*lower panels*) after administration of gold-labeled Mregs and were subsequently counterstained with H&E.

References

1. Geissler, E. K., and J. A. Hutchinson. 2013. Cell therapy as a strategy to minimize maintenance immunosuppression in solid organ transplant recipients. *Curr. Opin. Organ Transplant.* 18: 408–415.
2. Hilkens, C. M., and J. D. Isaacs. 2013. Tolerogenic dendritic cell therapy for rheumatoid arthritis: where are we now? *Clin. Exp. Immunol.* 172: 148–157.
3. Giannoukakis, N., B. Phillips, D. Finegold, J. Harnaha, and M. Trucco. 2011. Phase I (safety) study of autologous tolerogenic dendritic cells in type 1 diabetic patients. *Diabetes Care* 34: 2026–2032.
4. Brem-Exner, B. G., C. Sattler, J. A. Hutchinson, G. E. Koehl, K. Kronenberg, S. Farkas, S. Inoue, C. Blank, S. J. Knechtle, H. J. Schlitt, et al. 2008. Macrophages driven to a novel state of activation have anti-inflammatory properties in mice. *J. Immunol.* 180: 335–349.
5. Roncarolo, M. G., S. Gregori, B. Lucarelli, F. Ciceri, and R. Bacchetta. 2011. Clinical tolerance in allogeneic hematopoietic stem cell transplantation. *Immunol. Rev.* 241: 145–163.
6. Ferrer, I. R., J. Hester, A. Bushell, and K. J. Wood. 2014. Induction of transplantation tolerance through regulatory cells: from mice to men. *Immunol. Rev.* 258: 102–116.
7. Riquelme, P., E. K. Geissler and J. A. Hutchinson. 2012. Alternative approaches to myeloid suppressor cell therapy in transplantation: comparing regulatory macrophages to tolerogenic DCs and MDSCs. *Transplant. Res.* 1: 17.
8. Moreau, A., E. Varey, L. Bouchet-Delbos, and M. C. Cuturi. 2012. Cell therapy using tolerogenic dendritic cells in transplantation. *Transp. Res.* 1: 13.
9. Gregori, S., K. S. Goudy, and M. G. Roncarolo. 2012. The cellular and molecular mechanisms of immuno-suppression by human type 1 regulatory T cells. *Front. Immunol.* 3: 30.

10. Edinger, M., and P. Hoffmann. 2011. Regulatory T cells in stem cell transplantation: strategies and first clinical experiences. *Curr. Opin. Immunol.* 23: 679–684.
11. Barbon, C. M., J. K. Davies, A. Voskertchian, R. H. Kelner, L. L. Brennan, L. M. Nadler, and E. C. Guinan. 2014. Alloanergization of human T cells results in expansion of alloantigen-specific CD8(+) CD28(−) suppressor cells. *Am. J. Transplant.* 14: 305–318.
12. Broichhausen, C., P. Riquelme, E. K. Geissler, and J. A. Hutchinson. 2012. Regulatory macrophages as therapeutic targets and therapeutic agents in solid organ transplantation. *Curr. Opin. Organ Transplant.* 17: 332–342.
13. Hutchinson, J. A., P. Riquelme, B. Sawitzki, S. Tomiuk, P. Miqueu, M. Zuhayra, H. H. Oberg, A. Pascher, U. Lützen, U. Janssen, et al. 2011. Cutting Edge: Immunological consequences and trafficking of human regulatory macrophages administered to renal transplant recipients. *J. Immunol.* 187: 2072–2078.
14. Walter, L., P. Riquelme, S. Tomiuk, B. Sawitzki, M. Knauel, N. Ahrens, B. Banas, H. Schlitt, E. Geissler, and J. Hutchinson. Generation of BTNL8+ inducible Tregs by allogeneic human regulatory macrophages is IDO- and B7-dependent (abstr.). 2014 World Transplant Congress Abstracts. Am. J. Transplant 14(Suppl. 3): 396.
15. Riquelme, P., S. Tomiuk, A. Kammler, F. Fändrich, H. J. Schlitt, E. K. Geissler, and J. A. Hutchinson. 2013. IFN-γ-induced iNOS expression in mouse regulatory macrophages prolongs allograft survival in fully immunocompetent recipients. *Mol. Ther.* 21: 409–422.
16. Hutchinson, J. A., P. Riquelme, and E. K. Geissler. 2012. Human regulatory macrophages as a cell-based medicinal product. *Curr. Opin. Organ Transplant.* 17: 48–54.
17. Schormann, W., F. J. Hammersen, M. Brulport, M. Hermes, A. Bauer, C. Rudolph, M. Schug, T. Lehmann, A. Nussler, H. Ungefroren, et al. 2008. Tracking of human cells in mice. *Histochem. Cell Biol.* 130: 329–338.
18. Kircher, M. F., S. S. Gambhir, and J. Grimm. 2011. Noninvasive cell-tracking methods. *Nat. Rev. Clin. Oncol.* 8: 677–688.
19. Stojanov, K., E. F. de Vries, D. Hoekstra, A. van Waarde, R. A. Dierckx, and I. S. Zuhorn. 2012. [18F]FDG labeling of neural stem cells for in vivo cell tracking with positron emission tomography: inhibition of tracer release by phloretin. *Mol. Imaging* 11: 1–12.
20. Shyu, W. C., C. P. Chen, S. Z. Lin, Y. J. Lee, and H. Li. 2007. Efficient tracking of non-iron-labeled mesenchymal stem cells with serial MRI in chronic stroke rats. *Stroke* 38: 367–374.
21. Weissleder, R., M. Nahrendorf, and M. J. Pittet. 2014. Imaging macrophages with nanoparticles. *Nat. Mater.* 13: 125–138.
22. Guenoun, J., A. Ruggiero, G. Doeswijk, R. C. Janssens, G. A. Koning, G. Kotek, G. P. Krestin, and M. R. Bernsen. 2013. In vivo quantitative assessment of cell viability of gadolinium or iron-labeled cells using MRI and bioluminescence imaging. *Contrast Media Mol. Imaging* 8: 165–174.
23. Managh, A. J., S. L. Edwards, A. Bushell, K. J. Wood, E. K. Geissler, J. A. Hutchinson, R. W. Hutchinson, H. J. Reid, and B. L. Sharp. 2013. Single cell tracking of gadolinium labeled CD4+ T cells by laser ablation inductively coupled plasma mass spectrometry. *Anal. Chem.* 85: 10627–10634.
24. Hare, D. J., J. K. Lee, A. D. Beavis, A. van Gramberg, J. George, P. A. Adlard, D. I. Finkelstein, and P. A. Doble. 2012. Three-dimensional atlas of iron, copper, and zinc in the mouse cerebrum and brainstem. *Anal. Chem.* 84: 3990–3997.
25. Hutchinson, R. W., A. G. Cox, C. W. McLeod, P. S. Marshall, A. Harper, E. L. Dawson, and D. R. Howlett. 2005. Imaging and spatial distribution of beta-amyloid peptide and metal ions in Alzheimer's plaques by laser ablation-inductively coupled plasma-mass spectrometry. *Anal. Biochem.* 346: 225–233.
26. Hutchinson, J. A., P. Riquelme, E. K. Geissler, and F. Fändrich. 2011. Human regulatory macrophages. *Methods Mol. Biol.* 677: 181–192.
27. Kerr, S. L. 2008. Enhancing nucleic acid detection using inductively coupled plasma mass spectrometry, by means of metal and nano-particle labelling. Doctoral dissertation, Loughborough University, Loughborough, U.K.
28. Horstwood, M. S. A., G. L. Foster, R. R. Parrish, S. R. Noble, and G. M. Nowell. 2003. Accessory mineral U-Th-Pb geochronology by laser-ablation plasma-ionisation multi-collector mass spectrometry (LA-PIMMS). *J. Anal. Atomic Spectrometry* 18: 837–846.
29. Hutchinson, J. A., N. Ahrens, P. Riquelme, L. Walter, M. Gruber, C. A. Böger, S. Farkas, M. N. Scherer, C. Broichhausen, T. Bein, et al. 2014. Clinical management of patients receiving cell-based immunoregulatory therapy. *Transfusion.* DOI: 10.1111/trf.12641.
30. Tanner, S. D., V. I. Baranov, O. I. Ornatsky, D. R. Bandura, and T. C. George. 2013. An introduction to mass cytometry: fundamentals and applications. *Cancer Immunol. Immunother.* 62: 955–965.
31. Bendall, S. C., E. F. Simonds, P. Qiu, A. D. Amir, P. O. Krutzik, R. Finck, R. V. Bruggner, R. Melamed, A. Trejo, O. I. Ornatsky, et al. 2011. Single-cell mass cytometry of differential immune and drug responses across a human hematopoietic continuum. *Science* 332: 687–696.
32. Horowitz, A., D. M. Strauss-Albee, M. Leipold, J. Kubo, N. Nemat-Gorgani, O. C. Dogan, C. L. Dekker, S. Mackey, H. Maecker, G. E. Swan, et al. 2013. Genetic and environmental determinants of human NK cell diversity revealed by mass cytometry. *Sci. Transl. Med.* 5: 208ra145.
33. Broichhausen, C., P. Riquelme, N. Ahrens, A. K. Wege, G. E. Koehl, H. J. Schlitt, B. Banas, F. Fändrich, E. K. Geissler, and J. A. Hutchinson. 2014. In Question: The scientific value of preclinical safety pharmacology and toxicology studies with cell-based therapies. *Mol. Ther. Methods Clin. Dev.* In press.

US 20140224775A1

(19) **United States**
(12) **Patent Application Publication**
Sharp et al.

(10) **Pub. No.: US 2014/0224775 A1**
(43) **Pub. Date: Aug. 14, 2014**

(54) **LASER ABLATION CELL AND INJECTOR SYSTEM FOR A COMPOSITIONAL ANALYSIS SYSTEM**

(71) Applicant: **Electro Scientific Industries, Inc.**, Portland, OR (US)

(72) Inventors: **Barry L. Sharp**, LOUGHBOROUGH (GB); **David N. Douglas**, Plymouth (GB); **Amy J. Managh**, Bolton (GB)

(73) Assignee: **Electro Scientific Industries, Inc.**, Portland, OR (US)

(21) Appl. No.: **14/180,855**

(22) Filed: **Feb. 14, 2014**

Related U.S. Application Data

(60) Provisional application No. 61/764,976, filed on Feb. 14, 2013.

(30) **Foreign Application Priority Data**

Feb. 12, 2014 (US) PCT/US14/16085

Publication Classification

(51) **Int. Cl.**
H05H 1/26 (2006.01)

(52) **U.S. Cl.**
CPC *H05H 1/26* (2013.01)
USPC **219/121.5**

(57) **ABSTRACT**

A laser ablation system includes a sample chamber **102** configured to accommodate a target **104** within an interior **106** thereof, a sample generator **108** configured to remove a portion of the target **104** (which may be subsequently captured as a sample) and an analysis system **110** configured to analyze a composition of the sample. A sample capture cell in the chamber proximate to the target has a capture cavity configured to receive target material, a first inlet configured to transmit a flow of a carrier gas from a first location adjacent to an exterior of the capture cell into a region of the capture cavity; and an outlet configured to receive carrier gas from another region of the capture cavity. The sample chamber **102** includes an injection nozzle **120** configured to introduce, into the interior **106**, a fluid such as a carrier gas.

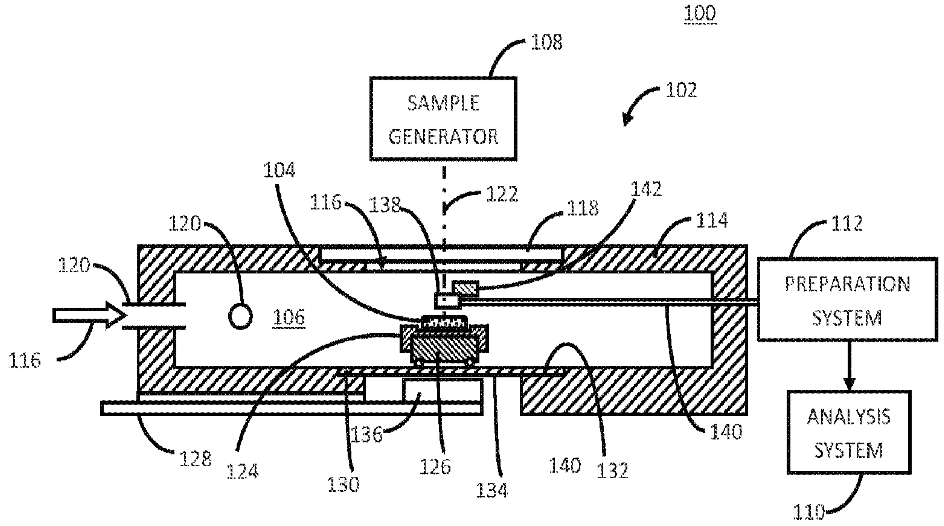

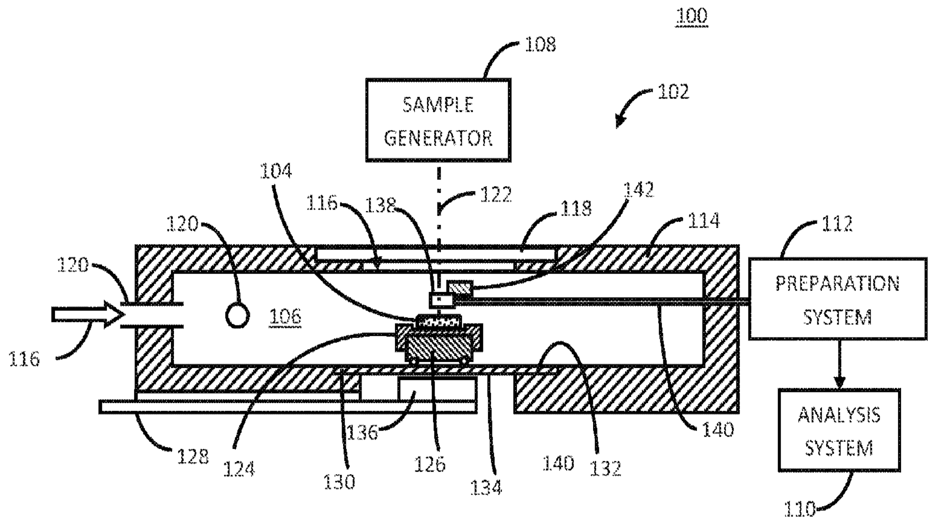
100
108
SAMPLE GENERATOR
102
104
116
138
122
118
142
114
112
PREPARATION SYSTEM
120
120
106
116
140
ANALYSIS SYSTEM
128
124
136
130
126
134
140
132
110

FIG. 1

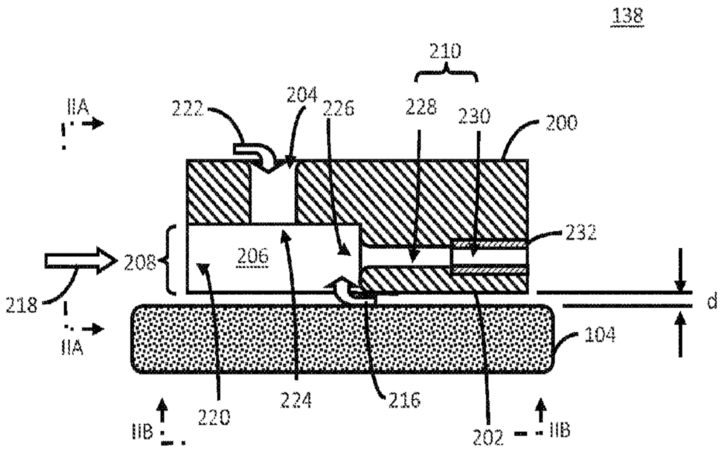
138
210
IIA
222
204
226
228
230
200
232
208
206
218
d
IIA
104
220
224
216
202
IIB
IIB

FIG. 2

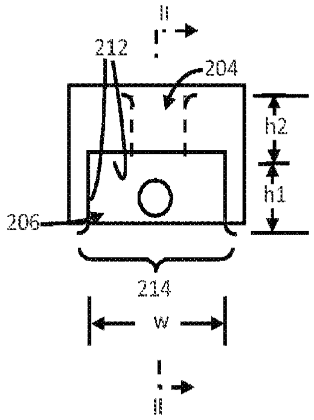

FIG. 2A

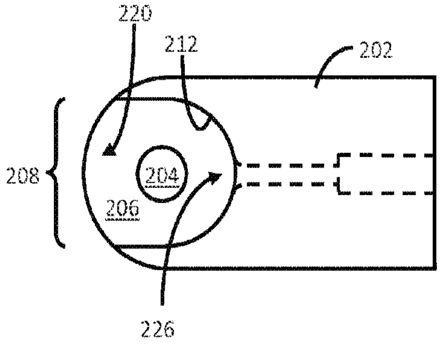

FIG. 2B

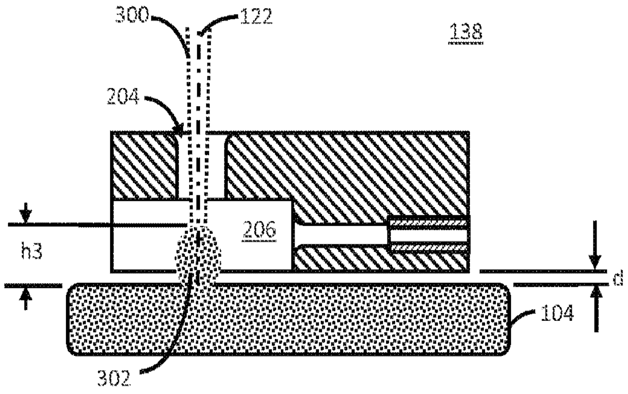

FIG. 3

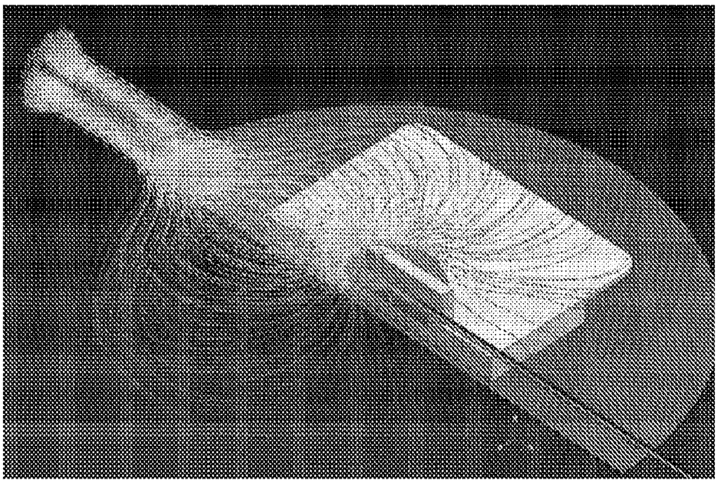

FIG. 4

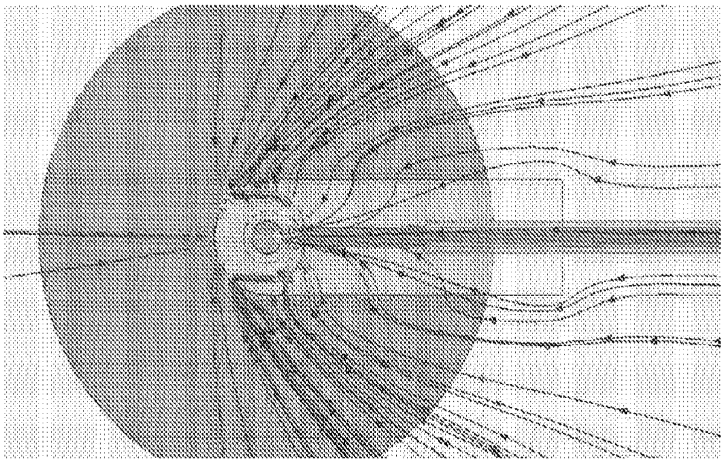

FIG. 5

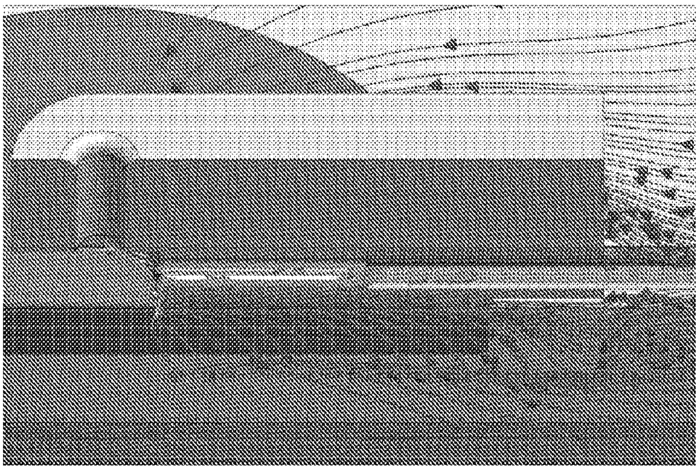

FIG. 6

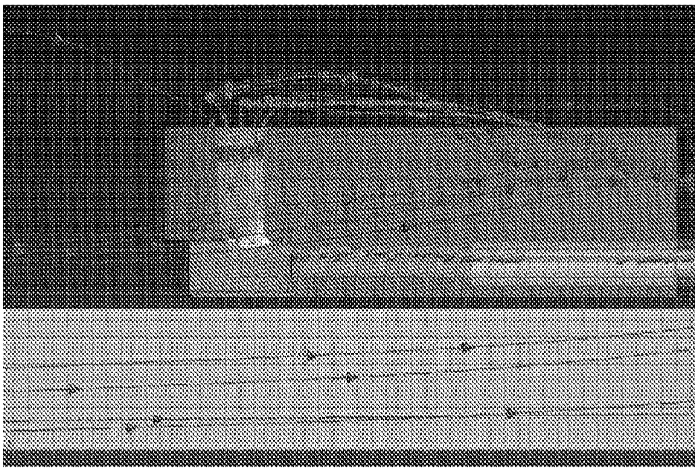

FIG. 7

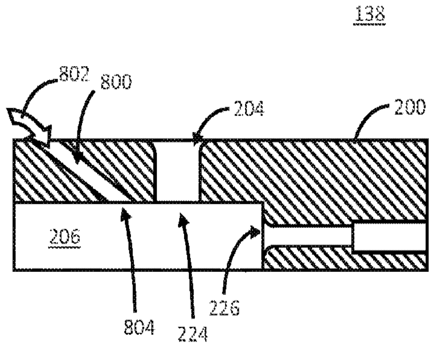
138
802
800
204
200
206
804
224
226

FIG. 8

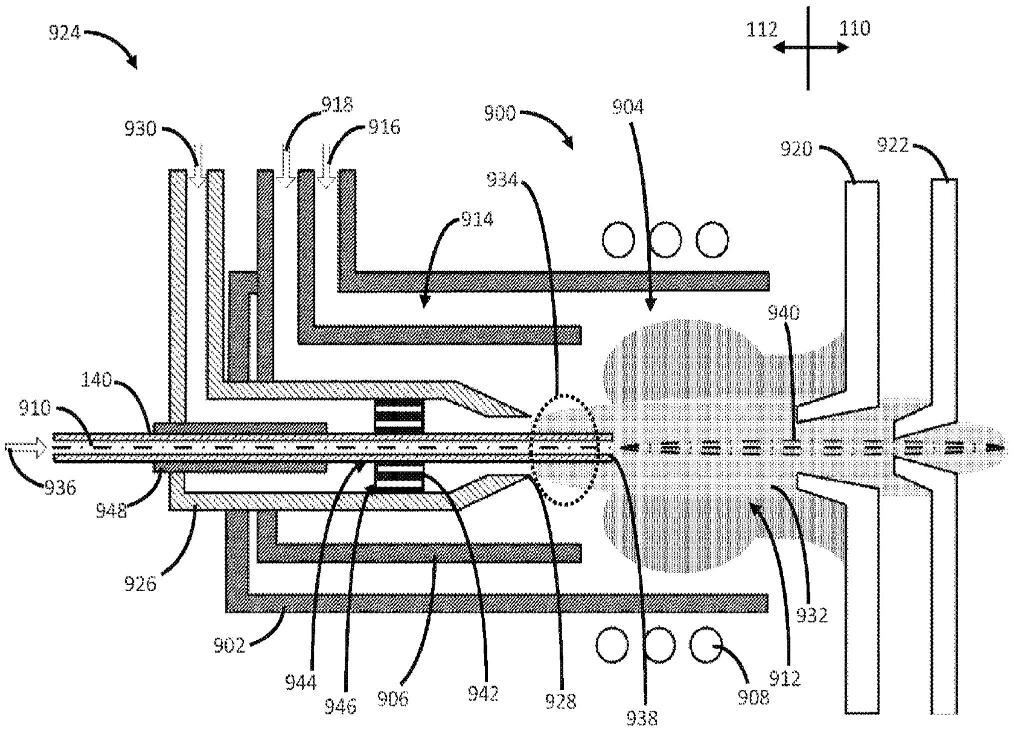
924
112
110
930
918
916
900
904
920
922
934
914
940
140
910
936
948
926
902
944
946
906
942
928
938
908
912
932

FIG. 9

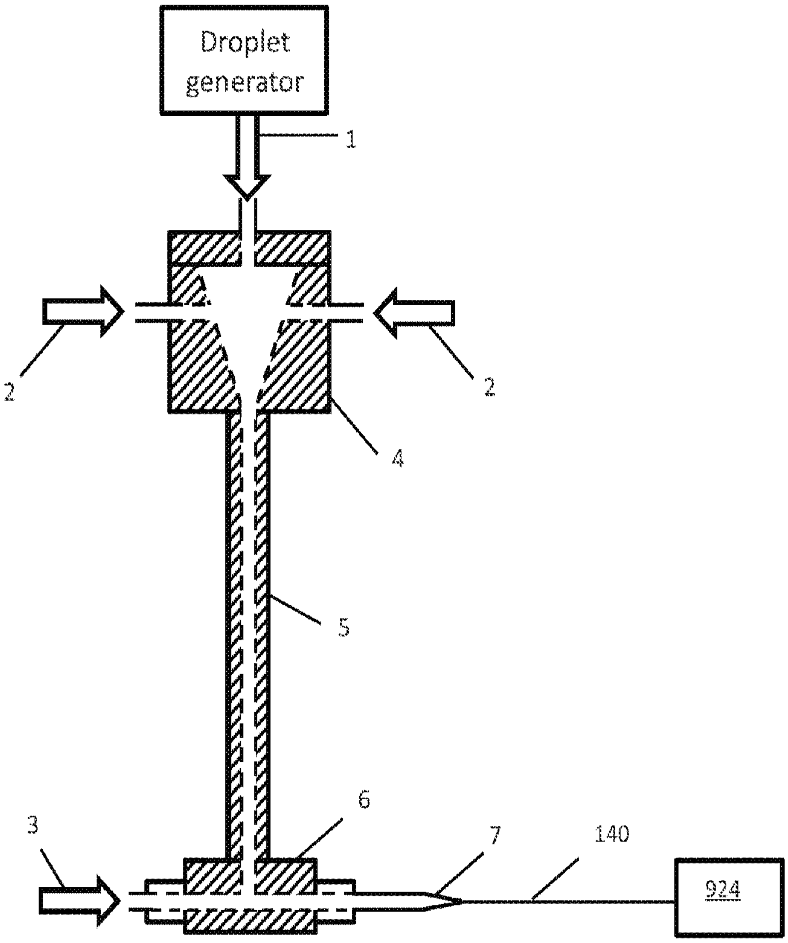

FIG. 10

LASER ABLATION CELL AND INJECTOR SYSTEM FOR A COMPOSITIONAL ANALYSIS SYSTEM

RELATED APPLICATIONS

[0001] This application claims benefit of U.S. Provisional Patent Application No. 61/764,976, filed on 14 Feb. 2013, which application is incorporated by reference as if fully set forth herein. This application also claims priority to PCT/US14/16085 filed on 12 Feb. 2014, which application is incorporated by reference as if fully set forth herein.

BACKGROUND

[0002] Embodiments of the present invention exemplarily described herein relate generally to apparatuses and methods for handling target material ejected or otherwise generated from a laser ablation site of a target (e.g., the form of particles and/or vapor). More particularly, embodiments of the present invention relate to apparatuses and methods for efficiently capturing target material, for efficiently transporting a sample containing the target material and for efficiently injecting a sample containing the target material into a sample preparation system. Embodiments of the present invention exemplarily described herein also relate generally to an apparatus for handling a target within a sample chamber. More particularly, embodiments of the present invention relate to apparatuses and methods for adjusting the position of a target holder with reduced lag and motion hysteresis.

[0003] Laser ablation Inductively Coupled Plasma Mass Spectrometry (LA-ICP-MS) or Laser ablation Inductively Coupled Plasma Optical Emission Spectrometry (LA-ICP-OES) techniques can be used to analyze the composition of a target (e.g., a solid or liquid target material). Often, a sample of the target is provided to an analysis system in the form of an aerosol (i.e., a suspension of solid and possibly liquid particles and/or vapor in a carrier gas, such as helium gas). The sample is typically produced by arranging the target within a laser ablation chamber, introducing a flow of a carrier gas within the chamber, and ablating a portion of the target with one or more laser pulses to generate a plume containing particles and/or vapor ejected or otherwise generated from the target (hereinafter referred to as “target material”), suspended within the carrier gas. Entrained within the flowing carrier gas, the target material is transported to an analysis system via a transport conduit to an ICP torch where it is ionized. A plasma containing the ionized particles and/or vapor is then analyzed by an analysis system such as an MS or OES system.

[0004] Conventional techniques such as LA-ICP-MS and LA-ICP-OES, however, are undesirably slow to carry out high-resolution compositional analysis (i.e., “imaging”) of a target within a reasonable time frame. For example, current techniques undesirably take up to about 278 hours to image an area of 100 mm^2 at a pixel resolution of 10 μm. In addition, current techniques such as LA-ICP-MS and LA-ICP-OES are also not sensitive enough for high-resolution imaging or analysis of micron-sized and sub-micron side particles (e.g., nanoparticles). Example embodiments disclosed herein address these and other problems associated with conventional compositional analysis techniques.

BRIEF DESCRIPTION OF THE DRAWINGS

[0005] FIG. **1** schematically illustrates one embodiment of an apparatus for handling a target and for handling target material ejected from or otherwise generated from the target, and includes a cross-sectional view of a sample chamber, a sample capture cell and a target holder.

[0006] FIG. **2** is a cross-sectional view, taken along line II-II shown in FIG. **2**A, schematically illustrating the sample capture cell shown in FIG. **1** according to one embodiment.

[0007] FIG. **2**A is a plan view schematically illustrating a first inlet, a second inlet, a capture cavity and an outlet of the sample capture cell when viewed in the direction indicated along line IIA-IIA in FIG. **2**.

[0008] FIG. **2**B is a plan view illustrating the first inlet, second inlet, capture cavity and outlet of the sample capture cell when viewed in the direction indicated along line IIB-IIB in FIG. **2**.

[0009] FIG. **3** is a cross-sectional view schematically illustrating laser light directed through the second inlet and capture cavity of the sample cell onto a target at a laser ablation site, and a resultant plume containing target material ejected from the target at the laser ablation site into the capture cavity of the sample cell.

[0010] FIG. **4** is a perspective, cross-sectional view schematically illustrating characteristics of the flow of carrier gas within the interior of the sample chamber into the capture cavity of the sample capture cell shown in FIG. **2**.

[0011] FIG. **5** is an enlarged, top plan view schematically illustrating the characteristics of the flow of carrier gas shown in FIG. **4** into the capture cavity of the sample capture cell shown in FIG. **2**.

[0012] FIG. **6** is an enlarged perspective, cross-sectional view of the schematic shown in FIG. **4**, schematically illustrating characteristics of the flow of carrier gas through an opening of the capture cavity and into the outlet of the sample capture cell shown in FIG. **2**, from a region between the sample capture cell and the target.

[0013] FIG. **7** is an enlarged side, cross-sectional view of the schematic shown in FIG. **4**, schematically illustrating characteristics of the flow of carrier gas through the second inlet and into the outlet of the sample capture cell shown in FIG. **2**.

[0014] FIG. **8** is a cross-sectional view schematically illustrating the sample capture cell shown in FIG. **1** incorporating an auxiliary inlet, according to another embodiment.

[0015] FIG. **9** is a cross-sectional view schematically illustrating one embodiment of an injector coupled to a sample preparation system, and a portion of an analysis system.

[0016] FIG. **10** is a partial cross-sectional view schematically illustrating one embodiment of a desolvation unit coupled between a droplet generator and an injector such as the injector shown in FIG. **9**.

DETAILED DESCRIPTION OF THE ILLUSTRATED EMBODIMENTS

[0017] Example embodiments are described below with reference to the accompanying drawings. Many different forms and embodiments are possible without deviating from the spirit and teachings of the invention and so the disclosure should not be construed as limited to the example embodiments set forth herein. Rather, these example embodiments are provided so that this disclosure will be thorough and complete, and will convey the scope of the invention to those skilled in the art. In the drawings, the sizes and relative sizes of components may be exaggerated for clarity. The terminology used herein is for the purpose of describing particular example embodiments only and is not intended to be limiting.

It is to be understood that various orientational terms such as "front" and "back" and "rear", "left" and "right", "top" and "bottom", "upper" and lower" and the like are used herein only for convenience, and not with the intention of limiting what is described to any absolute or fixed orientation relative to any environment in which any described structures may be used. As used herein, the singular forms "a," "an" and "the" are intended to include the plural forms as well, unless the context clearly indicates otherwise. It will be further understood that the terms "comprises" and/or "comprising," when used in this specification, specify the presence of stated features, integers, steps, operations, elements, and/or components, but do not preclude the presence or addition of one or more other features, integers, steps, operations, elements, components, and/or groups thereof. Unless otherwise specified, a range of values, when recited, includes both the upper and lower limits of the range, as well as any sub-ranges therebetween.

[0018] FIG. **1** schematically illustrates one embodiment of an apparatus for handling a target and for handling target material ejected from or otherwise generated from the target, and includes a cross-sectional view of a sample chamber, a sample capture cell and a target holder.

[0019] Referring to FIG. **1**, an apparatus, such as apparatus **100**, for handling a target and for handling target material ejected from or otherwise generated from the target may include a sample chamber **102** configured to accommodate a target **104** within an interior **106** thereof, a sample generator **108** configured to remove a portion of the target **104** (which may be subsequently captured as a sample) and an analysis system **110** configured to analyze a composition of the sample. Examples of materials that can be provided as a target **104** include, for example, archaeological materials, biological assay substrates and other biological materials, ceramics, geological materials, pharmaceutical agents (e.g., pills), metals, polymers, petrochemical materials, liquids, semiconductors, etc. The apparatus **100** may optionally include a sample preparation system **112** configured to excite (e.g., ionize, atomize, illuminate, heat, or the like or a combination thereof) one or more components of the sample before the sample is analyzed by the analysis system **110**. As will be described in greater detail below, the sample preparation system **112** may include a plasma torch (e.g., an ICP torch), or the like. Further, the analysis system **110** may be provided as an MS system, an OES system, or the like.

[0020] The sample chamber **102** may include a frame **114** having an optical port **116** extending therethrough to permit optical communication between the sample generator **108** and the interior **106** of the sample chamber **102**. Optionally, a transmission window **118** may be coupled to the frame **114** and to span the optical port **116**. The transmission window **118** is typically formed of a material (e.g., quartz) that is at least substantially transparent to laser light generated by the sample generator **108**. The transmission window **118** may also be sealed to the frame **114** to prevent dust, debris or other unwanted gases or other sources of contamination from entering into the interior **106** through the optical port **116**. In one embodiment, the transmission window **118** is be sealed to the frame **114** also to prevent particles ejected from the target **104**, vapor generated from the target **104**, etc., (the particles, vapor, etc., being collectively referred to herein as "target material", which is removed from the target **104**), carrier gas or other fluids present within the interior **106**, from exiting the sample chamber **102** through the optical port **116**. Although the frame is illustrated as a single, integrally-formed piece, it will be appreciated that the frame **114** may be formed of multiple components that are coupled together, as is known in the art.

[0021] The sample chamber **102** may further include one or more injection nozzles **120** each configured to introduce, into the interior **106**, a fluid such as a carrier gas (e.g., helium, argon, nitrogen, or the like or a combination thereof) at a flow rate in a range from 20 mL/min to 1000 mL/min (e.g., in a range from 100 mL/min to 150 mL/min, or 125 mL/min, or thereabout). For example, each injection nozzle **120** may be inserted through a fluid port in the frame **114** and include an inlet configured to be fluidly coupled to a fluid source (e.g., a pressurized fluid source) outside the sample chamber **102** and an outlet exposed within the interior **106** the sample chamber **102**. Seals (not shown) may be provided between frame and the injection nozzles **120** to fluidly isolate the interior **106** of the sample chamber **102** with the environment outside the sample chamber **102**. Upon introducing a carrier gas into the interior **106**, a flow of the carrier gas (also referred to herein as a "carrier gas flow") is generated within the interior **106**. It will be appreciated that the velocity and direction of the carrier gas flow at different locations within the interior **106** can vary depending upon: the shape and size of the interior **106** of the sample chamber **102**, the configuration of the one or more injection nozzles **120**, the flow rate with which carrier gas is introduced into the interior **106** by any particular injection nozzle **120**, or the like or a combination thereof. In one embodiment, the pressure within the interior **106** can be maintained (e.g., to a pressure less than or equal to 11 psi) by controlling the flow rate with which carrier gas is introduced into the interior **106**.

[0022] The apparatus **100** may further include a target positioning system configured to adjust the position of the target **104** relative to the optical path **122**. In one embodiment, the positioning system includes a target holder **124** configured to support the target **104**, a carriage **126** configured carry the target holder **124**, a base **130** configured to support the carriage **126** within the interior **106** and a positioning stage **128** configured to move the carriage **126**. Although the target holder **124** and the carriage **126** are illustrated as separate, separatable components, it will be appreciated that the target holder **124** and the carriage **126** may be integrally formed. Optionally, a height-adjustment mechanism (not shown) such as a micrometer can be provided to adjust a position of the target holder **124** along a vertical direction (e.g., along the optical path **122**) to ensure that the target **104** is arranged at a suitable or beneficial position within the interior **106**.

[0023] The positioning stage **128** may be configured to linearly translate the carriage **126** along at least one direction (e.g., an X-direction, a Y-direction orthogonal to the X-direction, or the like or a combination thereof) relative to the optical path **122**, or may be configured to rotate the carriage **126** relative to the optical path **122**, or the like or a combination thereof. In one embodiment, the positioning stage **128** and the frame **114** may both rest on a common support surface such as a table (not shown). A portion of the frame **114** may be spaced apart from the support surface to define a stage-receiving space therebetween, and the positioning stage **128** may be disposed in the stage-receiving space.

[0024] The base **130** may include a first side **132** exposed within the interior **106** and a second side **134** opposite the first side **132**. The base **130** may be coupled to the frame **114** so as to fluidly isolate the interior **106** of the sample chamber **102**

with the environment outside the sample chamber **102**. Thus, as exemplarily illustrated, the carriage **126** and the positioning stage **128** are disposed at opposite sides of the base **130**. To facilitate movement and beneficial positioning of the target **104** within the interior **106**, the carriage **126** is magnetically coupled to the positioning stage **128** through the base **130**. For example, carriage **126** may include one or more magnets (not shown) arranged therein and the positioning stage **128** may include an end effector **136** having one or more magnets attached thereto. An orientation of the magnets within the carriage **126** and the end effector **136** may be selected to generate an attractive magnetic field extending between the end effector **136** and the carriage **126**, through the base **130**. It will be appreciated that the base **130** may be constructed in any suitable or beneficial manner to transmit a magnetic field of sufficient strength between the end effector **136** and the carriage **126**. For example, the base **130** may be formed from a material such as a metal, a glass, a ceramic, a glass-ceramic, or the like. In one embodiment, the base **130** may include a material formed of fluorphlogopite mica in a matrix of borosilicate glass.

[0025] To facilitate movement of the carriage **126** across the first side **132** of the base **130**, the first side **132** may have a relatively smooth surface (e.g., with a surface roughness, Ra, of about 0.4 μm to about 0.8 μm). In one embodiment, the positioning system may further include one or more bearings coupled to the carriage **126** and configured to contact the first side **132** of the base **130**. Although the apparatus **100** is illustrated as including the target positioning system, it will be appreciated that the target positioning system may be omitted, modified or substituted for any other suitable or beneficial mechanism for adjusting the position of the target **104** relative to the optical path **122**.

[0026] Constructed according to the various embodiments exemplarily described above, the target positioning system ensures repeatable lateral angular and positioning of the target **104** within the interior **106**, with low movement lag and motion hysteresis.

[0027] The sample generator **108** is configured to direct laser light along an optical path **122**, through the optical port **116** and into the interior **106** of the sample chamber **102** to impinge upon the target **104**. The laser light may be directed along the optical path **122** as one or more laser pulses generated by one or more lasers. One or more characteristics of the laser pulses may be selected or otherwise controlled to impinge a region of the target **104** to ablate a portion of the target **104**. Characteristics that may be selected or otherwise controlled may, for example, include wavelength (e.g., in a range from about 157 nm to about 11 μm, such as 193 nm, 213 nm, 266 nm, or the like), pulse duration (e.g., in a range from about 100 femtoseconds to about 25 nanoseconds), spot size (e.g., in a range from about 1 μm to about 9 mm, or the like), pulse energy, average power, peak power, temporal profile, etc. The sample generator **108** may also include laser optics (e.g., one or more lenses, beam expanders, collimators, apertures, mirrors, etc.) configured to modify laser light generated by one or more of the lasers. As used herein, a region of the target **104** that is impinged by a laser pulse is referred to as a "laser ablation site". Upon being ablated, target material is removed from a region of the target **104** located within or adjacent to the laser ablation site to form a plume containing the target material.

[0028] To facilitate handling of the target material (e.g., so that the composition of the target material can be analyzed at the analysis system **110**) the apparatus **100** may include a sample capture cell **138** configured to capture the target material when it is arranged operably proximate to the target **104**. Target material captured by the sample capture cell **138** is also herein referred to as a "sample" or a "target sample". The apparatus **100** may further include a transport conduit **140** configured to transport the sample to the sample preparation system **112**. In the illustrated embodiment, the apparatus may include a cell support **142** coupled to the sample chamber **102** (e.g., at the frame **114**) to fix the sample capture cell **138** within the interior **106**.

[0029] In one embodiment, the aforementioned optional height-adjustment mechanism may be used to adjust the height of the target holder **124** (and, thus, the target **104**) relative to the sample capture cell **138** to ensure that the sample capture cell **138** is operably proximate to the target **104**. In another embodiment, a height adjustment mechanism such as a micrometer may be optionally provided to adjust a position of the sample capture cell **138** relative to the target **104** (e.g., along the optical path **122**) to ensure that the sample capture cell **138** is arranged at a suitable or beneficial position within the interior **106**. Thus, in addition to (or instead of) adjusting a position of the target **104** relative to the sample capture cell **138**, the position of the sample capture cell **138** relative to the target **104** may be adjusted to ensure that the sample capture cell **138** is operably proximate to the target **104**. In one embodiment the sample capture cell **138** is operably proximate to the target **104** when the sample capture cell **138** is spaced apart from the target **104** by a gap distance, d (see, e.g., FIG. **2**) in a range from 0.01 mm to 1 mm (e.g., in a range from 0.05 mm to 0.2 mm, or in a range from 0.1 mm to 0.2 mm). It will be appreciated, however, that depending on factors such as the carrier gas flow velocity within a region of the interior **106** between the sample capture cell **138** and the target **104**, the gap distance can be less than 0.01 mm or greater than 1 mm, and may even contact the target **104**.

[0030] FIG. **2** is a cross-sectional view, taken along line II-II shown in FIG. **2**A, schematically illustrating the sample capture cell shown in FIG. **1** according to one embodiment. FIG. **2**A is a plan view schematically illustrating a first inlet, a second inlet, a capture cavity and an outlet of the sample capture cell when viewed in the direction indicated along line IIA-IIA in FIG. **2**. FIG. **2**B is a plan view illustrating the first inlet, second inlet, capture cavity and outlet of the sample capture cell when viewed in the direction indicated along line IIB-IIB in FIG. **2**. FIG. **3** is a cross-sectional view schematically illustrating laser light directed through the second inlet and capture cavity of the sample cell onto a target at a laser ablation site, and a resultant plume containing the target material from the laser ablation site into the capture cavity of the sample cell. FIG. **4** is a perspective, cross-sectional view schematically illustrating characteristics of the flow of carrier gas within the interior of the sample chamber into the capture cavity of the sample capture cell shown in FIG. **2**. FIG. **5** is an enlarged, top plan view schematically illustrating the characteristics of the flow of carrier gas shown in FIG. **4** into the capture cavity of the sample capture cell shown in FIG. **2**. FIG. **6** is an enlarged perspective, cross-sectional view of the schematic shown in FIG. **4**, schematically illustrating characteristics of the flow of carrier gas through an opening of the capture cavity and into the outlet of the sample capture cell shown in FIG. **2**, from a region between the sample capture cell and the target. FIG. **7** is an enlarged side, cross-sectional view of the schematic shown in FIG. **4**, schematically illustrating characteristics of the flow of carrier gas through the second inlet and into the outlet of the sample capture cell shown in FIG. **2**.

[0031] Referring to FIGS. **2**, **2**A and **2**B, the sample capture cell **138** may generally be characterized as having an upper surface **200** (e.g., configured to generally face toward the sample generator **108**) and a lower surface **202** (e.g., configured to generally face toward the target **104**), a front end region and a back end region opposite the front end region. Generally, the sample capture cell **138** is arranged within the interior **106** such that the front end region is disposed upstream of the back end region, relative to the predominant direction of the carrier gas flow at the location in the interior **106** where the sample capture cell **138** is arranged. In one embodiment, a surface of the sample capture cell **138** defining the front end region is configured so as to be convexly-curved. For example, and as best shown in FIG. **2**B, the surface of the sample capture cell **138** defining the front end region is circularly curved, centered on an axis of a second inlet **204** (discussed in greater detail below) with a radius in a range from 1.2 mm to 1.5 mm, or thereabout). It will be appreciated, however, that depending on factors such as the predominant direction of the carrier gas flow at the location in the interior **106** where the sample capture cell **138** is arranged, the location of the second inlet **204** within the sample capture cell **138**, and other dimensions of the sample capture cell **138**, the geometric configuration of the surface defining the front end region of the sample capture cell **138** may be varied in any manner that may be suitable or beneficial. It will further be appreciated that the location of the sample capture cell **138** within the interior **106** can be selected based upon factors such as the geometry of the interior **106**, and the number and location of injection nozzles **120** generating the carrier gas flow within the interior **106**. For example, if the interior **106** has a cylindrical geometry, and if only one injection nozzle **120** is used to introduce carrier gas into the interior **106** along the diameter of the cylindrical interior **106** at the aforementioned flow rate, then the sample capture cell **138** can be located at or near the center of the interior **106**.

[0032] According to one embodiment, the sample capture cell **138** may further include a capture cavity **206**, a first inlet **208** in fluid communication with the capture cavity **206**, an outlet **210** in fluid communication with the capture cavity **206**, and a guide wall **212** exposed within the capture cavity **206**. In a further embodiment, the sample capture cell may further include the aforementioned second inlet **204** in fluid communication with the capture cavity **206**. In one embodiment, the sample capture cell **138** can be provided as a monolithic body formed of any suitable material such as a glass, a ceramic, a polymer, a metal, or the like or a combination thereof. Moreover, two or more or all of the capture cavity **206**, the first inlet **208**, the second inlet **204**, the outlet **210**, and the guide wall **212**, may be integrally formed within the body by conventional techniques (e.g., by machining, grinding, cutting, drilling, 3-D printing, etc.). In another embodiment, however, two or more or all of the capture cavity **206**, the first inlet **208**, the second inlet **204**, the outlet **210**, and the guide wall **212**, may be separately formed from different components, which are subsequently coupled together.

[0033] The capture cavity **206** extends from an opening **214** formed in the lower surface **202** of the sample capture cell **138** and is configured to receive, through the opening **214**, the plume containing the target material ejected or otherwise generated from the laser ablation site on the target **104** when the sample capture cell **138** is arranged operably proximate to the target **104**. In an embodiment in which the sample capture cell **138** is spaced apart from the target **104**, carrier gas adjacent to the target **104** can be also be transmitted into the capture cavity **206** through the opening **214**. In the illustrated embodiment, the guide wall **212** defines the extent (e.g., lateral, vertical, etc.) of the capture cavity **206** within the sample capture cell **138**. In one embodiment, the volume of the capture cavity **206** can be in a range from 0.001 cm^3 to 1 cm^3 (e.g., 0.005 cm^3, or thereabout). It will be appreciated, however, that depending on factors such as the carrier gas flow velocity within the region of the interior **106** where the sample capture cell **138** is located, the size of the plume of target material, etc., the volume of the capture cavity **206** can be less than 0.001 cm^3 or greater than 1 cm^3.

[0034] As best shown in FIGS. **2** and **2**A, a transition region of the guide wall **212** extending from the lower surface **202** into the interior of the sample capture cell **138** is rounded or chamfered. By providing a rounded or chamfered transition region, the turbulence of a surface flow **216** of carrier gas entering into the capture cavity **206** from the a region near the surface of the target **104** through the opening **214** can be controlled to be suitably or beneficially small. In one embodiment, the round or chamfer of the transition region may have a radius of 0.1 mm, or thereabout. It will be appreciated, however, that depending on factors such as the carrier gas flow velocity within a region of the interior **106** between the sample capture cell **138** and the target **104** and the aforementioned gap distance, the radius of the transition region can be significantly more or less than 0.1 mm. A more detailed rendering of the flow of carrier gas into the capture cavity **206** via the opening **214** is exemplarily and schematically illustrated in FIGS. **4** and **6**. In some embodiments, the sample capture cell **138** can be configured such that the surface flow **216** is sufficient to lift target material from the surface of the target **104** into the capture cavity **206** through the opening **214** (where, thereafter, it can be transferred into the outlet **210**) when the sample capture cell **138** is operably proximate to the target **104**.

[0035] The first inlet **208** extends from the capture cavity **206** to a surface of the sample capture cell **138** defining the front end region. Accordingly, the first inlet **208** is configured to transmit a primary flow **218** of the carrier gas from a first location adjacent to the front end region of the sample capture cell **138** into a first region **220** of the capture cavity **206**, which is adjacent to the first inlet **208**. A more detailed rendering of the flow of carrier gas through the first inlet **208** into the first region **220** of the capture cavity **206** is exemplarily and schematically illustrated in FIGS. **4** and **5**. In the illustrated embodiment, the first inlet **208** extends vertically from the lower surface **202** toward the upper surface **200** to a height, h1 (see, e.g., FIG. **2**A), of 1 mm (or thereabout), and extends horizontally between the lower surface **202** and upper surface **200** across a width, w (see, e.g., FIG. **2**A), of 2.2 mm (or thereabout). It will be appreciated, however, that depending on factors such as the carrier gas flow velocity within a region of the interior **106** at the first location, the size and shape of any portion of the first inlet **208** (e.g., from the surface of the sample capture cell **138** defining the front end region to the capture cavity **206**) may be modified in any suitable or beneficial manner. Constructed as exemplarily described above, the first inlet **208** is configured to transmit the primary flow **218** into the first region **220** of the capture cavity **206** along a first direction that is generally (or at least substantially) parallel to a surface of the target **104**. Although, in the illustrated embodiment, the first inlet **208** extends from the lower surface **202** toward the upper surface **200**, it will be appreciated that, in other embodiments, the first inlet **208** may be spaced apart from the lower surface **202**. Although, in the illustrated embodiment, dimensions (e.g., height and width dimensions) of the first inlet **208** are illustrated as being the same as those of the capture cavity **206** at the first region **220**, it will be appreciated that, in other embodiments, dimensions (e.g., height and width dimensions) of the first inlet **208** may be different from those of the capture cavity **206** at the first region **220**.

[0036] The second inlet **204** extends from the capture cavity **206** to the upper surface **200** of the sample capture cell **138**. Accordingly, the second inlet **204** is configured to transmit a secondary flow **222** of the carrier gas from a second location, adjacent to the upper surface **200** of the sample capture cell **138**, into a second region **224** of the capture cavity **206**. A more detailed rendering of the flow of carrier gas through the second inlet **204** into the second region **224** of the capture cavity **206** is exemplarily and schematically illustrated in FIG. **7**. In the illustrated embodiment, the second inlet is a configured as a circular tube having a diameter in a range from 0.5 mm to 0.85 mm (or thereabout), aligned with and extending along the optical path **122** from the capture cavity **206** to the upper surface **200** so as to a height, h2 (see, e.g., FIG. **2**A), of 2 mm (or thereabout). It will be appreciated, however, that depending on factors such as the carrier gas flow velocity within the interior **106** at the second location, the size and shape of any portion of the second inlet **204** (e.g., from the upper surface **200** of the sample capture cell to the capture cavity **206**) may be modified in any suitable or beneficial manner.

[0037] As best shown in FIGS. **2** and **2**A, a transition region of a wall extending from the upper surface **200** into the second inlet **204** is rounded or chamfered. By providing a rounded or chamfered transition region, the turbulence of the flow of carrier gas entering into the second inlet **204** can be controlled to be suitably or beneficially small. In one embodiment, the round or chamfer of the transition region may have a radius of 0.25 mm, or thereabout. Thus, the second inlet **204** may have a relatively large first diameter at the upper surface **200** and a relatively small second diameter at a location below the transition region (e.g., 0.85 mm, or thereabout). It will be appreciated, however, that depending on factors such as the carrier gas flow velocity within a region of the interior **106** over the upper surface **200** of the sample capture cell **138**, the radius of the transition region can be significantly more or less than 0.25 mm.

[0038] Constructed as exemplarily described above, the second inlet **204** is configured to transmit the flow of the carrier gas into the second region **224** of the capture cavity **206** along a second direction that is generally (or at least substantially) perpendicular to a surface of the target **104**. In another embodiment, however, the second inlet **204** may be configured to transmit the flow of the carrier gas into the second region **224** of the capture cavity **206** along a second direction that is substantially oblique to a surface of the target **104**. Further, and as best shown in FIG. **3**, the second inlet **204** is configured such that the sample generator **108** is in optical communication with a region of the target **104** (e.g., along the optical path **122**) through the second inlet **204** and the capture cavity **206**. Accordingly, laser light **300** may be directed from the sample generator **108** along the optical path **122**, through the second inlet **204** and the capture cavity **206** to impinge upon the target **104** at a laser ablation site. When the directed laser light **300** impinges the target **104** at the laser ablation site, a plume **302** containing the target material ejected or otherwise generated from the target **104**.

[0039] Depending on factors such as the material of the target **104**, characteristics of the directed laser light **300**, the velocity of the carrier gas flow, etc., vertical expansion of the plume may occur very rapidly. For example, the plume may extend to a height, h3 (see, e.g., FIG. **3**) above the target **104** of about 2 mm within less than 0.5 ms (e.g., about 2 ms) after the directed laser light **300** impinges the target **104** at the laser ablation site. By transmitting a flow of the carrier gas through the second inlet into the third region via along the second direction, the vertical expansion of the plume may be prevented or otherwise minimally re-entrained, thereby reducing or minimizing the volume that the plume of target material would otherwise occupy within the capture cavity **206**. By reducing or minimizing the volume that the plume of target material occupies within the capture cavity **206**, target material within the can be efficiently captured and transferred into the outlet **210**, as will be described in greater detail below.

[0040] The outlet **210** extends from a surface of the sample capture cell **138** defining the back end region to a region of the guide wall **212** exposed within the capture cavity **206**. Accordingly, the outlet **210** is configured to receive carrier gas from a third region **226** of the capture cavity **206** so that the received carrier gas can be transmitted to a location outside the sample capture cell **138** (e.g., via the transport conduit **140**). In the illustrated embodiment, the outlet **210** includes a first bore **228** having an inlet arranged at the third region **226** of the capture cavity **206**, and a second bore **230** axially aligned with the first bore **228** and extending from the first bore **228** to the surface of the sample capture cell **138** defining the back end region. The first bore **228** and the second bore **230** are generally configured to accommodate a portion of the transport conduit **140**. In the illustrated embodiment, the first bore **228** has a circular cross-section with a first diameter and the second bore **230** has a circular cross-section with a second diameter larger than the first diameter to additionally accommodate an outlet conduit seal **232**. The first diameter may be equal to or slightly larger than the outer diameter of the transport conduit **140** (e.g., so that the transport conduit **140** may be inserted into the first bore **228**), or may be less than or equal to the inner diameter of the transport conduit **140**. In one embodiment, the first bore **228** may have a first diameter in a range from 0.5 mm (or thereabout).

[0041] As best shown in FIGS. **2** and **2**B, a transition region of a wall extending from the guide wall **212** into the outlet **210** is rounded or chamfered. By providing a rounded or chamfered transition region, the turbulence of the flow of carrier gas entering into the outlet **210** can be controlled to be suitably or beneficially small. In one embodiment, the round or chamfer of the transition region may have a radius of 0.1 mm, or thereabout. Thus, the outlet **210** may have a relatively large diameter at the inlet of the first bore **228** (i.e., at the guide wall **212**) (e.g., 0.82 mm, or thereabout) and a relatively small diameter at a location within an intermediate region of the first bore **228** (e.g., corresponding to the aforementioned first diameter of the first bore **228**). It will be appreciated, however, that depending on factors such as the carrier gas flow velocity within the third region **226** of the capture cavity **206**, the radius of the transition region can be significantly more or less than 0.1 mm.

[0042] The guide wall **212** is configured to deflect, vector or otherwise direct one or more flows of the carrier gas introduced into the capture cavity **206** (e.g., via one or more of the opening **214**, the first inlet **208** and the second inlet **204**) such that at least a portion of the plume of target material received within the capture cavity **206** through the opening **214** are entrained by the directed flow of carrier gas, thereby so as to be transferrable into the outlet **210** (see, e.g., FIG. **5**). For purposes of discussion herein, target material transferred into the outlet **210** is "captured" by the sample capture cell **138** and, therefore, may also be referred to as a "sample" of the target **104** or as a "target sample". In one embodiment, the guide wall **212** is configured to direct the one or more flows of the carrier gas such that the flow of carrier gas into the plume **302** or into the outlet **210** is laminar or quasi-laminar. In another embodiment, however, the guide wall **212** is configured to direct the one or more flows of the carrier gas such that the flow of carrier gas into the plume **302** or into the outlet **210** is turbulent. Similarly, one or more of the aforementioned features of the sample capture cell **138** (e.g., the lower surface **202**, the guide wall **212**, the opening **214**, the first inlet **208**, the second inlet **204**, or the like) may be configured such the flow of carrier gas over the surface of the target **104** and outside the capture cavity **206** is laminar, quasi-laminar, turbulent or a combination thereof.

[0043] As best shown in FIG. **2**, the guide wall **212** is configured such that the inlet of the first bore **228** is recessed relative to a surface defining the front end region of the sample capture cell **138** by a distance of 2.5 mm (or thereabout). It will be appreciated, however, that depending on factors such as the carrier gas flow velocity within the capture cavity **206** and the location and orientation of the second inlet **204** within the sample capture cell **138**, the distance by which the inlet of the first bore **228** is recessed relative to a surface defining the front end region of the sample capture cell **138** can be significantly more or less than 2.5 mm. As best shown in FIG. 2B, the guide wall **212** is configured so as to be curved in a region adjacent to the inlet of the first bore **228** (e.g., circularly curved, centered on an axis of the second inlet **204** with a radius in a range from 0.9 mm to 1.1 mm, or thereabout). It will be appreciated, however, that depending on factors such as the carrier gas flow velocity and direction within the capture cavity **206** and the location and orientation of the second inlet **204** within the sample capture cell **138**, the geometric configuration may be varied in any manner that may be suitable or beneficial.

[0044] If the sample capture cell **138** is coupled to the transport conduit, the sample transferred into the outlet **210** can be transported to a location outside the sample capture cell **138** (e.g., via the transport conduit **140**). To couple the transport conduit **140** to the sample capture cell **138**, an end of the transport conduit **140** (also referred to as a "first end" or a "sample receiving end") is inserted into the second bore **230** and through the outlet conduit seal **232**. Optionally, and depending upon the diameter of the first bore **228**, the transport conduit **140** may be further inserted into the first bore **228**. In one embodiment, the transport conduit **140** is inserted into the first bore **228** such that the sample receiving end is recessed within the first bore **228**. For example, the sample receiving end can recessed within the first bore **228** to be spaced apart from the inlet of the first bore **228** by a distance in a range from 1 mm to 3 mm (or thereabout). In other embodiments, however, the transport conduit **140** is inserted into the first bore **228** such that the sample receiving end is recessed flush with, or extends beyond, the inlet of the first bore **228**. Upon coupling the transport conduit **140** to the sample capture cell **138** in the manner described above, the carrier gas received at the outlet can also be received within the transport conduit **140** and transported to a location outside the sample chamber **102** (e.g., to the sample preparation system **112**).

[0045] In addition to the sample receiving end, the transport conduit **140** may further include a second end (also referred to herein as a sample injection end) that is opposite the sample receiving end. Generally, the transport conduit **140** is at least substantially straight from the sample receiving end to the sample injection end, with a length (defined from the sample receiving end to the sample injection end) in a range from 20 mm to 2 m (e.g., in a range from 50 mm to 500 mm, or in a range from 100 mm to 600 mm, or in a range from 200 mm to 500 mm, or in a range from 200 mm to 450 mm, or thereabout) and an inner diameter in a range from 50 μm to 1 mm (e.g., in a range from 50 μm to 500 μm, or 250 μm, or thereabout). It will be appreciated, however, that depending on factors such as the pressure within the interior **106**, the inner diameter of the transport conduit **140**, the configuration of the sample chamber **102** and the sample preparation system **112**, the length of the transport conduit **140** may be less than 20 mm or greater than 2 m. Similarly, depending on factors such as the pressure within the interior **106** and the length of the transport conduit **140**, the inner diameter of the transport conduit **140** may be less than 50 μm or greater than 1 mm. The inner diameter of the transport conduit **140** at the sample receiving end may be same or different (i.e., larger or smaller) than the inner diameter of the transport conduit **140** at the sample injection end. Further, the inner diameter of the transport conduit **140** may be at least substantially constant along the length thereof, or may vary. In one embodiment, the transport conduit **140** is provided as a single, substantially rigid tube having no valves between the sample receiving end and sample injection end. Exemplary materials from which the transport conduit **140** can be formed include one or more materials selected from the group consisting of a glass, a polymer, a ceramic and a metal. In one embodiment, however, the transport conduit **140** is formed of fused glass. In another embodiment, the transport conduit **140** is formed of a polymer material such as a fluoropolymer (e.g., perfluoroalkoxy, polytetrafluoroethylene, or the like or a combination thereof), polyethylene terephthalate, or the like or a combination thereof. In yet another embodiment, the transport conduit **140** is formed of a ceramic material such as alumina, sapphire, or the like or a combination thereof. In still another embodiment, the transport conduit **140** is formed of a metal material such as stainless steel, copper, platinum, or the like or a combination thereof.

[0046] Constructed as exemplarily described above, the transport conduit **140** can efficiently transport a sample from the sample capture cell **138** to the sample preparation system **112**. Efficient capture and transfer of a sample from a laser ablation site to the transport conduit **140**, coupled with efficient transport of the sample from the sample capture cell **138** to the sample preparation system **112**, can enable the analysis system **110** to generate signals (e.g., corresponding to the composition of target sample) that have relatively short peak widths (e.g., in a range from about 10 ms to about 20 ms (e.g., 12 ms, or thereabout), measured relative to a baseline where 98% of the total signal is observed within 10 ms) and correspondingly fast wash-out times. Generating signals having such relatively short peak widths and fast wash-out times, can help to facilitate high-speed and high sensitivity compositional analysis of the target **104**. Similarly, depending on factors such as the pressure within the interior **106** and the length of the transport conduit **140**, the inner diameter of the transport conduit **140**, the peak width may be beneficially increased to 1 s or thereabout.

[0047] FIG. **8** is a cross-sectional view schematically illustrating the sample capture cell shown in FIG. **1** incorporating an auxiliary inlet, according to another embodiment.

[0048] Referring to FIG. **8**, the aforementioned sample capture cell may further include an auxiliary inlet, such as auxiliary inlet **800**, extending from the capture cavity **206** to the upper surface **200** of the sample capture cell **138**. Accordingly, the auxiliary inlet **800** is configured to transmit an auxiliary flow **802** of the carrier gas from a third location, adjacent to the upper surface **200** of the sample capture cell **138**, into a fourth region **804** of the capture cavity **206**. Upon being introduced into the fourth region **804**, the auxiliary flow **802** may mix with the directed flow(s) of carrier gas present within the capture cavity **206** and, thereafter, transferred into the outlet **210**. In the illustrated embodiment, the fourth region **804** is closer to the first region **220** than the third region **226**. In other embodiments, however, the fourth region **804** may be closer to the third region **226** than the first region **220**, or may be equidistant between the first region **220** and the third region **226**.

[0049] In the illustrated embodiment, the auxiliary inlet is configured as a circular tube having a diameter equal to or different from (e.g., larger than or smaller than) the diameter of the second inlet. It will be appreciated, however, that depending on factors such as the carrier gas flow velocity within the interior **106** at the second location, the size and shape of any portion of the auxiliary inlet **800** (e.g., from the upper surface **200** of the sample capture cell to the capture cavity **206**) may be modified in any suitable or beneficial manner. Although not illustrated, the auxiliary inlet may include a wall having a transition region extending from the upper surface **200** into the auxiliary inlet **800** and configured in the manner discussed above with respect to the second inlet **204**. Constructed as exemplarily described above, the auxiliary inlet **800** is configured to transmit the auxiliary flow **802** into the fourth region **804** of the capture cavity **206** along a third direction that is for example, different from the aforementioned first direction and second direction. In one embodiment, the third direction may be substantially oblique, at least substantially parallel or at least substantially perpendicular to the surface of the target **104** when the sample capture cell **138** is operably proximate to the target **104**.

[0050] Although the auxiliary inlet **800** is illustrated as being integrally formed within the body of the sample capture cell **138**, it will be appreciated that the auxiliary inlet **800** may be separately formed from a different component, which is subsequently coupled to the body of the sample capture cell **138**. Further, although the auxiliary inlet **800** is illustrated as transmitting the auxiliary flow **802** of carrier gas into the fourth region **804** of the capture cavity **206**, the auxiliary inlet **800** may be positioned, oriented or otherwise configured to transmit the auxiliary flow **802** of carrier gas into the first region **220**, the third region **226**, or the second region **224** (e.g., the auxiliary inlet **800** may extend to the second inlet **204**). In the illustrated embodiment, the auxiliary inlet **800** is configured to transmit the auxiliary flow **802** of carrier gas into the capture cavity **206** along a third direction that extends toward the outlet **210** and the target **104**. In other embodiments, however, the third direction may extend toward the outlet **210** and away from the target **104**, toward the first inlet **208** and the target **104**, toward the first inlet **208** and away from the target **104**, or the like or a combination thereof.

[0051] Although the auxiliary inlet **800** is described above as being configured to transmit the auxiliary flow **802** of carrier gas from the third location adjacent to the upper surface **200** of the sample capture cell **138** into the capture cavity **206**, it will be appreciated that the auxiliary inlet **800** may be configured to transmit a flow of the carrier gas from any location adjacent to any surface of the sample capture cell **138**. Moreover, although the auxiliary inlet **800** is described above as being configured to transmit a flow of carrier gas into the capture cavity **206**, it will be appreciated that the sample capture cell **138** may be configured such that the auxiliary inlet **800** can be coupled to an external auxiliary fluid source (e.g., containing a fluid such as helium gas, argon gas, nitrogen gas, water vapor, atomized or nebulized fluids, atomized or nebulized solvents, discrete droplets containing microparticles, nanoparticles, or biological samples such as cells, or the like, or a combination thereof). In such a configuration, the auxiliary inlet **800** may transmit a fluid that is different from the carrier gas into the capture cavity **206**, or may transmit an auxiliary flow of the carrier gas into the capture cavity **206**, the auxiliary flow having a different characteristic (e.g., a different temperature, a different flow rate, etc.) from the carrier gas flow generated by the one or more injection nozzles **120**. It will be appreciated that any fluid introduced into the capture cavity **206** by the auxiliary inlet **800** may mix with the directed flow(s) of carrier gas present within the capture cavity **206** and, thereafter, transferred into the outlet **210**. In one embodiment, when coupled to an auxiliary fluid source, the auxiliary inlet **800** may transmit one or more fluids such as nitrogen gas or water vapor to facilitate sample counting, laser ablation standardization, calibration, or the like or a combination thereof.

[0052] FIG. **9** is a cross-sectional view schematically illustrating one embodiment of an injector coupled to a sample preparation system, and a portion of an analysis system.

[0053] In the embodiment exemplarily illustrated in FIG. **9**, the sample preparation system **112** may be provided as an ICP torch **900** including an outer tube **902** (also referred to herein as a "confinement tube **902**") enclosing a space **904** where a plasma can be generated, an inner tube **906** (also referred to herein as a "plasma gas tube **906**") arranged within the confinement tube **902**, coaxial with an injection axis **910** of the confinement tube **902**, and a coil **908** configured to ionize gas within the space **904** to generate a plasma **912** (e.g., occupying the darkly-shaded region within the space **904**) when energized by an RF source (not shown). Although the sample preparation system **112** is illustrated as including a coil **908**, it will be appreciated that the sample preparation system **112** may alternatively or additionally include ionization mechanisms of other configurations. For example, a set (e.g., a pair) of flat plates may be disposed outside the confinement tube **902** to ionize the plasma gas within the space **904** to generate the plasma.

[0054] In the illustrated embodiment, the confinement tube **902** and the plasma gas tube **906** are spaced apart from each other to define an annular outer gas transmission conduit **914** (also referred to as a "coolant gas transmission conduit") that may be coupled to a gas source (e.g., a reservoir of pressurized gas, not shown) to receive an outer flow **916** (also referred to as a "coolant flow") of gas (e.g., argon gas) and transmit the received outer flow **916** of gas into the space **904** (e.g., at a flow rate in a range from 10 L/min to 15 L/min, or thereabout). Gas introduced into the space **904** via the outer flow **916** can be ionized to form the aforementioned plasma **912**. Generally, plasma **912** generated has a power of about 1.5 kW or less. In one embodiment, however, the plasma **912** generated can have a power higher than 1.5 kW (e.g., sufficient to melt the confinement tube **902**). In such an embodiment, the gas introduced into the space **904** via the outer flow **916** can also be used to cool the confinement tube **902**, preventing the confinement tube **902** from melting.

[0055] Optionally, the plasma gas tube **906** may be coupled to an auxiliary gas source (e.g., a reservoir of pressurized gas, not shown) to receive an intermediate flow **918** (also referred to as an "auxiliary flow") of gas (e.g., argon gas) and transmit the received intermediate flow **918** of gas into the space **904** (e.g. at a flow rate in a range from 1 L/min to 2 L/min). Gas introduced into the space **904** via the intermediate flow **918** can be used to adjust the position the base of the plasma **912** along the injection axis **910** relative to the confinement tube **902**.

[0056] A portion of the plasma **912** generated within the space **904** is then transferred into the analysis system **110** (e.g., an MS system) by passing sequentially through an interface (e.g., an interface including a sampling cone **920** and a skimmer cone **922**) of the analysis system **110**. Although the analysis system **110** is illustrated as having an interface with the sampling cone **920** and the skimmer cone **922**, it will be appreciated that the interface may be differently configured in any manner suitable or beneficial manner. If the aforementioned target material generated within the sample chamber **102** is introduced in the plasma generated within the space **904**, then the target material may transferred into the analysis system **110** for compositional analysis.

[0057] To facilitate introduction of the sample through the transport conduit **140** into a sample preparation system such as sample preparation system **112**, the apparatus **100** may include an injector, such as injector **924**. The injector **924** may be detachably coupled to, or otherwise arranged operably proximate to, the sample preparation system **112** by any suitable or beneficial mechanism. In the illustrated embodiment, the injector **924** may include an outer conduit **926** having a fluid injection end **928**, and the aforementioned transport conduit **140**.

[0058] Generally, the outer conduit **926** is arranged within the plasma gas tube **906**, coaxial with the injection axis **910** and is configured to be coupled to a fluid source (e.g., one or more reservoirs of pressurized gas, not shown) to receive an outer injector flow **930** of a fluid (e.g., argon gas). Fluid within the outer injector flow **930** is injectable into the space **904** through a fluid injection end **928** of the outer conduit **926**. Generally, the inner diameter of the outer conduit **926** at the fluid injection end **928** is in a range from 1.5 mm to 3 mm (e.g., 2 mm, or thereabout). Upon injecting the fluid into the space **904** from the fluid injection end **928**, a central channel **932** (e.g., occupying the lightly-shaded region within the space **904**) can be formed within or "punched through" the plasma **912**. Further, fluid injected into the space **904** through the fluid injection end **928** tends to generate a first zone **934** relatively close to the fluid injection end **928**, which is characterized by a relatively high turbulence of fluid (e.g., including fluid from the outer injector flow **930** and possibly gas from the intermediate flow **918**). Turbulence quickly decreases along the injection axis **910** with increasing distance from the fluid injection end **928** into the plasma **912**. Accordingly, a second zone relatively distant from the fluid injection end **928** along the injection axis **910** and located within the central channel **932**, can be characterized by a relatively low turbulence of fluid (e.g., including fluid from the outer injector flow **930** and possibly gas from the intermediate flow **918**).

[0059] Generally, the transport conduit **140** configured to direct a carrier flow **936** containing the aforementioned target sample, along with any other fluids that carry the sample through the transport conduit **140** (e.g., the aforementioned carrier gas, any fluid introduced into the capture cavity **206** by the auxiliary inlet **800**, or the like or a combination thereof) through the aforementioned sample injection end (indicated at **938**). When directed through transport conduit **140** and past the sample injection end **938**, the carrier flow **936** (and, thus, the sample contained therein) is injectable into the space **904** (e.g., along the injection axis **910**), where it can be ionized and subsequently transferred to the analysis system **110**.

[0060] In one embodiment, the transport conduit **140** may be arranged within the outer conduit **926**, coaxial with the injection axis **910**, such that the sample injection end **938** is locatable within the outer conduit **926**, locatable outside the outer conduit **926**, or a combination thereof. For example, the transport conduit **140** may be arranged within the outer conduit **926** such that the sample injection end **938** is located within the outer conduit **926**, and is spaced away from the fluid injection end **928** by a distance in a range from 0 mm to 20 mm. In another example, transport conduit **140** may be arranged within the outer conduit **926** such that the sample injection end **938** is located outside the outer conduit **926**, and is spaced away from the fluid injection end **928** by a distance in a range from greater than 0 mm to 15 mm (e.g., by a distance in a range from 6 mm to 12 mm, or by a distance in a range from 8 mm to 12 mm, or by a distance in a range from 10 mm to 12 mm, or by a distance of 12 mm, or thereabout). Depending on factors such as the configuration of the outer conduit **926**, the flow rate of the outer injector flow **930** exiting the outer conduit **926**, and the configuration of the sample preparation system **112**, it will be appreciated that the sample injection end **938** may be located within the outer conduit **926** and spaced away from the fluid injection end **928** by a distance greater than 20 mm (or may be located outside the outer conduit **926** and spaced away from the fluid injection end **928** by a distance greater than 15 mm). The position of the transport conduit **140** may be fixed relative to the outer conduit **926**, or may be adjustable.

[0061] In one embodiment, the relative position of the sample injection end **938** may be selected or otherwise adjusted to be positioned at a location (e.g., within the space **904**) characterized by a fluid turbulence which is less that associated with the aforementioned first zone **934**. For example, the sample injection end **938** may be positioned to be disposed within the aforementioned second zone. When the carrier flow **936** is injected from the sample injection end **938** when located within the second zone, lateral diffusion of the ionized target sample within the central channel **932** of the plasma **912** can be reduced significantly compared to the central channel **932** (e.g., as indicated by the relatively focused beam **940** of the ionized target sample). As a result, the beam **940** can be kept at least substantially on-axis relative to the interface of the analysis system **110** to enhance the sampling efficiency obtainable by the analysis system **110** and the sensitivity of the analysis system **110**.

[0062] In one embodiment, the injector **924** may include a centering member **942** configured to maintain the radial position of the transport conduit **140** within the outer conduit **926**. As exemplarily illustrated, the centering member **942** may be disposed within the outer conduit **926** and include a central bore **944** though which the transport conduit **140** can be inserted and a plurality of peripheral bores **946** disposed radially and circumferentially about the central bore **944** to permit transmission of the outer injector flow **930** from the aforementioned fluid source to the fluid injection end **928**. In one embodiment, the injector **924** may further include a conduit guide **948** configured to help guide insertion of the transport conduit **140** into the centering member **942** from a location outside the injector **924**.

[0063] Constructed as exemplarily described above, the outer conduit **926** of the injector **924** may have the same primary function as a conventional ICP torch injector, in that it provides a fluid flow (e.g., Ar, or admixtures thereof with helium gas or nitrogen gas), that establishes the central channel of the plasma **912** into which the sample is introduced. In the injector **924** described above, the transport conduit **140** need not be coupled to the sample capture cell **138** as described above. In other such embodiments, the transport conduit **140** may alternatively or additionally be used to introduce a standard (e.g., to enable optimization of instrumental parameters, to enable calibration, etc.) into the analysis system **110** via a sample preparation system such as the sample preparation system **112**, or the like. Such a standard could be introduced as an aerosol or dried aerosol (e.g. from a nebuliser, or as discrete droplets from a droplet generator, or as a gas or vapor generated by chemical or thermal means, etc.). The standard could even be an aerosol from a sample chamber other than the sample chamber **102**. In other such embodiments, the transport conduit **140** may alternatively or additionally be used to introduce additional gases into the sample preparation system **112** (e.g. helium gas, nitrogen gas, water vapor derived for example from thermal vaporization or a nebulizer or droplet generator, etc.).

[0064] In one embodiment, the sample chamber **102** may be substituted or used in conjunction with a discrete droplet generator (e.g., derived from piezoelectric or thermal ink jet technologies, although any source of discrete droplets capable of delivering particles of less than 25 μm, or thereabout, to the sample preparation system **112** would work). In some applications, a continuous source of droplets, such as from a nebulizer, or continuous flow of vapor (e.g., water vapor). In such embodiments, the droplet generators may be coupled to a desolvation stage to carry out prior evaporation (which may be complete or partial) of the droplets. Droplet/desolvation technologies are well known and widely published.

[0065] In one embodiment, the droplet generator and accompanying desolvation unit may include two modes of operation. In a first mode of operation, the droplet generator and accompanying desolvation unit may replace the sample chamber **102** as the sample source, in which case a sample may be introduced directly into the transport conduit **140** of the injector **924** as a sequence of discrete droplets having diameters in the low or sub-micron range (after desolvation). These droplets may contain variously, for example, liquid samples, liquid droplets containing biological samples such as single cells, or micro or nano-particles. In a second mode of operation, the droplet generator and accompanying desolvation unit may run simultaneously and in synchronicity with the sample generator **108** and sample chamber **102** so that the liquid droplets can be introduced into the transport conduit simultaneously with the aerosol containing the target material, or sequentially in single or multiple events alternated with the aerosol containing the target material. This second mode of operation provides a mechanism for calibration (e.g., if the droplets contain standards), a mechanism for control of plasma conditions (e.g., if the droplets contain a solvent), or a mechanism for a quasi-continuous signal output that can be used for optimisation of instrumental parameters.

[0066] FIG. **10** is a partial cross-sectional view schematically illustrating one embodiment of a desolvation unit coupled between a droplet generator and an injector such as the injector shown in FIG. **9**.

[0067] Referring to FIG. **10**, the desolvation unit may include an adaptor **4** configured to receive a flow of droplets and/or vapor (e.g., as indicated at **1**) and one or more desolvator gas flows (e.g., as indicated at **2**) where the received droplet(s), vapor(s) and other gas flows can be mixed and thereafter be transported (e.g., vertically downwardly under the influence of gravity/and or the desolvating gas flow) through a tube **5** (e.g., a stainless steel tube) into a first inlet of an adaptor coupling **6**, which may further include a second inlet configured to receive a flow of a make-up fluid (e.g., as indicated at **3**). Within the adaptor coupling **6**, the mixed droplet(s), vapor(s) and other gas flows are entrained by the flow of make-up fluid, transported through a tapered reducer **7** and into the transport conduit **140** and, thereafter, into the aforementioned injector **924**. It will be appreciated that the taper provided by the tapered reducer **7** can be made sufficiently gradual to avoid introducing undesirable turbulence and particle loss.

[0068] Constructed as described above, the illustrated droplet generator and associated desolvation unit replace the sample chamber **102** and sample capture cell **138** discussed above. In another embodiment, however, the illustrated droplet generator and associated desolvation unit may be placed in-line with the sample chamber **102** and/or sample capture cell **138**. In such an embodiment, an opening may be formed in the transport conduit **140** at a location between the sample receiving end (which is disposed within the sample chamber **102**, coupled to the sample capture cell **138**) and the sample injecting end **938** (which is disposed within the injector **924**), and the adaptor coupling **6** may be coupled to the transport conduit **140** to place the tube **5** in fluid communication with the interior of the transport conduit **140**.

[0069] The foregoing is illustrative of example embodiments of the invention and is not to be construed as limiting thereof. Although a few example embodiments have been described, those skilled in the art will readily appreciate that many modifications are possible without materially departing from the novel teachings and advantages of the invention. Accordingly, all such modifications are intended to be included within the scope of the invention as defined in the following claims.

What is claimed is:

1. An apparatus, comprising:

an injector configured to be arranged operably proximate to a plasma torch configured to generate a plasma within a confinement tube thereof, the injector including:

an outer conduit having a fluid injection end, wherein the outer conduit is configured to transport an outer injector flow of a fluid to the fluid injection end such that the fluid is injectable into the confinement tube from the fluid injection end; and

a transport conduit disposed within the outer conduit at the fluid injection end and having an sample injection end, wherein the transport conduit is configured such that a carrier flow containing material is injectable through the sample injection end.

2. The apparatus of claim **1**, wherein:

the outer conduit is configured to generate, within the confinement tube, a first zone containing a fluid flow having a relatively high turbulence and a second zone containing a fluid flow having a relatively low turbulence, wherein the first zone is closer to the fluid injection end than the second zone; and

the transport conduit has a sample injection end located within the second zone, wherein the transport conduit is configured such that the carrier flow containing material is injectable into the second zone from the sample injection end.

3. The apparatus of claim **2**, wherein the outer conduit extends from the fluid injection end along an injection axis and the transport conduit extends from the sample injection end along the injection axis.

4. The apparatus of claim **2**, wherein the outer conduit and the transport conduit are coaxial.

5. The apparatus of claim **2**, wherein sample injection end extends beyond the fluid injection end by a distance in a range greater than 1 mm.

6. The apparatus of claim **2**, wherein sample injection end extends beyond the fluid injection end by a distance in a range less than 15 mm.

7. The apparatus of claim **1**, wherein the sample injection end is located within the outer conduit.

8. The apparatus claim **1**, wherein the sample injection end is located outside the outer conduit.

9. The apparatus of claim **1**, wherein a position of the transport conduit relative to the outer conduit is fixed.

10. The apparatus of claim **1**, wherein a position of the transport conduit relative to the outer conduit is adjustable.

11. The apparatus of claim **1**, wherein the transport conduit further includes an sample receiving end opposite the sample injection end and configured to receive the target material.

12. The apparatus of claim **1**, wherein the transport conduit is configured to transport at least a portion of the material received at the sample receiving end to the sample injection end.

13. The apparatus of claim **12**, wherein the transport conduit is configured to transport at least a portion of the material received at the sample receiving end to the sample injection end, and the transport conduit is configured such that at least substantially all of the material is transportable from the sample receiving end to the sample injection end.

14. The apparatus of that claim **1**, further comprising the plasma torch.

15. The apparatus of claim **1**, further comprising the plasma torch, wherein the plasma torch comprises an inductively coupled plasma (ICP) torch having the confinement tube.

16. The apparatus of claim **15**, wherein the ICP torch includes an induction coil disposed outside the confinement tube and configured to ionize the fluid and the aerosol.

17. The apparatus of claim **15**, wherein the ICP torch includes a set of flat induction plates disposed outside the confinement tube and configured to ionize the fluid and the aerosol.

18. The apparatus of claim **1**, further comprising a sample chamber having an interior configured to accommodate a target from which the material is removed.

19. The apparatus of claim **18**, wherein the sample receiving end of the transport conduit is disposed within the sample chamber.

20. The apparatus of claim **1**, further comprising a sample capture cell coupled to the sample receiving end of the transport conduit and configured to be arranged operably proximate to the target, wherein the sample capture cell is configured capture the material and transfer the captured material to the transport conduit.

21. The apparatus of claim **20**, wherein the sample capture cell is arranged within the interior of the sample chamber.

22. The apparatus of claim **1**, further comprising a droplet generator in fluid communication with an interior of the transport conduit, the droplet generator is configured to deliver particles into the interior of the transport conduit.

23. The apparatus of claim **22**, further comprising a desolvation unit coupled between the droplet generator and the transport conduit.

* * * * *